UNIVERSITÀ DELLA CALABRIA

UNIVERSITA' DELLA CALABRIA

Dipartimento di Ingegneria per l'Ambiente e il Territorio e Ingegneria Chimica

Dottorato di Ricerca in

Scienze e Ingegneria dell'Ambiente, delle Costruzioni e dell'Energia

CICLO

XXIX

TITOLO TESI

Synthesis, characterization and catalytic assessment of zeolite-based catalysts for dimethyl ether production

Settore Scientifico Disciplinare ING-IND/27

Coordinatore: Ch.mo Prof. Pietro Salvatore PANTANO

Firma

Supervisore/Tutor: Ch.mo Prof. Massimo MIGLIORI

Firma

Dottorando: Dott. Enrico CATIZZONE

Firma

To Ludovica

Preface

This work has been performed at the Laboratory for Industrial Chemistry and Technologies of the Department of Environmental and Chemical Engineering of University of Calabria (UNICAL, Italy) from November 2013 until now under the supervision of Professor Massimo Migliori. I have spent four months at the Laboratory of Catalysis and Spectroscopy (LCS), CNRS ENSICAEN, University of Caen (France) under supervision of Professor Valentin Valtchev. This work was co-financed by the Italian National Agency for New Technologies, Energy and Sustainable Economic Development (ENEA). Some physicochemical characterizations (as N_2O titration and TEM) and CO_2-to-DME hydrogenation tests were carried out in collaboration with the Institute for Advanced Energy Technologies (CNR-ITAE) "Nicola Giordano", Messina, Italy. Synthesis and characterization of some FER-type materials were carried-out in collaboration with LCS laboratory.

At the end of this work, I want to express my deep gratefulness to my adviser, Professor Massimo Migliori, for providing me the opportunity to start my research here in UNICAL. I know him in 2008, during first year bachelor degree in Chemical Engineering. Furthermore, he was supervisor of my master thesis in Chemical Engineering in November 2013. I have learned a lot from you during these years, not only your insightful academic discussion and encouragement, but also your enthusiasm and sensitive attitude in science finding. Thanks, thanks, thanks.

I would like to thank my co-adviser Professor Girolamo Giordano for welcoming me into your research group. I know, I still have much to learn but I hope that, thanks to your experience, I hope to become a good researcher.

I also want to thank Professor Valentin Valtchev from LCS (Caen). Despite I have spent just four months in your laboratory, I wish to say you thank for the special experience that I have lived with guys of your high-level equipe and for your paramount scientific discussions.

The special acknowledgment should be given to ENEA for the financial support.

I want gratefully acknowledge Dr. Francesco Frusteri and Dr. Giuseppe Bonura for analytical support and fruitful discussions.

I would like to thank Dr. Alfredo Aloise (for the wise theological lessons and equally wise discussions on zeolites), Dr. Danilo Vuono (for the long discussion on carbon nanotubes and equally long laughter), master thesis students of the Laboratory for Industrial Chemistry and Technologies and all the people that I have had the honour of meeting. Thanks a lot to you, my sweet love.

I dedicate this thesis to my sweet nephew, Ludovica, and I thank my wonderful family…for what? for everything.

Enrico Catizzone

May, 2017

Abstract

Dimethyl ether (DME) has represented a reliable alternative fuel for Diesel engines since decades and, more recently, this compound is receiving a renewed attention also as intermediate for olefins production. Together with many other technologies this application can contribute to reduce the CO_2 footprint, mitigating the environmental impact of fossil fuels. Apart from classic liquid phase production process via methanol dehydration, new promising direct gas-phase routes have been proposed, starting from either syngas mixture or via-carbon dioxide hydrogenation.

Whatever the route, the acid-catalysed step of methanol dehydration plays a key role in catalyst durability, DME productivity and production costs. Therefore, in view of economically sustainable large-scale gas-phase DME production, low temperature activity, performances and stability are essential factors to consider when developing a reliable catalyst for this step. γ-Al_2O_3 traditionally plays acid function for direct conversion of methanol to dimethyl ether, but it was also considered as first option co-catalyst for the direct route from syngas coupled with redox catalyst (e.g. $Cu/ZnO/Al_2O_3$), promoting the alcohol formation via-CO/CO_2 hydrogenation. At reaction temperature traditionally adopted for both direct and indirect routes for (up to 300°C), γ-Al_2O_3 offers high selectivity towards DME and, due its low acidity, it also inhibits olefins formation. Despite this unchallengeable advantage, this catalyst requires relatively high temperatures and it is rapidly deactivated by strong water adsorption as demonstrated by several studies. As already mentioned some interesting studies were recently carried out on the gas phase process, replacing CO with CO_2 during direct route, adding more value to DME as "green chemical" because of the CO_2 footprint reduction. In this process, the revers water gas shift reaction significantly increases the amount of produced water, therefore a stable acid function is once more necessary to prevent catalyst deactivation by water adsorption on acid sites. In this concern, exhibiting both higher activity (even at low reaction temperature) and higher resistance to water adsorption, zeolites (manly MFI and modified-MFI) were proposed as catalyst alternative to γ-Al_2O_3. On the other hand, by using zeolites for selective DME synthesis, both acidity and structure have to be to tuned, in order to mitigate or inhibit undesired reactions such as olefins formation (by hydrocarbon pool mechanism). In fact, zeolites as MFI, BEA, CHA, TON are well-known catalysts for Methanol-to-Hydrocarbons (MTH) processes, catalysed by strong acid sites presents on the framework of these materials. On the other hand, the shape-selectivity

offered by zeolites, may permits to act on coke formation, increasing catalyst stability and selectivity. Moreover, investigations are still necessary in order to individuate the suitable channel system to produce DME over zeolites ensuring high DME productivity, selectivity and resistance to carbon deposition.

This Ph.D thesis consists of four main objectives.

The first objective was to synthesise and characterize zeolites with different channel system (MOR, MTW, EUO, TON, FER, CHA, BEA and MFI), different acidity (aluminium content or Brønsted/Lewis distribution) and different crystals morphology and characterize them by classical analytic techniques as XRD, porosimetry, TG/DTA, SEM, TEM, NH_3-TPD and FT-IR. The main results are summarized in Chapter 4.

The second objective was to carried out a preliminary screening in order to individuate the most suitable channel system for DME production by methanol dehydration reaction in terms of activity, DME selectivity, stability and coke deposition. 2-dimensional FER structure exhibited reliable catalytic performances whilst 1-dimensional and 3-dimnesional channel system exhibits fast deactivation, low selectivity towards DME or high carbon deposition. Analysis of spent catalysts showed that channel configuration affects strongly both coke composition and location. Commercial γ-Al_2O_3 was used as benchmark exhibiting high selectivity towards DME but usually lower activity than zeolites. The main results are summarized in Chapter 5.

The third objective was to elucidate the role of acid sites (concentration, type, distribution and strength) and crystal size of FER-type catalysts during methanol dehydration reaction. Results showed that acid properties affect strongly catalytic performances. In particular, catalytic activity increases as aluminium content increases but the presence of Lewis acid sites improves catalytic performances in terms of overall turnover frequency of the catalyst. Decreasing crystal size of FER-type material it was possible to reduce drastically the amount of deposited coke. The main results are summarized in Chapter 6.

Finally, the fourth objective of this thesis was to evaluate catalytic performances of CuZnZr-zeolite hybrid systems for one-step CO_2-to-DME hydrogenation, by assessing the effect of the topology of three different zeolites (MOR, FER and MFI) on the distribution of metal-oxides during catalyst preparation, revealing how such distribution can affect the nature and the interaction of the active sites generated. The catalytic results clearly evidenced a net difference in behaviour among the hybrid systems, both in term

of CO_2 conversion and product distribution. In particular, CuZnZr-FER catalyst exhibited superior performances as the consequence of better efficiency in mass transferring ensured by the interaction of neighbouring sites of different nature on ferrierite after metal-oxide co-precipitation. A progressive decay of activity was observed during a long-term stability test caused, probably, to strong adsorbing of water on oxygen vacancies where CO_2 activated. The main results are sumamrized in Chapter 7.

Table of Contents

CHAPTER 3

Experimental

CHAPTER 4

Physicochemical properties of investigated catalysts

CHAPTER 5

Methanol dehydration over zeolites: the effect of channel system

CHAPTER 1
DME: a friend molecule

Introduction

World energy demand is strongly increasing. The continue growing of the world's population, the enhancement of welfare, industrialization and fast-growing emerging economies development (e.g. China, India) cause a continue growing in the demand of energy [1]. It is estimated that energies consumption is increasing by 34% in the last twenty years. Fossil fuels remain the main source of energy especially in transport and industry sectors. In this concern, transport accounting for almost two-thirds of the total liquid fuels demand. This important demand of liquid fuel for transport application is strongly increasing because the sharp increasing in vehicle number in emerging economies from one billion of vehicles to around 2.5 billion in just twenty years in the world, due to the fast economy growing mainly of China and India. This *need* of high energy demand is in contrast with the *need* of reducing pollution emission, minimizing the impact of energy utilization on the environment and reducing the pollutants emission due to tumultuous growing of manufacturing. For these reason during the next twenty-thirty years fossil sources will be the most used energy sources even though production of energy from renewable and eco-friendly sources (solar, wind, water, tides, biomass) is quickly increasing (around 6.6 % per annum). Among the fossil fuel source demand of natural gas represents the fastest growing, promoted also by supportive environmental policies. Indeed, natural gas valorisation represents a reliable way to overtake the other fossil fuel in terms of availability, accessibility, versatility, lower cost and a reduced environmental footprint. Due to either new sources availability (such as shale gas) or to innovative valorization strategies, the International Energy Agency (IEA) estimated global demand of natural gas rise to more than 50% in 2035 [2]. Production of syngas (mixture of H_2, CO and CO_2) by partial oxidation, steam reforming or autothermal treatment of methane or natural gas, represents an high efficient way to valorise these energy sources with production of high value products [3] as well as environmental and economic sustainability of important syngas-based industrial processes which are strongly affected by syngas production system (e.g. Fischer-Tropsch synthesis, Methanol-to-Gasoline, Methanol-to-Olefins, Ammonia synthesis). Furthermore, the

production of syngas from biomass gasification is a reliable alternative route to strongly increase the sustainability of above mentioned industrial processes [4, 5, 6]. Also, environmental impact of the chemical usage, is an important task of both academic and industrial research, in order to increase sustainability of these energetic sources. In this concern, production of dimethyl ether (DME) from natural gas or biomass permits to obtain an alternative fuel for Diesel engines, because to its high cetane number (>55), with an high efficiency well-to-wheel compared with other fuel (i.e. methane, ethanol, and Fisher-Tropsch fuel), represents a reliable alternative fuel with very high sustainability, due to the significant reduction of NO_x emissions and total absence of SO_x and particulate matter in engines exhaust gases [7, 8]. In this chapter the properties, the perspectives and production system of DME will be described, by emphasising mainly the characteristics of the catalysts used for its synthesis, the open-challenges and the state-of-art knowledge necessary for the development of this thesis.

1.1DME: characteristics

Dimethyl ether (DME) is the simplest of ether with molecular formula C_2H_6O (MW: 46.07 g/gmol) and molecular structure reported in Figure 1.1.

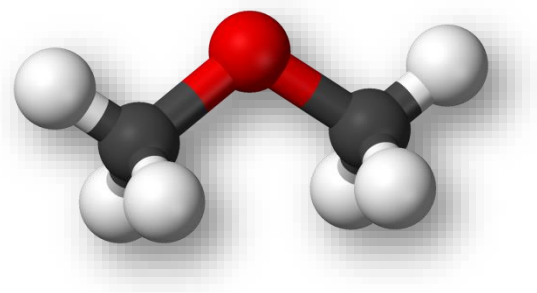

Figure 1.1 – Structure of DME

DME is a colourless, non-toxic, non-corrosive, non-carcinogenic and environmentally friendly compound with a boiling point of -25°C, and can be liquefied above 0.5 MPa at room temperature [8].

DME chemical and physical properties are similar to those of LPG, and published studies suggested that the technologies developed for storage and transport of LPG can be easily converted to accommodate DME with similar safety guidelines and codes [9]. DME is also an important chemical intermediate for production of widely used chemicals, such as diethyl sulphate, methyl acetate and light olefins [10]. Nowadays, DME is mainly used as an aerosol propellant in several spray cans, replacing the banned ozone-destroying

CFC compounds but in the last decades, it is receiving a growing attention as an alternative eco-friendly fuel. In 1995, an extensive collaborative research effort among Amoco (actual BP), Haldor Topsoe and Navistar International Corporation, demonstrated that DME could be a reliable alternative fuel for diesel engines with low-emission of NO_x, SO_x and particular matter, to be produced at large-scale from methanol by a simple dehydration technology [11]. These studies renewed attention on the outstanding performances of DME as alternative fuel to diesel and showed total compliance with the most stringent California ULEV (ultra-low emission vehicle) emission regulations for medium-duty vehicles. Because of the necessity to change the fuel distribution infrastructures and the modifications to engine devices, DME market as diesel alternative fuel was challenging. Indeed, the primary DME market was the blending of with LPG cut because of their very similar chemical-physical properties and Amoco patented a DME/LPG blend for automotive application [12]. The current key markets perspecitve of use of DME as fuel are: (1) blending with LPG, (2) alternative fuel for diesel engines, (3) fuel for power generation by gas turbines plant, and (4) chemical intermediate for olefins and synthetic-gasoline production as described in the next paragraph. It is important to remark that the market of dimethyl ether is strongly affected by production costs and price, availability, accessibility and safety of the starting raw material. As will be described later, DME can be produced from a variety of feedstocks such as natural gas, crude oil, residual oil, coal and biomass. As showed previously, natural gas price is the most important factor to be considered in order to correctly evaluate the market accessibility of DME, and the fast growth in natural gas demand offers reliable opportunities for DME market. Nevertheless, in recent years, CO_2 valorization represents the main goal of several research projects. In this concern, gas-phase synthesis of DME/methanol starting from CO_2, is a reliable way to valorize and reduce emission of this green-house gas [13, 14]. Therefore, the synthesis of DME from CO_2 can be a reliable process because it can balance the eventual economic disadvantages for natural gas valorization (i.e. changes in price or environmental policies) with the indisputable advantages from CO_2 recycling.

1.2 DME: perspectives

As already mentioned, DME is nowadays mainly used as propellant in several spray cans in substitution of dangerous CFC compounds. In the last decades, DME ranked on the top as alternative energy source (e.g. alternative fuel) because a lot of benefits [15]. Some of the benefits are demonstrated here [16]:

- DME is clean: if DME is used as alternative diesel fuel provides smokeless combustion, low CO and NO_x emissions compared with the standard automotive fuels; furthermore, DME is a biodegradable colourless gas, non-corrosive and doesn't contaminate soil or aquifers in the event of a leak;
- DME is efficient: several lifecycle analysis studies demonstrate that DME is the most efficient fuel produced from renewable feedstock ranking as the fuel with the highest total efficiency among the known synthetic fuels (e.g. methanol, Fisher-Tropsch diesel);
- DME is portable: DME can be transported in liquid-phase by using LPG technologies;
- DME is safe: DME is non-carcinogenic, non-mutagenic and non-toxic indeed it is used for decades in the personal care industry (as a benign propellant aerosol)
- DME is versatile: DME can be used in a wide veriety of applications as alternative fuel for diesel engines and LPG-based device (e.g. indoor applications), electric power generation and production of hydrogen and olefins.

In this paragraph a brief review about the main perspective of DME utilization suggested by literature is reported.

1.2.1 DME as alternative transportation fuel

As reported in the previous paragraph, since the mid of 1990s DME has been promoted as reliable diesel substitute for auto-transportation and chemical-physical properties comparison between diesel fuel and DME is reported in Table 1.1, allowing to identify both advantages and disadvantages of using DME as alternative fuel for diesel engine. Emission of particular matter is characteristic of compression-ignition engine with diesel fuel causing the necessity to use an anti-particulate filter in order to reduce these emissions. The high oxygen content and the absence of C-C bonds in DME molecule does not permit formation of soot during combustion eliminating the just described problem associated to combustion of diesel fuel.

	Unit	**DME**	**Diesel**
Carbon content	mass%	52.2	86
Hydrogen content	mass%	13	14
Oxygen content	mass%	34.8	0
Carbon-to-hydrogen ratio	-	0.337	0.516
Liquid density	kg/m^3	667	831
Cetane number	-	>55	40-50
Autoignition temperature	K	508	523
Stoichiometric air/fuel mass ratio	-	9.6	14.6
Normal boiling point	K	248.1	450-643
Enthalpy of vaporization	kJ/kg	467.1	300
Lower heating value	MJ/kg	27.6	42.5
Ignition limits	vol% in air	3.4/18.6	0.6/6.5
Modulus of elasticity	N/m^2	$6.37 \cdot 10^8$	$14.86 \cdot 10^8$
Liquid kinematic viscosity	cSt	<0.1	3
Surface tension (at 298K)	N/m	0.012	0.027
Vapour pressure (at 298 K)	kPa	530	<<10

Table 1.1 – Chemical-physical properties of DME and diesel fuels [15]

The lower boiling point than diesel one, leads to fast evaporation when liquid DME is injected into the engine cylinder improving the combustion. In addition, the low auto-ignition temperature allows to obtain a higher cetane number of DME than that offered from diesel fuel. Generally, a higher cetane number results in easier ignition, more complete combustion and cleaner exhausted gases; in addition a higher cetane number of fuel, reduces the smoke emission during enginge warm-up, reduces noise, reduce fuel consumption and exhausted gas emissions [16, 17]. In addition, based on the similar chemical-physical properties between DME and LPG, several devices as the storage bomb and fuel line used in LPG-based engines can be used for DME.

On the other hand, some disadvantages have to be accounted to fulfill evaluation of DME as diesel substitute. First of all, DME exhibits a LHV much lower than diesel (27.6 MJ/kg vs 42.5 MJ/kg) fuel and for this reason a larger amount of injected volume and longer injection period for DME is necessary in order to deliver the same amount of energy. Other disadvantages are related to necessity to change engine configuration if diesel fuel is substituted with DME fuel. Indeed, the much lower viscosity of DME causes the necessity application of special gaskets in order to avoid leakage. Furthermore, DME is able to dissolve organic compounds and is not compatible with elastomers and plastic

materials. Therefore, a careful selection of sealing materials is required [18]. The diesel-fueled compression ignition (CI) engine offers several advantages compared to a gasoline-fueled spark ignition (SI) engine (e.g. better fuel economy, higher power performances, and expected life). Nevertheless, CI engine has several well-known disadvantages. Because the higher combustion chamber temperature and the chemical-physical characteristics of diesel fuel, harmful pollutants such as nitrogen oxides (NO_x), particular matter (PM), hydrocarbon compounds (HC), carbon monoxide (CO) and sulphur oxides (SO_x) are emitted in the exhausted gases. As reported by Park *et al.* [18], emissions of HC and CO are lower if DME is burned in a CI engine as showed in Figure 1.2.

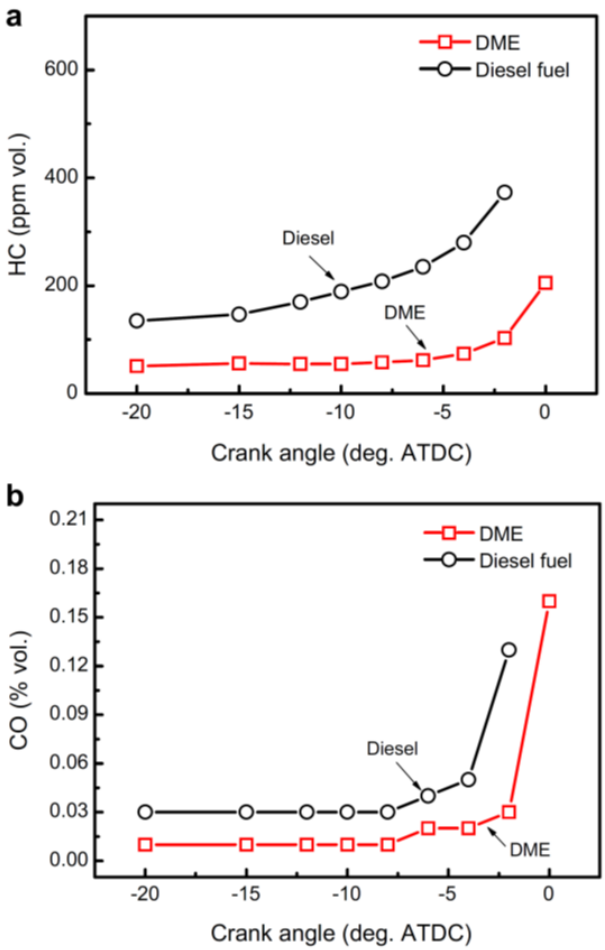

Figure 1.2 – Comparison between Diesel fuel and DME in emission of hydrocarbon compound (a) and carbon monoxide (b) vs cranck angle of a CI engine [17]

As elsewhere described, the absence of sulphur in DME fuel, allows to obtain SO_x-free exhausted gases. The presence of high oxygen concentration in DME molecule allows a better combustion performances limiting formation of C-C bonds responsible of soot

emissions; experimental results reported by Sidhu et al. [19] show that the relative particulate yields from DME was just 0.026% versus the value of 0.51% exhibit from both diesel and bio-diesel fuels. For this reason, a diesel particulate filter (DPF) is not required in DME-fueled engines. Thanks to this advantage, installation and application of oxidation catalysts for further reduction of both HC and CO is possible in terms of economy and vehicle space.

A right evaluation and comparison of NO_x emission from CI engines by using DME or diesel fuel is not easy to perform experimentally because results depend strongly on the engine conditions and the fuel supply system. Usually, a higher NO_x level was detected when diesel fuels is substituted with DME, as reported be Park *et al*. and Kim *et al.* [18, 20] but opposite results have been published by SAE International studies [21, 22]. Unlike diesel fuel, the reduced emission of the other pollutants, allows to use high exhaust gas recirculation (EGR) in order to reduce NO_x level without an increase in PM and soot emission [17].

On the other hand, combustion performance it is not the only parameter to account of when assessing a fuel characteristics. Indeed, it is necessary to carefully evaluate the efficiency of each step, from the supplying of raw material to utilization of the final fuel. In this concern, a *well-to-wheels* (WTW) analysis is usually performed. A *well-to-wheels* analysis consist on a *well-to-tank* (WTT) and a *tank-to wheels* (TTW) analysis [16]. The WTT analysis can be carried out by calculating the *WTT efficiency* as the ratio between the energy of the fuel (e.g. LHV) and the sum of the energy consumptions in each manufacturing step, from feedstock recovery to fuel distribution. Among the derived alternative fuels from natural gas, biomass or electrolysis (e.g. DME, methanol, synthetic diesel, hydrogen, etc.), DME exhibits the highest WTT efficiency [16]. TTW analysis includes everything related to the vehicle and its operations and for these reason different fuel have to be compared with vehicle with the same technology. In this context, DME exhibits high engine efficiency for several vehicle technologies. Globally, by comparing WTT and TTW analysis in order to estimate a WTW efficiency, Semelsberg et al. [16] according to Arcoumanis et al. [8], suggest that DME ranks on the top among different alternative fuel for several vehicle technologies. The WTW efficiency of DME is comparable with LPG and CNG (compressed natural gas) fuelled vehicles, but lower than vehicle operating with diesel fuel. Emission of CO_2 in well-to-wheel analysis is also important in order to evaluate correctly the alternative fuel footprint. Table 1.2 shows relative total CO_2 emitted between feedstocks recovery and fuel combustion in different

vehicle technologies (WTW CO_2 emissions). DME offers similar WTW CO_2 emissions of diesel fuel for CI and DI engine and CNG fuel for SI vehicle. It is important to notice that the diesel and DME offer the lowest carbon dioxide emissions among the fossil fuel derivatives.

Fuel	**Engine type**	**Relative well-to-wheel CO_2 emissions (Diesel=1)**	
		Light-duty vehicles	Heavy-duty vehicles
Diesel	CI, DI	1.00	1.00
DME	CI, DI	1.01	1.02
DME renewable	CI, DI	0.17	0.17
Gasoline	SI, λ=1	1.47	1.46
LPG	SI, λ=1	1.28	1.29
CNG	SI, λ=1	1.14	1.09

Table 1.2 – Well-to-wheel CO_2 emission of different fuel for compression-ignition (CI), direct ignition (DI) and spark-ignition (SI) engines [17].

Obviously, if DME is produced from renewable source (e.g. biomass), the emission of CO_2 drop drastically giving to DME a high relevance as alternative "eco-friendly" fuel.

1.2.2 DME as a fuel of power generation in gas turbines

Because of the clean emission offered from DME combustion, DME is also suggested as fuel for power generation by using gas turbines. In the last decade, several companies, including BP, Snamprogetti/ENI S.p.A, Haldor Topsoe [11], have tested DME as a gas turbine fuel in the case that they cannot easily import natural gas. Indeed, as above mentioned, thanks to the similar chemical-physical properties of DME and LPG, ocean transport can be carried out by using conventional LPG tankers without any additional precautions about safety and technologies. Several studies demonstrate that DME is a reliable, clean, fuel compared with natural gas in terms of both NO_x and CO [23, 24]. Depending on operation conditions, DME can emits more CO than NO_x [25] but this disadvantage can be overcame by nozzle modifications [26].

1.3 DME as hydrogen source

Among the several chemical processes developed until now, production of hydrogen is receiving growing attention and it can be considered as the energy source of the future because its highest energy content per unit of mass and its lowest pollutant emissions during utilization among the known fuels (e.g. fuel cells) [27, 28]. Production of hydrogen by steam reforming of methane or gasoline is the main industrial process to produce hydrogen. These processes require high temperature (above 600 °C for methane and above 800 °C for gasoline), high energy supply, stable catalysts and expensive refractory reactors. Recently, steam reforming of methanol is receiving attention because relative low process temperature (around 300°C) and simpler reactor configurations [29]. Nevertheless, the high toxicity of methanol represents an important disadvantage to use this alcohol. DME is reliable candidate for hydrogen production by steam reforming (by adopting similar operation condition of methanol steam reforming and over a bi-functional catalysts, namely acid function of DME hydrolysis to methanol and copper-based catalyst for the alcohol reforming) because it is not toxic and because its high hydrogen content, as it is confirmed by several studies [30 – 33].

1.4 DME as chemical intermediate

DME can be utilized as intermediate for several chemicals in the processes traditionally using methanol as reactant because DME is usually an intermediate of most of the reactions involving methanol. By substituting methanol with DME it is possible to process a non-toxic compound (methanol exhibits a high toxicity for human health) and generally the process is more sustainable. As described later methanol is produced from syngas, and then from methane or biomass, over a copper-based catalyst. The main problem of methanol synthesis process is the thermodynamic limitation, resulting in low syngas conversion in the reactor. The addition of the acid function to the catalytic system, promoting the on-site methanol-to-DME dehydration, positively impacts on the thermodynamics of the overall syngas conversion reaction scheme. For instance, methyl acetate can be synthesised by carbonylation of DME usually catalysed by acidic zeolites under operation condition similar to the traditional process operating for methanol as reactant taking the advantage of a safer reactant [34, 35]. For similar reason synthesis of formaldehyde by selective oxidation of DME was studied and hopefully results will be obtained by using MO_x/Al_2O_3 catalyst [36, 37].

1.4.1 DME as intermediate for olefins and synthetic-gasoline production

Production of olefins and synthetic-gasoline are very attractive processes to convert methanol to higher value products by the well-known Methanol-to-Olefins (MTO) and Methanol-to-Gasoline processes. It is important to remark that methanol is industrially produced starting from natural gas. Actually, the total known worldwide natural gas (NG) reserves are estimated by EIA to be around 200 trillion of cubic meter [38]. For this reason, the strong comprehensive focus should be on the conversion of natural gas to liquids (GTLs) and higher added value products. Different production plants configurations have been developed in the last decades. Figure 1.3 show a simplified process scheme of an MTG process developed by Haldor-Topsøe in the 1980s [39].

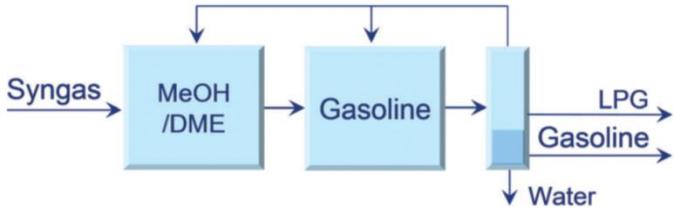

Figure 1.3 –Haldor-Topsøe syngas-to-gasoline process [39]

Industrially, methanol conversion to gasoline is carried out by using HZSM-5 (medium-pore-sized zeolite) as catalys at reaction temperature of 400 °C and methanol pressure of around 20-30 atm [40]. The amount of light products (LPG and ligh olefins) is around 40%. Production of olefins can be increased by rising of the reaction temperature to 500°C to favour cracking of large molecules. In order to switch the process to production of light olefins (mainly ethylene and propylene), SAPO-34 (small-pore-sized zeotype) was selected. It is the best catalyst for production of olefins by UOP thanks to its unique shape-selectivity towards light compounds [39, 41]. A scheme of a MTO process developed by collaboration of INEOS (UOP and Norsk Hydro) and Total is shown in Figure 1.4.

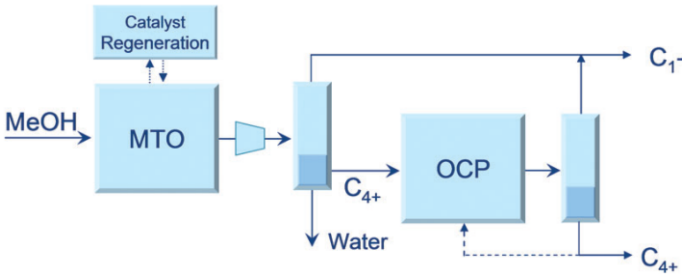

Figure 1.4 –INEOS methanol-to-olefins process combined with UOP/Total olefin cracking unit [39]

This process, developed in the nineties, consist of a fluidized-bed reactor coupled with a combustion unit for a continuous regeneration of SAPO-34 catalyst (due to its rapid deactivation) and a cracking unit, with the aim to increase the olefins yield up to 80%. By using highly siliceous modified H-ZSM-5, reaction temperature of about 450 °C and pressure close to the atmospheric [42], it is possible to drive the process toward propylene production (methanol-to-propylene, MTP). A Lurgi MTP plant scheme is shown in Figure 1.5.

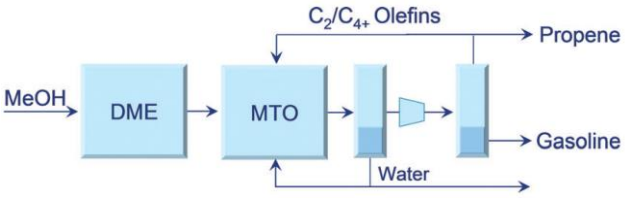

Figure 1.5 –Lurgi MTP process [39]

In Lurgi MTP process propylene and gasoline are the main products. Water is partially recycled to the reactor in order to improve selectivity toward propylene.

As showed in MTG, MTO and MTP processes, methanol can be partially replaced by DME taking into account that methanol dehydration to DME is the first step for any MTH process [39, 43].

1.4.1.1 The hydrocarbon pool mechanism

Because olefins formation is an unlike phenomenon for DME production during methanol conversion step, a more detailed description of the reactions mechanisms involved to the MTH processes is necessary for a correct interpretation of results reported in this thesis.

During MTH processes, methanol reacts with an adsorbed methyl group (CH_3-H) forming methane and formaldehyde followed by decomposition of methane to CH_3- that reacts

with formaldehyde to form ethanol that is rapidly converted to the ethylene and water [44, 45]. On the other hand, Li *et al*. [46] report the role of DME on formation of the first olefins: DME reacts with methoxy groups to form $CH_3OCH_2^+$ specie. This specie reacts with another DME molecule to form 1,2-dimethoxy ethane or 2-methoxy ethanol. After several methylation and deprotonating reactions propylene is formed. During these reactions methane is the main component generated [47]. Ethylene or propylene lead to the formation of aromatics or heavier olefins by methylation, oligomerization, cyclization and H-transfer reactions on acid sites of zeolite, creating an autocatalytic system knows as hydrocarbon pool mechanism as illustrated in Figure 1.6 [39, 48, 49].

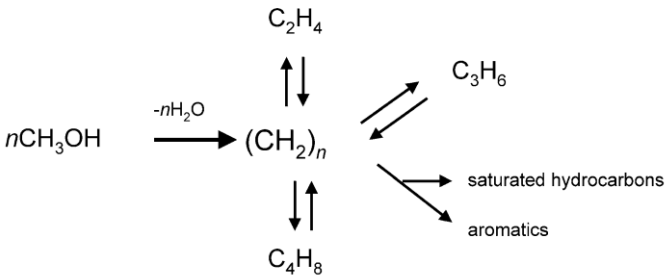

Figure 1.6 – Simplified illustration of hydrocarbon-pool mechanism [39]

The period during the formation of heavy hydrocarbons is known as induction period. High temperature, small catalyst crystals or the presence of impurities in reactant feed or on the catalyst surface (e.g. due to a not perfect calcination of the sample) strongly reduce the duration the induction period in which hydrocarbon pool molecules are formed [41, 47, 50]. Hydrocarbon pool route (HCP) is the most effective mechanism to form olefins but remains an open challenge to understand how the HCP molecules are formed during the induction period. HCP mechanism can consist on an aromatic-based cycle or an olefin-based cycle. The aromatic-based cycle is the most important mechanism on production of light olefins (mainly ethylene and propylene). Two distinct reaction routes were proposed to explain olefins formation: side-chain methylation and paring routes, as it is shown in Figure 1.7.

The side-chain methylation route proceeds via the methanol methylation of polymethyl benzene carbocations trapped on the cage of the catalyst and subsequent elimination of side chain groups to produce olefins; on the other hand, paring route involves the contraction of 6-member-ring ions and expansion of 5-member-ring ions [51].

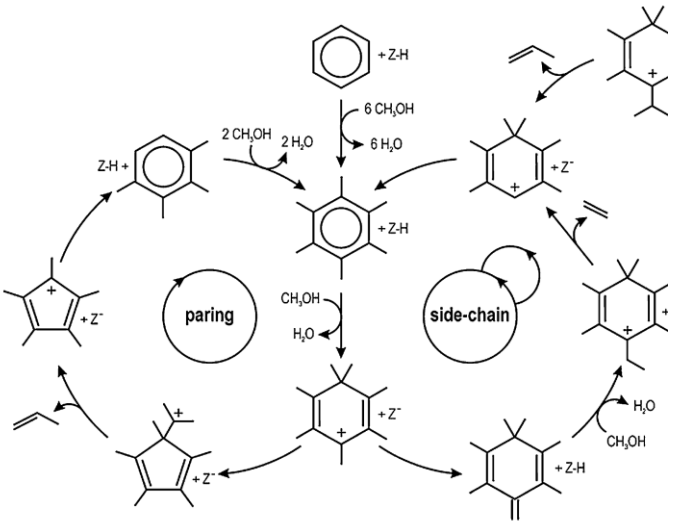

Figure 1.7 – Pair and side-chain reaction mechanisms in MTH process [39]

Olefins-based cycle consists of cracking of heavy olefins obtaining at high selectivity toward propylene despite of ethylene formation [52]. Catalyst structure (channel size and configuration) is the most important factor which affect the types of molecules formed during the induction period (zeolite structure allows the possibility to drive the reaction mechanism toward aromatic- or olefin- based cycle) and also to the olefins selectivity. Zeolite structures with large cage or 3-D channel system, such as SAPO-34, BEA and MFI, lead preferably to the formation of an aromatic-based cycle but the selectivity towards olefins depends strongly on the channel size. Indeed, SAPO-34 show the highest selectivity towards ethylene and propylene, while BEA forms a higher amount of C_4 compound than MFI [51, 52]. Zeolite structure affects strongly the reactivity of the trapped molecules too. Indeed, trimethyl benzene is the most active specie on MFI, while hexamethylbenzene is the most active for olefins formation on SAPO-34 and BEA [53]. 1-D small/medium channels allow the formation of an olefins-based cycle as observed on TON and MTT structures [53, 54]. Recently, Park *et al.* [55] reported that a high selectivity towards propylene formation was observed on low acid dealuminated MCM-68, showing that acidity (amount, type and strength of acid sites) also affect strongly the products distribution. Even catalyst structure modification (e.g. hierarchical structure) can affect strongly both olefins selectivity and hydrocarbon pool mechanism. For instance, in a recent paper, Liu *et al.* [56] report a comparison about the catalytic performances of hierarchical and microporous BEA in MTO reaction, showing that the sample with mesoporosity exhibits a lower selectivity towards ethylene; this behaviour was attributed to the shorter diffusion path of hierarchical structure that allows an easier diffusion of

methyl-benzene compounds without undergoing further dealkylation reactions and the olefins-based cycle becomes predominant. Usually, both olefins-based and aromatics-based hydrocarbon-pool mechanisms can occur simultaneously. For this reason, the *dual-cycle* concept was introduced [39] and shown in Figure 1.8.

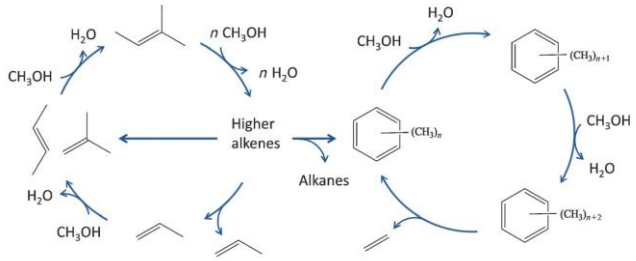

Figure 1.8 – Dual-cycle reaction mechanisms in MTH process [39]

Therefore, by a careful selection of catalyst structure it is possible to convert methanol according to a preferable cycle, driving the process toward the desired product distribution. Zeolite deactivation in both MTH processes occurs mainly by the coke deposition, while the catalyst structure and acidity strongly affect the mechanism of coke formation and consecutively on the catalyst lifetime. Campelo *et al.* [57] report a comparison between several silico- aluminophosphate with different channel configuration (1-, 2- and 3-dimensional). It was shown that on a 3-dimensional structure (as SAPO-34), the oligomers formed in the channel can migrate to the big cage of the structure, where it reacts at strong acid sites formimg of heavier oligomers and aromatics that cannot go back to the channel causing a rapid catalyst deactivation by pore blocking. On the other hand, deactivation of 1-dimensional large channel (e.g. SAPO-5) is due to the adsorption of multi branched chains on the strong acid sites causing blocking of the pore system. Structures with both small/medium channels and cages, as MFI type, don't allow trapping of heavy compounds inside the crystal and coke is preferably formed on external surface of crystals and catalyst deactivation occurs by coke deposition on the pore openings [58, 59]. Catalyst deactivation rate is also affected by crystal morphology; small or hierarchical crystals exhibits higher resistance to deactivation by coke deposition than large crystal with only microporous voids [60, 61].

1.5 DME production

As mentioned before, DME can be produced from a variety of feed-stock including natural gas, coal, crude-oil residual oil, and biomass [62, 63]. First, raw-materials are converted into synthetic gas (syngas), a combination of carbon monoxide and hydrogen.

The fossil-derived hydrocarbons can be converted to syngas by the traditional well-known technologies. Steam reforming is the most used way to produce syngas using a nickel-based catalyst and by adopting reaction temperature and reaction pressure in the range of 700 – 900°C and 30 – 50 bar, respectively [64]. The cost of the syngas production strongly depend on price on raw material (mainly natural gas) and its market economy. Syngas can be produced also from non-fossil sources. For instance, gasification of biomass (thermal or catalytic) is a sustainable way to produce syngas [65-67]. After syngas production, DME synthesis can be performed in two different ways. One way is a conventional two-step process (*indirect synthesis*) which consist of methanol synthesis from syngas followed by methanol dehydration in two distinct reactors; the other ways is a one-step process (*direct synthesis*) which directly produce DME from syngas as illustrated in Figure 1.9.

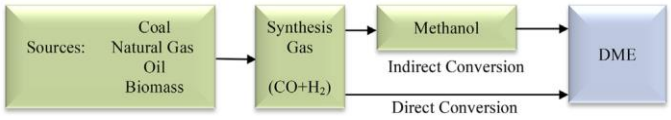

Figure 1.9 – DME production system [68]

The major part of the research is focused on the optimization of the catalyst for mainly direct synthesis as showed in the publications trend reported in Figure 1.10.

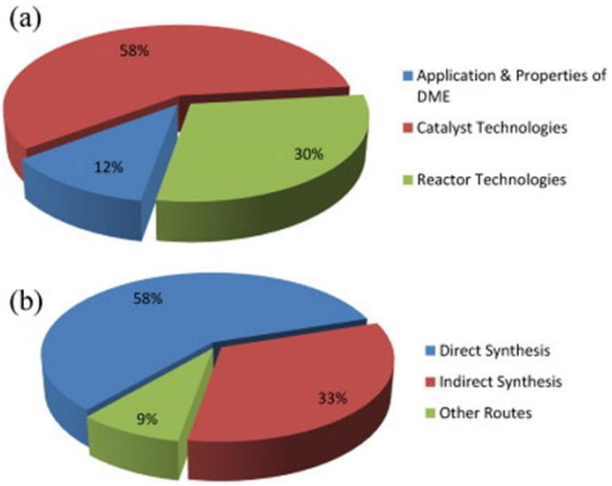

Figure 1.10 – Publications on (a) DME use and production technology and (b) synthesis pathways [68]

In the following chapter, the knwn technologies and the catalyst systems are briefly described.

1.5.1 Indirect synthesis

Indirect synthesis of DME is the traditional way to produce the ether. This route goes via methanol dehydration reaction, reported below:

$$2CH_3OH = CH_3OCH_3 + H_2O$$

Methanol dehydration is an exothermic reversible reaction ($-\Delta\widetilde{H}_r^0(298K) = 23.5\ kJ/mol$) that proceeds without reactant/products mole number variation. For this reason, reaction pressure does not affect conversion equilibrium, while lower reaction temperatures have a thermodynamic benefit toward DME production. Methanol dehydration is a reaction catalysed by acid catalysts and several investigations have been published in order to identificate an active, selective and stable catalyst at relative low temperature for the above-mentioned thermodynamic advantages. Depending on catalyst characteristics, methanol dehydration can be carried out in both vapour and liquid phase, with reaction temperature in the range 100-300 °C, and pressure up to 20 bar. Methanol dehydration is known as an acid-catalysed reaction. γ-Al_2O_3 is the traditional catalyst for methanol dehydration. It is very attractive catalyst due its low cost, high surface area, high thermal and mechanical stability, and because it exhibits high selectivity toward DME also under extreme temperature (up to 400 °C) thanks to weak Lewis acid sites. Unfortunately, these acid characteristics don't offer high activity in terms of methanol conversion. A minim temperature of 250-270°C is necessary to promote methanol conversion [69]. Catalyst activity can be improved by modifying γ-Al_2O_3 surface with silica, phosphorous, titanium, niobium, boron and others species [70-74]. Although γ-Al_2O_3 is active for methanol dehydration, it tends to strongly adsorb the water produced during the reaction causing losing of activity and deactivation as demonstrated by several investigations [71, 75 - 78]. As described later, an important amount of water is produced especially during the *direct synthesis* process. Thus, γ-Al_2O_3, in spite of its advantages, is not classified as catalyst for DME production by direct synthesis. Research is focusing on use of zeolites as catalysts for methanol dehydration. As described in the next chapter, zeolites are microporous crystalline aluminosilicates that exhibit high versatility in terms of acidity and structure offering the possibility to modulate strength, distribution and concentration of acid sites and pores opening, in order to drive reaction mechanism toward desired product distribution. Several investigations were focused on use of H-ZSM-5 catalyst for methanol dehydration reaction, where a temperature control can be sufficient to stop the reaction at moment of sufficient DME formation. First of all, HZSM-5, unlike γ-Al_2O_3, exhibits high resistance toward water adsorption as demonstrate by dedicated studies. [75, 77]. Furthermore, thanks to its stronger acid sites (Lewis and/or

Brønsted type), exhibits high activity at relative low reaction temperature. For instance, Vishwanathan *et al.* [79] report a value of methanol conversion of about 80% over H-ZSM-5 at 230°C, while over γ-Al_2O_3 conversion was just 5% and it is necessary to increase the temperature to 320 °C to reach 80%. Therefore, high activity of zeolites at relatively low temperature is important in terms of process economy. High activity is retained because H-ZSM-5 possesses medium and strong acid sites that allow a fast methanol conversion. Unfortunately, these high active acid sites causes successive reactions of formation of the by-products as olefins and coke. High catalytic performances in terms of DME selectivity were obtained by decreasing acid sites strength by modifying zeolite surface [80 – 82] or by decreasing total acidity [79, 83-85]. Also hydrophobicity can be improved by changing acidity. Zeolite structure is an important factor which should be optimized in order to obtain high shape selectivity toward DME formation and to inhibits successive reactions. For instance, Khandan *et al.* show that H-MOR (1-dimendional, large channel system) exhibits an high activity toward both methanol dehydration and DME production among other investigated structures (BEA, MFI, FER, Y), but the large by-products accommodated in its channels lead a fast deactivation but its stability can be improved by surface modifications via wet-impregnation of Cu, Zn, Ni, Al, Zr and Mg species [86]. Coke formation can be reduced by post-synthesis treatment or by a careful *tailoring* of the textural properties. A dual pore size distribution (e.g. micro- and meso-pores) is a reliable configuration to reduce coke formation and postepone catalyst deactivation. Tang *et al.* [87] report that a ZSM-5/MCM-41 composite material with both microporous and mesoporous allows to obtain higher activity and higher stability compared with ZSM-5 with only microporous structure. Similar results were obtained by Rutkowska *et al.* [88] where synthesized hierarchical ZSM-5 material (interconnected pores) obtain a lower coke formation rate than micro-porous ZSM-5. Therefore, both acidic and textural properties strongly affect catalyst performances.

Several mechanisms are proposed for methanol dehydration to DME. The most reliable hypothesis suggest that methanol is dehydrated over both Lewis and Brønsted acid base pair sites. For instance, Bandiera and Naccache [89] report that methanol dehydration over dealuminated zeolite Mordenite can be modelled by adopting a Langmuir-Hinshelwood equation suggesting a dual sites mechanism where an acid site H^+ and its adjacent basic site O^{2-} are included the dehydration process. According with this hypothesis, methanol is protonated on acid site to form $[CH_3{\cdot}OH_2]^+$ specie which is

rapidly decomposed to $[CH_3]^+$ and water, while on the adjacent base site another methanol molecule reacts to form $[CH_3O]^-$ and $[OH]^-$ species. DME is formed by combination between $[CH_3]^+$ and $[CH_3O]^-$ nearly adsorbed species while water reacts with $[OH]^-$ in order to restore catalytic species as illustrated in the following mechanism where $[H^+]$ is the acid site and $[O^{2-}]$ the basic site on the zeolite surface:

$$\mathbf{CH_3OH} + [H^+] \rightarrow [CH_3OH_2]^+ \rightarrow [CH_3]^+ + [H_2O]$$

$$\mathbf{CH_3OH} + [O^{2-}] \rightarrow [CH_3O]^- + [OH]^-$$

$$[CH_3O]^- + [CH_3]^+ \rightarrow [CH_3OCH_3] \rightarrow \mathbf{CH_3OCH_3}$$

$$[H_2O] + [OH]^- \rightarrow [H_3O^+] + [O^{2-}]$$

$$[H_3O^+] \rightarrow [H^+] + \mathbf{H_2O}$$

Another mechanism is reported by Kubelková *et al.* [90] which suggest that a methanol molecule is protonated on surface of HY and HZSM-5 zeolites to produce $[CH_3]^+$ and $[H_2O]$ as reported above, but a second methanol molecule reacts directly with $[CH_3]^+$ specie to form dimethyl ether and restore the acid site of zeolite. Despite the several proposed mechanisms for DME formation, methanol dehydration is usually carried out in fixed bed reactor due to its low capital and operating costs and easiness of scale-up [68]. Plant configuration for DME production by *indirect synthesis* is described by the illustration in Figure 1.11.

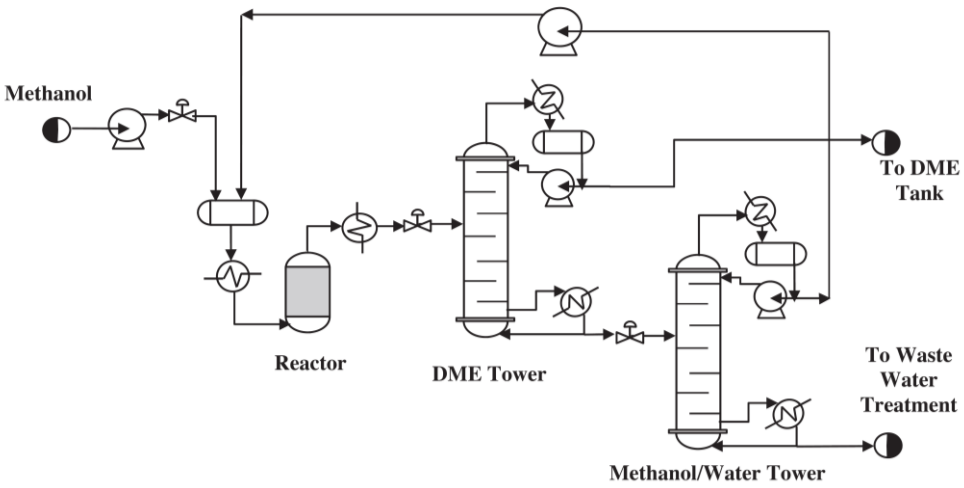

Figure 1.11– A scheme of process for indirect synthesis of DME [68]

As shown in Figure 1.11, DME plant required two distillation columns for DME purification and methanol/water separation and recycling of non-converted methanol. The DME distillation is carried out under about ten atmospheres. More efficient process

configuration is suggested by Kiss and Suszwalak in order to improve sustainability of DME production [91].

1.5.2 Direct synthesis

In the *direct synthesis* way methanol synthesis (typically from a CO/H_2 mixture) and dehydration process to produce dimethyl ether is carried out in a single reactor unit over a redox/acid catalyst. Table 1.3 reports the set of chemical equations and their heat of the reactions in direct synthesis process.

	Reaction	Reaction heat [kJ/mol]
(a)	$3CO + 3H_2 = CH_3OCH_3 + CO_2$	-246
(b)	$2CO + 4H_2 = CH_3OCH_3 + H_2O$	-205
(c)	$CO + 2H_2 = CH_3OH$	-182
(d)	$2CH_3OH = CH_3OCH_3 + H_2O$	-24
(e)	$CO + H_2O = CO_2 + H_2$	-41

Table 1.3 – Direct synthesis ste of chemical equations and their reaction heat

The main steps occurring during the direct synthesis process are usually the synthesis of methanol from syngas (c) over redox catalytic function, methanol dehydration to DME over acid function (d) and eventual water gas shift reaction (WGSR) catalysed by the redox function (e) of the catalyst. If these three steps occur during the process the global reaction can be illustrated by equation (a); on the contrary, when WGSR does not take place, equation (b) can be used to describe thermodynamics of the process. The factors that affect theoretical equilibrium conversion are generally temperature, pressure and initial composition. The methanol synthesis reaction occurs with a strongly decreasing number of moles number of products, compared with reactants and it is exothermic, favourable for high syngas pressure and low reaction temperature. The effect of these two parameters on syngas conversion in both methanol synthesis and DME direct synthesis is shown in Figs 1.12. and 1.13 as repored by Ref. [92]. The presence of WGSR is a thermodynamically beneficial factor in terms of syngas conversion but produce CO_2 as by-product lowering DME yield. The effect of pressure on methanol synthesis is also reported. By increasing reaction pressure from 5 MPa to 9 MPa at 300 °C the syngas equilibrium conversion increases from 20% to above 40%. The negative effect of an increasing of temperature is evident for both methanol synthesis and DME synthesis.

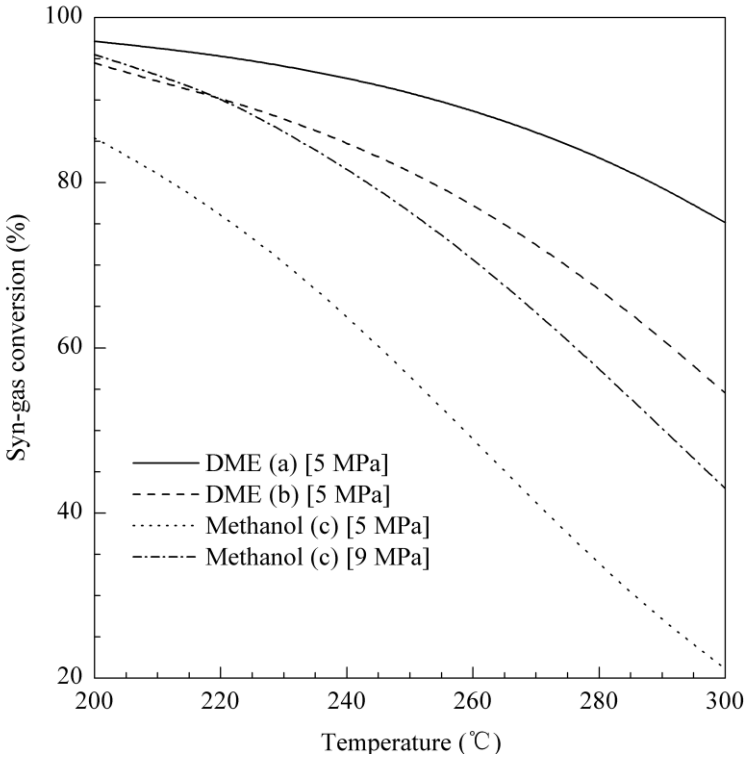

Figure 1.12– Effect of reaction temperature and pressure on syngas equilibrium conversion calculated for H_2:CO=2:1 [92]

The syngas conversion trends shown in Fig. 1.12, suggest that direct synthesis of DME allows higher syngas equilibrium conversion than methanol synthesis (or indirect synthesis). Fig. 1.13 reports the effect of feed composition on syngas equilibrium conversion in both methanol or DME synthesis (proceding via route a or b, see Table 1.3), evaluated at 5 MPa and 260 °C. The maximum syngas equilibrium conversion is obtained by feeding a stoichiometric mixture of H_2 and CO.

In the thermodynamic analysis of the process discussed above, the presence of other side-reactions such as methane, olefins and soot formation was neglected for simplicity. Although a more complex reactions set should be considered, this analysis permites to compare direct and indirect route for DME synthesis.

The traditional catalyst for direct synthesis of DME is a redox/acid bifunctional catalyst operating at reaction condition similar to those adopted for methanol synthesis (250-280 °C and 5 – 10 MPa [93]). A redox function is necessary to promote H_2/CO combination (reaction c in Table 1.3) to form methanol, while acid function is necessary to dehydrate the alcohol to the ether. The traditional catalyst for methanol synthesis is Cu/Zn/Al_2O_3 (CZA), used for redox function in DME synthesis. Copper, in the metallic form, is the catalytic specie while ZnO species and alumina are promoters.

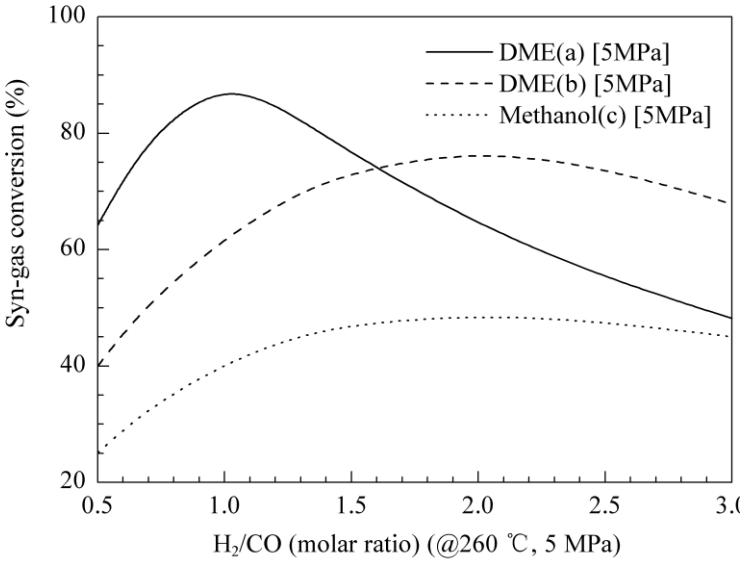

Figure 1.13– Effect of feed composition on syngas equilibrium conversion [92]

Studies demonstrate that zinc is a key element for CO hydrogenation to methanol. ZnO species play a role on copper dispersion [94], they are responsible of adsorption of H_2 and they enhance the capability of copper to adsorb CO and for this reason an intimal contact between Cu and ZnO is necessary in order to obtain high activity [95]. Alumina offers high thermal resistance and improve resistance to deactivation by sintering [96]. Sintering of copper is the main cause of deactivation of CZA catalysts and it is promoted by high temperature and presence of steam in the reaction system. Both factors are present during methanol synthesis [97]. Presences of sulfur, chloride and other compounds are responsible of deactivation by poisoning but this aspect is less important than sintering because poisons are eliminated during feed compounds purification [98].

The catalyst for DME direct synthesis is the combination of the just described catalyst and an acid function catalyzing methanol dehydration described in the previous paragraph (γ-Al_2O_3 or zeolites). Studies demonstrate that CO conversion strongly depend on characteristics of acid function showing that the zeolites are highly performing acid catalysts for DME direct synthesis compared with γ-Al_2O_3. Due to higher amount and stronger acid sites than γ-Al_2O_3 zeolite can operate at relative lower temperature and to promote a fast transformation of methanol to DME with consequent increasing of CO conversion [99]. Among known investigated structures, FER seems to offer the highest activity in terms of CO conversion (or high Cu dispersion) and DME selectivity [100].

The system in which redox and acid functions are combined, strongly affects the activity of the final catalyst, and several methods can be applied to prepare these hybrid catalysts. Usually, redox function is insert over pre-synthesized acid catalyst, while co-precipitation, sol-gel, impregnation and physical mixture are methods to synthesize the catalyst having combinee redox and acid function [99, 101]. The most used method is the co-precipitation one, in which salts (e.g. nitrates) of copper, zinc and aluminum are precipitated on acid catalyst surface, followed by calcination [102]. Different parameters affect final characteristics of hybrid catalyst prepared by co-precipitation method. For instance, precipitant agent can modify properties of acid catalyst. By using non-metal carbonates ($(NH_4)_2CO_3$ rather than $(Na/K)_2CO_3$) is possible to preserve catalytic characteristics of acid catalyst [103]. Baek *et al.* [104] also report that copper source strongly affects activity of final bi-functional catalyst in terms of acidity preservation, suggesting copper acetate as the best metal precursor compared with copper nitrate and chloride. Furthermore, Zhang *et al.* [105] suggest that a calcination temperature of 623 K for 2 h is the optimal condition to obtain highly dispersed small copper particles affecting positively CO conversion. On the other hand, Moradi *et al.* [101] report that the method of sol-gel impregnation can give a higher copper dispersion improving catalysts' activity. Using this method, acid catalyst is stirred in a solution of salts of copper and zinc dissolved in ethanol, followed by adding of oxalic acid to promote precipitation and consequently implementation of redox function. Recently, García-Trenco *et al.* [106] report that a catalyst prepared by simple physical mixing of pre-synthesized redox and acid catalysts exhibits a higher activity compare to the above mentioned methods. The authors claim that with physical mixing method is possible to preserve both acid and textural properties of acid function determining, as above-described, methanol dehydration rate and consequently DME yield. Furthermore, as reported by Cai *et al.* [107], DME productivity increases with decreasing of crystals size of acid function (e.g. H-ZSM-5) by reducing of mass transfer limitations during methanol dehydration step. In another work carried out on modified H-ZSM-5 catalysts, Ordomsky *et al.* [108] found that acid function can affect alfso stability of redox function. They report that acid sites on the external surfaces of the zeolite crystals promote copper sintering, but the problem can be avoided by neutralization of these sites by silylation.

As above-described Cu/Zn co-operation is crucial for CO conversion. A work published by Wang *et al.* [109] shows that Cu/Zn ratio strongly affect products selectivity. Low Cu/Zn ratio (1/4 or 1/2) is beneficial for WGS reaction with high selectivity toward CO_2,

while higher ratio increases CO conversion and an optimal ratio of Cu/Zn=1/1 is selected as the best redox catalyst composition in terms of DME selectivity.

Obviously, operation conditions affect process performances. Hayer *et al.* [110] show the effect of reaction temperature (210 – 300°C) and pressure (10 – 60 bar), contact time (4500 – 60000 NmL/gcat/h) and feed composition (H_2/CO from 1 to 4) on DME productivity. Results suggest that both high temperatures or pressures improve both CO conversion and DME selectivity while low contact time are beneficial toward DME productivity inhibiting CO_2 formation [109]. Finally, a H_2/CO ratio equals to one in the feed mixture exhibits the highest DME selectivity (around 60-70 %). Different results are reported in a paper published by Ereña *et al.* [111] where the effect of feed composition (H_2/CO ratio) and acid function (γ-Al_2O_3 and NaH-ZSM5). Results reveals that for γ-Al_2O_3 an H_2/CO ratio equals to 6 is necessary to inhibit CO_2 formation obtaining a maximum DME selectivity near to 80% with no hydrocarbon by-products formation (methane and ethylene). By using NaH-ZSM-5 similar results in terms of DME selectivity and CO conversion is obtained for a H_2/CO ration equals to 2, while for H_2/CO=1 a high selectivity toward CO_2 formation is observed at the expense of DME production by using both acid catalytic functions.

Usually, H_2, N_2 CO, CO_2, CH_4, CH_3OH, DME and H_2O are the main species circulating in the whole direct synthesis process and a carefully designed plant configuration is necessary to obtain high purity DME [112].

After reaction methanol and water are condensed while DME is recovered by adsorption with water. Gas phase outlet from absorber (H_2, N_2 CO, CO_2, CH_4) are partially recycled to the reactor. Liquid phase containing H_2O, DME, CH_3OH and dissolved gases is treated in a distillation system similar to that used in indirect synthesis process in order to obtain high purity DME.

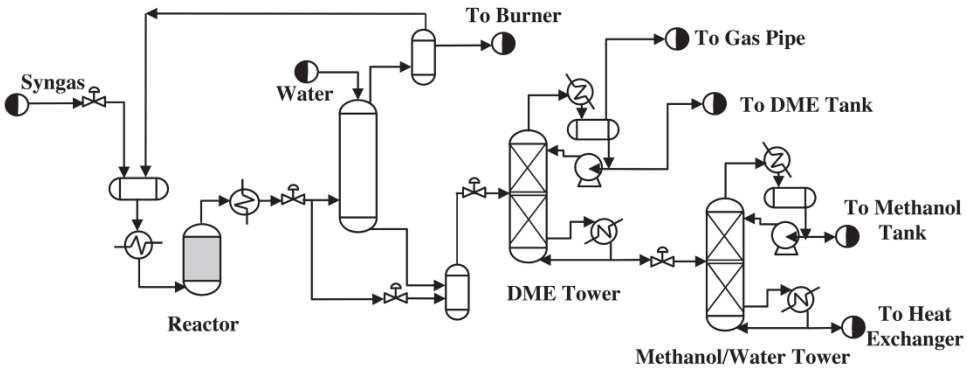

Figure 1.14– A scheme of process for direct synthesis of DME [68]

In terms of reactor configuration both bubbling slurry and fluidized bed reactors are suitable for DME production from syngas, due to the high heat flow to export from the system in order to avoid dangerous rising of temperature during the reactions. Between the two above-mentioned configurations, fluidized bed reactor exhibits better performances than slurry reactor, due to lower mass transfer limitations. Compared with methanol dehydration process, direct synthesis exhibits a higher syngas conversion process performance without the step for methanol purification that results in much lower DME production costs. According to the economic evaluation study, the cost of DME production by direct synthesis is two-thirds of the cost of DME production by indirect synthesis [113].

1.5.3 CO_2-to-DME: a green challenge

The Nobel Prize in Chemistry, Prof. George A. Olah, asserts: "*Recycling of CO_2 into methanol, dimethyl ether (DME), and derived fuels and materials is a feasible approach to address our carbon conundrum. It would free humankind from its dependence on fossil fuel while at the same time help mitigate the problems associated with excessive CO_2 emission. The energy needed for this carbon cycle can come from renewable sources (hydro, solar, wind) as well as atomic energy"* introducing the emerging concept of *Methanol Economy* [114]. In the *Methanol Economy* concept, the production of DME by CO_2 hydrogenation represent an important challenge. The goal of this project is reduce utilization of fossil-derived energy and reduce pollutant emission without significantly changing in life-style of humanity. For instance, production of DME from CO_2 can represent a *green challenge* if CO_2 is captured from highly CO_2-emitter (e.g. thermo-electric power plants, vehicles and other organic fuel-based systems) and if H_2 is produced by water electrolysis by utilization of renewable energy (e.g. sun). The fuel produced by CO_2 hydrogenation (DME), is used for energy production in the above-mentioned fuel-based systems emitting mainly CO_2 and H_2O and reuses these combustion productsin recycle, for the starting components.Taking into account the fact that use of H_2, as ultimate green chemistry fuel, is still not solved [115], research is focusing on process optimization of DME production be feeding mixture of $CO/CO_2/H_2$ or only CO_2/H_2. DME is produced by following sum reaction:

$$2CO_2 + 6H_2 = CH_3OCH_3 + 3H_2O$$

CO_2 hydrogenation to DME is an exothermic reaction that releases around 122 kJ of heat for each molecule of DME formed. The traditional *direct synthesis* process from syngas, during DME production is a series of reactions occur into the reactor, reported in Table 1.4:

	Reaction	Reaction heat [kJ/mol]
(a)	$2CO_2 + 6H_2 = CH_3OCH_3 + 3H_2O$	-122
(b)	$CO_2 + 3H_2 = CH_3OH + H_2O$	-49
(c)	$2CH_3OH = CH_3OCH_3 + H_2O$	-24
(d)	$CO_2 + H_2 = CO + H_2O$	+41

Table 1.4 – CO_2-to-DME: reactions set

The catalyst for the direct CO_2-to-DME conversion should be able to efficiently catalyse both reaction methanol synthesis (b) and its dehydration (c), minimizing the yield of CO formed by the Reverse Water Gas Shift (RWGS) side reaction (d) [116]. By comparing the above described set of reactions (a) with the set of reactions (Table 1.3) occurring in direct synthesis from syngas, it is possible to note that for each mole of DME produced from CO_2 three moles of water are also formed (DME:Water = 1:3), while from syngas the ratio DME:Water is almost 1:1. This important amount of water formed during the synthesis of DME via CO_2 hydrogenation is the main limit of this process. A huge amount of water in the reaction system thermodynamically limits methanol dehydration obtaining a low DME yield. De Falco *et al.* [14] assert that in situ H_2O removal (e.g. by hydrophilic membranes) is the only way to increase DME yield, due to the accelerating of both CO formation (and thus methanol formation) and methanol dehydration reactions.

Generally, a mechanical mixture of mixed oxides and a zeolite, typically ZSM-5 [116 - 129], has been mainly proposed a performing catalytic system. The acid catalyst must be stable in presence of water and the acid sites must be well distributed and not to strong in order to inhibit olefins formation [68, 72, 125, 130 - 136]. In this sense, zeolites seem to offer the highest versatility in terms of hiogher number of acid sites, water resistance and shape-selectivity toward desired compound. Montesano *et al.* [137] have recently published some results using different zeolites (*i.e.*, Theta-1, ZSM-23, ferrierite, mordenite, ZMS-5) in mixture with a $Cu/ZnO/Al_2O_3$ catalyst for the conversion of syngas into DME. The authors report a superior catalytic performance in presence of ferrierite and 1-dimensional zeolites at 250-270 °C and 3.0 MPa, thanks to the topology of ferrierite

that limits the formation of hydrocarbons, possibly by providing a preferential path for the diffusion of small reactants and products (*i.e.*, methanol and dimethyl ether). However, considering the limitations encountered using a mechanical mixture [85], recently the attention has been addressed on the possibility of preparing multimetallic-acidic single grain hybrids to enhance the mass transfer phenomena, so that the multifunctionality necessary for the reaction is grain-to-grain ensured [130]. Frusteri *et al.* have recently published some interesting results demonstrating that a "homogeneous" multi-sites system is more efficient in terms of CO_2 conversion and DME/CH_3OH yield with respect to a mechanical mixture [85]. It was also shown that the acidity of the systems, naturally, plays a determining role in the production of DME; however, it is preferable to have a system characterized by acid sites not too strong and homogeneously distributed on surface; normally, too strong acid sites do not lead to the formation of DME. A summary of recent publications about DME syntehsis *via* CO_2 hydrogenation is reported in Table 1.5.

Catalyst	**H_2/CO_2**	**GHSV [NmL·g^{-1}·h^{-1}]**	**P;T [MPa;°C]**	**X_{CO2} [%]**	**Y_{CO} [%]**	**Y_{MeOH} [%]**	**Y_{DME} [%]**	**Rif.**
Cu/Zn/Al/Cr ZSM5	3	6600 1500	3;260			-	6.8 12.5	78
Cu/Zn/Al/Zr ZSM5	3	3100	3;260	24.1	7	10.6	6.4	138
Cu/Zn/Zr Ga-Sil1	3	1200	3;250	19.0	6.4	4	8.6	139
Cu/Ti/Zr ZSM5	3	1500	3;250	15.6	6.1	2.0	7.4	119
Cu/Zn/Zr/V ZSM5	3	1500	3;270	32.5	9.1	4.3	19.1	140
Cu/Zn/Al/Zr ZSM5	3	6000	5;270	27.5	-	5.0	16	118
Cu/Zn/Al/La ZSM5	3	3000	3;250	43.8	0.11	1.9	31.2	141
Cu/Mo ZSM5	2	1500	3;240	12.4	2	0.7	9.5	142
Cu/Zn/Zr/Pd ZSM5	3	1800	3;200	18.7	2.4	2.5	13.8	143
Cu/Zn/Al ZSM5+CNTs	3	1800	3;260	46.2	8.9	16.4	21	144
Cu/Zn/Al HZSM5 Cu/Zn/Al	3	3000	5;260	31 20	2	9.3 8	19 0.4	145

γ-Al2O3					11.6			
Cu/Zn/Zr FER	3	8800	5;260	23.6	9.2	3.5	10.6	85
Cu/Zn/Al ZSM5 Cu/Zn/Al γ-Al2O3	8	750	4;275	50 40	-	-	35 17	111
Cu/Zn/Al ZSM5 Cu/Zn/Al γ-Al2O3	3	750	4;275	35 40	-	-	23 10	111
Cu/Zn/Al Amorphous silica-alumina	3	1800	3;270	47.1	12.3	14.7	20.1	146
Cu/Fe/Zr ZSM5	5	1500	3;260	28.4	2.2	4.2	18.3	147

Table 1.5 – Scientific results about CO_2-to-DME reaction

Traditional operation conditions are 3 -5 MPa, 200 – 280 °C and GHSV = 1000 – 10000 NmL/h/g. Results suggest that zeolites, as H-ZSM-5, are much more active than γ-Al_2O_3 for DME production because it is much more able to dehydrate the alcohol thanks to its higher acidity [111, 145]. Modification of CuO-ZnO-Al_2O_3/ZrO_2 redox function with vanadium or lanthanum via co-precipitation method was made to sensibly increase the activity in terms of CO_2 conversion and DME yield [140, 141]. It is possible to increase the DME productivity by increasing H_2/CO_2 ratio [111], but this solution is not so profitable because until-now hydrogen is mainly produced from fossil sources. Finally, DME yield can be rised by increasing contact time [78]. Therefore, zeolites can be selected as reliable catalyst with built ib acid function for DME production *via* CO_2 hydrogenation and a DME yield value around 20-25%, until-now it is a promising value but a lot of research of catalyst, technology and operation conditions is necessary in order to obtain profitability from this *green chemistry challenge*.

CHAPTER 2

Zeolites in catalysis

Introduction

Since the aim of this work is to investigate the use of zeolites as catalysts for DME production by both methanol dehydration and CO_2 hydrogenation, in this Chapter, the main physicochemical properties of zeolites are discussed. The nature of acid sites and the *shape-selective* of zeolite catalysts are described with the aim to give an adequate background to discuss the results presented in the next chapters. Furthermore, the parameters affecting coke deposition and catalyst deactivation especially during methanol conversion processes, are particularly analysed.

2.1 Physico-chemical properties of zeolites

Zeolites are crystalline aluminosilicates with a three-dimensional framework that forms uniformly nanometric-sized channels and cages. As the intracrystalline voids preferentially allow the diffusion to the molecules that fit snugly inside the channels and exclude the molecule of larger size, zeolites act as sieves on molecular scale. Thank to their unique crystal structure, zeolites exhibit high porosity and large surface area. The nanosized structure voids of zeolites is generated by a network of SiO_4 and AlO_4 tetrahedra (TO_4) linked together by a shared oxygen atom. Therefore, zeolites are tecto-silicate materials. Aluminium can be substituted with other trivalent atoms (e.g. Fe, Ga, B, Ge) giving to the structure different chemical-physical properties depending on the incorporated metal [148]. Due to the presence of trivalent atoms in the tetrahedral units, the framework has a negative charge, which needs to be balanced with a non-framework exchangeable cation. The exchangeable cations are generally elements of the group IA and group IIA such as sodium, potassium magnesium and calcium [149] but also an organic cation can balance the negative charge of network [150]. Since they have exchangeable cations, zeolites can be used as materials in ion exchange applications, especially for waste-water treatment [151, 152].

Zeolites chemical composition can be generally written in oxide form:

$$M_{2/n}O \cdot Al_2O_3 \cdot x\ SiO_2 \cdot y\ H_2O$$

where *n* is the cation valence charge, *x* can vary from 2 to infinity, and *y* represents the water contained in the voids of the zeolite. An important properties of zeolites is the non-random arrangement of TO_4 tetrahedra in the lattice of the material. For instance, in zeolite structure, Al-O-Al bonds are not present as asserted by Loewentstein's rule [153]. Zeolites can be classified according to Si/Al ratio as suggested by Flanigen [154]:

- *low-silica* zeolites with Si/Al <2 as A and X;
- *intermediate-silica* zeolites with 2<Si/Al<10 as erionite, chabazite, mordenite, Y, L, omega;
- *high-silica* zeolites with 10<Si/Al<100 as MFI and BEA;
- *zeosils* with Si/Al= ∞ as Silicalite-1.

By particular treatment known as *dealumination* (by steam and/or acid treatment) it is possible to extract aluminium from the framework of the starting materials, increasing the Si/Al ratio [155].

The aluminium content strongly affects zeolite performances whatever the application, as it is explained later in this chapter.

Zeolites can be classified also according to the framework structure. As mentioned before, zeolite structure consists of channels and cages generated by three-dimensional arrangement of tetrahedral units. The channels size of zeolites is determined by the number of T-atoms forming the entrance (MR, member ring size) to the interior of the crystal. According to this number, zeolites can be classified in [149]:

- *Small pores* zeolites with up to 8 member-ring channel openings;
- *Medium pores* zeolites with up to 10 member-ring channel openings;
- *Large pores* zeolites with up to 12 member-ring channel openings.

In addition, zeolite structures are classified according to the connections between channels and how they are arranged in the space. Indeed, the channels can be *one-dimensional*, *two-dimensional* and *three-dimensional* as represented in Figure 2.1.

iIn the present thesis the following zeolite structures are investigated:

MFI: *medium-pores* structure with *3-dimensional 10-member rings* channels;

BEA: *large -pores* structure with *3-dimensional 12-member rings* channels;

CHA: *small-pores* structure with *3-dimensional 8-member rings* channels;

FER: *small/medium-pores* structure with *2-dimensional 8/10-member rings* channels;

MOR: *large-pores* structure with *1-dimensional 12-member rings* channels;

MTW: *large-pores* structure with *1-dimensional 12-member rings* channels;

EUO: *medium-pores* structure with *1-dimensional 10-member rings* channels;

TON: *medium-pores* structure with *1-dimensional 10-member rings* channels.

Chemical-physical properties of zeolites can be modified during synthesis or by post-synthesis treatment.

Synthesis of zeolites usually starts from a hydrogel system containing silica and aluminium sources and consist in three basic steps: achievement of supersaturation, nucleation and crystal growth. All these steps, strongly depend on synthesis conditions (e .g. concentration of reactants, temperature, time, ageing) [156, 157].

The main silica sources used for large-scale production are sodium silicate solutions or amorphous precipitated silica, while for scientific investigation purest and more expensive silica sources as pyrogenic silica, colloidal silica and tetraethyl-orthosilicate are often used. It is well known that silica source affects both crystallization rate, crystal size and might favour a specific phase [158]. Aluminium sources can be sodium aluminate, aluminium hydroxide, aluminium sulphate and aluminium nitrates. In order to permits dissolution of silica source a basic medium (pH>8) is usually adopted; alternatively, the synthesis can be carried out in acid conditions by using F^- ions [159]. Sodium hydroxide solution is often used to obtain basicity except in some cases in which Na^+ ions do not allow formation of desired phase. One of the primary role of inorganic cation (e.g. Na^+) is to balance the zeolite framework charge created by the incorporation of trivalent aluminium. In addition, the structure of inorganic cation's idrate layer can affect the morphology of zeolite crystals acting on nucleation period [160].

The synthesis of high-silica zeolites is often carried out in presence of organic template or structure directing agents SDA (e.g. alkylammonium salts, alkylammonium hydroxide, amines, alcohols or ethers). Templates are agents that kinetically and/or thermodynamically contribute to the formation of zeolite lattice during the crystallization process. Organic template can play an import role during the gelation and/or nucleation process, allowing TO_4 units self-organization surrounding the organic molecules directing the structure growth [161]. On the other hand, experimental investigations demonstrated that synthesis of some structures can be performed also in absence of organic template or by using different organic templates. Obtained material of the same structure but different chemical-physical characteristic, for instance, in terms of aluminium localization [162, 163] showing that organic molecule's role depends strongly on the *gel chemistry* [161]. So far, it is not possible to correctly predict which template is required for a desired structure and experimental investigations are always necessary.

Others parameters affecting zeolites crystallization are temperature and time. In general, both temperature and time have a positive effect on zeolite formation. The rates of both nucleation and crystal growth paths rises by increasing synthesis temperature. The relative rates of nucleation and crystal growth are important in terms of final material characteristics. For instance, low temperature ageing can favour nucleation promoting the formation of large number of nuclei, leading to the formation of nanosized crystals, as discussed by Valtchev *et al.* [164]. Time has similar effect of temperature on crystallization: by increasing time an increase in crystallinity of final material is usually observed. Unfortunately, it is valid over determined conditions, as zeolite synthesis is governed by the occurrence of successive phase transformations. It is often that initially formed a thermodynamically metastable phase is gradually replaced by more stable one [165]. Among the several factors governing these processes, temperature and time play a key role. For this reason, it is important to monitoring crystallization in order to know the kinetics of the phase transformations occur.

A complete comprehension of the zeolite formation mechanism is still an open challenge and *recipes* "optimised" for a desired phase are often published without a complete explanation of phenomena occurring during the synthesis. Recent research is focusing on tailor-made zeolites in order to obtain controlled characteristics for specific industrial applications.

Zeolites are industrially applied in several applications such as *ion exchange* (e.g. as detergent builders for water softening), *adsorption* (e.g. gas/liquid treatment and/or purification) and *catalysis* (oil industry, many organic chemistry reactions) [166].

2.2 Catalysis: general concepts

In order of a chemical reaction occurrence, reactant molecules must overcome an energy barrier (activation energy) to be transformed in products. Catalyst decreases this energy barrier speeding reaction rate by changing reaction path without affecting thermodynamic (the overall change in free energy for the catalysed reaction is the same of that of un-catalysed reaction). Furthermore, at the end of reaction, catalyst is theoretically unchanged being available for another reaction cycle.

Catalysis can be homogenous or heterogeneous. In homogenous catalysis the catalyst is in the same phase of reacting system, usually liquid phase. On the contrary, in heterogeneous catalysis, the catalyst is in a different phase of the reactant system;

typically, heterogeneous catalysis involves a solid catalyst for both liquid/vapour/gas-phase reactions. Both homogenous and heterogeneous have advantages and disadvantages. For instance, in homogenous catalysis, all catalyst active sites are available for reaction and temperature control is usually easy to design. On the other hand, the separation of the catalyst is usually expensive and it produces waste-streams which have to be treated causing additional process costs. In addition, for reaction catalysed by acids, reactor unit have to be built using expensive materials to prevent corrosions. The advantages of use of solid heterogeneous catalysis are in easy separation of the catalyst from the reaction system, the corrosion problems are avoided and desired products distribution can be obtained by using shape-selective materials, as zeolites. For this reason, heterogeneous catalysis is usually more selective, cheaper and with fewer process problems than homogenous catalysis. Nevertheless, some important disadvantages cannot be omitted: the active sites are usually located inside the solids particles and only a fraction of chemical potential of the species is utilized to promote diffusion of reactant and product in and from the catalyst particles. In addition, the heat transfer limitations inside the solid make the temperature control at the catalyst surface a challenge task to be achieved. Taking intro account the above-mentioned aspects, heterogeneous catalysts in more industrially adopted than the homogenous one. Heterogeneous catalysis involves several consecutive steps:

- Diffusion of reactant molecules from bulk phase (liquid/vapour/gas) to the external surface of the catalyst (*material external transport resistance*). This resistance can be modulated by changing fluid-dynamics operation condition of the reactor;
- Diffusion of reactant molecules from the external surface of the catalyst in the internal pores (*material internal transport resistance*). This resistance depends on several factors as catalyst pellet/crystal size, diffusivity of the species and temperature and it can be reduced by decreasing internal diffusion path (e.g. reduction of crystal size or increasing pore openings)
- Chemical reaction on catalyst surface that consist of reactants adsorption involving the active sites, superficial reaction and desorption of unconverted reactants and products.
- Diffusion from the internal channels to the bulk phase of both unconverted reactants and products.

The effect of a solid catalyst on reaction energies can be illustrated in Fig. 1.2 where is shown that the catalyst offers an alternative path for the reaction which can be more complex but energetically more favourable.

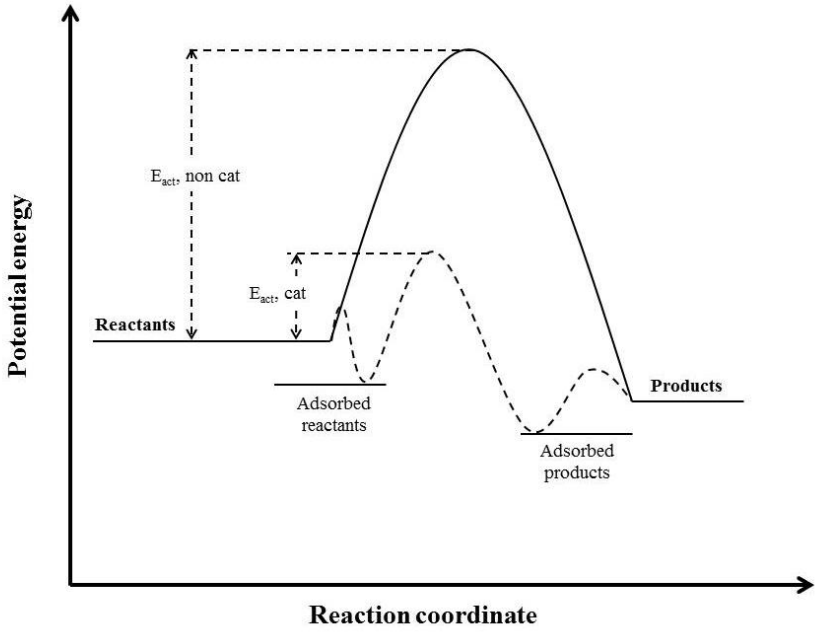

Figure 2.1 – Qualitative potential energy variation during catalysed and non-catalysed reaction

The above described steps are just theoretical informations about reaction path. Indeed, practical cases of heterogeneous catalysis are not so easy to investigate because of the several phenomena simultaneously occurring during the reaction. In particular, catalysis with zeolites involve too many factors to understand perfectly both reaction path and mechanism requiring sophisticated techniques (e.g. solid NMR, operando FT-IR [167]), in addition to the traditional catalytic tests in lab-scale reactors.

Zeolites are ranked as reliable acidic catalysts for several industrial applications mainly in oil industry. For instance, C_5/C_6 isomerization, dewaxing and fluid catalytic cracking (FCC) are important zeolites-based processes. Zeolites receive a growth attention from both industrial and academic research because their unique catalytic performances due to their high versatility in both structure, crystal size and acid sites distribution/strength permitting to optimize these factors in order to drive the reaction toward the desired products distribution. Catalytic characteristics of zeolites can be modulated during synthesis of material or by post-synthesis treatment.

2.3 Shape-selectivity of zeolites

The large use of zeolites in catalysis is due to the unique molecular shape-selectivity properties offered by these microporous materials. It is possible to define shape-selectivity as a reaction specificity deriving from the presence of a sterically confined environment in which the molecule of reactant can be converted in the products and the transformation of reactants into products depend on how the molecules spatially fit the active sites of the catalyst. Therefore, by using zeolites as catalysts, only molecules with dimensions smaller than a critical size can enter the pore, to be adsorbed on the internal catalytic sites and react, while only molecules that can leave the crystal appear in the final product. Shape-selectivity depends on molecules size and pore size of zeolites. Zeolites offer high versatility in this sense. As mentioned above, pores are formed by arrangement of tetrahedral units and the size of the pore depend of the number of these units and it is possible to synthesize zeolitic structures with tailored channels size and configuration depending on the catalytic application. It is possible to distinguish various types of shape-selectivities depending on whether channel size limits the entrance of the reacting molecules, or the *spillage* of the product molecules, or the formation of transition states. It is very easy to imagine these phenomena. For instance, if a feedstock contains molecules with different size only the molecules with kinetic diameter less than channel size of zeolites can diffuse inside and to be converted while the larger ones are excluded. Products selectivity is used for instance in MTO processes described in the previous chapter where methanol is converted over SAPO-34 catalyst exhibiting narrow channels (3.8 Å, 3-dimensional) suitable to obtain only ethylene and propylene in the products stream but contains also special cages permitting hydrocarbon pool mechanism [43]. Another type of shape-selectivity offered by zeolites is toward transition state. The reaction intermediates leading a specific molecule can be larger or smaller than the available space near to catalytically active sites in the zeolite crystal and thus, they can be constrained by the size and the geometry of zeolites channels and cavities. Disproportion and trans-alkylation of alkyl-aromatic compounds are examples of this type of selectivity [168]. Among the different types of shape-selectivities, the importance of the diffusion in zeolites cannot be overemphasized due to the comparable sizes between molecules and zeolite channels. In zeolites, the diffusing molecules continuously feel the interaction with the wall and this type of intracrystalline diffusion in zeolites is known as *configurational diffusion* in order to differentiate it from faster Knudsen diffusion [169]. In general, one molecule reacts or is formed preferentially and selectively if its diffusivity is at least one or two orders of magnitudes higher than that of competing molecules. For

instance, selective production of p-xylene via toluene alkylation with methanol over ZSM-5 is favoured by presence of this type of shape-selectivity that inhibits and/or slows down the diffusion of the m- and o-xylenes [170]. When this type of diffusion mechanism governs the catalytic process, diffusion path plays a key role in terms of activity and selectivity. In this sense, crystal size is an important parameter to select [171]. For instance, olefins production via MTO process is affected strongly by crystal size of SAPO-34 used in the reaction. Too small crystals don't form hydrocarbon pool species due to the too fast diffusion of species and DME is the main reaction product; too large crystals have a too slow diffusion of the species causing a fast deactivation for pore filling; therefore, an optimized crystal size is necessary to obtain high olefin selectivity [172]. The constrained diffusion in zeolites blocks reactant molecules to easy reach the active sites localized inside the crystal causing low catalyst effectiveness. Diffusion can be improved by reducing crystal size. Synthesis of nano-sized zeolites is an interesting field in which research dedicating several works by adopting using different techniques in both synthesis and porst-synthesis steps [157, 164, 173 – 175]. Recently, zeolites with microporous-mesoporous pores interconnected to each other can be a reliable way to reduce diffusion limitations and to preserve the shape-selectivity via micropores. These types of structures are recently well known as *hierarchical structures* [176, 177]. Experimental investigations demonstrate that both nano-sized and hierarchical zeolites exhibit better mass transfer and higher resistance to the deactivation by coke deposition due to a shorter residence time of coke precursor molecules inside the zeolite crystal [178 – 181].

2.4 Acid and base sites in zeolites

Beside the above-mentioned shape-selectivity, surface acidity and basicity is perhaps the most important property to consider when zeolites are used as catalysts. It is important to know the typology of acid/base sites (Brønsted or Lewis sites), their concentration or density, strength and strength distribution, and localization (inside the channels, on the external surface, inside cavities, etc.). A full knowledge on acid/base sites gives important information about both catalyst characteristics and reaction mechanism.

2.4.1 Nature of acid sites of zeolites

As described above, in aluminosilicate-type zeolites, the +4 charge on silicon situated on the zeolitic framework and the -2 charges on four coordinating oxygen atoms lead to neutral framework tetrahedra $TO_{4/2}$. If the silicon cation is substituted by another metal cation with a 3^+ charge (typically aluminium) the formal charge of tetrahedron changes from neutral to -1. This negative charge is balanced by a metal cation (e.g. sodium, potassium, litium) or by a hydroxyl proton H^+ forming a weak Lewis acid site or a strong Brønsted acid sites, respectively [149, 182]. The latter is important for catalysis. Brønsted acid sites are related to framework aluminium tetrahedrally coordinated with the silicon as following illustration [183]:

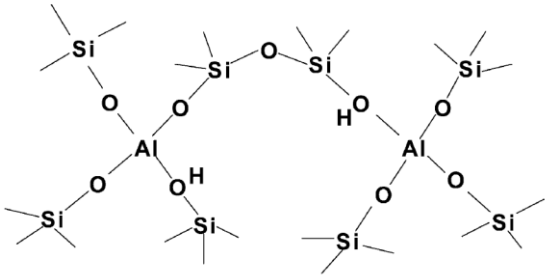

Figure 2.2 – Generation of Brønsted acid sites in zeolites [183].

The amount of Brønsted acid sites can be modulated by varying the tetrahedral aluminium content. In this sense, zeolites offer a high versatility as it is possible to vary the aluminium content in the framework during the synthesis. For instance, MFI can be synthesised in a wide range of Si/Al, from around 15 to ∞ [184, 185] obtaining materials with similar structure characteristics and shape-selectivity but different acid sites distribution. The strength of hydroxyl proton in SiOHAl bridge, can be modulated by isomorphous substitution of aluminium with other trivalent cations as gallium, boron, and iron. In particular, the strength of generated Brønsted acid sites follows the order SiOHAl>SiOHGa>SiOHFe>>SiOHB [186]. The strength of acid sites depends also on the angle of Si-O-T bridge. Si-O-T angle strongly affect the negative partial charge and thus the acid strength [187].

Despite to Brønsted acid sites, the origin of Lewis acid sites in zeolites is still matter of debate. In general, Lewis acid sites are sites without proton but with a positive vacancy able to accept an electron pair.

Usually, extra-framework aluminium species (octahedral aluminium) is referred as Lewis acid sites in zeolites. These species are formed during calcination treatments (above 500

°C) causing dehydroxilation of two Brønsted to form one Lewis acid site [149] as illustrated in Figure 2.3.

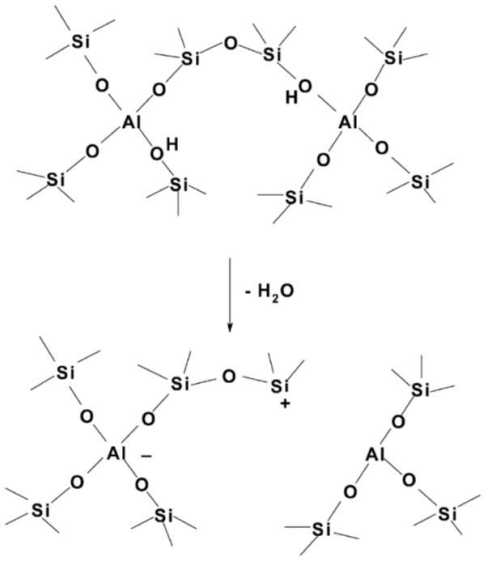

Figure 2.3 – Generation of Lewis acid sites in zeolites [183].

Furthermore, during dealumination extra-framework species as AlO^+, $Al(OH)_2^+$, AlO(OH) and $Al(OH)_3$ are generated acting as Lewis acid sites [183, 188, 189]. On the other hand, several studies demonstrate that zeolites can exhibit Lewis acidity also with no octahedral or extra-framework aluminium species. For instance, investigation on ZSM-5 by Woolery *et al.* [190] demonstrated that despite the absence of extra-framework species, the solid exhibits Lewis acid sites and the authors suggest that these sites can be located within the zeolite framework attributable to partially coordinated aluminium atoms (trigonal species) [191]. Similar experimental evidences were observed over Beta zeolite by Jansen *et al.* [192]. Furthermore, as reported by Wichterlová *et al.* [193] it is possible to change acid sites distribution by changing calcination temperature. Indeed, increasing the calcination temperature of zeolite ferrierite from 400 °C to 720 °C, Lewis acid sites increase from 80 µmol/g to 730 µmol/g with a decreasing of Brønsted acid sites affecting catalyst performances in skeletal insomerization of n-butenes. Also in this case no extra-framework aluminium species were detected by NMR measurements. Studies demonstrate that the presence of as Lewis acid site near to a Brønsted one, generates a site with a *superacid* behaviour [188].

A proper tuning of acid sites distribution is a key factor for catalysis. Beside the control of both acid sites concentration (related to aluminium content) or and typology (Brønsted and Lewis), it is important to control the location of acid sites inside the crystal. For

instance, Pinar *et al.* [163] suggest that is possible to control aluminium localization in FER structure by changing SDA molecule. The authors synthesize FER by using a combination of organic molecule in absence of inorganic cations observing that, after calcination in ozone at low temperature, aluminium is present in tetrahedral coordination with a related Brønsted acid site, but acid sites localization (10 MR, 8 Mr or cages) depends on SDA size affecting acid sites accessibility and catalytic performances in isomerizartion of m-xylene. Despite the fact that the effect of SDA molecule on acid sites distribution is not clearly demonstrated, FER structure offers high versatility. For this reason, in this Ph.D. work, FER crystals with different SDA were synthesised and their catalytic behaviour evaluated in Methanol dehydration to DME.

Analysis of acidity of zeolites can be carried out by several techniques. The number and the strength of acid sites can be estimated by acid sites titration with ammonia (NH_3-TPD measurements), despite this technique is not able to discriminate between Brønsted and Lewis acid sites [192]. In order to overcome this experimental limit, other techniques as FT-IR of adsorbed probe molecules as acetonitrile, pyridine, ammonia and CO [193 – 198] can be performed. Furthermore, a deep knowledge of origin of acid sites in zeolites can be offered by NMR analysis (about ^{1}H-, ^{27}Al-, ^{29}Si-, ^{23}Na-NMR) [199 – 202].

2.4.2 Nature of base sites of zeolites

The basicity of zeolites is much less documented than acidity. Anyway, it is possible to distinguish Lewis base sites from Brønsted: Lewis base sites are related to framework oxygen (able to donate an electron pair) and Brønsted base sites to extra-framework OH species [149]. The basicity of framework oxygen strongly depends on counter-cation of near aluminium atom. For instance, the negative charge of oxygen increase from Li^+ to Na^+ exchanged zeolites, documented by Deka et al. [182]. A lower basicity is observed over proton exchanged zeolites but it allows H^+ mobility favouring formation of reaction intermediates [203]. As described in the previous chapter, DME production is promoted by combination of H^+ site with its adjacent basic site O^{2-} [89]. With the aim to generate highly basic zeolite catalyst, impregnation with various alkali salts, such as cesium hydroxide, is adopted for catalytic applications [204].

2.5 Catalyst deactivation by coke deposition on zeolites

Catalyst deactivation by coke deposition is a key-aspect when acid zeolites are used in catalytic processes involving organic compounds [205]. The discussion of catalyst deactivation by coke deposition is often wrongly restricted to graphitic species deposited on the catalyst. Several investigations were carried out in order to elucidate composition, location and mechanism of coke formation, as reported by Guisnet and Magnoux [206]. The term *coking* is referred to retention of heavy products in the pores on the outer surface, that cause catalyst deactivation due to the poisoning of the active sites or/and to pore blockage. Therefore, any molecule too large, or too strongly affine to acid sites, slow down the diffusion through the nanosized channels of zeolites, blocking the access to and from the acid sites, leading to deactivation.

Coke deposition is a reversible phenomenon due the possibility to burn it with oxygen or air at high temperature. After regeneration the catalyst perfrormance can be affected by this thermal treatment (due to high temperatures spots) and the main problem is the progressive loss of activity with further regeneration cycles. For instance, zeolites, during coke combustion can be dealuminated due to the presence of the water at high temperature produced by coke combustion [207]. The coke formation in industrial hydrocarbon processing cannot be underestimated from an economic point of view: even though the activity of a coked zeolite catalyst can be recovered by coke combustion, regeneration is frequently incomplete and it requires additional investment to the regeneration costs and adding of fresh catalyst. For this reasons, a deep understanding about coke deposition and the effect of catalyst properties on its formation is important during catalyst assessment.

Formation of coke strongly depends on several factors such as operating conditions (temperature, contact time), reactants composition and catalyst characteristics. Because in this thesis an important effort was focused on coke formation in methanol conversion to DME, the main factors of catalyst deactivation by coke deposition are briefly discussed in this paragraph.

As reviewed by Guisnet *et al.* [207], composition, location and formation of coke in zeolites are determined by:

- The features of reaction: kinetic of both desired and undesired reaction, size and shape of reactant and product molecules and characteristics of the reactor;
- The operation condition: mainly temperature and contact time;
- The features of the catalyst: (i) acid sites distribution in terms of amount, typology (Brønsted/Lewis), location and strength, (ii) size, shape and configuration of the channels and (iii) crystals size and morphology.

Coke is preferentially formed over acid catalysts because they can promote reactions such as oligomerization, cyclization and condensation what lead formation heavy products that cannot be easily desorbed form the catalyst. Guisnet *et al.* [207] summarize very well the catalyst characteristics required to limit coke formation. Catalyst should to have a pores structure large enough to allow the desired reaction (fast diffusion of both reactants and products) but narrow enough to limit formation of heavy molecule (coke precursor) and have a fast desorption of these molecules from catalyst surface. Beside a well tailored structure, the catalyst should have low density acidity and weak strength in order to limit consecutive reaction of fast oligomerization and cyclization, typically formed in the presence of strong acid sites. From this viewpoint, zeolites offer a high versatility in terms of both structure configuration and acidic properties.

2.5.1 Coke formation during methanol conversion reaction

As adverted in the previous chapter, coke deposition during methanol conversion processes is the main challenge, especially during MTO where the process is affected by a rapid catalyst deactivation. In this concern, many research efforts have been focused towards improving the stability of the catalyst. As mentioned before, coke formation is affect strongly on catalyst characteristics. For instance, the particular channel topology exhibited from SAPO-34 (small channels with wide cage), allows to obtain an high yield in olefins due the very active hydrocarbon pool mechanism but, at the same time, a fast deactivation is generally observed, due the trapping of heavy molecules inside the cages [179]. For instance, it is possible to delay catalyst deactivation by decreasing crystal size, but an optimal size is necessary to have a fast diffusion of coke precursor molecules but not too fast to avoid conversion of methanol/dimethyl ether molecules. Chen *et al.* [179] suggest that a crystal size of 0.4-0.5 μm should be a reliable compromise between olefin production and catalyst deactivation on SAPO-34, but this value depends on reaction conditions. In the same work, the authors showed that a determined amount of coke is beneficial for olefins formation. Of course, this beneficial effect is attributed to presence of reactive coke like *pool* molecules. Because the constraining *configurational diffusion* in these catalysts, coke deposition can affect product selectivity. Chen *et al.* [208], found that partially coked SAPO-34 exhibits a higher selectivity towards ethylene than the fresh catalyst, because coke improves the transition-state shape selectivity that govern the olefins formation in MTO mechanism [209]. As mentioned before, catalyst deactivation during methanol conversion reaction is affected strongly on pore structure of the catalyst

itself and to find a reliable relation is an open challenge. For instance, a catalyst with a three-dimensional channel configuration with large intersection should lead to the formation of heavier compound and causes a faster deactivation than a catalyst with smaller intersection that should inhibits formation of large molecule. On the contrary, Djieugoue *et al.* [210], compared silicoaluminophosphates with similar channel size but different cage size such as SAPO-34 (large cages) and SAPO-35 (small cages) and found out that the catalyst deactivation depends on the probability how the coke precursor molecules can diffuse from the cages. SAPO-34 has six 8-membered ring openings in each cages, while SAPO-35 just three 8-membered ring openings. The probability of molecular diffusion in and out of the cages is related to the number of cage openings, and a smaller number of rings causes a faster deactivation. Coke location is also important to understand the phenomena. For instance, it is well known that ZSM-5 exhibits much higher stability toward coke deposition than SAPO-34 during methanol conversion. This results are well documented by Bjørgen *et al.* [211] which show that for ZSM-5 catalyst, coke is preferentially formed on the external surface and catalyst deactivation is caused by preventing diffusion by the coke from external surface of crystal on the pore openings. Similar results were published by Schulz [212], investigating also the effect of reaction temperature on catalyst deactivation. He showed that a relatively low reaction temperature (270 – 300 °C) casuses deactivation of ZSM-5 due to the deposition on the external surface of monocyclic aromatics polisubstitutes formed by alkylation of benzene rings with ethylene and propylene. At higher temperature (470 °C), these alkylation reactions are reversed and an improved stability of the catalyst was observed. High temperature catalyst deactivation is caused by dehydrogenation reaction between methanol and aromatic species to form heavier compounds that block pore openings. During this reaction methane is an indicator molecule. Therefore, to study the right effect of structure on catalyst deactivation is tough issue due to the presence of several factors and different operation conditions which strongly affect catalyst deactivation. So, clear comparison among the several published results is not easy. In addition, beside textural properties, other factors, as amount and strength of acid sites, affect coke formation and catalyst deactivation, even if with a slighter influence. For instance, Bleken *et al.* [213] compare catalytic behavior of H-SSZ-13 and SAPO-34 catalyst in MTO reaction. Both catalyst have CHA framework type with similar number of acid sites but different acid strength. The authors found that H-SSZ-13 exhibit higher initial activity and deactivation rate than H-SAPO-34 due to its more strength acid sites.

Therefore, coke formation during the reaction of methanol conversion to DME, catalyst should have weak/medium acid sites capable to promote alcohol-to-ether conversion inhibiting further reaction, with a structure exhibiting a high shape selectivity, and textural properties useful to promote a fast diffusion of both DME and coke precursor molecules. Suitable are nanosized and/or hierarchical zeolites [178 – 181, 214].

CHAPTER 3

Experimental

Introduction

Aim of this chapter is to illustrate the methods and the techniques use to synthesise the investigated catalysts and characterise them in terms of the main chemical-physical properties. Crystals phase and morphology were analysed by XRD, SEM and TEM methods while N_2 adsorption isotherms were performed in order to estimate textural properties as specific area and micropore volume. NH_3-TPD and FT-IR analysis were also used with the aim to characterise the investigated catalysts in terms of acid sites amount and type (Brønsted and Lewis). Finally, a description of experimental apparatuses for catalytic tests for DME synthesis by both methanol dehydration or CO_2 hydrogenation route were also reported in this chapter.

3.1 Catalysts synthesis

In order to investigate the effect of catalyst structure on methanol dehydration step, zeolites with different channel system are synthesized. MFI, FER, CHA, BEA, TON, EUO, MOR and MTW are compared. In particular, for MFI and FER structures, catalysts with different acidity are also prepared.

All of the investigated catalysts used in this thesis are in-home synthesized. All the syntheses are carried out under hydrothermal conditions using Teflon-lined stainless steel autoclaves. Before the synthesis the autoclaves are cleaned by using nitric acid (65%) to remove eventual traces of organic compounds and hydrofluoric acid (48%) to eliminate eventual traces of crystals of previous synthesis and rinsed with distilled water until the pH of the autoclave reach the neutral value. A deeper investigation about synthesis of FER catalyst is performed because, as demonstrate in the discussion of results, FER exhibits the best catalytic performances for DME production compared with the other investigated catalysts. The performance benchmark was obtained by evaluating the catalytic activity of commercial γ-Al_2O_3 (Alfa Aesar, UK).

Table 3.1 report the main structure characteristics of the investigated samples.

Topology	Material	Channel orientation	Member rings	Channel size [Å]	Maximum diameter of a sphere that can be included [Å]
MFI	ZSM-5	3D	10	5.1x5.5 <>5.3x5.6	6.36
BEA	Beta	3D	12	6.6 x 7.7 <> 5.6 x 5.6	6.68
CHA	SAPO-34	3D	8	3.8 x 3.8	7.37
FER	ZSM-35	2D	10 x 8	4.2 x 5.4 <> 3.5 x 4.8	6.31
MOR	Mordenite	1D	12 // 8	6.5 x 7.0 <> 2.6 x 5.7	6.70
MTW	ZSM-12	1D	12	5.6 x 6.0	6.08
TON	ZSM-22	1D	10	4.6 x 5.7	5.71
EUO	EU-1	1D	10	4.1 x 5.4	7.0

Table 3.1 – List and structure characteristics of the investigated catalysts

3.1.1 Synthesis of MFI-type sample

Four MFI-type zeolites were prepared starting from the following molar composition:

$$0.1\ Na_2O - 0.08\ TPABr - 1\ SiO_2 – 0.02\ Al_2O_3 - 20\ H_2O$$

The synthesis gel was prepared following procedure: 2.66 g of sodium hydroxide (Aldrich) was added to 119.40 mL of distilled water. The appropriate amount of aluminum hydroxide (Aldrich) was added to the basic solution and, after its dissolution, 7.10 g of tetrapropylammonium hydroxide (Aldrich) was added to the gel. As last step, the addition of 19.95 g of precipitated silica (Merck) in the batch was followed by stirring (2 h) at room temperature. The crystallization was carried out in 150 mL PTFE-lined stainless steel autoclave in static conditions at 175 °C. After 96 h of crystallization, the solid phase was separated from the liquid by filtration, washed several times with distilled water and dried at 100 °C overnight

3.1.2 Synthesis of FER-type samples

As mentioned before, a particular attention is focused on FER structure due to its reliable catalytic performances for DME production in both direct and indirect synthesis. Indeed, the effect of gel synthesis composition (organic SDA and aluminum content) on the

catalytic properties of the final material is investigated. For clarity, only the optimized syntheses are reported in this chapter.

3.1.2.1 Synthesis of FER8 by using ethylendiammine

The synthesis of FER with Si/Al≈8 by using ethylendiammine (En) as SDA follows the procedure suggested in Ref. [215] by adopting the following starting molar composition:

$$1.3\ En - 0.122\ Na_2O - 1\ SiO_2 - 0.066\ Al_2O_3 - 40\ H_2O$$

In a typical synthesis, 0.303 g of NaOH (Aldrich) were dissolved in 64.1 g of H_2O followed by dissolution of 1.31 g of sodium alluminate (Aldrich, assay ~54%$_{wt}$ of Al_2O_3). After complete dissolution 8.2 g of ethylnediammine (Aldrich) was added dropwise. After 1 h of stirring 15.8 g of LUDOX AS40 (Aldrich, assay 40%$_{wt}$ of colloidal SiO_2) was added dropwise and the gel was stirred for 1 h. The crystallization was carried out in 150 mL PTFE-lined stainless steel autoclave at dynamic conditions using 20 rpm at 175 °C. A Teflon-coated magnetic bar was put into the autoclave in order to have a homogenous tumbling during the crystallization. After 10 days of crystallization, the solid phase was separated from the liquid by filtration, washed several times with distilled water and dried at 100 °C overnight. The sample is named En-FER8

3.1.2.2 Synthesis of FER(8) by using pyrrolidine

The synthesis of FER with Si/Al≈8 by using pyrrolidine (Py) as SDA follows the procedure suggested in Ref. [215] by adopting the following starting molar composition:

$$0.6\ Py - 0.080\ Na_2O - 0.05\ Al_2O_3 - 1\ SiO_2 - 20\ H_2O$$

In a typical synthesis, 1.69 g of sodium alluminate and 0.165 g of NaOH were disoolved in 39.8 g of distilled water. 6.3 g of pyrrolidine (Aldrich) were added dropwise and the gel was stirred for 30 min. 22 g of LUDOX AS40 were added dropwise and the gel was stirred for 1h. The crystallization was carried out in 90 mL PTFE-lined stainless steel autoclave in tumbling conditions at 20 rpm at 175 °C. A Teflon-coated magnetic bar was put into the autoclave in order to permit a homogenous tumbling during the crystallization. After 72 h of crystallization, the solid phase was separated from the liquid by filtration, washed several times with distilled water and dried at 100 °C overnight. The sample is name Py-FER8.

3.1.2.3 Synthesis of FER(8) by using tetrahydrofuran

The synthesis of FER with Si/Al≈8 by using tetrahydrofuran (THF) as organic template follows the procedure suggested in Ref. [216] by adopting the following starting molar composition:

$$0.5\ THF - 0.215\ Na_2O - 1\ SiO_2 - 0.05\ Al_2O_3 - 20\ H_2O$$

In a typical synthesis, three solutions (A, B, C) were prepared in the following way:

A: 6.1 g of $Al_2(SO_4)_3x18H_2O$ (Fluka) was dissolved in 23.3 g of H_2O followed by adding of 27.5 g of LUDOX AS40. Stirring for 30 min.

B: 3.16 g of NaOH were dissolved in 23.3 g of H_2O

C: The solution A was added dropwise to the solution B, stirred for 1 h, and 6.67 g of THF (Aldrich) were added dropwise and the mixture was stirred vigorously for 1h.

The crystallization was carried out in 90 mL PTFE-lined stainless steel autoclave in a static oven kept at 200 °C. After 6-12 days of crystallization, the solid phase was separated from the liquid by filtration, washed several times with distilled water and dried at 100 °C overnight. As discussed in the next chapter, crystallization time is a key factor to obtain pure ferrierite phase. The sample is named THF-FER8.

3.1.2.4 Synthesis of FER(8) by using 1,8-diamminoctane

1,8-diammioctane (DAO) is not referred as a structure directing agent molecule for synthesis of ferrierite. Nevertheless, by partial substituting of ethylendiammine (En) with DAO, pure phase ferrierite was obtained as discussed in the next chapter. The syntheses were carried out by adopting a DAO/En ratio between 0.25 and ∞ according to the following gel composition:

$$x\ En - 0.122\ Na_2O - 1\ SiO_2 - 0.066\ Al_2O_3 - 40\ H_2O - y\ DAO$$

with $0<x<1.3$ and $0.33<y<1.3$

The synthesis of ferrierite sample with only DAO as organic molecule is carried out by mixing three solutions (A, B, C) prepared in the following way:

A: 0.300 g of NaOH and 1.29 g of sodium alluminate were dissolved in 21 g of distilled water.

B: 7.80 g of 1-8diamminooctane (Aldrich)) were dissolved in 42 g of water.

C: The solution A was added to the solution B and 15.5 g of LUDOX AS40 were added dropwise.

The gel was kept under stirring condition for 1 h and put in 90 mL PTFE-lined stainless steel autoclave in dynamic conditions at 20 rpm at 175 °C. A Teflon-coated magnetic bar was put into the autoclave in order to permit a homogenous tumbling during the

crystallization. After 8 days of the solid is completed crystallized; it was separated from the liquid by filtration, washed several times with distilled water and dried at 100 °C overnight. The sample is name DAO-FER.

3.1.2.5 Synthesis of nanosized FER-type crystals

Synthesis of nanosized ferrierite crystals is successfully performed by using pyrrolidine as SDA and sodium lauryl sulphate (SLS) acting surfactant. The effect of surfactant on crystal size is discussed in Ref. [217]. The following gel composition:

$$0.6\ Py - 0.080\ Na_2O - 0.05\ Al_2O_3 - 1\ SiO_2 - 20\ H_2O - 0.015\ SLS$$

Three solution (A, B, C) were prepared in the following way:

A: 0.06 g of NaOH and 0.494 g of sodium alluminate were dissolved in 4.7 g of distilled water.

B: 0.226 g of sodium lautyl sulphate (SLS) were dissolved in 9.4 g of distilled water and 2.23 g of pyrrolidina (Py) was added dropwise. Stirring for 30 min.

C: The solution A was added to the solution B and 7.8 g of LUDOX AS40 were added dropwise.

In order to investigate the effect of seeding on crystal size distribution, a wt. 3% based on SiO_2 of pre-synthesized ferrierite nano-crystals with size around 300-500 nm (synthesized at 175°C, 20rpm for 72 h) was added to solution C before addition of silica source.

The final mixture is stirred for 1 h and transferred to the 20 mL PTFE-lined stainless steel autoclave. The gel was stirred at 80°C for 2 days. After the ageing period, the aucoclave is transferred to the tumbling oven (20 rpm). The effect of crystallization temperature on crystal size was also investigated by varying it between 120°C and 175°C. After 72 h (for synthesis temperature between 140-175°C) and 6 days (at 120°C) of the solid is completely crystallized; it was separated from the liquid by filtration, washed several times with distilled water and dried at 100 °C overnight.

3.1.2.6 Synthesis of FER30

Synthesis of FER with gel Si/al=30, namely FER30 and the next-discussed FER with gel Si/Al=60, namely FER60, are synthesized adopting gel synthesis composition suggested by Okubo *et al.* [218], using pyridine as SDA. The synthesis gel molar composition adopted to synthesize FER(30) is the follow:

$$0.6\ Pyridine - 0.087\ Na_2O - 0.0167\ Al_2O_3 - 1\ SiO_2 - 25\ H_2O$$

In a typical synthesis procedure 1.48 g of NaOH and 0.89 g of sodium aluminate are dissolved in 127 g of distilled water. Therefore, 5.41 g of pyridine (Aldrich) is added dropwise and the solution. After 30 minutes, 17 g of silica fumed (Aldrich, 200 m^2/g) is added to the solution. The obtained pasty gel is homogenized using a spatula for 30 minutes. The crystallization was carried out in 150 mL PTFE-lined stainless steel autoclave in tumbling conditions at 20 rpm at 165 °C. A Teflon-coated magnetic bar was put into the autoclave in order to permit a homogenous tumbling during the crystallization. After 7 days of crystallization, the solid phase was separated from the liquid by filtration, washed several times with distilled water and dried at 100 °C overnight. The sample is named FER30.

3.1.2.7 Synthesis of FER60

Similar procedure is adopted to synthesize ferrierite with gel Si/Al of 60, by adopting the following gel molar composition:

$$2\ \text{Pyridine} - 0.0575\ Na_2O - 0.0083\ Al_2O_3 - 1\ SiO_2 - 25\ H_2O$$

The crystallization is performed at the same temperature of FER30 but for 5 days. A longer synthesis time leads to the formation of the quartz phase. The obtained sample is named FER60.

3.1.3 Synthesis of BEA-type sample

Synthesis of sample with BEA structure and Si/Al on the gel equals to 25 is synthesized by using tetra-ethyl-ammonium-hydroxide (TEAOH) as SDAby adopting the following gel molar compostion:

$$0.2\ \text{TEAOH} - 0.1\ Na_2O - 0.02\ Al_2O_3 - 1\ SiO_2 - 10\ H_2O$$

In a typical synthesis procedure, 4.29 g of NaOH and 1.67 g of aluminium hydroxide (Merck) are dissolved in 32.83 g of water. After complete dissolution of the solutes, 79 g of a solution of TEAH (Merck, 20% in water) is added dropwise to the solution. At the end, 32.2 g of precipitated silica (BDH, Merck) is added to form a mixture that is stirred for 2 h. The crystallization is carried out in 150 mL PTFE-lined stainless steel autoclave under static conditions at 150 °C. After 6 days of crystallization, the solid phase was separated from the liquid by filtration, washed several times with distilled water and dried at 100 °C overnight. The sample is named BEA(25).

3.1.4 Synthesis of SAPO-34 sample

SAPO-34 (CHA topology) was synthetized using diethylamine (DEA) as a template [219] with following final gel composition:

$$4.2\ DEA - 1.67\ Al_2O_3 - 1.33\ P_2O_5 - 1\ SiO_2 - 83\ H_2O$$

In a typical synthesis 17.4 g of aluminium hydroxide was added in a solution containing 10.2 g of phosphoric acid (85%) and 92 g of distilled water. After stirring for 1 hour 20.44 g of SDA was added slowly followed by addition dropwise of 10 g of LUDOX AS40. The synthesis gel stirred for 2 hours at room temperature and left in a 150 mL PTFE-lined stainless steel autoclaves at 200 °C. After 48 h of crystallization, the solid phase was separated from the liquid by filtration, washed several times with distilled water and dried at 100 °C overnight. The sample is named SAPO-34

3.1.5 Synthesis of 1-D structures

3.1.5.1 Synthesis of MOR-type sample

Mordenite phase is synthesized without organic SDA by adopting the following gel molar composition:

$$0.2\ Na_2O - 0.02\ Al_2O_3 - 1\ SiO_2 - 20\ H_2O$$

The gel is prepared by dissolving 0.76 g of NaOH and 0.21 g of sodium aluminate in 25.73 g of water. After dissolution of solutes, 3.3 g of precipitated silica is added and the gel is stirred for 1 h at room temperature and left in a 30 mL PTFE-lined stainless steel autoclaves at 170 °C for 6 days in static conditions. After crystallization, the solid phase is separated from the liquid by filtration, washed several times with distilled water and dried at 100 °C overnight. The sample is named MOR.

3.1.5.2 Synthesis of TON-type sample

Synthesis of TON phase is performed referring to the procedure reported on IZA website *http://www.iza-online.org/synthesis/* by adopting the following gel composition by using 1,8-diamminooctane (DAO) as SDA:

$$0.3\ DAO - 0.140\ K_2O - 0.011\ Al_2O_3 - 1\ SiO_2 - 40\ H_2O$$

The synthesis gel is prepared mixing a solution A obtained by dissolution of 0.88 g of $Al_2(SO_4)_3x18H_2O$ (Fluka) in 9.1 g of distilled water with a solution B obtained by dissolution of 2 g of KOH (Carlo Erba) in 9.1 g of distilled water. A third solution C obtained by dissolution of 5.2 g of DAO in 36.4 g of distilled water is added. After mixing for 1 h, 17.1 g of distilled water and 17.1 g of LudoxAS40 are added dropwise to for the

final gel that is stirred at room temperature for 30 min. After that, the gel is transferred in a 100 mL PTFE-lined stainless steel autoclaves, kept under stirring condition at 500 rpm at 160 °C. After 72 h of crystallization, the solid phase was separated from the liquid by filtration, washed several times with distilled water and dried at 100 °C overnight. The sample is named TON.

3.1.5.3 Synthesis of EU-1 sample

The synthesis of zeolite with EUO structure (EU-1) is carried out by using hexamethonium bromide ($HMBr_2$) as SDA using a slight modification of the synthesis gel composition suggested by Giordano *et al.* [220]:

$$0.15\ HMBr_2 – 0.3\ N_2O – 0.0167\ Al_2O_3 – 1\ SiO_2 – 45\ H_2O$$

The synthesis gel is prepared by dissolving 0.36 g of aluminium nitrate (Aldrich) and 0.68 g of NaOH in 18.7 g of distilled water. After complete dissolution, 1.55 g of $HMBr_2$ (Aldrich) are added to the solution and homogenized by vigorous stirring. At last, 5.7 g of colloidal silica (LUDOX AS40) are added and the gel is stirred for 10 minutes. Therefore, the gel is transferred in a 50 mL PTFE-lined stainless steel autoclaves kept in tumbling condition at 20 rpm at 160 °C. After 14 days of crystallization, the solid phase was separated from the liquid by filtration, washed several times with distilled water and dried at 100 °C overnight. The sample is named EU-1.

3.1.5.4 Synthesis of MTW-type sample

The synthesis of zeolite with MTW structure is carried out using methyl tetraethyl ammonium bromide (MTEABr) as SDA using the following synthesis gel composition:

$$0.2\ MTEABr – 0.1\ N_2O – 0.01\ Al_2O_3 – 1\ SiO_2 – 20\ H_2O$$

The synthesis gel is prepared by dissolving 0.0.14 g of aluminium hydroxide and 0.72 g of NaOH in 16.1 g of distilled water. After complete dissolution, a solution containing 16.1 g of H_2O and 3.51 g of MTEABr (Aldrich) is added to the solution and homogenized by vigorous stirring. At last, 5.4 g of precipitated silica are added and the gel is stirred for 1 h. Therefore, the gel is transferred in a 60 mL PTFE-lined stainless steel autoclaves kept at 140 °C. After 6 days of crystallization, the solid phase was separated from the liquid by filtration, washed several times with distilled water and dried at 100 °C overnight. The sample is named MTW.

3.1.6 Synthesis of hybrid catalyst for CO_2 hydrogenation to DME

The procedure adopted for the preparation of the single grain hybrid catalysts consists in the *in situ* combination of CuZnZr species with the H-form zeolite powder (MOR, MFI or FER(8) material). $Cu(NO_3)_2 \cdot 2.5H_2O$, $Zn(NO_3)2 \cdot 6H_2O$ and $ZrO(NO_3)_2 \cdot nH_2O$ (in a Cu/Zn/Zr atomic ratio of 60/30/10) were dissolved in ethanol and coprecipitated by oxalic acid at room temperature, under vigorous stirring, in a solution containing the zeolite finely dispersed (particle size < 100 μm), giving a final CuZnZr-zeolite weight ratio of 2:1. The precipitate was stirred for 3 h, aged overnight, then filtered, dried at 110 °C for 16 h and calcined at 350 °C for 4 h. The obtained hybrid materials are named CZZ-MOR, CZZ-MFI and CZZ-FER.

3.1.7 Activation of the catalysts

The synthesised zeolite samples contain organic molecules inside the channels and sodium as counter-ion to framework aluminium atoms. In order to eliminate the organic from the channels of the zeolite samples, a calcination is carried out. The calcination procedure is performed by heating in static air at 550 °C for 8 h. Temperature rate was 5 °C/min. In order to exchange the sodium ions with protons, an ion exchange with NH_4Cl 1 M at 80°C for 2 h is performed twice. A second calcination at 550 °C decomposes ammonium ion, leaving a proton as counter-ion of framework aluminium.

On the other hand, activation of hybrid catalyst was performed directly in the reaction system by reduction *in situ* at 300 °C for 1 h in pure hydrogen flow, at atmospheric pressure.

3.2 Catalyst characterization

All of the investigated catalysts are characterized by XRD, porosimetric analysis, chemical analysis, thermogravimetric/differential thermal analysis (TG/DTA), scanning electron microscopy (SEM) and thermal programmed desorption of pre-adsorbed ammonia (NH_3-TPD). Some of them (MFI25, FER8, FER30, FER60, BEA and MOR) are also characterized by Fourier transform infrared spectroscopy (FT-IR).

3.2.1 XRD

Powder X-Ray diffraction is a technique traditionally applied to study the crystalline phases of solid materials based on the well know Bragg's equation [221]. By applying this analysis on zeolites powders, it is possible to study the evolution of crystallization, the purity of the synthesized material and other information such as sample crystallite size. XRD pattern consistes of peaks that reflects crystal structure of the material. Peak position (Bragg's reflexes) represents interplanar atoms distances, while their intensity reflects atoms concentration (electron density). By comparing this list with the published references, it is possible to identify the obtained phase (or phases) according to the peaks position, while by analyzing peaks intensity and shape, it is possible to calculate samples crystallinity. XRD patterns of the investigated catalysts were obtained by a APD 2000 Pro diffractometer operating at 40 kV and 30 mA, employing the Cu K_α radiation (λ=1.5406 Å) in the 2θ range 5–50°.

3.2.2 Porosimetric analsysis

The main textural properties of the investigated samples are estimated by analysis of isotherm adsorption/desorption of nitrogen in a range of relative pressure 0 – 99 P/P° at 77 K by using ASAP 2020 (Micromeritics). The superficial specific area is estimated by BET model, while external area, micropore area and micropore volume using *t*-plot method [222]. Prior to the analysis, the sample is evacuated to 5.3 Pa at 300 °C for 6 h (5°C/min).

3.2.3 Chemical analysis

All samples are characterized by atomic adsorption spectroscopy (GBC 932 AA) in order to calculate their chemical composition for aluminum, sodium and silicon. Before the measurement, the zeolite is dissolved in HF (Merck, 40% suprapure) and HNO_3 (Merck, 65% suprapure) and diluted according to the calibration range of the instrument.

3.2.4 TG/DTA

Both thermogravimentric (TG) and differential thermal (DT) analysis are carried out in order to:

- estimate the amount of organic SDA trapped inside the channels of the synthesized materials and its combustion temperature;
- Estimate the amount of coke deposited during the reaction.

All TG/DTA measurements are carried out using a DTG-60 (Shimadzu) instrument by heating the sample (around 10-15 mg) from room temperature to 850 °C with a thermal ramp of 10°C, with air flow of 20 mL/min.

3.2.5 SEM

Crystals morphology of the synthesized compound is analyzed by Scanning Electron Microscopy on a MIRA-LMH (TESCAN) instrument. Before the analysis, the zeolite powder is sprinkled on a carbon tape mounted on an aluminum stub and metalized by a platinum vapour.

3.2.6 TEM

Some samples are also characterized by Transmission Electron Microscopy (TEM) in collaboration with Prof. Fransceco Frusteri of CNR-ITAE, Nicola Giordano, (Messina, Italy). The analysis are carried out on a Philips CM12 instrument. Powder samples are dispersed in 2-propanol under ultrasound irradiation and the resulting suspension put drop-wise on a holey carbon coated support grid.

3.2.7 NH_3-TPD

Temperature Programmed Desorption of Ammonia (NH_3-TPD) is a technique largely applied to estimate the amount of acid sites on catalyst surface and their strength. Several reviews were published about NH_3-TPD, even if some aspects are until now unclear [223]. The analysis consists of adsorption of ammonia on the sample followed by its desorption with a programmed thermal ramp and detection of desorbed ammonia molecule by TCD or MS detectors. The amount of acid sites can be estimated by calculating the amount of ammonia desorbed, while their strength can be derived by analysis of temperature desorption maxima. The analysis conditions strongly affect the results as it is well documented by Niwa *et al.* [224, 225]. For this reason the same operation conditions are used in order to compare the investigated catalysts. The analyses are performed on a TPDRO 1100 (ThermoScientific) instrument using the following procedure:

- 100 mg of dry catalyst powder (partially dried at 180°C for three hours, in order to remove the main part of moisture that can affect the weight of the analyzed sample) is loaded to a quartz tubular reactor and put between two layers of quartz wool. The analysis procedure is consisted of:

- Pretreatment of the sample:
  - drying at 300 °C in helium flow (20 mL/min) for 30 minutes, followed by cooling a 150 °C holding this temperature for 5 minutes;
  - adsorption of ammonia at 150 °C using a diluted ammonia stream (NH_3/He, 10%v/v) with a flow rate of 20 mL/min for 120 minutes;
  - removal of physically-adsorbed ammonia by purging the sample with helium flow (20 mL/min) for 90 minutes.
  - cooling of the sample to 100 °C.
- Desorption of pre-adsorbed ammonia is carried out in helium flow (20 mL/min) by heating of the sample between 100 °C and 950 °C with a constant thermal ramp of 10 °C/min
- Analysis of obtained profiles using a software (PeakFit 4.12, Seasolve, USA) able to deconvoluteof the obtained peak and calculate of the area related to the detected ammonia quantity.

From the area of the the obtained NH_3-TPD profiles is possible to calculated the total amount of NH_3 desorbed (NH_3-uptake). The shape of the curve is related to acid sites distribution. The curve profile usually consists of temperature depending peaks where maximum desorption temperature (MDT) is related to the strength of acid sites, and their relative amount is calculable from the area of the peaks. For instance, peaks at lower desorption temperature refer to weaker acid sites than the peaks obtained at higher desorption temperature. Therefore, the analysis of the observable peaks can give estimated acid sites distribution (e.g. fraction of weak, medium and strong acid sites). The heat of the adsorbed ammonia can be estimated using measurements of different heating rate (r). The heating rate affects the desorption maximum temperature of the obtained desorption peaks (T_M). By plotting $\log(T_M^2/r)$ versus $1/T_M$ a linear correlation is usually derived, whose slope is related to the ammonia desorption energy as reported by Cvetanović [226]. Higher is the value of this parameter, stronger are the acid sites represented by the analyzed peaks. In this work, thermal ramps of 10°C/min, 20 °C/min and 30 °C/min are used to estimate the strength of acid sites of the investigated samples. Unfortunately, NH_3-TPD is not able to discriminate Brønsted from Lewis acid sites. For this purpose, vacuum FT-IR analysis is the mostly used technique.

3.2.8 FT-IR

FT-IR analysis of adsorbed probe molecule is the main technique used in order to discriminate Brønsted from Lewis acid sites on solid catalysts such as zeolites. This techniques is based on adsorption of a specific probe molecule and analysis of the obtained FT-IR spectra. Indeed, the interaction between the zeolite active sites with the probe molecule (that is a base molecule for acidity evaluations) results in changes of the absorption energy in the infrared region. By FT-IR spectra analysis it is possible to determine the type of the active acid sites [167].

Infrared spectra are recorded with a Nicolet Magna 550-FT-IR spectrometer with a 4 cm^{-1} optical resolution, using D_3-acetonitrile as probe molecule. Prior to the measurements, the samples in acid form were pressed in discs (density around 10 mg/cm^2) and treated in the IR cell attached to a vacuum line (cell pressure: 10^{-4} Pa) at 300 °C for 4 h (5 °C/min from room temperature). The adsorption of D3-acetonitrile was performed at room temperature with a pressure of 1333 Pa. After 15 minutes of probe molecule adsorption, the cell was evacuated at room temperature until a cell pressure of 10^{-4} Pa was established in order to remove the physisorbed molecules. In order to estimate the acid sites strength a D_3-acetonitrile temperature programmed desorption was performed at the temperatures of 25, 50, 100, 150, 200, 250 and 300 °C (before spectra recording at each temperature the sample was evacuated under vacuum for 15 minutes). The amount of D_3-acetontrile adsorbed on Brønsted and Lewis was determined by using the molar absorption coefficient proposed by Wichterlová *et al.* [195]. The number of Brønsted sites was calculated by the integrated area of the bands observed at 2297 cm^{-1} using an extinction coefficient of 2.05 cm/µmol, while the number of Lewis acid sites were calculated by integrated area of the bands between 2310 – 2325 cm^{-1} using an extinction factor of 3.6 cm/µmol.

3.2.9 ^{27}Al-NMR

The samples with FER structure synthesized with different SDA, are characterized also by ^{27}Al-NMR in order to evaluate the effect of SDA on aluminum coordination (tetrahedral or octahedral). ^{27}Al-NMR spectra were acquired at 130.3 MHz on a Bruker Avance III-HD 500 (11.7 T), using 4.0-mm outer diameter probe. Rotors were spun at 14 kHz and the recycle delay used was 1 second.

3.2.10 CO_2-TPD

Surface concentration of basic sites of redox/acid hybrid catalysts was determined by temperature programmed desorption of carbon dioxide. Before CO_2-TPD measurements, the catalyst (50 mg) was reduced, at atmospheric pressure, by flowing hydrogen (60 STP mL/min) in a linear quartz micro-reactor from room temperature to 300 °C, at a heating rate of 10°C/min. Then, the sample was maintained under hydrogen flow at 300 °C for 30 min. After cleaning with helium, the sample was saturated for 60 min in flow of a gas mixture containing 20 vol% of CO_2/He at a total flow rate of 25 mL/min. Then, the sample was purged in helium flow until a constant baseline level was attained. The measurements were performed in the temperature range 50-450 °C at a rate of 10 °C/min using helium (25 STP mL/min) as carrier flow.

3.2.11 N_2O-titration

Copper surface area (S_{Cu}) and dispersion (D_{Cu}) values for hybrid catalysts were measured by "single-pulse" N_2O-titration at 90°C. Before measurements the samples were reduced at 300 °C in flowing H_2 (100 STP mL/min) for 1 h, then "flushed" at 310 °C in nitrogen carrier flow (15 min) and further cooled down to 90 °C. S_{Cu} and D_{Cu} values were calculated assuming a Cu:N_2O=2:1 titration stoichiometry and a surface atomic densisty of 1.46×10^{19} Cu_{at}/m^2.

3.3 Catalytic evaluations

In this work the effect of zeolite structure and acidity is evaluated in the production of DME from both ways: indirect route (via methanol dehydration) and direct route (via CO_2 hydrogenation). The above described zeolites are tested in methanol dehydration step and the more promising catalysts are used as acid support of a Cu/Zn/Zr_2 for synthesis of DME from CO_2 in collaboration with Dr. Francesco Frusteri, CNR-ITAE "Nicola Giordano" (Messina, Italy). In this paragraph the experimental setup and reaction operation conditions are described.

3.3.1 Experimental system for methanol dehydration to DME

Methanol conversion reaction is carried out in a home-made atmospheric experimental system illustrated in Fig. 3.1.

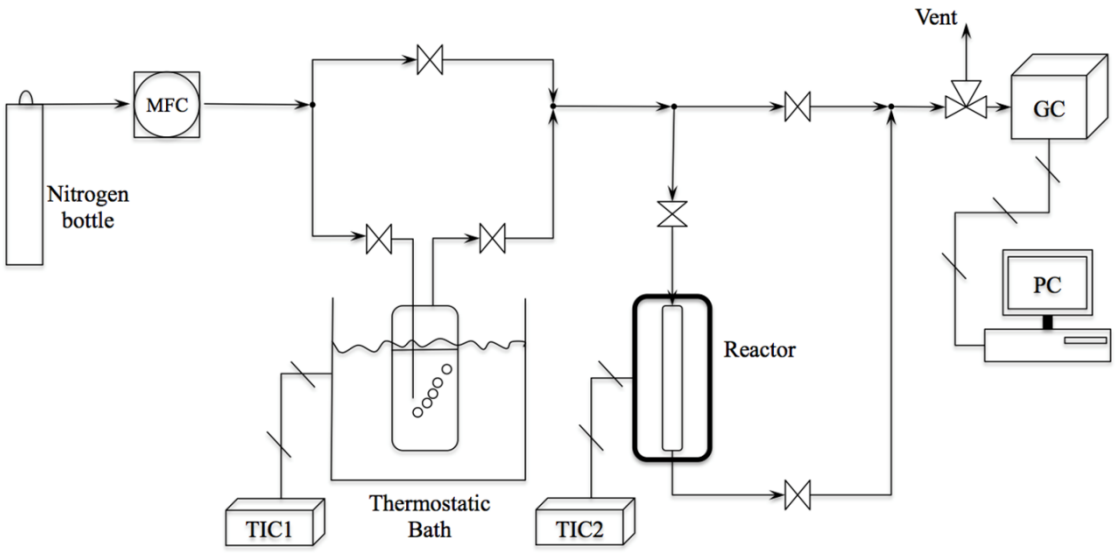

Figure 3.1 – Scheme of the experimental apparatus for catalytic test

As reported in the figure, nitrogen, acting as carrier under moderate overpressure, was bubbled through liquid methanol in a thermostatic bath (Julabo F12-ED) by controlling the carrier flow rate via Mass Flow Controller (Bronkhorst). The methanol molar fraction in the feed stream was regulated, according to its vapour pressure, by varying the bath temperature. Most of the experiments are carried out with an initial methanol vapour fraction of 0.06 (by setting the temperature of bath at around 8°C) and a carrier flow of 60 NmL/min.

3.3.1.1 Catalytic tests

Vapour phase dehydration of methanol is carried out at steady state conditions in a vertical reactor (Pyrex vessel, i.d. = 15 mm and length = 40 mm, DISA Milano) where the catalytic bed was hold by a porous septum as reported in Figure 3.2.

Figure 3.2 – Reactor used for methanol conversion reaction

Typically, the 70 mg of fresh catalyst (pellets of 300-500 μm) is loaded in the reactor for the catalyst tests achieving a Weight Hourly Space Velocity (WHSV) of 4.5 h^{-1} ($g_{MeOH} \cdot h^{-1} \cdot g_{cat}^{-1}$). Before weight of the catalyst, it was pre-dried at 180 °C for 3 hours in a static oven in order to minimize the effect of the adsorbed moisture on the mass of loaded catalyst. By using these experimental conditions both external and internal resistance of the pellets can be neglected as demonstrate elsewhere [227].

The reactor is located in a vertical tubular oven in which it is possible to control the temperature by a thermocouple located near to the catalytic bed.

Before any test, the freshly loaded catalyst sample was dried under nitrogen flow at 240°C for three hours. The investigated reaction temperatures are usually in the range of 180 – 280 °C. All detected points of conversion and selectivity are calculated on the basis of at least three independent measurements. Catalysts stability is evaluated by catalytic tests in Time-On-Stream over 60 h.

The composition of the stream leaving the reactor was analysed by using GC (Agilent 7890 A) equipped with a specific column (J&W 125-1032) and a FID detector using hydrogen as carrier and fuel. During the analysis, the GC oven is heated from 35 °C to 150 °C with a thermal ramp of 10°C/min.

The analysed components such as methanol, dimethyl ether, methane, ethylene and propylene, are calibrated by injection of a mixture with a known composition.

3.3.1.2 Coke analysis

The deposited coke is analysed in terms of amount and composition. As discussed before, the amount of coke deposited after reaction test is estimated by thermogravimetric analysis (TG/DTA) considering *coke* as the weight loss between 300°C and 750 °C [228]. Coke composition was analysed by GC-MS (Agilent 7820 A) equipped with a HP-5 MS column (30 m x 0.250 mm x 0.25 µm) using helium as carrier flowing at 1 NmL/ min and a thermal ramp of 5°C/min from 40 to 300°C. Before GC-MS analysis, coke molecules were extracted from the solid by dissolution of zeolite structure in HF (40%, Suprapur®, Merck CAS 7664-39-3) followed by liquid-liquid extraction with CH_2Cl_2 by slightly modifying the procedure suggested by Guisnet *et al.* [207]: 10 mg of zeolite was mixed with 1 ml of HF solution and left 15 min until complete solid dissolution. Then, 5 ml of CH_2Cl_2 were added and, after 2 min of vigorous stirring, the system was left 1 h to complete the organic phase extraction. An amount of 1 µL of extracted solution was injected in gas-chromatograph apparatus with a 4 minutes solvent time delay. Detected molecules are identified by comparing of mass spectra with known from library of NIST98 database.

Furthermore, carbon deposit location was estimated by *t*-plot of micropores volume analysis by N_2 isothermal adsorption at -196°C after a sample preparation with vacuum conditions at 250°C for 6 hours with a thermal ramp of 5°C/min.

3.3.2 Experimental system for CO_2 hydrogenation to DME

DME synthesis via one-pot CO_2 hydrogenation catalytic tests were carried out in collaboration with CNR-ITAE "Nicola Giordano" of Messina (Italy) and the materials and methods adopted to perform the tests are published in Ref. [85].

The catalytic activity was investigated in a fixed-bed stainless steel reactor (i.d., 4 mm; l., 200 mm) at temperature ranging from 200 to 280 °C and a total pressure in the range 3-5.0 MPa (GHSV=8,800 NL/g_{cat}/h; CO_2:H_2:N_2=3:9:1). As described before, prior to

each test, the catalyst was reduced at 300 °C for 1 h in pure hydrogen flow at atmospheric pressure. The reaction stream was analyzed by a GC equipped with a two-column separation system connected to a flame ionized detector (FID) and thermal conductivity detector (TCD) respectively.

CHAPTER 4

Physicochemical properties of investigated catalysts

Introduction

In this chapter the main physicochemical properties of investigated catalysts are discussed. All of investigated catalysts exhibit high crystallinity with crystals properties according with literature data. Acid sites evaluation by both NH_3-TPD and FT-IR analysis suggest that aluminium content and SDA type strongly affect the distribution and strength of FER-type material, revealing the possibility to tune physicochemical properties of this material during the hydrothermal synthesis. Analysis of hybrid system suggest that metal oxides are well dispersed on FER catalyst (CZZ-FER) while large cluster and non-homogenous dispersion were observed over MOR (CZZ-MOR) and MFI (CZZ-MFI) crystals. Furthermore, metal co-precipitation reduces total acidity of zeolites but this effect is less evident on FER-type crystals.

4.1 XRD

XRD patterns of investigated catalysts are reported in Figure A1-A5 in Appendix A showing that all of the synthesized samples exhibit both high purity and crystallinity according to the reference patterns published on http://www.iza-online.org/.

4.2 Textural properties

Adsorption isotherms of N_2 at 77 K of the investigated samples are reported in Figure B1 – B5 in Appendix B. All samples were characterized in terms of superficial specific area (*B.E.T*), micropore area (*M.A.*, estimated by *t*-plot method), external area (*E.A.*, estimated by *t*-plot method), micropore volume (*M.V.*, estimated by *t*-plot method) and total pore volume (*P.V.*)

Nitrogen adsorption isotherms of MFI sample (see Figure B1, Appendix B) reveal the typical pattern of type I isotherm, confirming the microporous characteristics of the synthesized samples [184, 222]. Estimated textural properties are summarized in Table 4.1.

Sample	*B. E. T.* $[m^2/g]$	*M.A.* $[m^2/g]$	*E. A.* $[m^2/g]$	*P. V.* $[cm^3/g]$	*M. V.* $[cm^3/g]$
MFI	360	211	149	0.194	0.094
BEA	583	436	148	0.376	0.202
SAPO-34	370	347	23	0.169	0.167

Table 4.1 – Textural properties of investigated 3-dimensional zeolite samples

The N_2 adsorption isotherms of BEA and SAPO-34 samples are also reported in Figure B.1 (Appendix B). SAPO-34 exhibits a totally microporous structure while a slight mesoporosity is observed on BEA sample.

As reported in Chapter 3, BEA is a 3-dimensional zeolite with channel openings of 6.6 x 7.7 <> 5.6 x 5.6 Å causing the observed high micropore volume compared with the other investigated structures. SAPO-34 was the material with the smallest channel openings (3.8 x 3.8 Å) among the investigated samples. The obtained high micropore volume reported in Table 4.1 is related to the presence of large cages generated by intersection of channels that can accommodate molecule large as a sphere with diameter 7.37 Å as reported in Chapter 3. These cages are responsible for hydrocarbon pool mechanism reaction, generated in MTO process as discussed in Chapter 1.

Nitrogen adsorption isotherms of FER samples synthesized with different Si/Al ratios (see Figure B2, Appendix B) also reveal the typical pattern of type I isotherm, confirming the microporosity of the synthesized samples [222]. As reported in Table 4.2, FER8 exhibits the highest superficial area and micropore volume, while FER30 and FER60 have very similar textural properties. The reported values are in agreement literature data [215, 218].

Sample	*B. E. T.* $[m^2/g]$	*M.A.* $[m^2/g]$	*E. A.* $[m^2/g]$	*Total P. V.* $[cm^3/g]$	*M. V.* $[cm^3/g]$
FER (8)	339	291	48	0.226	0.136
FER (30)	272	231	41	0.170	0.108
FER (60)	275	238	38	0.163	0.110

Table 4.2 – Textural properties of investigated FER samples synthesised with different Si/Al ratio

The effect of textural properties of FER samples synthesised using different organic molecules are summarized in Table 4.3, while the relative adsorption isotherms are reported in Figure B3 in Appendix B.

Sample	*B. E. T.* $[m^2/g]$	*M.A.* $[m^2/g]$	*E. A.* $[m^2/g]$	*P. V.* $[cm^3/g]$	*M. V.* $[cm^3/g]$
Py-FER	329	291	48	0.226	0.136
En-FER	306	245	61	0.218	0.127
DAO-FER	287	247	40	0.211	0.115
THF-FER	280	242	29	0.173	0.125
Nano-FER	340	285	51	0.283	0.133

Table 4.3 – Textural properties of investigated FER samples synthesised with different SDA and nanosized FER

All synthesised samples exhibit a microporous structure but with different textural properties. Sample synthesised with tetrahydrofurane (THF) exhibits the lowest specific area, external area and pore volume while sample synthesised with pyrrolidine offer the highest specific area and micropore volume. The highest pore volume values were observed for nanosized ferrierite crystals.

Nitrogen adsorption isotherms of 1-dimensional zeolite samples are collected in Fig. B4 (Appendix B). MOR and MTW samples shows the typical pattern of type I isotherm, confirming the microporous characteristics of the synthesized samples, while a slight mesoporosity is observed for TON and EU-1 samples [222].

Estimated textural properties are summarized in Table 4.4.

Sample	*B. E. T.* $[m^2/g]$	*M.A.* $[m^2/g]$	*E. A.* $[m^2/g]$	*P. V.* $[cm^3/g]$	*M. V.* $[cm^3/g]$
MOR	348	326	23	0.178	0.152
TON	210	169	42	0.174	0.074
EU-1	384	314	70	0.211	0.146
MTW	294	248	47	0.151	0.115

Table 4.4 – Textural properties of investigated 1-dimensional zeolite samples

The reported values are related to the channel network characteristics of these samples. MOR sample exhibits the highest micropore volume due its large channel size (12

member-ring, 6.5 x 7.0 Å) followed by MTW (10-membered ring, 5.6 x 6.0 Å) and TON (10-membered ring, 4.6 x 5.7 Å). On the contrary, EU-1 samples exhibits a high micropore volume as MOR samples despite its narrower channels (10-membered ring, 4.1 x 5.4 Å). The high micropore volume exhibited by EU-1 is related to the presence of large side-pockets in the channels of this structure. As reported by Giordano and coworkers [220], side pockets in EU-1 structure have size 5.8 x 6.8 Å in cross-position and 8.1 Å deep, causing the observed relative high micropore volume.

Commercial γ-Al_2O_3 exhibits a B.E.T. specific area of 199 m^2/g.

4.3 SEM

SEM images of investigated 3-dimensional molecular sieves are reported in Fig. 4.1.

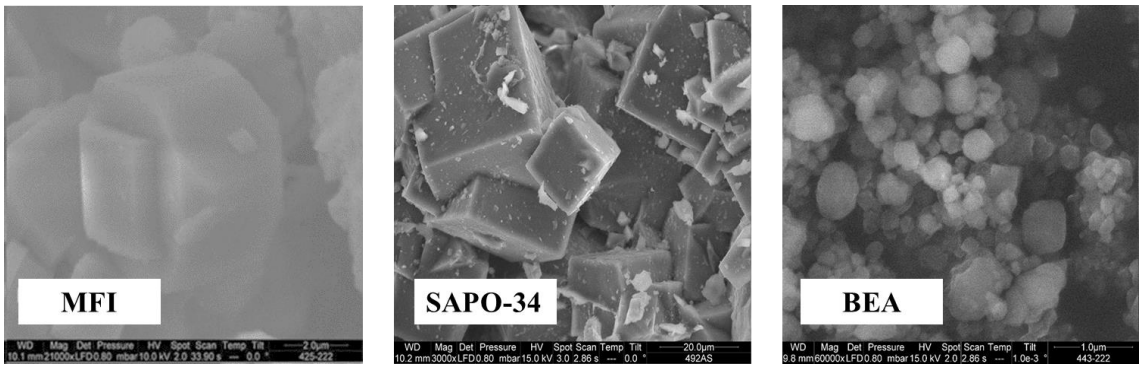

Figure 4.1 – SEM images of investigated 3-dimensional molecular sieves

MFI crystals show a well-formed typical prism-like mostly intergrowths crystals with characteristic dimensions: length 6 µm, width 5 µm and the thickness 3 µm, whilst the intergrowths crystals show smaller dimensions. Nanometric crystals were observed for BEA sample with spherical shape. On the contrary, SAPO-34 exhibits large cubic-like crystals with non-uniform size in the range 15-35 µm

SEM images of FER crystals synthesized at different Si/Al are collected in Fig. 4.2.

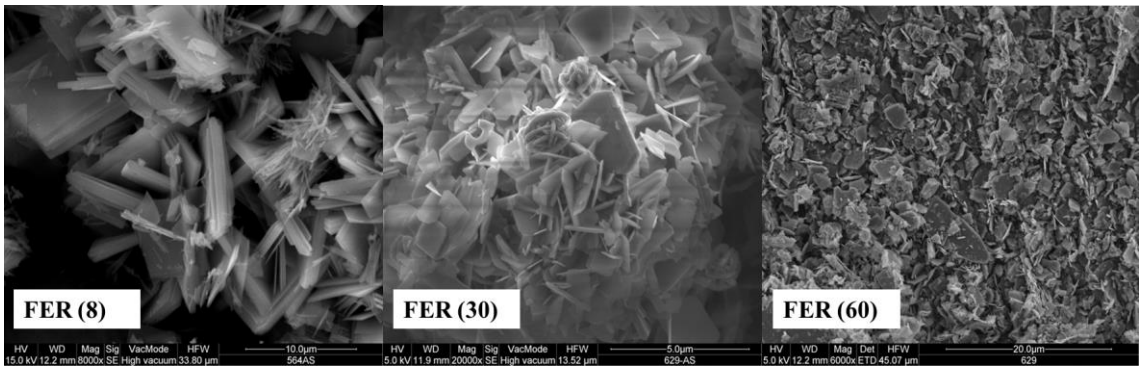

Figure 4.2 – SEM images of investigated FER-type materials synthesized with different Si/Al ratio in the starting gel (the Si/Al value is indicated in brackets)

The typical plate-like morphology with a well-developed {1 0 0} face is observed for FER-type crystals [215, 218]. However, some differences between the samples at different Si/Al ratio are observed. FER8 crystals consist of overlapping flat structure with thickness 200-500 nm, length 8-10 µm and length/width ratio about 2. FER30 consist of plate-like crystals agglomerates and single crystals have thickness about 100 nm, length 1-3 µm and length/width ratio below 2. Similar crystals morphology is observed for sample FER60 except for rare presence of crystal with length about 10 µm.

A different morphology was observed by using tetrahydrofuran as organic molecule during THF-FER sample synthesis. In fact, a plate-like crystals were obtained for En-FER (Fig. 4.3), Py-FER (Fig. 4.4) and DAO-FER (Fig. 4.5) with crystal size of 1-2 µm, 5-8 µm and around 1 µm, respectively.

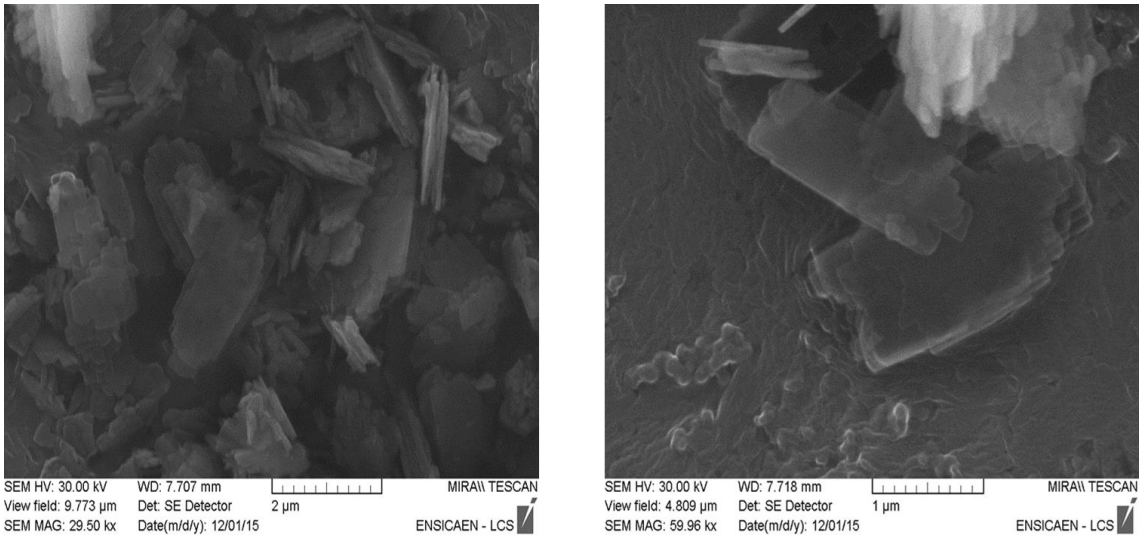

Figure 4.3 – SEM images of investigated FER-type materials synthesized with ethylendiammine (En-FER)

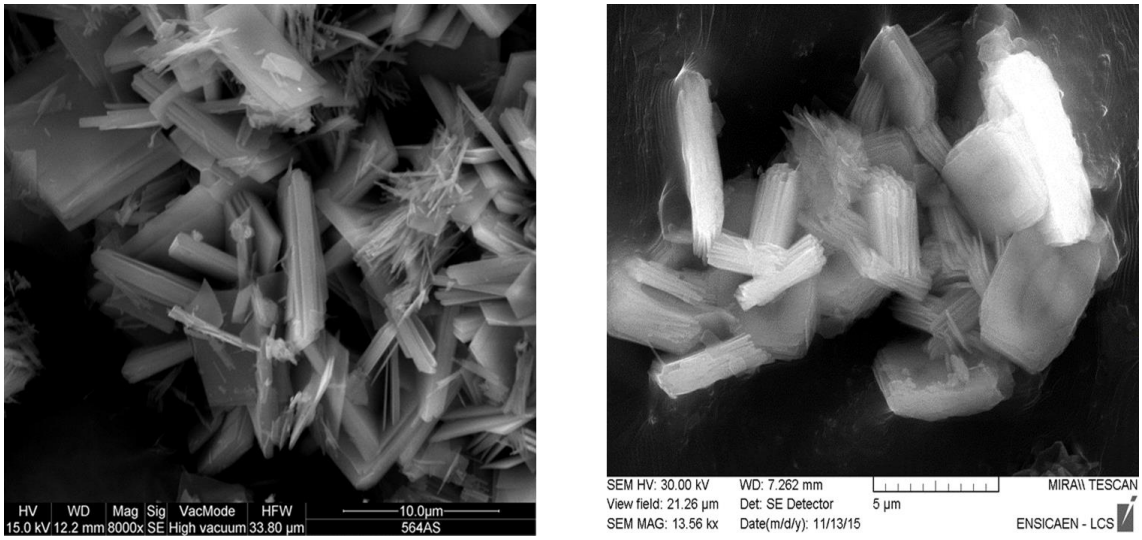

Figure 4.4 – SEM images of investigated FER-type materials synthesized with pyrrolidine (Py-FER)

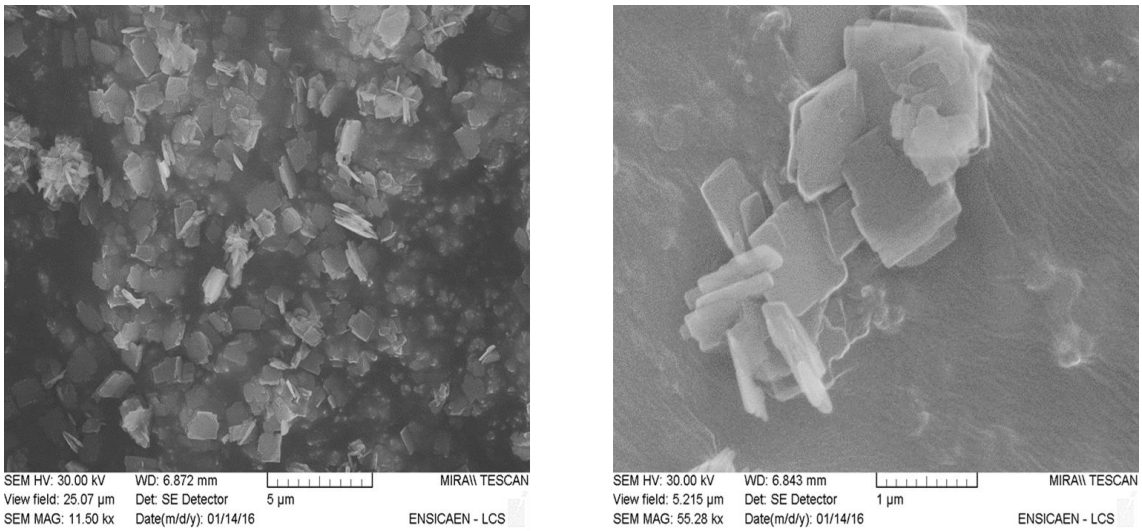

Figure 4.5 – SEM images of investigated FER-type materials synthesized with 1,8-diamminoctane (DAO-FER)

On the contrary, as reported in Fig. 4.6, large crystals as 10-15 µm were obtained when THF was used as organic molecule in the synthesis gel (THF-FER).

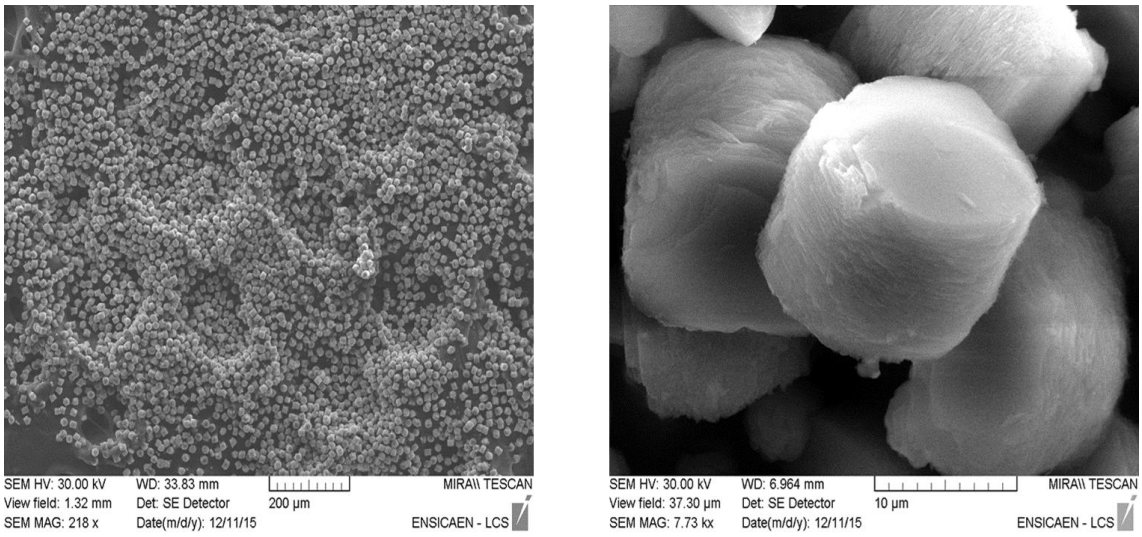

Figure 4.6 – SEM images of investigated FER-type materials synthesized with tetrahydrofuran (THF-FER)

Results show that organic molecules as well as synthesis gel molar composition strongly affect crystal morphology of the obtained materials.

A 300-500 nm crystal size was obtained when surfactant was added to the synthesis of Py-FER (nano-FER) as reported in Fig. 4.7.

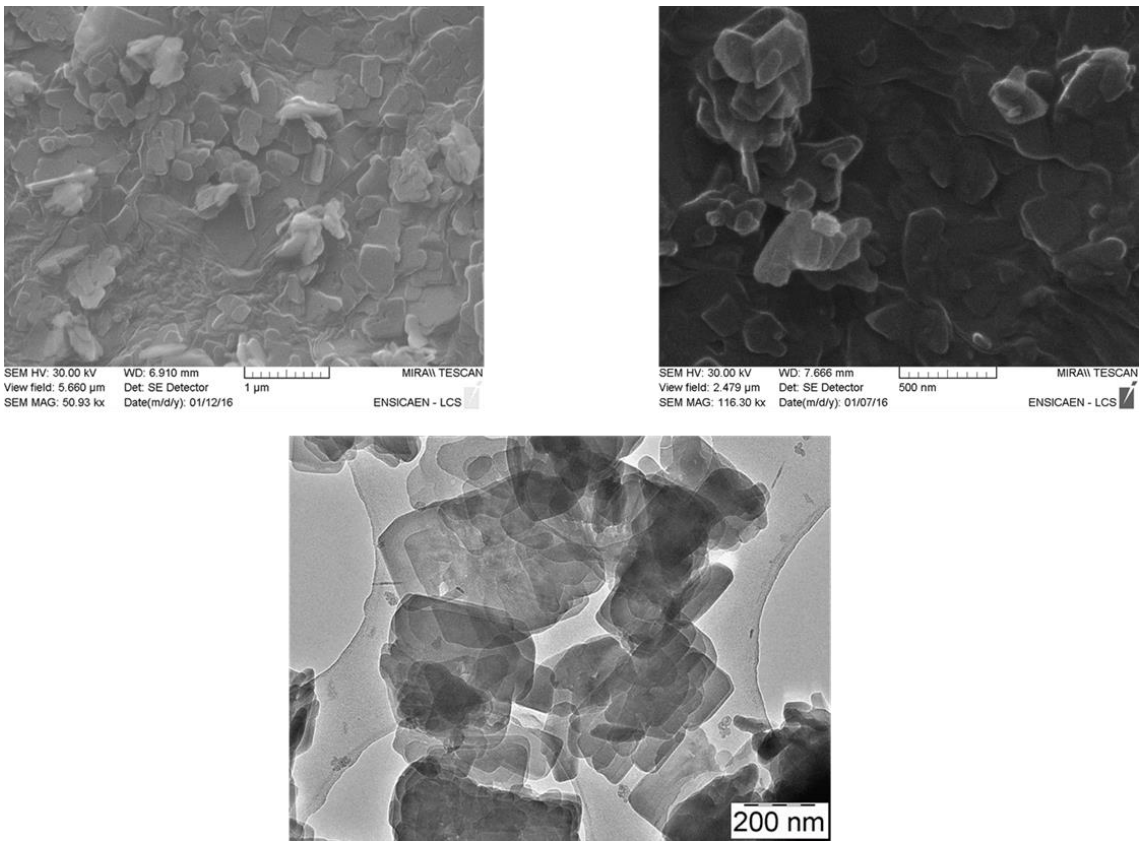

Figure 4.7 - SEM (up) and TEM (down) pictures of nano-sized FER

SEM pictures of investigated zeolites with 1-dimensional channels are reported in Fig. 4.8.

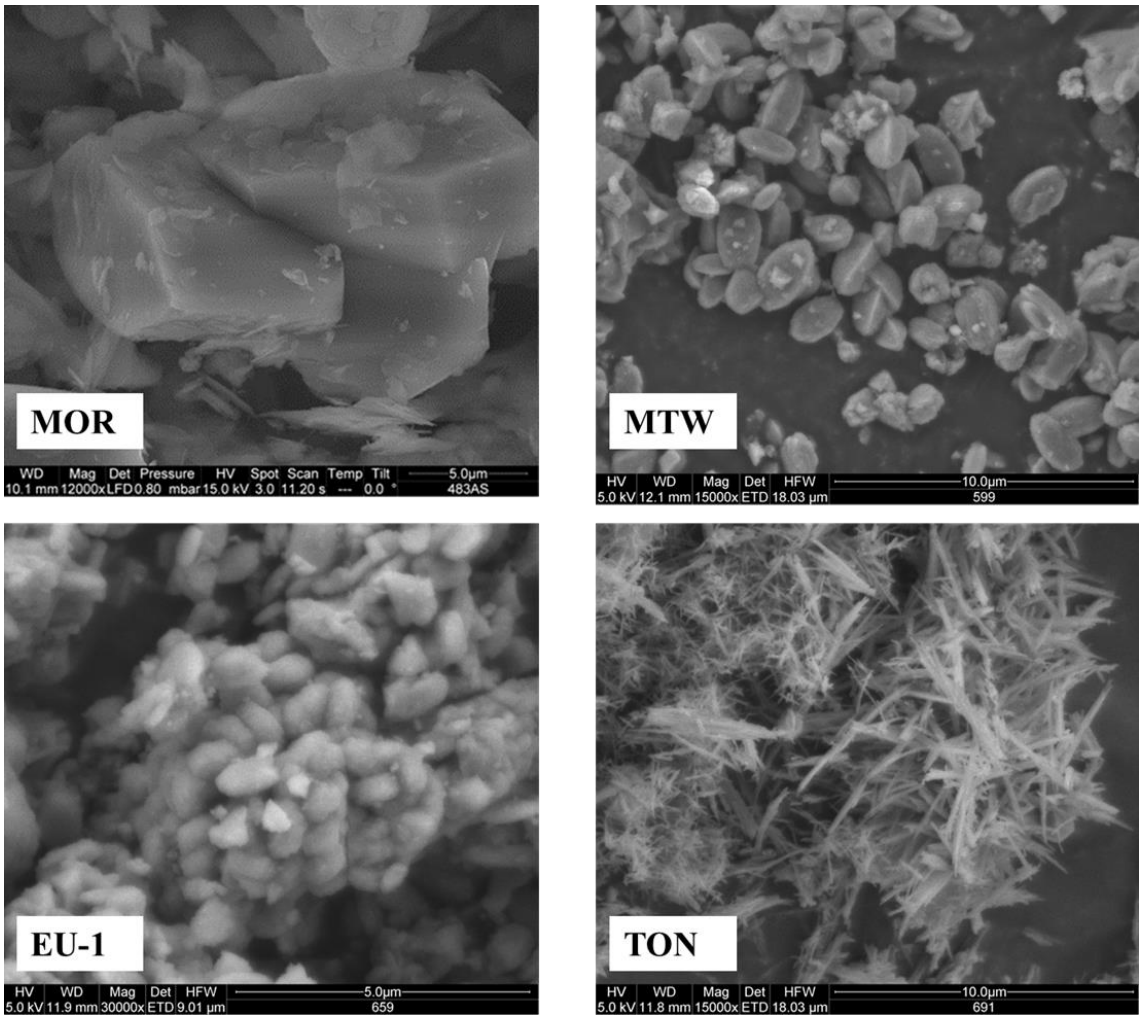

Figure 4.8 - SEM images of investigated molecular sieveswith 1-dimensional channels

The crystal morphology of MOR sample appears as uniform large micro-blocks of hexagonal prisms (10–15 µm), decorated by irregular crystal aggregates, with evident intercrystalline gaps. TON sample shows needle-like crystals length 5-10 µm and nanometric thinkness [229]. MTW crystals exhibit a well-defined rice-grain like shape with length 2.5 µm and width ca. 1.2 µm. Agglomeration of sub-micrometric rice-grain like crystals were observed for EU-1 sample.

4.4 TGA and chemical analysis

In this paragraph, the main chemical characterizations of the investigated samples are reported.

Table 4.5 summarizes the chemical analysis results of MFI, BEA and SAPO-34 samples. Despite a high degree of crystallinity exhibited by all the samples the increase of the Si/Al bulk ratio of BEA and MFI proves that not all the aluminum added to synthesis gel is incorporated in the catalyst [230, 231]. On the contrary, no change in Si/Al ratio was observed for SAPO-34 sample.

Sample	*SDA* *[%wt][a]*	*Si/Al* *[mol/mol][b]*
MFI	9.9	38
BEA	13.2	38
SAPO-34	13.8	0.4

Table 4.5 - Chemical composition of BEA and SAPO-34 samples [a] measured by TGA, SDA= tetrapropyl ammonium bromide for MFI, SDA=tetra-ethyl ammonium bromide for BEA and SDA=diethyl ammine for SASPO-34; [b]referred to active form material.

A different trend is observed for FER samples synthesised with different Si/Al ratio. As reported in Table 4.6 the Si/Al rations resulted in the synthesised material are lower the initial one used in the synthesis gel. Similar results were obtained by Kaminura *et al.* [218].

Sample	*SDA* *[%wt][a]*	*Si/Al* *[mol/mol][b]*
FER (8)	10.3	8.4
FER (30)	6.0	23
FER (60)	7.2	45

Table 4.6 – Chemical composition of FER samples synthesized with different Si/Al ratio; [a] measured by TGA, SDA=Pyrrolidine for FER(8) and SDA=Pyridine for FER(30) and FER(60), [b]referred to active form material.

Thermogravimetric analysis shows that incorporation of SDA is higher in FER(8) than FER(30) and FER(60) but this result can be related to both higher aluminium content or higher affinity of pyrrolidine for FER structure than pyridine. Further analysis (e.g. ^{13}C-NMR) are necessary for a deeper investigation.

Table 4.7 summarize chemical analysis results of FER samples synthesized by using different organic molecules as SDA.

Sample	*Na/Al [mol/mol]*[a]	*SDA [%wt]*[b]	*Si/Al [mol/mol]*[c]
En-FER	0.09	10.7	7.4
Py-FER	0.10	10.3	8.4
THF-FER	0.84	4.5	7.7
DAO-FER	0.61	6.7	6.6

Table 4.7 – Chemical composition of FER samples synthesized with different Si/Al ratio; [a]referred to as-synthesised materials; [b]measured by TGA, SDA=Ethylediammine for En-FER, SDA=Pyrrolidine for Py-FER, SDA=tetrahydrofurane for THF-FE and SDA=1,8-diamminoctane for DAO-FER; [c]referred to active form material.

As discussed in Chapter 2, it is well-known that zeolite structure is generated by a network of SiO_4 and usually AlO_4^- tetrahedrals linked together by a shared oxygen atom. Due the presence of trivalent atoms (e.g. aluminium) in the tetrahedral units, the framework offers a negative charge which needs to be balanced with a non-framework exchangeable cations that are generally elements of the group IA and group IIA as sodium, potassium, magnesium and calcium [209]. In this work, because sodium is used to synthesised FER-type materials, sodium cations are candidate to balance negative charges associated to aluminium atoms. Furthermore, the high quantity of tetrahedral aluminium species detected by NMR analysis (see Paragraph 4.6.1), suggests that the Na/Al ratio should be around one. Strikingly, chemical analysis reported in Table 1 shows that Na/Al is about 0.10 for Py-FER and En-FER, 0.6 for DAO-FER and 0.9 for THF-FER. These results disagree with the previous theoretical assumption, suggesting that an important amount of aluminium species in tetrahedral position are not balanced by sodium cations. Vuono *et al.* [232] reported a Na/Al ratio value below to unity (around 0.60) for MCM-49 materials synthesised in presence of hexamethylenimine despite aluminium was mainly tetra-coordinated as in our case. Forbes *et al.* [233, 234] report that during the synthesis of ZSM-5/Theta-1 materials in presence of diethanolammine, the organic molecules was considered to have both a pore-filling role and charge –compensatory role. Furthermore, Rollmann *et al.* [235] assert that protonated amine (e.g. ethylamine, pyrrolidine, hexamethylenimine) play the role as counterion of negative charge associated to

tetrahedral aluminium atoms located into zeolite framework, also for FER-type materials. Therefore, because in this work, aluminium atoms are mainly present in tetrahedral coordination, protonated organic molecules can be reasonably present to compensate negative charge of zeolite lattice, but more sophisticated analytic techniques (e.g. ^{13}C MAS NMR) could confirm or disprove the previous speculations. THF-FER exhibits a relative higher Na/Al ratio (around 0.9) showing that AlO_4^- species needs the presence of (sodium) cations to be balanced because THF is not able to play a role of counterion as reported in Ref. [236]. Nevertheless, also for THF-FER the Na/Al ratio is equals to one, suggesting the presence of extra-framework aluminium species not detected by NMR analysis. This aspect will be elucidated during FT-IR results discussion. An investigation by NMR analysis (^{23}Na-, ^{12}C-, ^{14}N- and ^{1}H-NMR) could give a much deeper characterisation of these synthesised materials.

Chemical analysis of Nano-FER are practically equals to Py-FER samples showing that the adding of surfactant during the synthesis affects just the crystals morphology but not their aluminium concentration.

Table 4.8 summarizes the chemical analysis results in terms of Si/Al ratio and the SDA content measured by thermogravimetric analysis for the investigated 1-dimensional channels zeolite materials. MOR exhibits the lowest Si/Al ration followed by EU-1, MTW and TON.

Sample	*SDA [%wt]*[a]	*Si/Al [mol/mol]*[b]
MOR	-	7
TON	6.3	43
EU-1	8.1	21
MTW	12.5	32

Table 4.8 - Chemical composition of 1-dimensional zeolite samples [a] measured by TGA, SDA=1,8-diammioctane for TON, SDA=hexamethonium bromide for EU-1 and SDA=methyl tretraethyl ammonium bromide for MTW; [b]referred to active form material.

An important variation in Si/Al ratio is observed for MOR sample as the Si/Al ratio changes from 25 (in the synthesis gel) to 7 (in the bulk of crystallized material) [237, 238]. The obtained Si/Al ratio of MTW material is according with the results as reported

by Giordano [239]. Similarly, for EU-1 sample, the estimated aluminium atoms per unit cell is ca. 4.5 according with the values reported by Giordano *et al.* [220].

4.5 NH_3-TPD measurements for 1-D and 3-D molecular sieves

Because the investigated reaction is catalyzed by acid function, the investigated materials were characterized by NH_3-TPD in order estimate the amount, the strength and the distribution of acid sites. In this paragraph the main results of NH_3-TPD measurements of synthesised catalysts are reported and discussed for each class of investigated catalysts.

4.5.1 Acidity of 3-dimensional molecular sieves samples

The NH_3-TPD profiles of the studied 3-dimensional molecular sieves in acidic form are reported in Fig. 4.9.

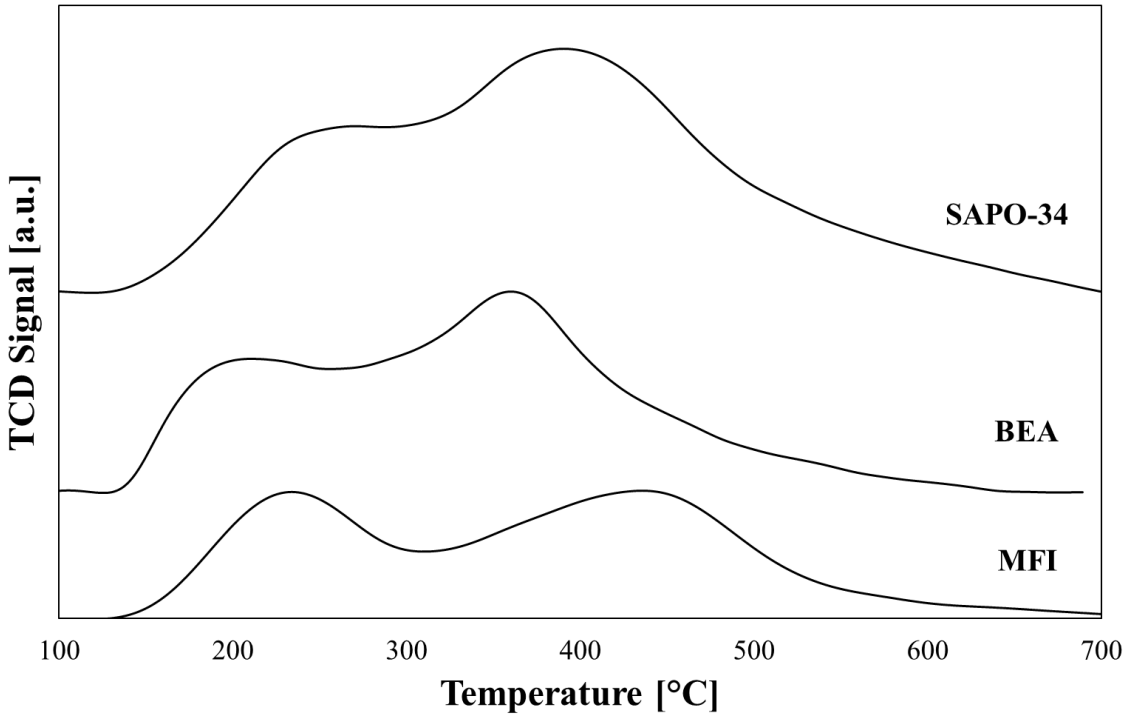

Figure 4.9- NH_3-TPD profiles pf investigated 3-dimensional molecular sieves

NH_3-TPD profiles display two main peaks according to the ammonia maximum desorption temperature (T_M), reflecting the interaction of ammonia with weak and strong acid sites, at low (150-250 °C) and high temperature (350-450 °C), respectively [240, 241]. Although by NH_3-TPD measurements is not possible to discriminate Brønsted and Lewis acidity, the interpretation of weaker sorption causing a low-temperature TPD peak is generally associated either to the presence of weak Lewis acid sites on zeolite

framework sites or to extraframework aluminum oxide/hydroxide species [190, 242], also eliminable by long flushing times [243,244] or steam treatment prior to adsorption [245]. The ammonia desorbed at this relativly low temperature can be associated to physi-adsorbed molecules and the associated acid sites are not usually related to catalytic active sites [225, 246]. Instead, the peak at higher temperature is usually associated to Brønsted or Lewis acid sites responsible for catalysis [225, 246, 247].

In quantitative terms, Table 4.9 reports the overall NH_3-uptake for each sample, which represents the total amount of acidic sites, and the relative population of *weak* and *strong* sites at low and high temperature respectively.

Sample	*NH_3-uptake* *[µmol/g_{cat}]*	*$T_{M,w}$ [a]* *[°C]*	*x_w [b]*	*$T_{M,s}$ [c]* *[°C]*	*x_s [d]*	*R^2*
MFI	602	213	0.45	406	0.55	0.988
BEA	609	215	0.42	348	0.58	0.988
SAPO-34	1174	265	0.37	398	0.63	0.989

[a] Temperature of maximum desorption of NH_3 between 100 and 300°C

[b] Fractional population of sites between 100 and 300°C

[c] Temperature of maximum desorption of NH_3 between 300 and 500°C

[d] Fractional population of sites between 300 and 500°C

Table 4.9 – Quantitative data of NH_3-TPD and acid sites distribution of 3-dimensional molecular sieves samples

MFI and BEA show similar acid sites concentration while SAPO-34 sample ranks as most acidic 3-dimensional catalyst.

4.5.2 Acidity of 1-dimensional molecular sieves samples

NH_3-TPD profiles of investigated zeolites with 1-dimensional channels are showed in Fig. 4.10 and quantitative results are reported in Table 4.10.

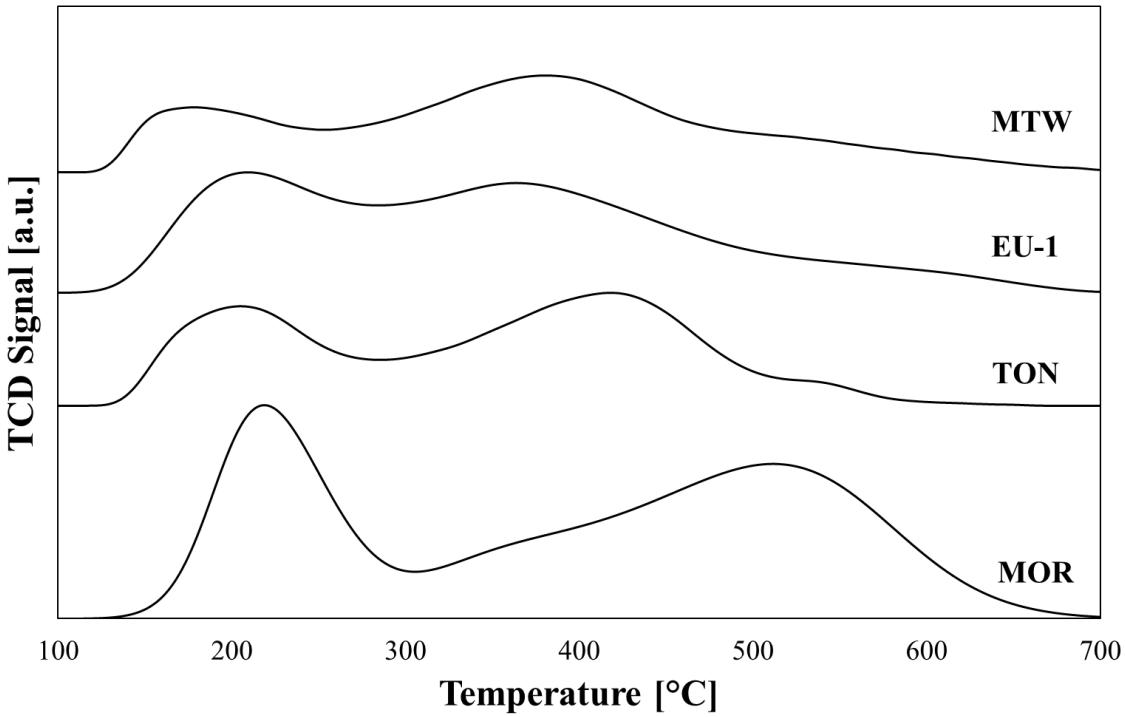

Figure 4.10- NH_3-TPD profiles pf investigated 1-dimensional molecular sieves

Sample	*NH_3-uptake [µmol/g_{cat}]*	*$T_{M,w}$ [a] [°C]*	*x_w [b]*	*$T_{M,s}$ [c] [°C]*	x_s [d]	R^2
MOR	714	219	0.26	514	0.74	0.984
TON	313	199	0.27	414	0.73	0.991
EU-1	431	206	0.42	360	0.58	0.994
MTW	274	153	0.37	371	0.63	0.993

[a] Temperature of maximum desorption of NH_3 between 100 and 300°C

[b] Fractional population of sites between 100 and 300°C

[c] Temperature of maximum desorption of NH_3 above 300°C

[d] Fractional population of sites above 300°C

Table 4.10 – Quantitative data of NH_3-TPD and acid sites distribution of investigated 1-D zeolites

The total acid sites concentration follows the order MOR>EU-1>TON>MTW. This trend is according to Si/Al for MOR (Si/Al=7), EU-1 (Si/Al=21) and TON (Si/Al=43) samples. On the contrary, MTW sample with a Si/Al=32 have less acid sites concentration than TON sample with Si/Al=43 showing that some aluminum atoms in MTW sample does not exhibit acid function. Referring to strong acid site family, the acid sites strength follows the order MOR>TON>MTW>EU-1. In particular, MOR sample ranks as the catalyst with the highest strength among all the investigated catalysts.

Comemrcial γ-Al_2O_3 exhibits a total acidity of 283 µmol/g with a fraction of strong acid of 0.79 with a maximum desorption peak temperature of 329 °C.

4.6 Acid properties of FER-type materials

In this paragraph, the main acid properties of investigated FER-type materials on the basis of NH_3-TPD, FT-IR and ^{27}Al-NMR analysis are discussed. The more detailed analysis about acidity of FER-type materials were performed because FER structure exhibited reliable catalytic behavior in both indirect and direct DME synthesis as discussed in the next chapter.

4.6.1 Effect of SDA on acidity and aluminum incorporation

The NH3-TPD profiles of FER-type zeolites synthesised with the different OSDA are reported in Fig. 4.11.

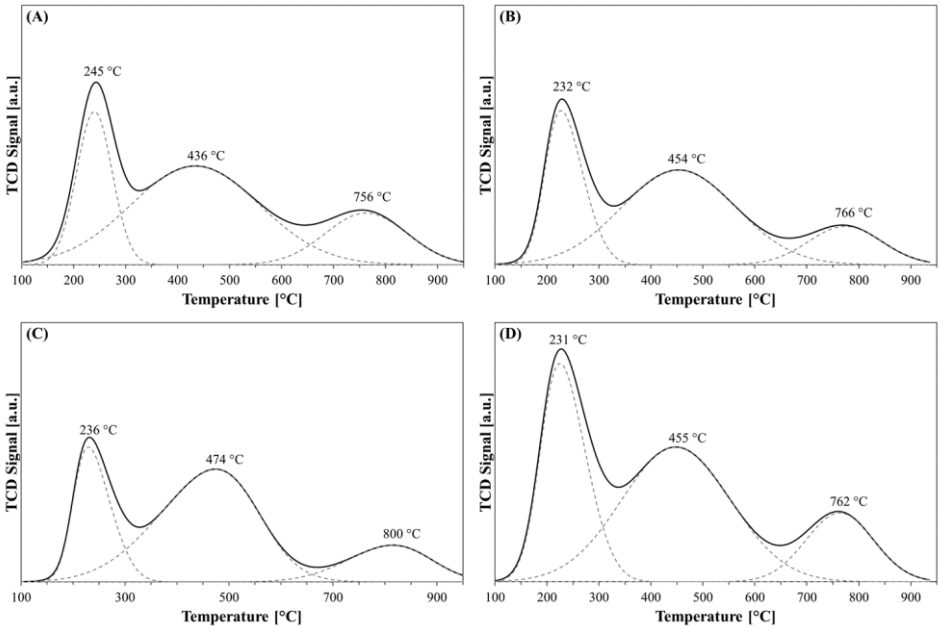

Figure 4.11 - NH_3-TPD profiles of En-FER (A), Py-FER (B), THF-FER (C) and DAO-FER (D)

For all of the investigated samples, the obtained experimental profiles display three main peaks characterized by different ammonia maximum desorption temperatures peaks (T_M) indicated on the Figure. Any portion of the curve can be theoretically related to different acid sites family in the way of a higher T_M as an indication of stronger acid sites. Similar NH_3-TPD profiles were obtained for both Py-FER and SLS-Py-FER (see Fig. 4.12), confirming again that the presence of surfactant affects only crystal morphology.

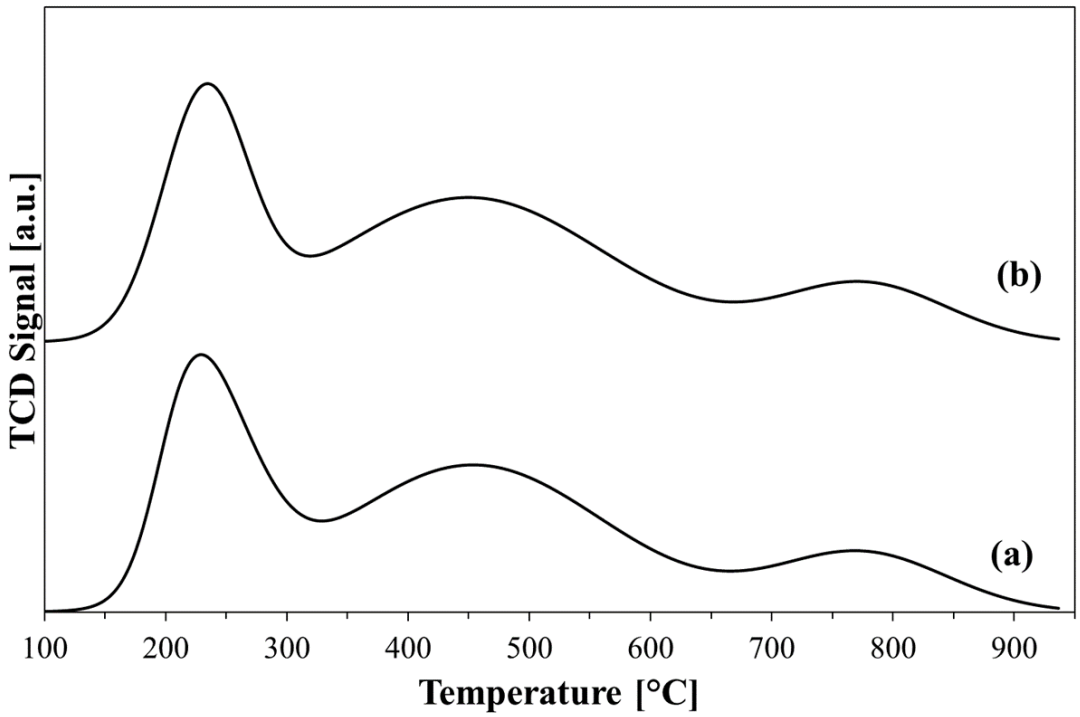

Figure 4.12 - NH_3-TPD profiles of Py-FER (a) and SLS-Py-FER (b) samples

Some considerations are necessary to obtain a good interpretation of the peaks. For instance, as clearly reported by Niwa and Katada [225, 246], the interpretation of peak with T_M<300 °C may be quite misleading because, for peak temperature below 300°C, the desorption effect may be mainly related to physically adsorbed ammonia hydrogen bonded to NH_4^+ ions generated by the preceding adsorption of ammonia on effective acid sites. In this condition, also the presence of weak acid sites (i.e. having desorption energy comparable to physisorbed ammonia) cannot be properly detected. On the contrary, the peaks with 300 °C<T_M<500 °C are reasonably associated to ammonia molecules desorbed from strong acid sites (both Brønsted and Lewis acid sites). The peak with T_M>700 °C can be associated to dehydroxylation phenomena [248, 249] since it is observed both in NH_3-TPD experiments and in the corresponding "blank" TPD experiments, the latter performed over the same catalyst and under the same experimental conditions but without NH_3 admission (see Fig. 4.11b)

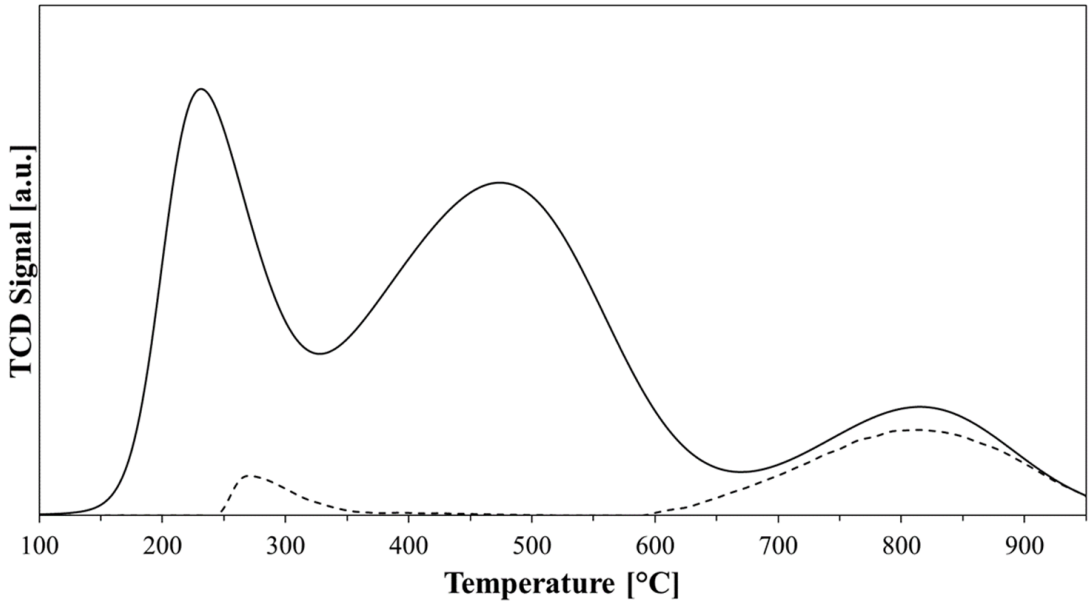

Figure 4.12b –NH_3-TPD profiles of THF-FER sample (continuous line) and the corresponding blank experiment, done over the same catalyst and under the same experimental conditions but without NH_3 admission

For all of these reasons, NH_3-TPD peaks with T_M>700 °C are not computed into the calculation of acid sites concentration. In this concern, quantitative results of NH_3-TPD measurements are reported in Table 4.11.

Sample	*NH_3-uptake [µmol/g_{cat}]*	*$T_{M,w}$[a] [°C]*	*x_w[b]*	*$T_{M,s}$[c] [°C]*	*x_s[d]*	*R^2*
Py-FER	787	232	0.44	454	0.56	0.991
En-FER	1052	245	0.30	436	0.70	0.995
THF-FER	929	236	0.31	474	0.69	0.997
DAO-FER	1418	231	0.40	455	0.60	0.993
SLS-Py-FER	787	235	0.45	458	0.55	0.995

[a] Temperature of maximum desorption of NH_3 between 100 and 300°C

[b] Fractional population of sites between 100 and 300°C

[c] Temperature of maximum desorption of NH_3 above 300°C

[d] Fractional population of sites above 300°C

Table 4.11 – Quantitative data of NH_3-TPD and acid sites distribution FER-type materials synthesized with different SDA

The total acid sites concentration follows the Si/Al ratio on the solid.

For instance, since DAO-FER sample possess the lowest Si/Al ratio (see Table 4.7), it exhibits the highest acid sites concentration.

Figure 4.13 depicts FT-IR spectra of H-ferrierite samples in the OH-stretching region. Two main bands can be observed at 3745 $cm^{-1}$and 3600 cm^{-1} associated to terminal silanol Si-OH and Brønsted acid sites Al-OH-Si groups, respectively [250, 251].

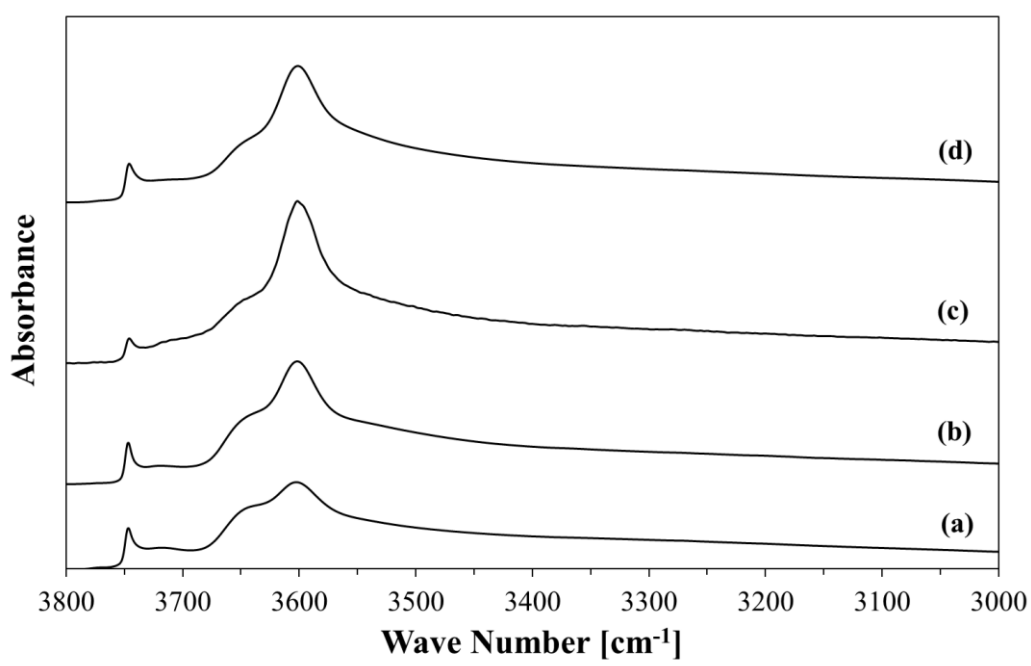

Figure 4.13 - FT-IR spectra of OH groups of En-FER (a), Py-FER (b), THF-FER (c) and DAO-FER (d) after evacuation at 300 °C for 4h.

A shoulder at around 3645 cm^{-1} is also present and similar results were also observed from other authors [215, 252] but its identification is not well-clarified. Peixoto *et al.* [253] suppose that the observed shoulder can be associated to a silanol group anchored on extra-framework aluminum species (e.g. octahedral aluminum) as reported also by Rachwalik *et al.* [254]. ^{27}Al-NMR spectra of investigated samples are reported in Fig. 4.14. NMR analysis suggests that octahedral aluminum species are absent or weakly present in the investigated samples. It is known from literature that aluminum in highly distorted coordination might become NMR silent and the observed band at 3645 cm-1 can be associated to OH groups connected to the so called 'invisible' aluminum species [255, 256] that can play a role of Lewis acid sites [257, 258]. The presence of these species can contribute to explain the Na/Al ratio below one discussed above.

THF-FER sample seems to possess a lower of concentration of both terminal silanol Si-OH and Al-OH groups compared with the other samples.

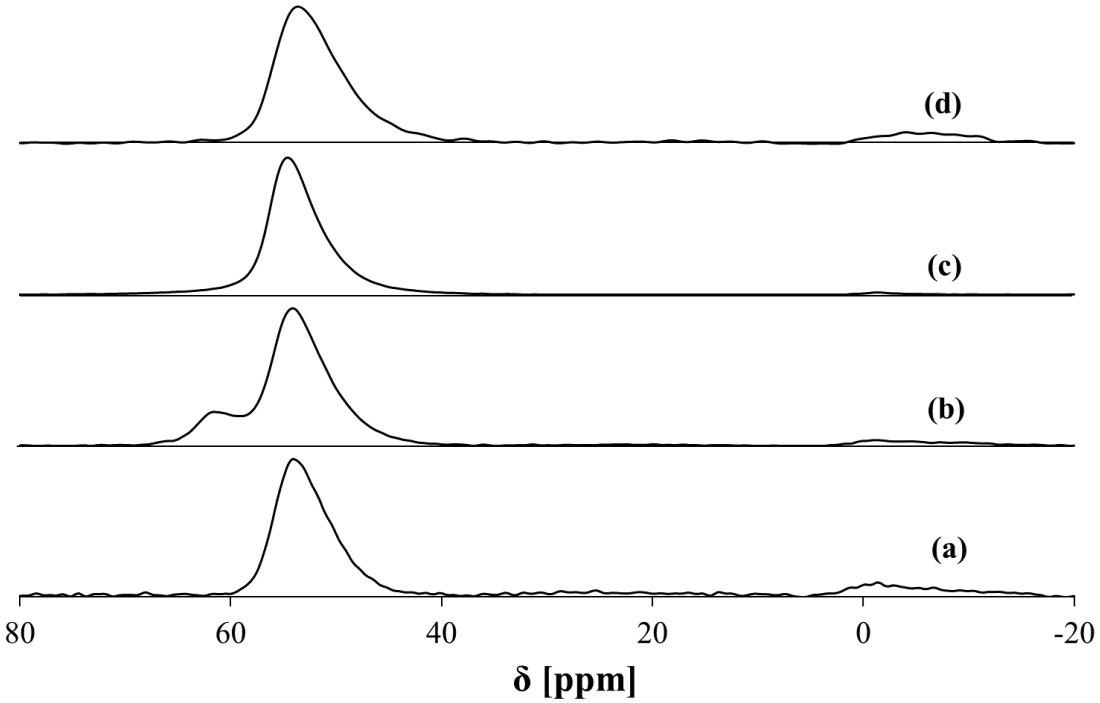

Figure 4.14 - ^{27}Al MAS NMR spectra of the H-forms of ferrierite synthesized with En (a), Py (b), THF (c) and DAO (d).

In order to better distinguish Lewis and Brønsted acid sites, deuterated acetonitrile (CD_3CN) was used as probe molecule following the FT-IR procedure discussed in the previous Chapter. FT-IR spectra of adsorbed CD_3CN at different evacuation temperatures for samples synthesized with different SDA are reported in Fig. 4.15.

The presence of two main bands at about 2296 cm^{-1} and 2322 cm^{-1} reveals the presence of both Brønsted and Lewis acid sites, respectively, in all of investigated FER-type catalysts. Smaller bands at lower wave number associated to physisorbed acetonitrile are also presents [195].

The concentration of Brønsted and Lewis sites were obtained from the integral intensities of the IR bands of adsorbed CD_3CN at 2296 cm^{-1} and 2322 cm^{-1}, respectively, by using the extinction factor coefficients reported in the previous Chapter. Brønsted and Lewis sites distribution of the investigated samples were calculated from area of bands recorded at 25 °C and quantitative results in terms of Lewis acid site percentage are summarized in Table 4.12.

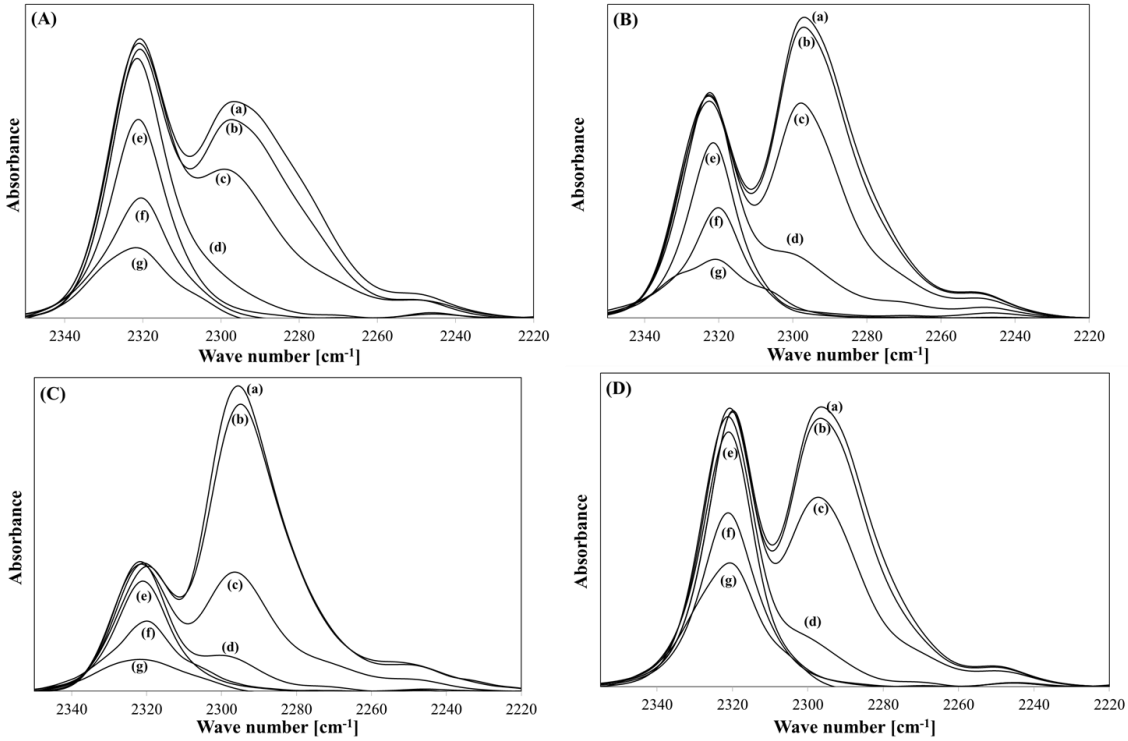

Figure 4.15 - FT-IR spectra of D_3-acetonitrile adsorbed on En-FER (A), Py-FER (B), THF-FER (C) and DAO-FER (D) evacuated at 25 °C (a), 50 °C (b), 100 °C (c), 150 °C (d), 200 °C (e), 250 °C (f) and 300 °C (g).

Sample	*Lewis acid sites fraction [%]*
Py-FER	34
En-FER	41
THF-FER	15
DAO-FER	40
Nano-FER	32

Table 4.12 – Lewis acid sites fraction of FER samples with different SDA and Nano-FER sample.

Results show that there is a strong effect of synthesis system on acid sites distribution. For instance, the catalyst synthesized with ethylediammine as SDA (sample En-FER) exhibits a high Lewis acid sites concentration (41%). Similar characteristics are observed about the catalyst synthesized with 1,8 – diammino octane. The sample synthesized with

tetrahydrofuran shows the lowest concentration of Lewis acid sites with a value of 15% that means that there is one Lewis acid site for six Brønsted acid sites. Both the samples synthesized with Pyrrolidine with or without surfactant exhibit a very similar concentration of Lewis acid sites (around 33%). At the light of this result and of the previous discussed NH_3-TPD measurements, it is possible to assert that Py-FER and SLS-Py-FER have a very similar acidity in terms of concentration, distribution and typology of acid sites but completely different crystal size as discussed before. In order to estimate the strength of both Brønsted and Lewis acid sites, temperature controlled desorption of D_3-acetonitrile was carried out and the results in terms of free fraction of Brønsted and Lewis acid sites are reported in Fig. 4.16.

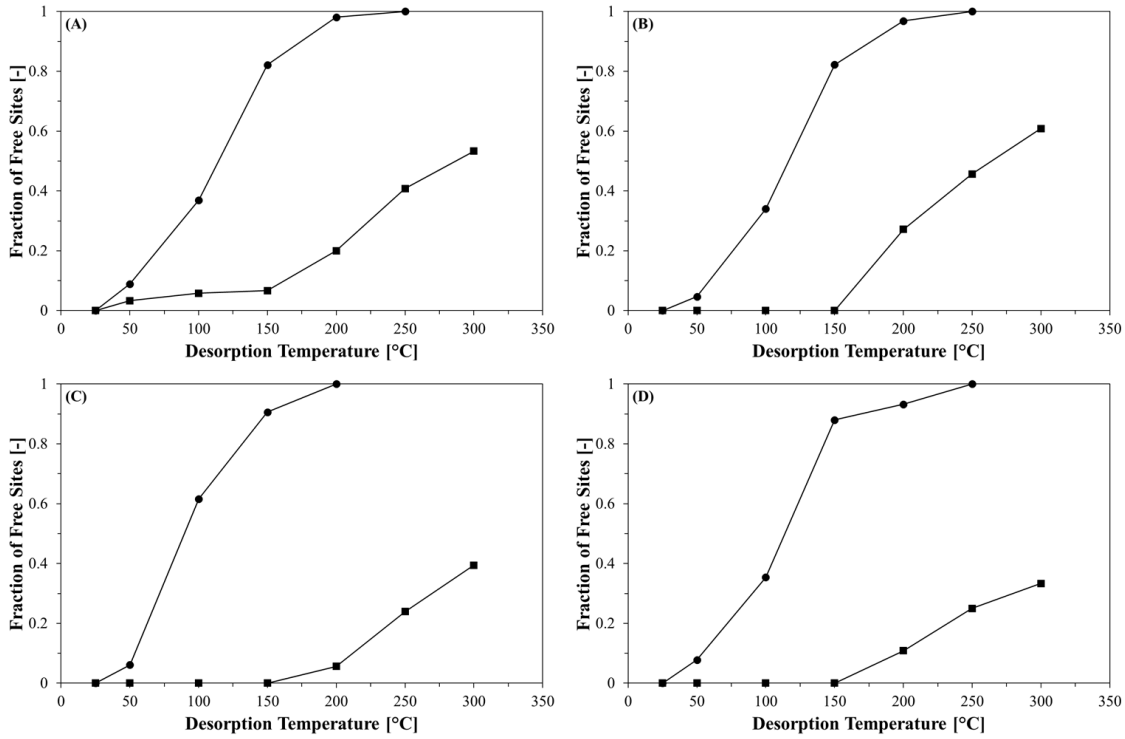

Figure 4.16 - Fraction of Brønsted (●) and Lewis (■) acid sites free of adsorbed D3CN molecules as a function of desorption temperature; En-FER (A), Py-FER(B), THF-FER(C) and DAO-FER(D).

Obtained data show that desorption of acetonitrile from Lewis acid sites is relevant only above 150 °C and there are occupied Lewis sites until 300 °C. Only En-FER sample seems to exhibit weaker Lewis acid sites since desorption of probed molecule from these sites starts at lower temperature. On the contrary, the acetonitrile molecules desorption starts from 50°C from Brønsted acid sites showing that Brønsted acid sites are weaker than Lewis ones for all investigated samples. En-FER, Py-FER and DAO-FER exhibit

similar trend while THF-FER had Brønsted acid sites weaker than the other catalysts. In fact, at 100 °C the 60% of the Brønsted acid sites are desorbed for THF-FER whilst about 30% of free Brønsted acid sites are free from probe molecule over the other samples at the same temperature. The observed Lewis acid sites can be associated to extra-framework NMR silent Al-OH species observed by FT-IR analysis previously discussed.

4.6.2 Effect of Si/Al ratio on acid sites concentration and strength

Fig. 4.17 reports the NH_3-TPD profiles of FER-type materials synthesised with different Si/Al ratio (indicated into brackets). The ammonia desorption peak with T_M>700 °C was not observed for both FER30 and FER60 indicating that dehydroxylation phenomena is not important for these samples.

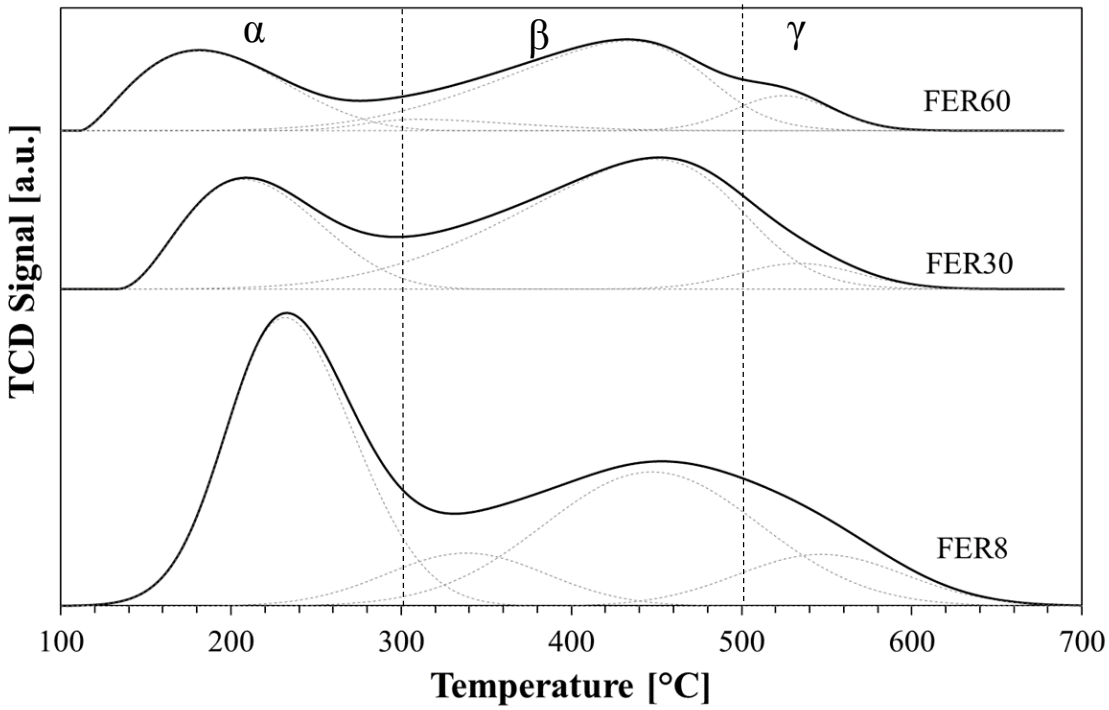

Figure 4.17 - NH_3-TPD profiles of FER8, FER30 and FER60

For all investigated samples, the obtained profiles can be deconvoluted in three main "dome-shape" curves characterised by different the ammonia maximum desorption temperatures peaks (T_M). Any portion of the curve is related to different acid sites family in the way of a higher T_M as indication of stronger acid sites. In this concern, the experimental profiles exhibited three different temperature peaks (labelled as α, β γ-peak)

indicating low-temperature acid sites (T_M < 300 °C), medium-temperature acid sites (300 °C < T_M < 500 °C) and high-temperature acid sites (T_M > 500 °C). According to this classification, the acid sites concentration and distribution for any investigated sample are summarized in Table 4.13 where it clearly appears that the total acid sites concentration strictly follows the Si/Al ratios (FER8>FER30>FER60).

Sample	*Total* [$\mu mol \cdot g^{-1}$]	*α-peak*[a] [-]	*β-peak*[b] [-]	*γ-peak*[c] [-]	$T_{M\alpha}$ [d] [°C]	$T_{M\beta}$ [e] [°C]	$T_{M\gamma}$ [f] [°C]
FER8	787	0.44	0.45	0.11	233	445	554
FER30	464	0.29	0.67	0.07	209	456	540
FER60	332	0.33	0.57	0.10	183	437	530

[a] Acid sites fraction with temperature of maximum desorption of NH_3 in the range 100-300 °C

[b] Acid sites fraction with temperature of maximum desorption of NH_3 in the range 300-500 °C

[c] Acid sites fraction with temperature of maximum desorption of NH_3 above 500 °C

[d] Temperature of maximum desorption of NH_3 in the range 100-300 °C

[e] Temperature of maximum desorption of NH_3 in the range 300-500 °C

[f] Temperature of maximum desorption of NH_3 above 500 °C

Table 4.13 – Quantitative data of NH_3-TPD and acid sites distribution FER-type materials synthesized with different Si/Al

According to Niwa and Katada recommendation discussed above [225, 246] the α-peak of NH_3-uptake cannot be considered as a reliable indication of active sites for catalysis. Catalytic results discussed in this paper consider only β- and γ-peaks as the real active sites for catalysis. This allows to calculate the effective acid sites concentration of the investigated samples as it follows: FER8 – 441 $\mu mol_{H^+}/g$; FER30 – 343 $\mu mol_{H^+}/g$; FER60 – 222 $\mu mol_{H^+}/g$, according to the increasing Si/Al ratio of the samples.

As the T_M values can be affected by NH_3 coverage [231], the analysis of this sole parameter cannot be considered a reliable method to estimate the strength of acid sites even though comparison of acid sites strength of different zeolites based on T_M were proposed [242]. As described in the Experimental section, in this work the strength of detected acid sites families was evaluated by calculating the value of heat of desorption of ammonia, as estimated from peak temperature at different heating rate. Desorption curves at different temperature rate (r) are reported in Fig. 4.18, whilst Table 4.14 summarised the values of T_M.

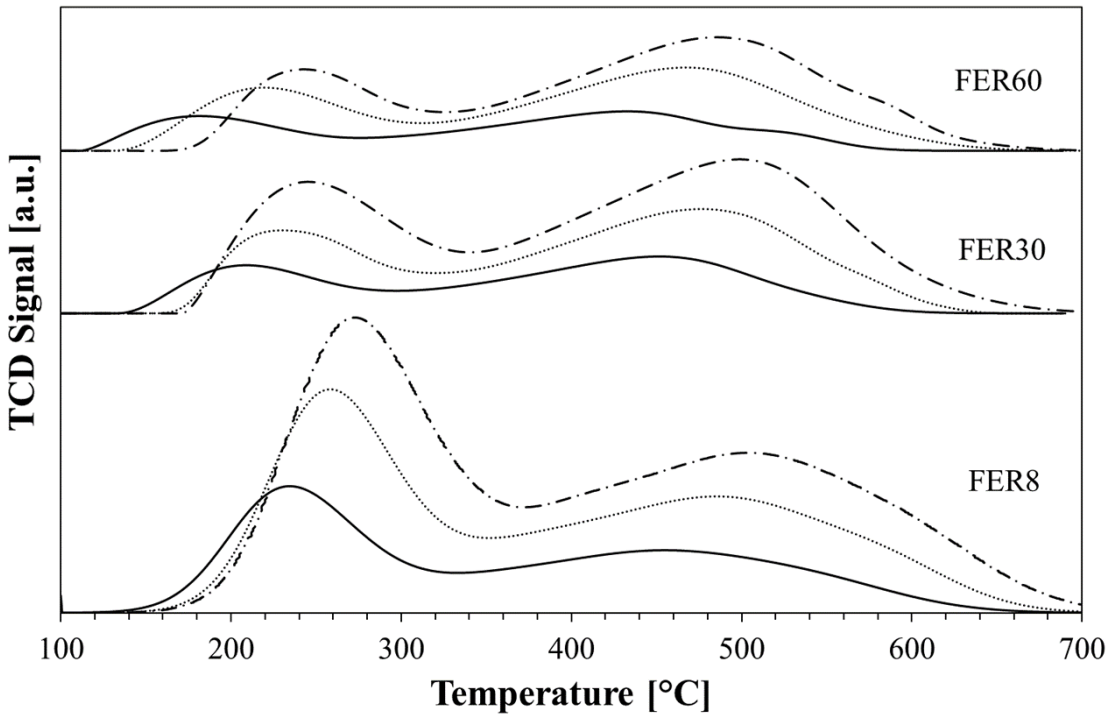

Figure 4.18 - NH_3-TPD profiles at different desorption heating rate (continuous line: 10°C/min; dotted line: 20°C/min, dashed and dotted line: 30 °C/min) of FER8, FER30 and FER60

r ***[°C·min^{-1}]***	***FER8***	***FER30***	***FER60***
	T_M, α-peak [°C]		
10	233	209	183
20	255	225	224
30	271	239	247
	T_M, β-peak [°C]		
10	445	456	437
20	468	482	475
30	489	501	494
	T_M, γ-peak [°C]		
10	554	540	530
20	587	571	590
30	602	586	576

Table 4.14 – Maximum desorption temperatures of ammonia (T_M) measured at different heating rate.

The values of $Q_{des,NH3}$ are reported in Table 4.15, suggesting that the strength of the acid sites families follow the order α-peak<β-peak<γ-peak for all investigated catalysts (the stronger the site, the higher the $Q_{des,NH3}$ value).

$Q_{des,\ NH3}$ [kJ/mol]	*FER8*	*FER30*	*FER60*
α-peak	58	67	25
(R^2)	(0.998)	(0.986)	(0.993)
β-peak	102	103	74
(R^2)	(0.989)	(0.998)	(0.995)
γ-peak	121	123	121
(R^2)	(0.997)	(0.996)	(0.999)

Table 4.15 – Calculated heats of desorption of ammonia (R^2: linear fitting correlation factor).

For sake of completeness, $Q_{des,NH3}$ calculated for α-peak are also reported and discussed, but is worthy to remind that those values (mainly attributed to physisorbed ammonia) will not be included in the discussion of catalytic performances as non-representative of effective acid sites. However, the obtained values for α-peak reveal that ammonia is weakly bounded on the catalysts surfaces for temperature below 300 °C even though these numeric values can be strongly affected by measurement conditions [225].

On the contrary, the obtained values of $Q_{des,NH3}$ for β-peak and γ-peak can be used as an indication of the acid sites strength. According to the values reported in Table 4.15, FER 8 and FER30 exhibit very similar acid sites strength for β-peak (102 $kJ \cdot mol^{-1}$ and 103 $kJ \cdot mol^{-1}$, respectively), higher than FER60 (74 $kJ \cdot mol^{-1}$). On the contrary, the strength of γ-peak is very similar for all of the investigated samples (above 120 $kJ \cdot mol^{-1}$), confirming the presence of strong acid sites in different amount in all samples.

A numerical quantification of Brønsted (B) and Lewis (L) acid sites is also important because this parameter may correctly address the discussion of some catalytic results such as methanol dehydration to DME, where reaction mechanism may strongly depend on the type of acid sites. In this concern, different mechanisms have been proposed for methanol dehydration to DME reaction and, apart from proton-based mechanisms [90]. One reliable hypothesis suggests that methanol is dehydrated over both Lewis acid-base pair

and Brønsted acid - Lewis base pair sites [89]. FT-IR spectra of adsorbed D_3-acetonitrile of FER-type samples synthesised with different Si/Al ratio are reported in Fig. 4.19

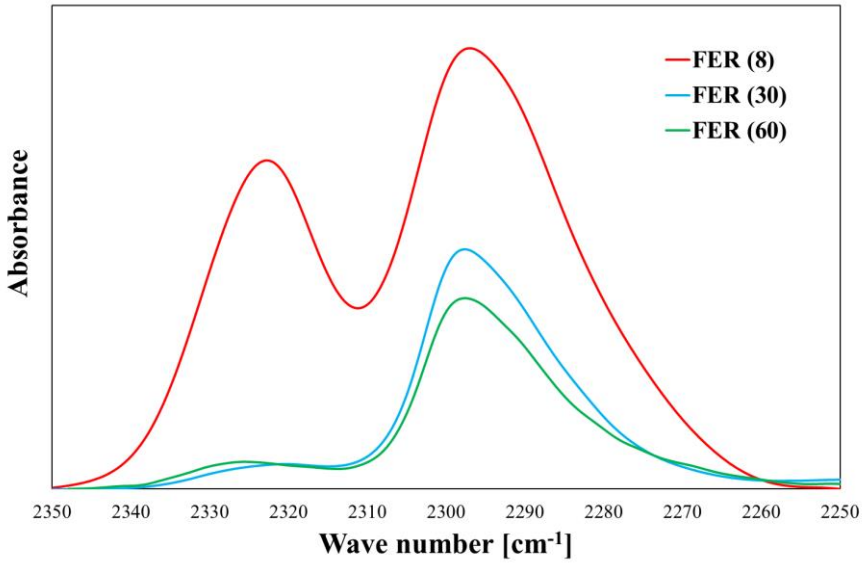

Figure 4.19 – FT-IR spectra on the acetonitrile stretch region of H-form FER samples synthesised with different Si/Al ration (indicated between brackets) recorded at room temperature and on vacuum condition after adsorption of probe molecule at room temperature and 1333 Pa.

The investigated samples exhibited a different Brønsted and Lewis acid sites distribution, as a function of the Si/Al ratio as reported in Table 4.16.

Sample	*Lewis acid sites fraction [%]*
FER(8)	34
FER(30)	7
FER(60)	6

Table 4.16 – Lewis acid sites fraction of FER samples with different Si/Al ratio.

The sample with higher aluminium content (FER8) posses 34% of Lewis acid sites (molar B:L= 3:1). On the contrary, when the Al content is decreased in the gel (FER30 and FER60) a significantly lower amount of Lewis acid sites is observed, leading to a reduced Lewis fraction with B:L = 14:1 and 16:1, respectively.

4.7 Physicochemical properties of hybrid catalysts

The main physicochemical properties of CZZ-MOR, CZZ-FER and CZZ-MFI are discussed in this paragraph. Table 4.17 shows chemical composition and textural properties of the investigated samples.

SAMPLE	*Atomic composition*[a]			SA_{Lang}[b]	*PV*[c]	*MV*[d]	*APD*[e]
	Cu	*Zn*	*Zr*	*[m²/g]*	*[cm³/g]*	*[cm³/g]*	*[Å]*
CZZ-MOR	60	29	11	217	0.372	0.048	69
MOR	-	-	-	348	0.178	0.152	21
CZZ-FER	61	29	10	182	0.335	0.038	73
FER	-	-	-	280	0.226	0.136	25
CZZ-MFI	58	28	14	195	0.292	0.025	60
MFI	-	-	-	360	0.190	0.072	19

[a] Determined from ICP analysis

[b] Langmuir surface area

[c] Total pore volume

[d] t-plot micropore volume

[e] Average pore diameter, 4·PV/SA

Table 4.17 – Chemical composition and textural properties of the investigated samples.

Table 4.18 shows that metal species composition is very similar over the three investigated hybrid catalysts. An evident reduction of surface area after co-precipitation was observed for CZZ-MOR and CZZ-MFI samples, whilst the surface exposure of the FER-based (CZZ-FER) material is better preserved. After co-precipitation both total pore volume PV) and average pore diameter (APD) increased with a parallel decreasing of micropore volume (MV) suggestion that metal oxides co-precipitation generated an extended mesoporosity on then hybrid systems.

Copper particles properties reported in Table 4.18 shows that metal surface area (27-33 m^2/g_{cat}), dispersion (11.1-13.5 %) and particle size (8-9 nm) are very similar for all the prepared hybrid systems.

Sample	S_{Cu}	D_{Cu}	d_{Cu}

	$[m^2/g_{cat}]^{[a]}$	$[\%]^{[b]}$	$[nm]^{[c]}$
CZZ-MOR	60	29	11
CZZ-FER	-	-	-
CZZ-MFI	61	29	10

[a] Copper surface area

[b] Copper dispersion

[c] Average copper particle size

Table 4.18– Results of N_2O chemisorption

How the oxides distributes on zeolite surface has been investigated by TEM analysis following the procedure discussed in the previous Chapter. From TEM images shown in Fig. 4.20, it seems enough clear that depending on zeolite morphology, the oxides distribute on surface in different ways.

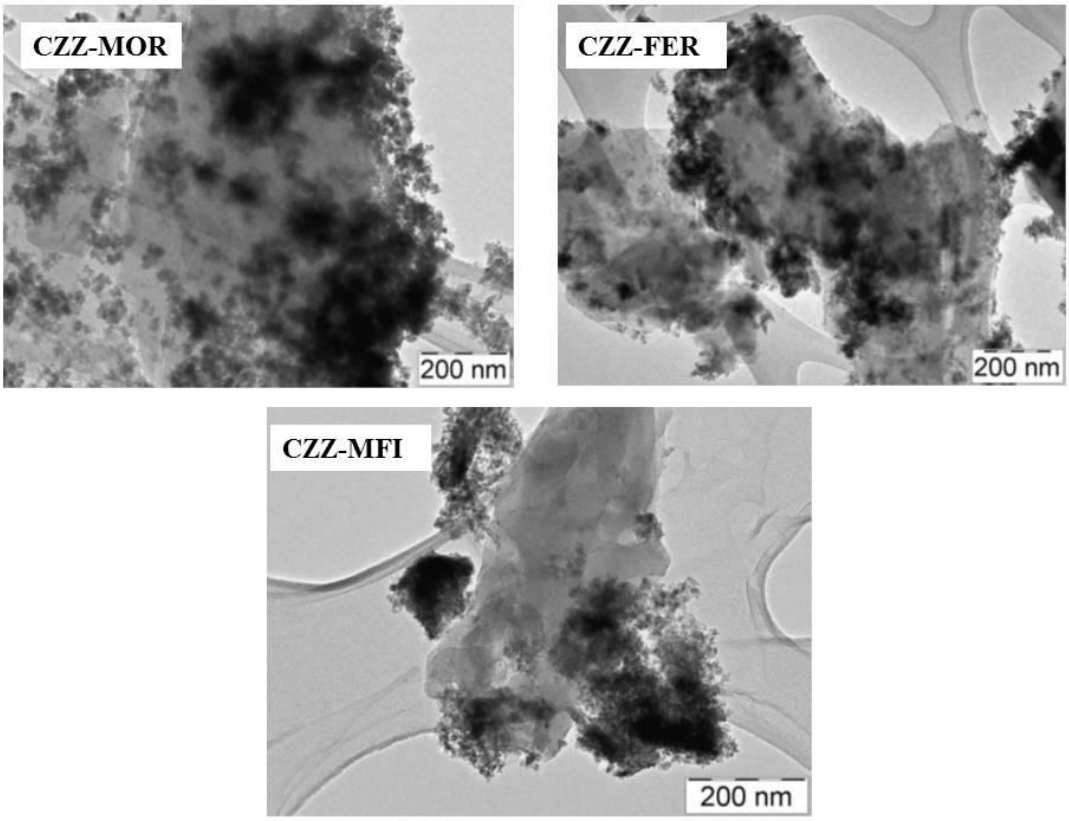

Figure 4.20 – TEM images of hybrid crystals

In particular, in case of CZZ-MOR, the mixed oxides distribute on the MOR crystal surface quite well but large agglomerats are present, suggesting that in this case there is not close surface contact. On CZZ-FER, the precipitate distributes on the FER crystals in

a more homogenous way, in form of smaller cluster with dimension ranging from 20 up to 100 nm. On CZZ-MFI, a poor distribution of metal-oxides over MFI crystals is observable and large and compact isolated clusters are present.

Fig. 4.21A shows the CO_2 desorption profiles obtained from the investigated hybrid catalysts, as the contribution of two main CO_2 desorption peaks for all the samples corresponding to CO_2 desorbed from weakly basic (at lower temperature) or strongly basic sites (at higher temperature).

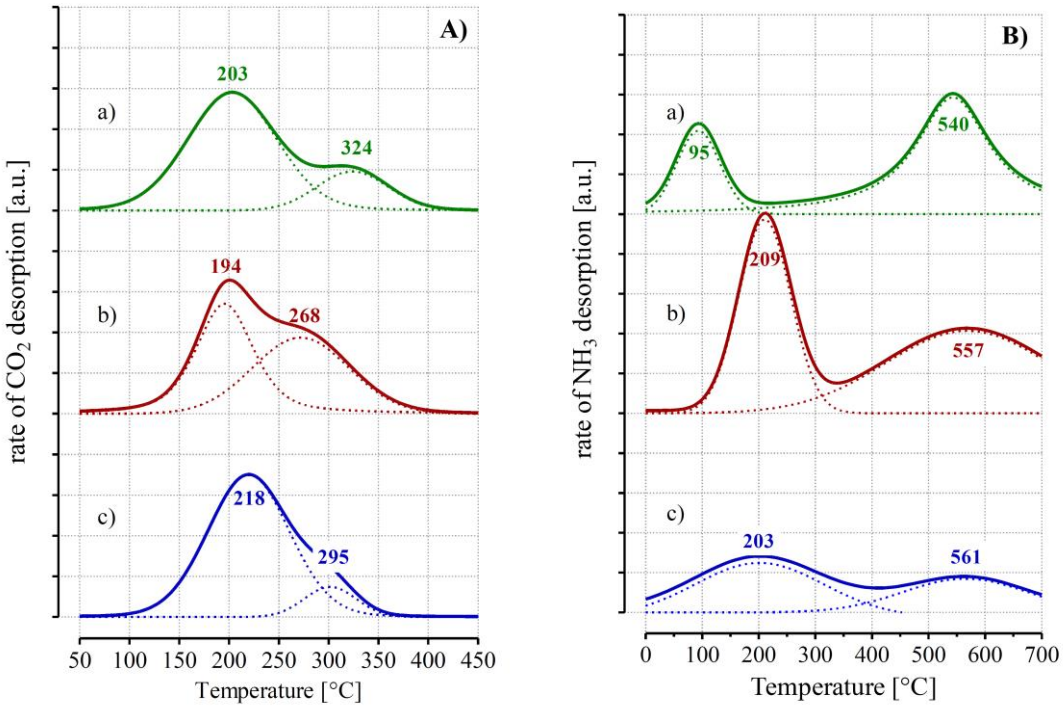

Figure 4.21 – TPD of CO_2 (A) and NH_3 (B) of CZZ-MOR (a), CZZ-FER (b) and CZZ-MFI (c)

In spite of a similar base capacity (123-132 $\mu mol_{CO2}/g_{cat}$), of CZZ-MOR and CZZ-MFI a prevailing population of basic sites (≥ 80%) mainly concentrates at lower temperature (50-250 °C), being ascribable to weak basic sites from surface hydroxyl groups or metal-oxygen pairs [259]. Differently, on CZZ-FER the contribution of the basic character is equally distributed between weak and strong basic sites, as the result of partial surface dehydroxylation generating coordinatively unsaturated O_2^- species [130].

These findings definitely confirm that the zeolite structure can significantly affect the oxide distribution, leading to the formation of different active sites, able to act either as Brønsted (CO_2 desorption temeprature below 250 °C) or as Lewis basic sites (at higher temperature).

SAMPLE	Base capacity[a]	Weak base sites[b]	Strong base sites[c]	Acid capacity[d]	Weak acid sites [e]	Strong acid sites[f]
	[$\mu mol_{CO2}/g_{cat}$]			[$\mu mol_{NH3}/g_{cat}$]		
CZZ-MOR	124	98	26	197	102	95
CZZ-FER	132	64	68	381	229	152
CZZ-MFI	123	109	14	138	112	26

[a] Cumulative CO_2-uptake in the range 50-450 °C

[b] CO_2-uptake in the range 50-250 °C

[c] CO_2-uptake in the range 250-450 °C

[d] Cumulative NH_3-uptake in the range 100-700 °C

[e] NH_3-uptake in the range 100-300 °C

[f] NH_3-uptake in the range 300-700 °C

Table 4.19 – TPD measurements of the investigated hybrid samples

In order to ascertain how the co-precipitation method affected the zeolite acid sites distribution, NH_3-TPD measurements of hybrid catalysts were also performed. As showed in Figure 4.21B, the hybrid catalysts exhibit NH_3-TPD profiles similar to fresh sample as discussed above, with the presence of both weak ($100<T_M<300$ °C) and strong ($T_M>300$ °C) acid sites. By comparing value of Table 4.19 with acid sites concentration of metal-free zeolite sample (see Table 4.9 for MFI, Table 4.13 for FER8 and Table 4.10 for MOR) it is clear that co-precipitation of metal precursors significantly depresses the total acid capacity of zeolites. However, the decreasing of acidity is much more limited on CZZ-FER, exhibiting, after co-precipitation, the highest acid capacity (381 µmol/g), as contribution of a larger population both of weak (229 µmol/g) and strong acid sites (152 µmol/g).

CHAPTER 5

Methanol dehydration over zeolite: the effect of channel system

Introduction

In this chapter the effect of channel system on deactivation of investigated molecular-sieve structures during vapour-phase methanol dehydration reaction is discussed. As discussed in Chapter 3, deactivation tests were carried out at 240 °C (typical reaction temperature for both indirect and direct synthesis of DME) for 60 h in Time-On- Stream. Investigated catalysts were also compared at lower temperature (200 °C) with the aim to estimate an apparent turnover frequency value (TOF). Tests at lower temperature were also carried out and obtained results permitted to estimate an apparent activation energy value for each of investigated material. Moreover, analysis of deposited coke emphasizes the effect of channel system on composition of retained carbonaceous species.

Obtained results exclude some molecular sieves from further investigation because of their low activity, fast deactivation, low DME selectivity or high carbon deposit level. In particular, both MFI and FER structures exhibited reliable catalytic behaviour in terms of resistance to deactivation even if acid sites of FER structure revealed a better efficiency in terms of DME production.

5.1 Initial catalytic activity

In this paragraph methanol conversion and DME productivity data are reported and discussed. Presented data are calculated as the 1 h of average reaction over three independent runs and a conversion variation below 5% was observed for all the catalysts. Fig. 5.1 shows the methanol conversion as a function of reaction temperature over 1-dimensional molecular sieves. As a common feature of all curves, is that the methanol conversion increases when increasing temperature, approaching the equilibrium value at 200 °C for MOR sample. The slight decreasing of methanol conversion from 220°C to 240 °C over MOR sample follows the downward trend of theoretical equilibrium conversion. Data shows clearly that catalytic activity follows the order MOR>EU-1>TON>MTW.

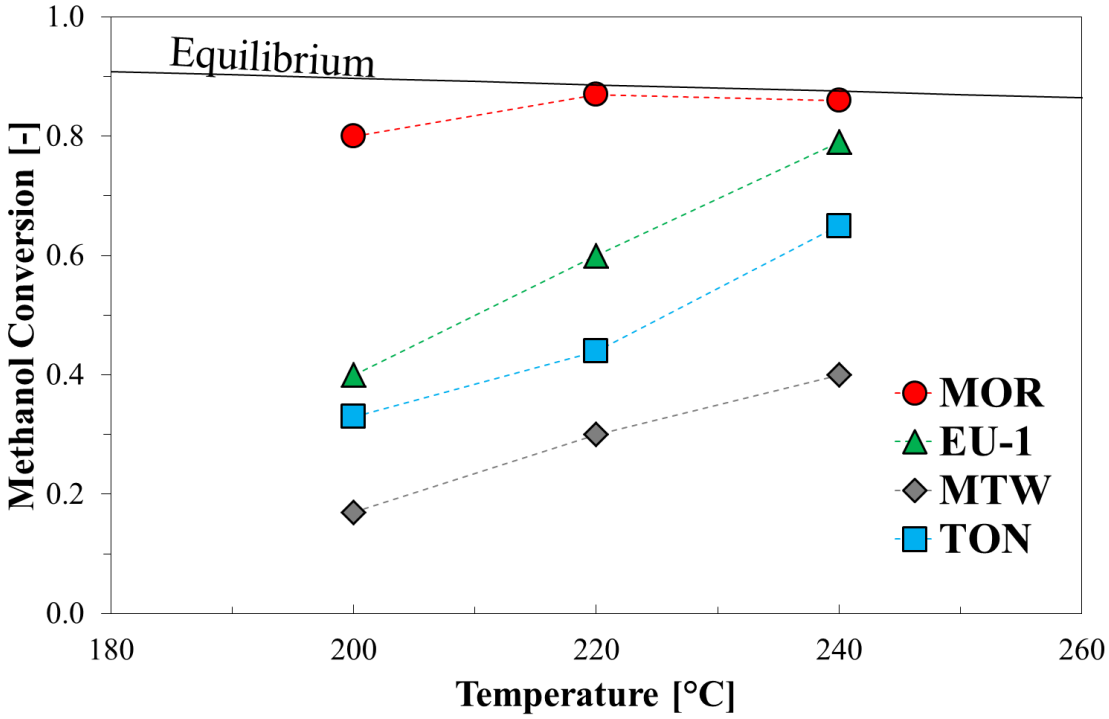

Figure 5.1 – Methanol conversion data of 1-dimensional molecular sieves

Fig. 5.2 shows methanol conversion data for FER-type catalyst (FER8) and commercial γ-Al_2O_3. FER8 exhibits a catalytic activity in terms of methanol conversion much higher than γ-Al_2O_3, approaching to the equilibrium value at 240 °C.

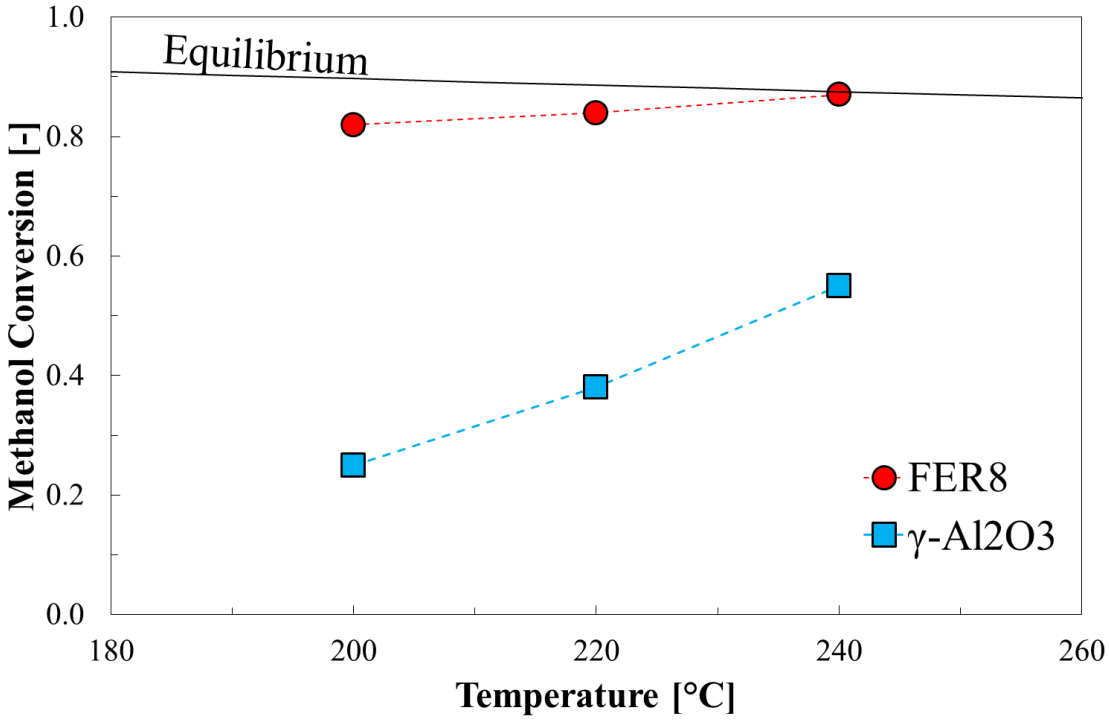

Figure 5.2 – Methanol conversion data of 2-dimensional molecular sieves (FER8) and commercial γ-Al_2O_3

3-dimensional molecular sieve exhibits similar activity as showed in Fig. 5.3.

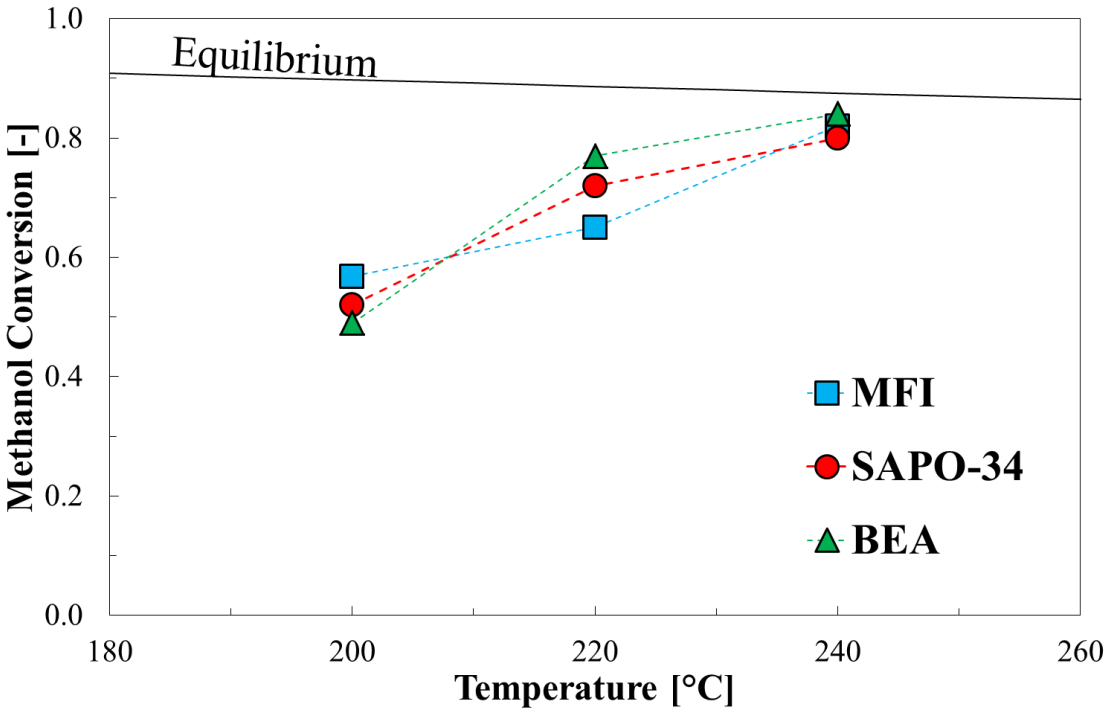

Figure 5.3 – Methanol conversion data of 3-dimensional molecular sieves

Obtained results show that, except for MTW, investigated zeolites are more active than commercial γ-Al_2O_3.

In order to properly compare catalytic behaviour of the investigated catalysts a Turnover Over Frequency value (TOF) at 200°C was estimated and results are reported in Fig. 5.4. It is well known that the difficulty in estimating a TOF value is not only in determining intrinsic reactant conversion rate but in counting of active sites that may not be all identical [251] in terms of type, strength and location. Therefore, because no intrinsic kinetic data were measured in this work and only acid sites concentration were measured, the TOF values reported in this paper would be considered as average/apparent value. According to Niwa recommendations [225, 246], only strong acid sites (T_M>300 °C, in this paragraph indicated as *h*-sites) were considered as active acid sites and the TOF values were calculated as it follows:

$$TOF = \frac{(WHSV / MW_{MeOH}) \cdot x_{MeOH}}{A \cdot x_h}$$

where the ratio $WHSV/MW_{MeOH}$ is the methanol molar hourly flow rate per gram of catalyst (μmol/g/h), x_{MeOH} is the observed methanol conversion, A is the total NH_3-uptake

(expressed as µmol/g) and and x_h is the fraction of acid sites with TM>300 °C measured by NH_3-TPD analysis (see Chapter 4).

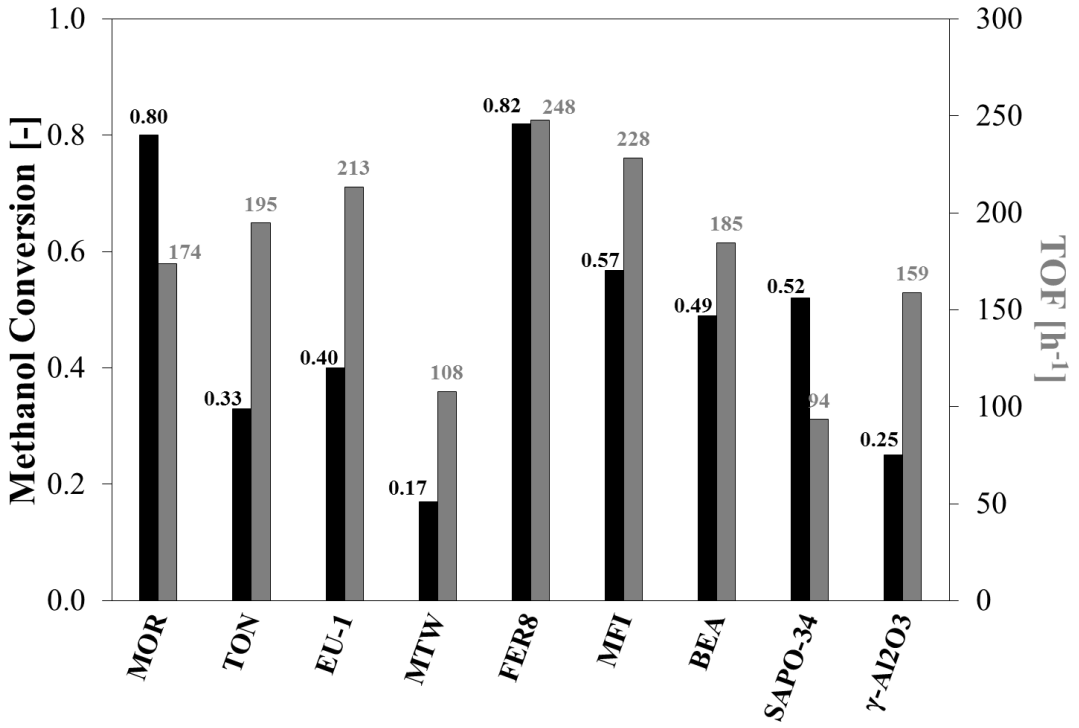

Figure 5.4 - Methanol conversion (black bars) and Turnover frequency value (grey bars) at 200 °C and WHSV= 4.5 h-1

Results reported in Fig. 5.4 clearly show that FER8 exhibits the highest acid sites efficiency with a TOF of around 250 h^{-1}. Referring to 1-D zeolites with similar h-sites acid site concentration, namely EU-1, MTW and TON, EU-1 exhibits the highest TOF value followed by TON and MTW. Furthermore, EU-1 offers a TOF value also higher than MOR sample (the richest in acid sites). It is useful to remark that the TOF values reported in this work may not be considered as an intrinsic turnover frequency of acid sites but as an apparent value. Obtained result is not surprising as it can demonstrate that parameters other than acidity, such as crystal morphology, location of acid sites, mass transfer resistances can play a role in catalyst activity. For instance, because the different crystal size, the high apparent TOF value estimated for EU-1 can be associated to diffusional path in EU-1 sample that are smaller than those in larger crystals of TON and MTW, but it is not excluded that other factors (e.g. acid sites location) can justify obtained data. In fact, by considering both channels openings [261] and crystal size, BEA-type material should offer lower mass transfer limitations than MFI-type material. Strangely, despite similar acid site concentration, MFI offers an apparent TOF value higher than BEA of about 20%, suggesting that other parameters can affect the apparent turnover

frequency value. With the reported analysis, the higher efficiency of MFI sample could be associated to the presence of stronger acid sites as mentioned in NH_3-TPD measurements discussion, even though further investigations are necessary to better discuss these aspects. On the other hand, the lower TOF value calculated for SAPO-34 sample can be mainly related to the higher mass transfer limitation due either to the narrow channels of CHA framework [261] and/or to the large crystal size, reducing catalyst efficiency and acid sites accessibility. Finally, except for MTW and SAPO-34, zeolites are usually more effective than commercial γ-Al_2O_3.

At the reaction temperature of 200 °C only DME was detected in the reactor out stream. The DME productivity observed at this temperature is reported in Figure 5.5.

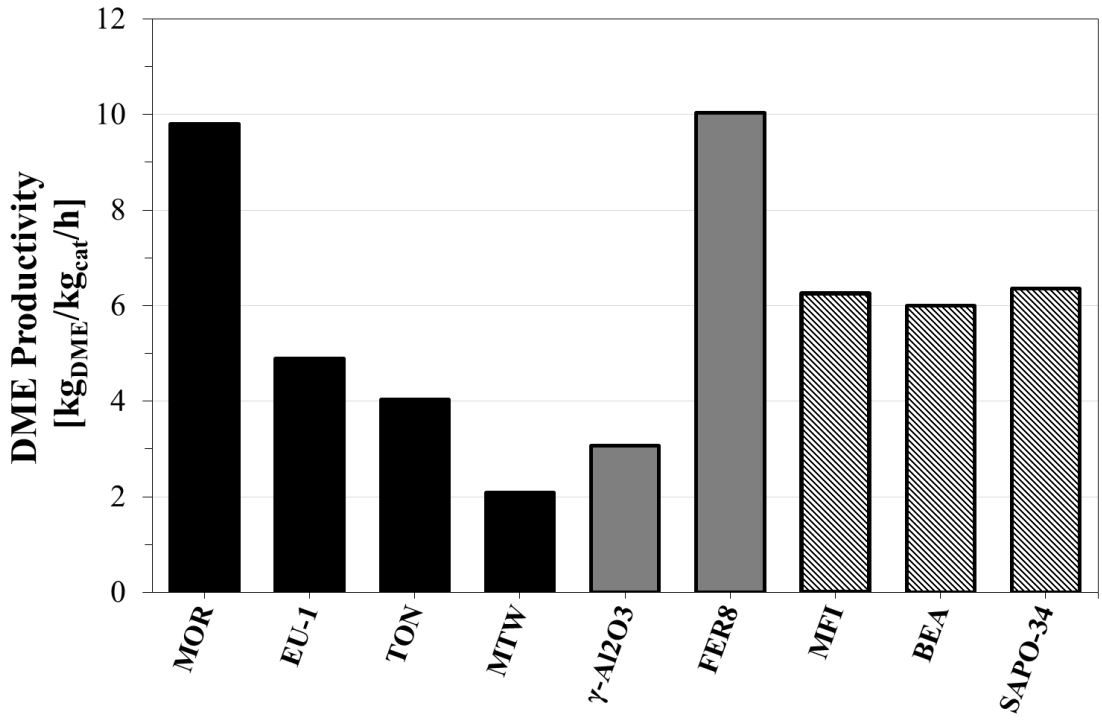

Figure 5.5 – DME productivity over the investigated samples at 200°C and WHSV=4.5 h^{-1}

Data clearly reveal that FER8 and MOR exhibit the highest DME productivity with a value of around 10 $kg_{DME}/kg_{cat}/h$. 3-dimensional molecular sieves (MFI, BEA and SAPO-34) exhibit a similar DME productivity of around 6 $kg_{DME}/kg_{cat}/h$. Lower productivity values were observed for EU-1 (around 5 $kg_{DME}/kg_{cat}/h$) and TON (around 4 $kg_{DME}/kg_{cat}/h$). On the contrary, γ-Al_2O_3 shows a DME productivity slightly higher than MTW. The more interesting result is that FER8 and MOR exhibit DME productivity four times higher than the traditional catalyst for DME production (γ-Al_2O_3). This result suggest that it should be possible to use zeolites as FER or MOR at reaction temperature

lower than for γ-Al_2O_3 having immediately a positive effect on the process economy (see Chapter 1).

For sake of completeness, apparent activation energy are also estimated by adopting Arrhenius model for all of the investigated samples (see Appendix E) and the results are collected summarized in Figure 5.6.

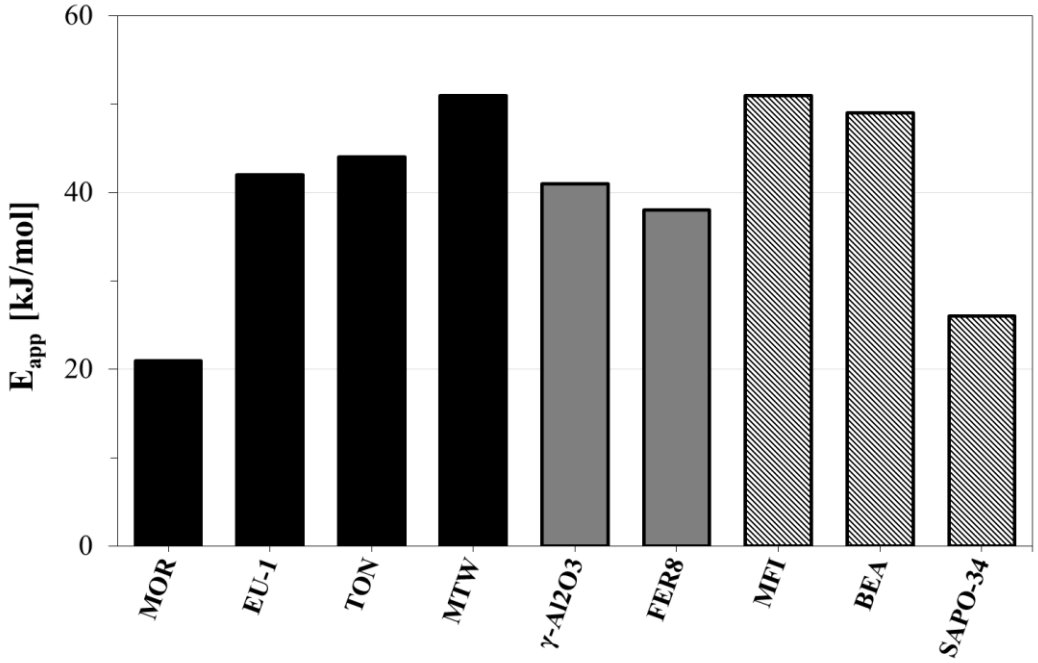

Figure 5.6 – Estimated apparent activation energy

A E_{app} value of around 40-50 kJ/mol was usually estimated for investigated catalysts, except for MOR and SAPO-34 that exhibit a lower value.

The effect of catalyst structure on selectivity and deactivation was evaluated at 240 °C. Figure 5.7 shows the DME selectivity and yield measured at 240 °C over the investigated samples.

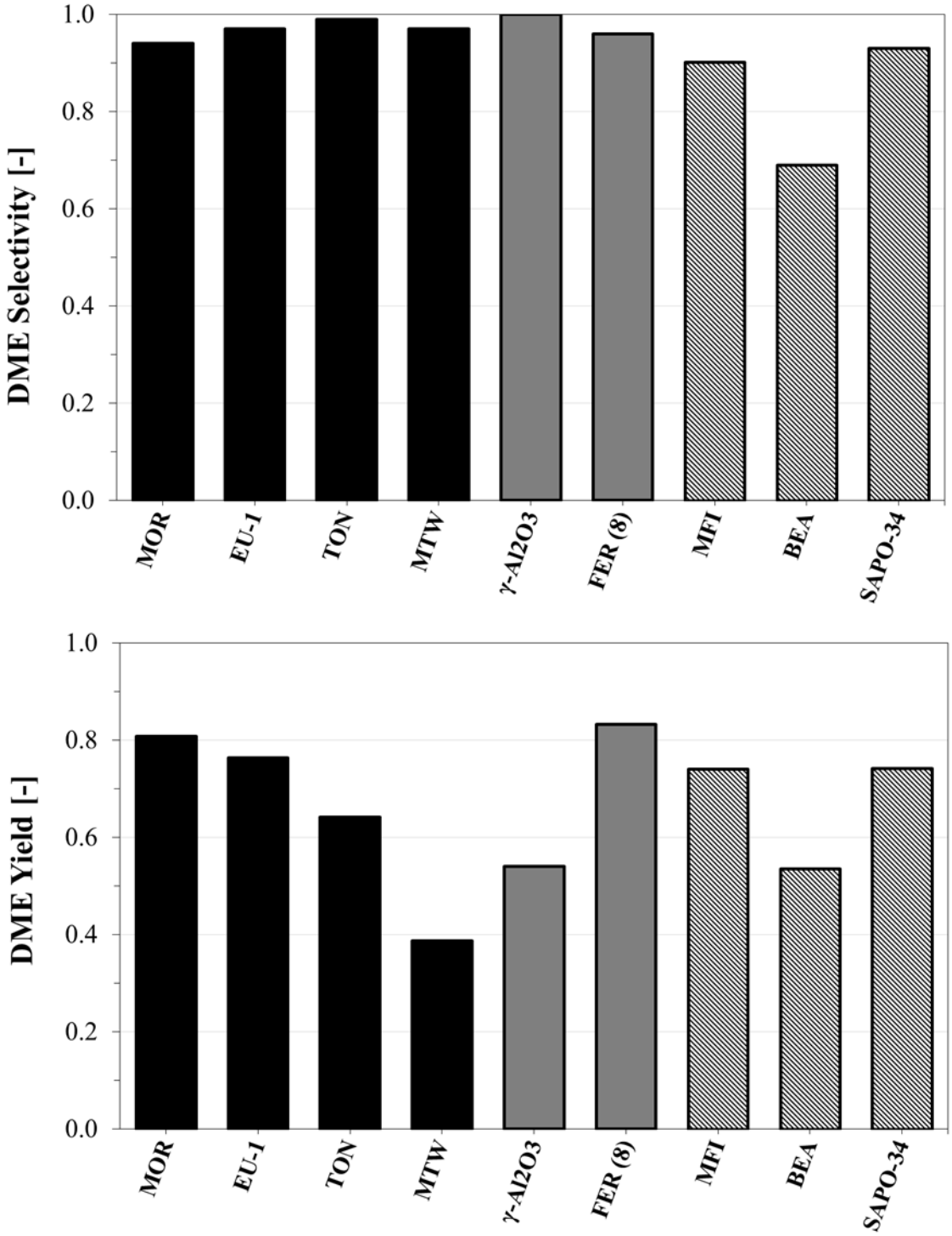

Figure 5.7 – DME selectivity (up) and DME yield (down) measured at 240 °C and WHSV=4.5 h^{-1} and during 30 min Time-On-Stream

Results show that zeolites are selective towards DME at exception for BEA that exhibits a low selectivity. γ-Al_2O_3 ranks as the most selective catalyst for DME production while FER(8) exhibits the highest DME yield. As discussed in the previous section, MTW is not a reliable catalyst for DME production compared with the tradition one (γ-Al_2O_3).

The main by-products detected on reactor outstream by GC analysis were methane, ethylene, propylene and butanes; heavier undefined compounds were observed on MFI and BEA. For instance, a liquid phase condensed on the reactor outline (namely at room temperature) when MFI was used as catalyst at 240 °C, while a white solid (GC-MS analysis suggests that it is hexamethyl benzene) was deposited when BEA reacts at temperature above 200 °C.

5.2 Catalyst deactivation

Despite the stability over 1 hour time of all catalysts, methanol conversion analysis in this short time range was not sufficient to fully investigate the catalytic behaviour. Therefore, stability tests over a wider time range (60 h) at the maximum investigated temperature (240 °C) were undertaken, in order to gain more insight about deactivation phenomena and coke deposition. Methanol conversion versus Time-On-Stream for the investigated catalysts is reported in Figs. 5.8-5.10.

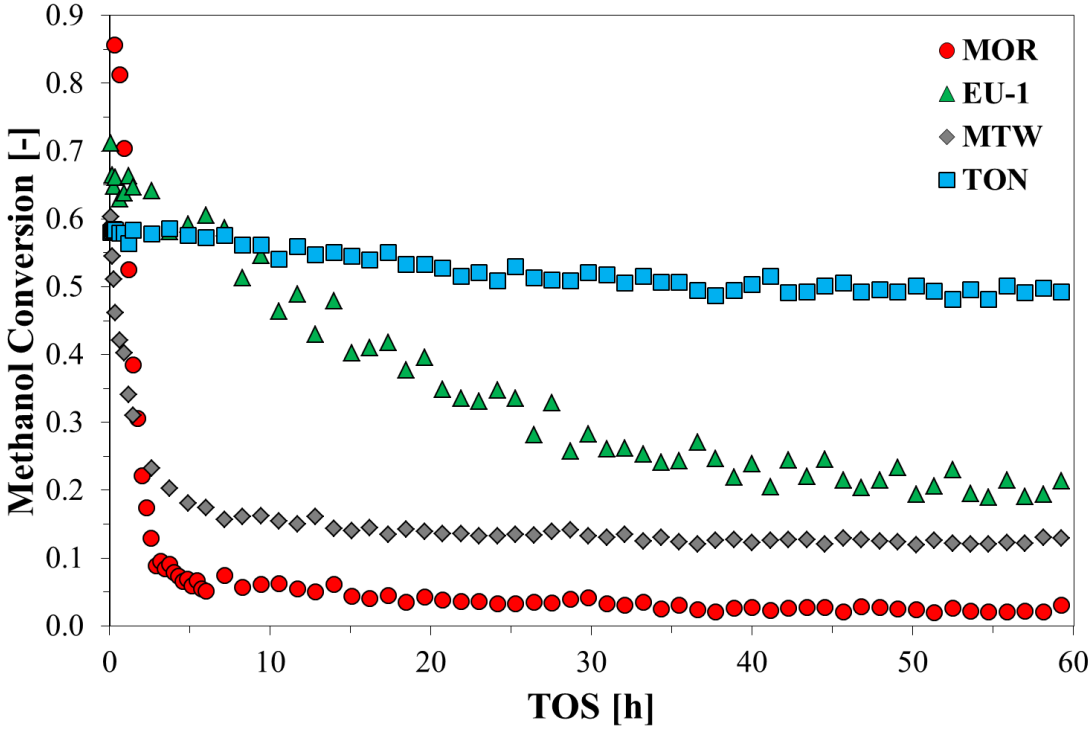

Figure 5.8 – Methanol conversion over time on 1-dimensional zeolites. Test conditions: 240 °C and WHSV=4.5 h^{-1}

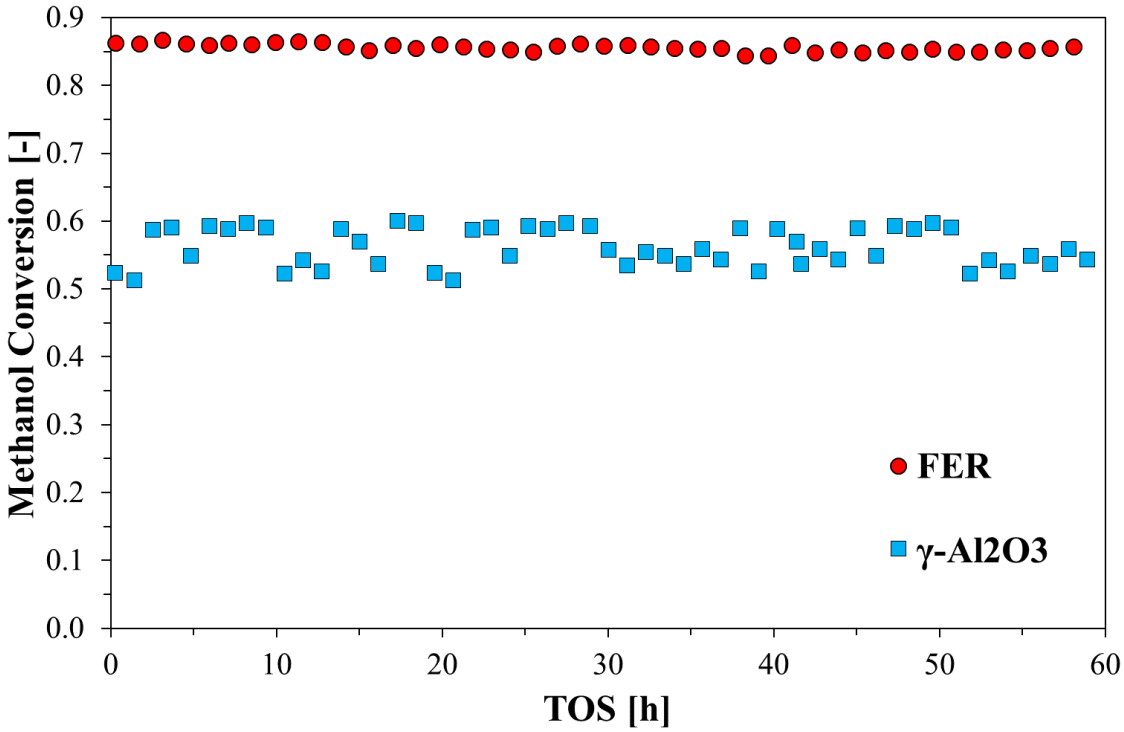

Figure 5.9 – Methanol conversion over time on FER8 and γ-Al_2O_3. Test conditions: 240 °C and WHSV=4.5 h^{-1}

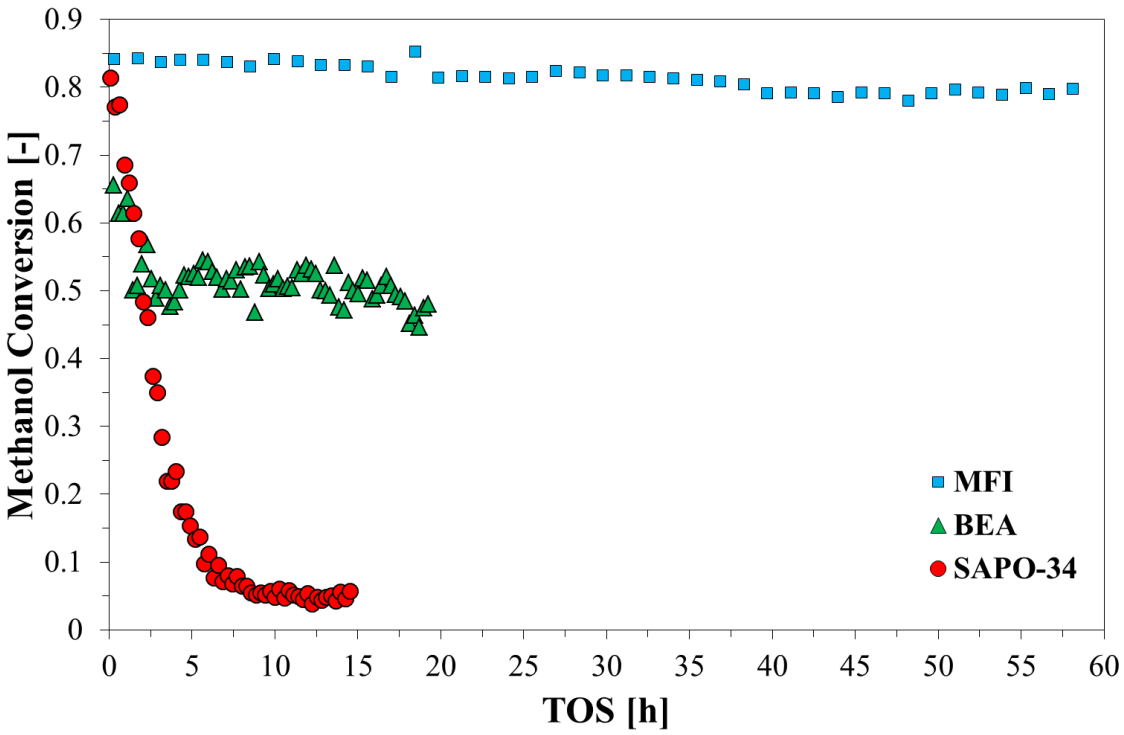

Figure 5.10 – Methanol conversion over time on 3-dimensional zeolites. Test conditions: 240 °C and WHSV=4.5 h^{-1}

A complete deactivation was observed for MOR and SAPO-34. The presence of strong acid sites on MOR may be responsible of retention of both coke precursors and coke molecules causing pore blocking of 1-dimensional 12-ring channels of MOR structure [39, 262]. On the contrary, deactivation of SAPO-34 may be reasonably attributed to the presence of large cages with narrow openings of CHA structure what is a trap system for coke molecules that cannot diffuse outside the crystal [263]. Despite the similar acidity of MTW, TON and EU-1 samples, a different behaviour towards deactivation was observed and attributed to channel system characteristics. Although similar channel openings, EU-1 is less resistant than TON, probably because coke molecule are formed and trapped in the side-pockets of EUO structure causing pore blocking [212]. More space-confined TON structure limit formation of coke on the external surface of crystals or near to the pore opening retarding deactivation [264]. It is well known that slight differences in channel openings may drastically change catalytic behaviour of zeolites. In fact, because its slightly larger channel openings than TON (just 0.3 Å), MTW undergoes an important deactivation with a higher carbon deposit level as discussed below. A partial deactivation was observed in the 3-D large channel system of beta, while MFI kept nearly constant performances as well as FER and commercial γ-Al_2O_3.

After 60 h, a DME selectivity improvement is observed at all of investigated catalyst. This behaviour may be associate to the deactivation of strong acid sites inhibiting formation of by-products compounds.

Fig. A6 (Appendix A) shows that there is no significant change of crystallinity of the spent catalysts.

5.3 Coke analysis

The amount of carbon deposited at 240 °C after 60 h reaction was measured by TGA of spent catalyst and results are summarized in Table 5.1.

Under investigated condition, SAPO-34 forms the highest amount of coke. The higher carbon deposition obtained in comparison to the other molecular sieves may be explained by the different porous structure of the investigated materials. In addition to the smaller size of SAPO-34 channels openings, the intersection between channels generates large cavities whose size allows formation and entrapment of a higher amount of carbonaceous species despite structure with more confined channel system as MFI. The highest carbon deposition observed over SAPO-34 would be attributed also to the highest h-sites

concentration measured on this sample. By comparing catalysts with similar h-sites value as TON, EU-1 and MTW it is possible to show how the structure affect coke deposition.

Sample	*Carbon deposit (after 60 h)*	
	[mg/g]	*[mg/mol$_{H+}$]*
MOR	72	117
TON	31	138
EU-1	90	361
MTW	72	439
FER8	45	102
MFI	60	181
BEA	79	224
SAPO-34	149	202
γ-Al$_2$O$_3$	-	-

Table 5.1 – Carbon deposit over spent catalyst after 60 h of reaction at 240 °C

The higher carbon deposit level per unit of catalyst-mass observed for H-EU-1 may be associated to the presence large 12-ring side-pockets of EUO structure [265]. Also channels openings play a crucial role towards coke deposition. In fact, although MTW and TON have just 0.3 Å difference in their pore sizes, the MTW-type catalyst allows deposition of coke about twice the TON-type catalyst [264]. Estimation of carbon deposition per mole of h-sites (see discussion of NH3-TPD results reported in previous paragraph) may emphasize this aspect. By analyzing values reported in the last column of Table 5.1, MTW is revealed to be the most active in terms of coke deposition while 2-D small channel system of FER seems to inhibit coke formation and prevent catalyst deactivation. It is also noteworthy that, under the investigated conditions, no carbon deposit was detected on γ-Al_2O_3 catalyst.

As general observation, with respect to any other sample, the efficiency of FER8 clearly appears when considering the amount of carbon formed per mole of acid sites, being H-FER8 the catalyst with the lowest value. As discussed for TOF analysis, further investigations are necessary (e.g. acid sites location and type) in order to better discuss the effect of other parameters of each structure towards coke deposition. The effect of acidity on coke deposition of FER-type crystals are discussed in the next chapters.

Following the extraction procedure of the carbonaceous species, no insoluble phase has been observed as solely soluble coke molecules were extracted in organic phase.

The analysis of coke composition via GC–MS spectra are reported in Fig. 5.11 showing that the deposit formed at 240°C mainly includes poly–methylbenzenes.

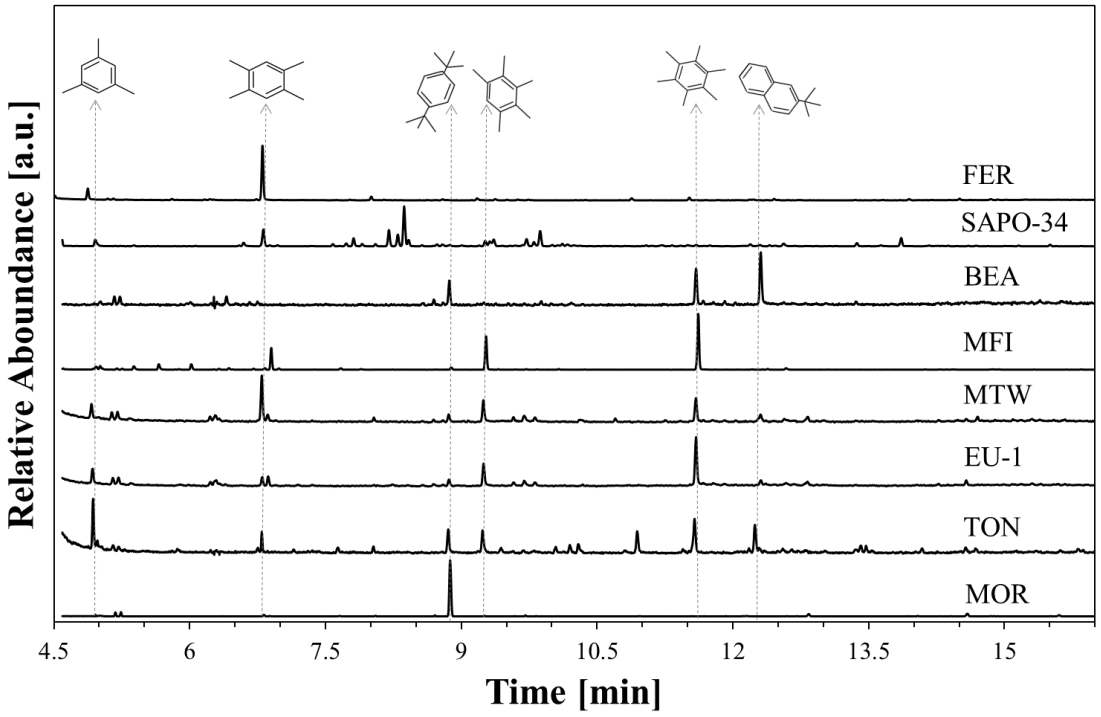

Figure 5.11 - GC–MS spectrum of coke molecules extracted from soluble coke.

The presence of different methylbenzene compounds confirm that zeolite structure can strongly affects the coke composition in the investigated reaction conditions [39, 266]. By considering 1-D molecular sieves, the effect of channel topology is evident: despite the similar channel openings, EU-1 carbon phase consist mainly of hexamethyl benzene while smaller molecules as trimethyl-benzene were mainly detected for TON sample. This difference can be attributed to the effect of EU-1 large side-pockets, able to accommodate large molecule as hexamethyl benzene that progressively deactivates the catalyst as previously discussed. On the contrary, the confined space of TON channels permits mainly the formation of benzenes with a lower alkylation degree and with a much more lower deposition level as previously discussed.

The presence on substituted naphthalene (polycyclic compound) was detected on TON exhausted sample and, because its bulky size it is believed to be deposited on the external crystal surface even though further investigation would be necessary to confirm this hypothesis. In fact, as general statement, it should be reminded that zeolite structure might

strongly affect the reaction-pathway involving methanol (any Methanol to Hydrocarbon reaction scheme) [267], leading to different intermediate and coke forming species. Therefore, apart from direct effect of zeolite shape and dimension, the absence/presence of some compounds could be, in principle, be determined also by the different reaction pathway promoted by the specific structure.

Also in BEA formed coke polycyclic species were detected, together with hexa-methylbenzene molecules that can be located in framework cavity [51]. The effect of channel openings can be observed by comparing MOR and MTW. MOR with its 6.5 x 7.0 Å channels permit formation of 1,2-dipropyl benzene that its bulkier than tetra-methyl benzene witch is observed on 5.6 x 6.0 Å channels of MTW.

Despite the relatively small channel size, the channel intersection of the 3D MFI structure offers space enough to host poly–methylbenzenes [134] and the GC–MS shows the presence of tetra–methylbenzene, penta–methylbenzene and hexa–methylbenzene [47]. The latter molecule is reasonably formed out of the structure [51]. As reported in the open literature for methanol conversion at relatively low temperature (e.g. 300 °C) [268], SAPO-34 carbon phase consist mainly of adamantane species with GC-MS elutriation time in the range 7.5-8.5 min (this elutriation time is affected by GC-MS procedure). Finally, FER structure carbon phase consists selectively of tetra-methyl benzene compound located in FER cages or external surface because there is insufficient space in the channels for cyclization reactions [134].

5.3.1 Coke location over MOR, FER and MFI catalysts

MOR, FER and MFI exhibited reliable performances in terms of initial methanol activity. Unfortunately, coke deposition deactivates MOR catalyst while FER and MFI exhibits higher stability. In this paragraph, coke deposition on these three catalysts is further investigated in terms of location of retained carbonaceous species.

With the aim to understand the origin of catalyst deactivation as a consequence of carbon deposition, BET and micropores volume measurements have been also carried out over either “exhausted” (after continuous test at 240°C) or regenerated samples (after 8 hours under 40 NmL/min of flowing air at 580°C). The measured values of BET superficial specific area, micropore volume and external area are reported in Fig. 5.12, 5.13 and 5.14, respectively.

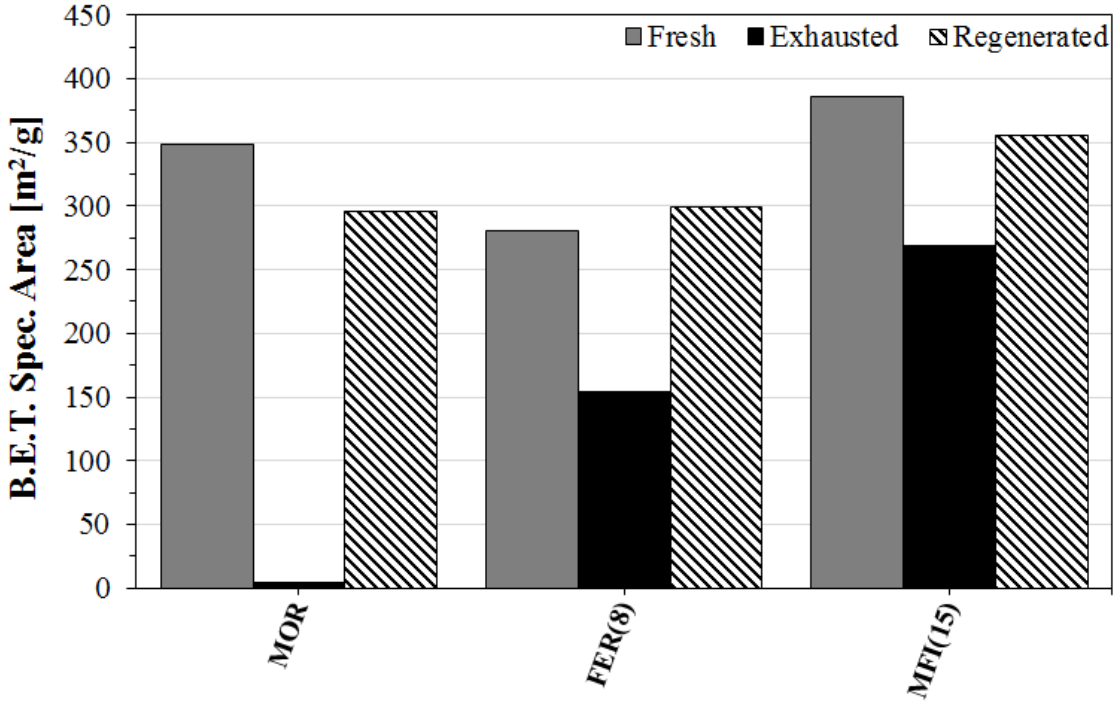

Figure 5.12 – B.E.T. Superficial Specific Area of fresh, exhausted (after TOS at 240°C) and regenerated MFI, FER(8) and MOR catalysts.

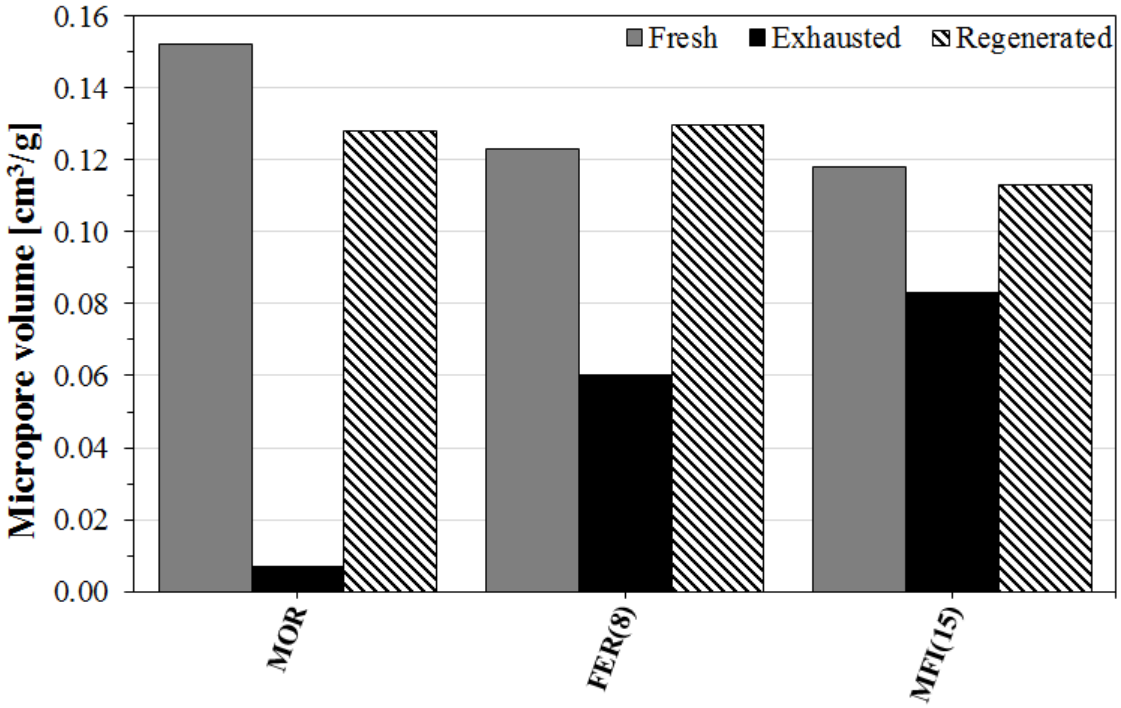

Figure 5.13 – *t*-plot micropore volume of fresh, exhausted (after TOS at 240°C) and regenerated MFI, FER(8) and MOR catalysts.

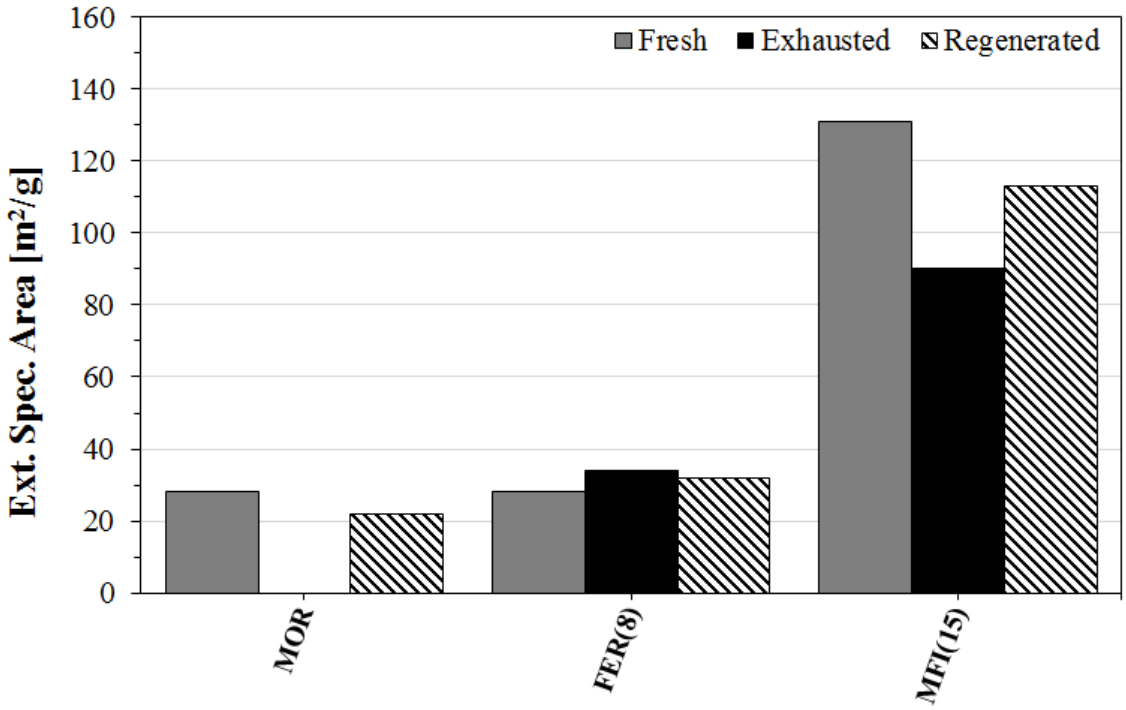

Figure 5.14 – External superficial area of fresh, exhausted (after TOS at 240°C) and regenerated MFI(15), FER(8) and MOR catalysts

By comparing the obtained values with the carbon deposited on fresh catalyst it again appears the fundamental role played by the zeolite structure.

In fact, the 1D large pore MOR structure exhibits a sharp decrease in specific surface area and micropore volume, as evidence of complete channel blocking resulting in a drop of the catalytic activity out of 10% conversion. On the contrary, the reduced amount of carbon deposit on FER and MFI (see values of Table 5.1) determines a decrease of specific surface area and micropore volume of 50% and 30% respectively, without any appreciable effect on methanol conversion over time. After the regeneration procedure, the textural properties are in line with those of the fresh sample, suggesting that the structural properties are recovered after the thermal treatment.

Some other important insights may be deduced by considering the effect of zeolite channel size and the dimensions of molecules. In the case of MOR, the big channel size coupled with the significant drop of micropore volume and specific surface area indicate that coke molecules are trapped inside the channels ending with a complete pore blocking and drop of calculated external surface area.

On the contrary, since only a partial reduction of both specific area and micropore volume is observed in the case of MFI and FER structure, it would be interesting to estimate how

much coke is trapped inside the structure and how much is deposited out of the catalyst surface. With this aim, an estimation of the deposited coke volume has been done, in a conservative way, by approximating coke molecules (tetra–, penta– and hexa–methylbenzenes) with an equivalent sphere with a kinetic diameter equals to the maximum diameter exhibited by the molecule. For sake of simplicity, because of the structure of the considered organic compounds, a molecular diameter of 8.6 Å (corresponding to an equivalent sphere volume: 333 $Å^3$/molecule) has been assumed as equal for any species [269]. By combining the amount of coke deposited on the catalyst (see values of Table 5.1), as measured by TGA, and the molecular weights of the poly–methylbenzenes, it is possible to estimate the volume of formed coke (expressed as cm^3_{coke}/g_{cat}) and compare it with the decreasing of micropore volume of exhaust. For FER structure, since only tetra–methylbenzene is present, coke molecules occupy a volume of 0.067 cm^3_{coke}/g_{cat}, in agreement with the measured decrease of micropore volume reported in Table 4 (0.123–0.06 = 0.063 cm^3/g). This result suggests that nearly the totality of the coke formed in FER structure is trapped inside the micropores (within the cages), as also confirmed by the constant values of the external surface area pre– and post– catalyst usage. A different result is obtained for MFI where the total volume occupied by deposited coke is 0.079 cm^3_{coke}/g_{cat}, calculated as the sum of tetra– (0.014 cm^3_{coke}/g_{cat}), penta– (0.026 cm^3_{coke}/g_{cat}) and hexa– (0.039 cm^3_{coke}/g_{cat}) methylbenzenes. This value is higher than the measured decrease of micropore volume of "exhausted" sample (0.035 cm^3/g), indicating that only a fraction of the formed coke may be entrapped in the structure. This is also confirmed by the external surface area measurements: with respect to the fresh sample, a drop is found in exhaust MFI sample (indicating the presence of some external carbon deposits). On the other hand, it is widely recognized that hexa–methylbenzene is a too big molecule to be formed and accommodate in MFI structure, as it has been observed only within a large channel system, such as BEA [52], while tetra– and penta–methylbenzene can be host within the MFI channel intersections [134]. In addition, by summing the volume occupied by these two molecules, the calculated amount (0.040 cm^3_{coke}/g_{cat}) is comparable with the overall micropore volume drop, suggesting that, like in the case of FER, the majority of these two molecules is entrapped in the structure while hexa–methylbenzene is deposited on the external crystal surface.

To confirm the hypothesis drawn to establish where carbon prevalently forms as a function of zeolite structure, SEM-EDX analysis have been performed and the results are shown in Fig. 5.15. Chemical maps were obtaining using not treated sample by acquiring the EDX signal for long time (about 20 h) to obtain high quality images of carbon deposit distribution on the catalyst surface.

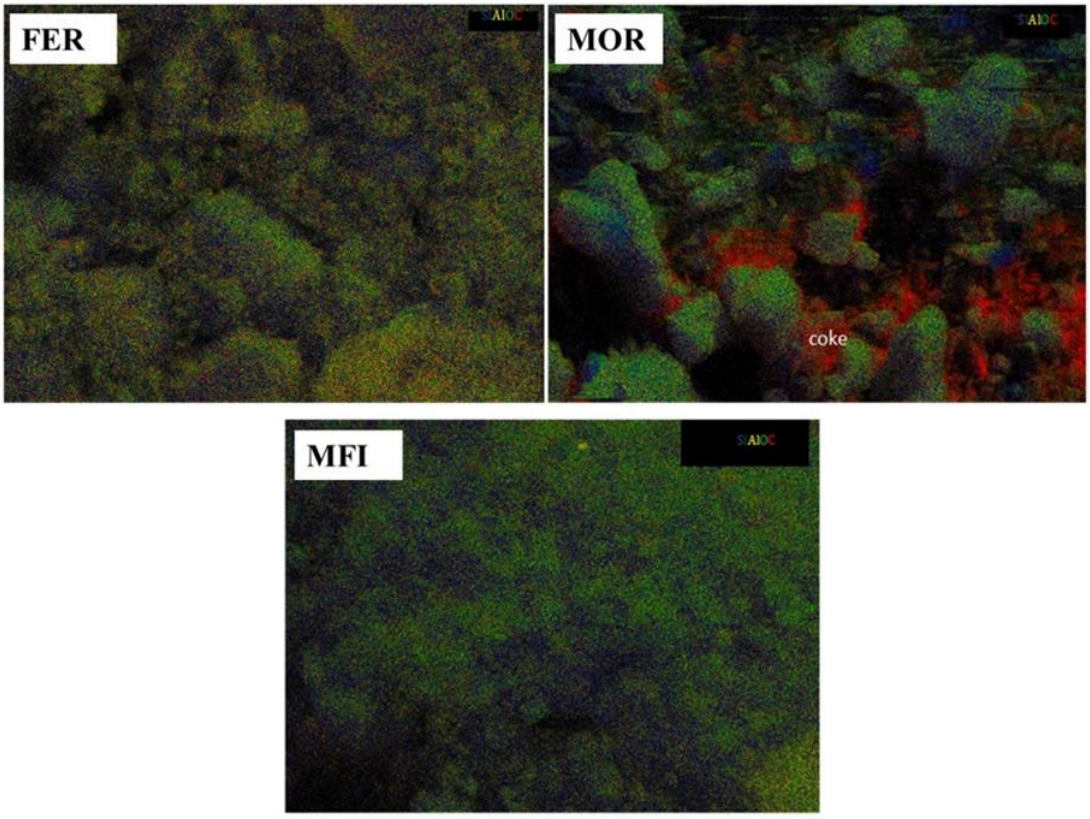

Figure 5.15 – SEM-EDX analysis pictures of exhausted FER(8), MOR and MFI(15) samples. Red color refers to carbon deposit.

Further to observe a higher surface concentration of coke on MOR, what is important to highlight is that the coke distribution significantly change among different zeolites investigated. Accordingly to the porosimetry data, on MOR large carbonaceous agglomerates form around zeolite particle, very probably occluding access of reactants inside pores, while on FER and MFI coke formation take place with different mechanism. In fact, on FER and MFI, coke distributes homogeneously on surface and no agglomerates were observed. From these data, as before inferred, it clearly appears that the zeolite dimension and structure play a fundamental role in coke precursor formation, mainly

determining the carbon deposit preferential location and distribution (i.e. extra-framework or inside the zeolite pores).

CHAPTER 6

Methanol dehydration over FER-type catalysts

Introduction

Preliminary catalytic results reported in Chapter 6 showed that FER-type channel system exhibit reliable catalytic performances in terms of DME selectivity, stability and coke deposition. As previously discussed, channel system of zeolites (channel openings, channel orientation, presence of cages or side-pockets) is not the only parameter of affective catalytic behavior of these materials. Acidity (acid sites concentration, strength and distribution) and crystal morphology may affect catalytic performances. In order to investigate the role of both acidity and crystal morphology on catalytic behavior of FER-type catalysts, vapour-phase methanol dehydration reaction was performed on ferrierite samples synthesized with different aluminum content or structure directing agent (SDA) and results are presented and discussed in this chapter.

6.1 The effect of Si/Al ratio on catalytic behavior of FER-type catalyst

In this paragraph catalytic performances of FER-type crystals synthesized with different aluminum content are presented. Table 6.1 shows the main physicochemical properties of investigated samples.

Sample	Si/Al_g[a]	Si/Al_b[b]	Acid capacity[c]	Weak sites[d]	Strong sites[e]	Lewis[f]	B. E. T. [g]	M. V.[h]
			[µmol/g]			[%]	[m^2/g]	[cm^3/g]
FER8	8	8.4	787	347	440	34	339	0.136
FER30	30	23	464	135	329	7	272	0.108
FER60	60	45	332	110	222	6	275	0.110

[a] Si/Al ration in the synthesis gel

[b] Si/Al in the final solid (measured by atomic absorption spectroscopy)

[c] Cumulative NH_3-uptake in the range 100-700 °C

[d] NH_3-uptake fraction in the range 100-300 °C

[e] NH_3-uptake fraction in the range 300-700 °C

[f] Lewis acid sites fraction measured by FT-IR analysis of adsorbed D_3-acetonitrile

[g] Specific area calculated by B.E.T. method

[h] Micropore volume by *t*-plot method

Table 6.1 – Physicochemical properties of investigated FER-type catalysts synthesised with different Si/Al ratio

6.1.1 Catalytic activity

Fig. 6.1 reports the methanol conversion over the investigated catalysts as a function of temperature and it clearly appears the effect of the catalyst acidity as the conversion increases according to the acid sites concentration (FER8>FER30>FER60) at any investigated temperature. In these conditions, methanol dehydration reaction may face thermodynamic limitation as it can be seen for FER8.

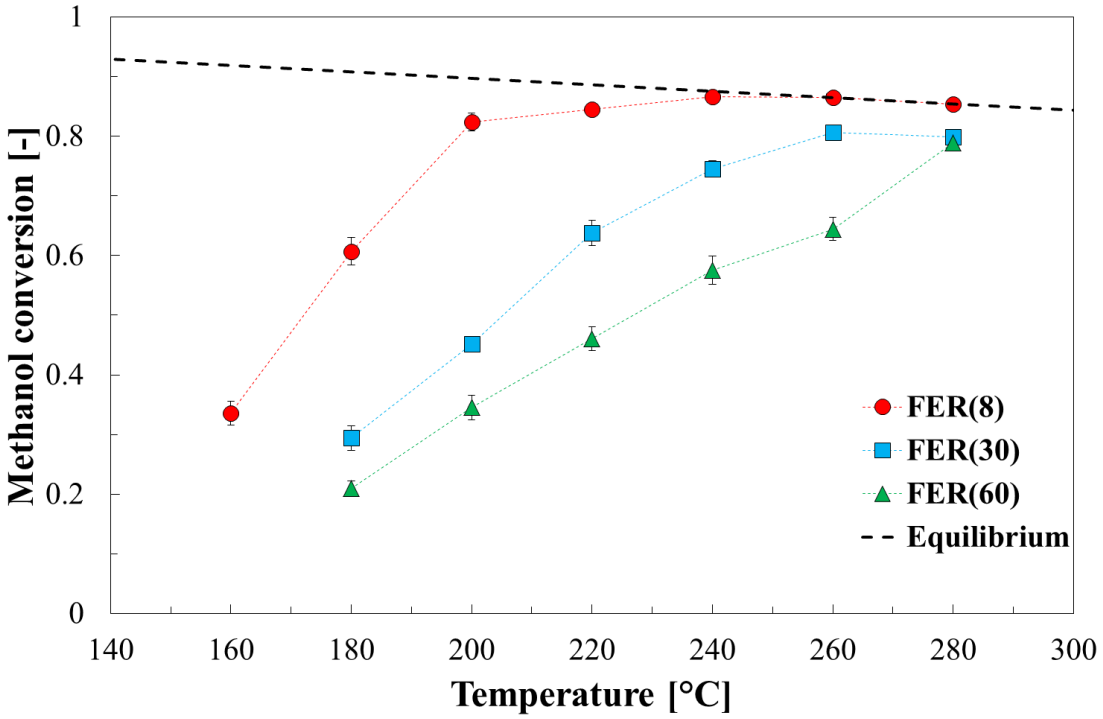

Figure 6.1 - Methanol conversion on FER(8), FER(30) and FER(60) at WHSV = 4.5 h^{-1}.

Data of Figure 6.1 showed that an increase of reaction temperature above 200 °C does not implies any significant increase in methanol conversion for FER8 and the theoretical thermodynamic conversion value is reached at 240°C.

In addition, the comparison of samples at different acidity reveals that a significant increase of the operating temperature is requested to promote the reaction when using the less acid catalyst. In fact, the methanol conversion value of ca. 0.6 is reached at 180 °C on FER8 while, a reaction temperature of 220 °C and 260 °C are needed to reach similar conversion level on FER30 and FER60, respectively (both catalyst are weaker in acid sites strength and lower in acid sites concentration). This result confirms that a more acidic catalyst can dehydrate the methanol with high activity at relatively lower temperature. On the other hand, in presence of similar physical properties (such as crystal size), in the case of higher amount of active sites for the reaction, such as for FER8, it seems quite obvious that the higher is the acid sites concentration the higher is the reactant conversion.

In order to compare the effectiveness of acid sites of the investigated catalyst a turnover-frequency (TOF) analysis is necessary to properly address the results discussion, the TOF was defined in Chapter 5 by considering as active acid sites only the sites of T_M>300 °C

(see Table 6.1). In order to get reliable results on sites activity, TOF analysis has to be performed using data far away from the equilibrium conditions. Therefore, FER8 have yield the closest to the theoretical thermodynamic yield and according to results of Fig. 6.1, the TOF analysis was performed using conversion data at 180°C. If 70 mg of catalyst are considered, 31 μmol_{H+} for FER8, 24 μmol_{H+} for FER30 and 16 μmol_{H+} for FER60 were loaded in the reactor. With a methanol hourly molar flow rate of 8830 $\mu mol \cdot h^{-1}$, the calculated TOF values are: 174 h^{-1} for FER8, 108 h^{-1} for FER30 and 119 h^{-1} for FER60. Apart from the higher acid sites concentration, these values clearly indicate that acid sites of FER8 are also more effective than acid sites of FER30 and FER60 for methanol conversion.

A direct estimation of the acid sites efficiency of FER30 and FER60 can be also obtained by loading the reactor with different masses of catalyst increasing the amount of acid sites as closets as possible to FER8-one. On this purpose, 148 mg of FER30 and 208 mg of FER60 were loaded, leading to a number of acid sites available equal to 51 μmol_{H+} for FER30 and 46 μmol_{H+} for FER60, slightly higher than FER8 acid sites (31 μmol_{H+}). Despite the higher acid sites number available for the reaction, FER30 and FER60 still exhibited a methanol conversion of 0.48±0.03 and 0.45±0.03, well below the value of 0.61±0.02 measured for FER8 (see above). This result clearly suggests that, apart from the higher acid sites concentration, FER8 exhibits a superior activity to convert methanol if compared to less acid FER samples. In addition to the difference in acid sites concentration (samples at different Si/Al ratio), comparison of data for FER30 and FER60 reveals that a similar methanol conversion level (about 0.47) was observed by loading a similar acid sites number (about 49 μmol_{H+}), indicating a similar sites efficiency for these two catalysts. Therefore, the differences in catalytic activity between FER30 on FER60 reported in Figure 6.1 are related only to the different amount of acid sites when loading the reactor with the same catalyst mass. On the contrary, as demonstrated by TOF values analysis, FER8 exhibit the highest activity to convert methanol and this effect can be also due to the difference in acidity type. In fact, as reported in Table 6.1, FER8 exhibits an amount of Lewis acid sites higher than FER30 and FER60 and, confirming the observation of Bandiera and Naccache [89], the presence of Lewis acid sites is a relevant parameter to promote methanol conversion.

The Arrhenius plot of the data at temperatures in which methanol conversion is far away from thermodynamic theoretical equilibrium (160-200 °C for FER8 and 180-220 °C for FER30 and FER60) is reported in Figure 6.2 and the calculated apparent activation energy

values are 38±6 kJ·mol-1 for FER8, 36±2 kJ·mol-1 for FER30 and 37±5 kJ·mol-1 for FER60.

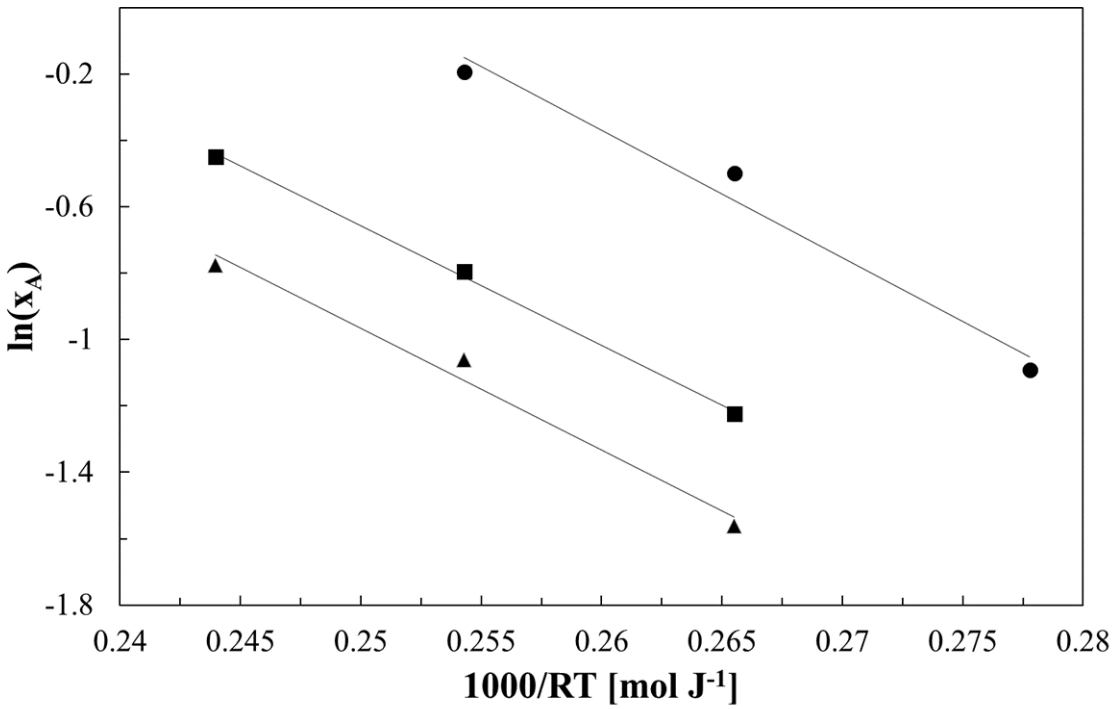

Figure 6.2 - Arrhenius plot for FER8 (●), FER30 (■) and FER60 (▲)

Despite the differences in terms of activity exhibited from the investigated catalysts, a similar activation energy was estimated for the three catalysts. This result can be explained by analysis of acid sites strength: we compared catalysts with the similar diffusion limitations (similar both crystal size and microporous structure) and with similar acid sites strength and the results, in terms of energies, lead clearly a similar apparent activation energy. The differences in terms of catalytic sites efficiency exhibited from the investigated catalysts can be mainly attributed to the frequency with which methanol molecules are converted on acid sites according to TOF analysis; also the presence of Lewis acid sites can contribute to improve TOF in FER8.

The high stability towards deactivation exhibited by FER structure reported in the previous Chapter was confirmed also for catalysts with different Si/Al ratios as reported in Figure 6.3.

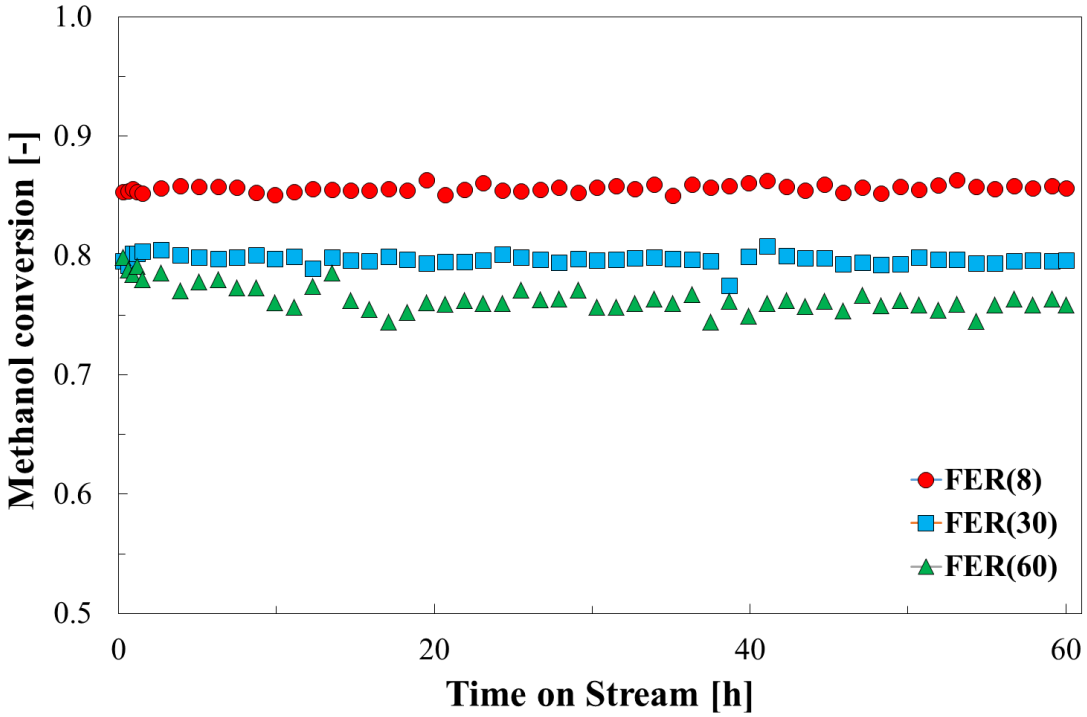

Figure 6.3 - Methanol conversion in Time-On-Stream on FER(8), FER(30) and FER(60) at 280 °C and WHSV = 4.5 h^{-1}.

The methanol conversion is constantly kept around 0.88, 0.85 and 0.77 for FER(8), FER(30) and FER(60), respectively, over 60 hours Time-on-Stream.

6.1.2 Products selectivity

Figure 6.4 shows the effect of reaction temperature on DME selectivity for the three investigated samples. All the catalysts were very effective toward DME production as DME selectivity approaches the unity at 180 °C for FER30 and FER60, while at the same temperature it is 0.97 for FER8. By increasing reaction temperature, a slight decrease in DME selectivity is observed but the effect is more evident for sample FER8, where DME selectivity drops from 0.97 to 0.91 by increasing of the reaction temperature from 180 °C to 260 °C, while the same value (above 0.98) is observed on FER30 and FER60 at 180°C and it is preserved up to 260 °C. At higher temperature a DME selectivity drop was also observed for these samples.

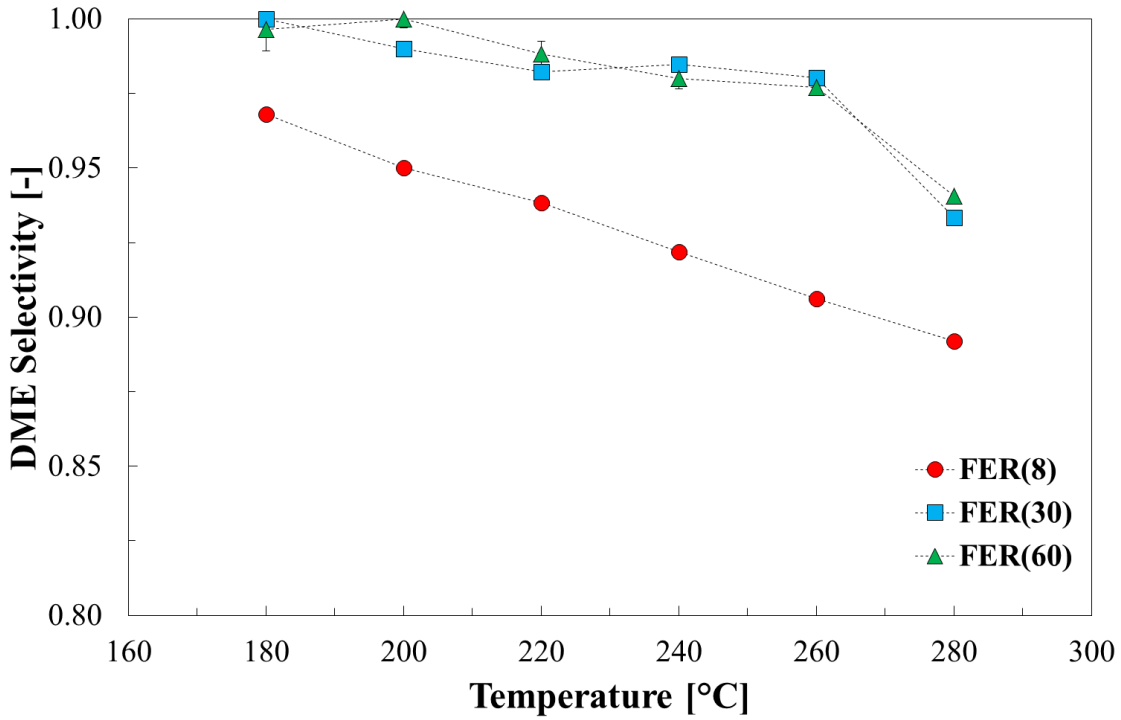

Figure 6.4 – DME selectivity on FER(8), FER(30) and FER(60) at WHSV = 4.5 h^{-1}.

At the investigated maximum temperature of 280 °C, a DME selectivity equals to 0.89, 0.94 and 0.93 are observed for FER8, FER30 and FER 60, respectively. These values increases to c.a 0.97 after 60 h of reaction, showing that acid sites responsible of selectivity loss are progressively deactivated overtime more than the acid sites responsible for DME production.

The results on DME selectivity follows the same trend of the acidity measurements as the more acid catalyst (FER8) exhibits lower DME selectivity compared with samples with a lower acidity (FER30 and FER60). It is interesting to note that FER30 and FER60 exhibit a very similar trend in terms of DME selectivity, despite FER30 possess a higher amount of acid sites. Therefore, the lower DME selectivity observed on FER8 should be attributed to the presence of Lewis acid sites as well as to the highest acid sites concentration.

In order to gain information about the selectivity loss and by-product formation, products of the Time-on-Stream at 280°C were analysed and it was found that methane, ethylene, propylene are the main species, with some residual trace of butenes. The presence of olefins is expected, according to the Methanol-to-Olefins mechanism, while methane formation during methanol conversion can derive directly from methanol/DME molecules [172] or by reaction between methoxy- groups and coke molecules [262, 270].

The distribution of by-products is reported in Figure 6.5 at different sampling times. as molar fraction calculated considering only methane, ethylene and propylene.

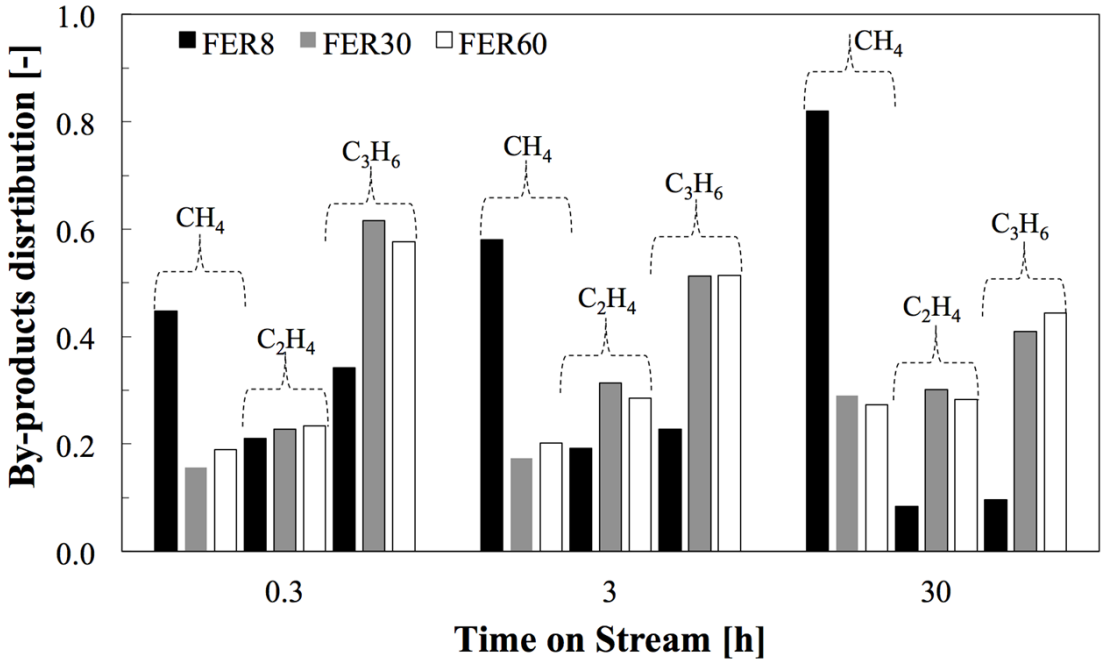

Figure 6.5 - Light by-products distribution at 280 °C and WHSV = 4.5 h^{-1}.

Also in the case of side-reactions, FER8 exhibits a different behaviour compared with FER30 and FER60, because methane is the main light by-product observed on FER8, while propylene is preferentially formed on FER30 and FER60 at any investigated time. In addition, it is also noteworthy the evolution over time of the by-products distribution from Figure 6.5: after 0.3 h of test, the molar fraction of methane is 0.45, 0.16 and 0.19 on FER8, FER30 and FER60, respectively. These values tend to increase with progress of the reaction, reaching the values of 0.82, 0.29, 0.27, respectively, after 30h. The increase in molar fraction, from 0.45 to 0.82 over time, indicates a clear attitude of FER8 to form methane, whilst FER30 and FER60 still tend to preferably form C2= and C3=. The similar value and trend of methane fraction observed on FER30 and FER60 suggest, also in this case, that the remarkable increase in methane formation on FER8 is due to the combined effect of Lewis acid sites and highest acid sites concentration.

6.1.3 Coke analysis

The amount of deposited coke was measured after 60 h Time-On-Stream at 280 °C and WHSV = 4.5 h^{-1} and the following value were found: 78 mgcoke·gcat-1, 39 mgcoke·gcat-1 and 35 mgcoke·gcat-1 for FER8, FER30 and FER60, respectively. According to methanol, conversion, DME selectivity and light by-products distribution data, despite their different amount of acid sites, FER30 and FER60 exhibit a similar behaviour, at constant WHSV. On the contrary, FER8 tends to form the highest amount of coke, suggesting that the presence of Lewis acid sites may significantly promote the coke deposition. This results can also justify the high methane production observed on FER8 after 60 h Time-On-Stream. When considering the carbon deposit, no insoluble coke was observed during the extraction procedure [207]. From composition spectra reported in Figure 6.6, it clearly appears that the coke phase deposited on catalyst surface during the reaction mainly consists of tetra-methyl benzene. Even though the presence of small quantities of bulkier compounds (hexa-methylbenzenes, 4-propyl-toluene and naphthalenes) was observed for FER30 and FER 60 (the lowest in acidity and less efficient), results confirms that channel network is the most relevant parameter, determining the type of carbon deposit in the investigated temperatures range [262].

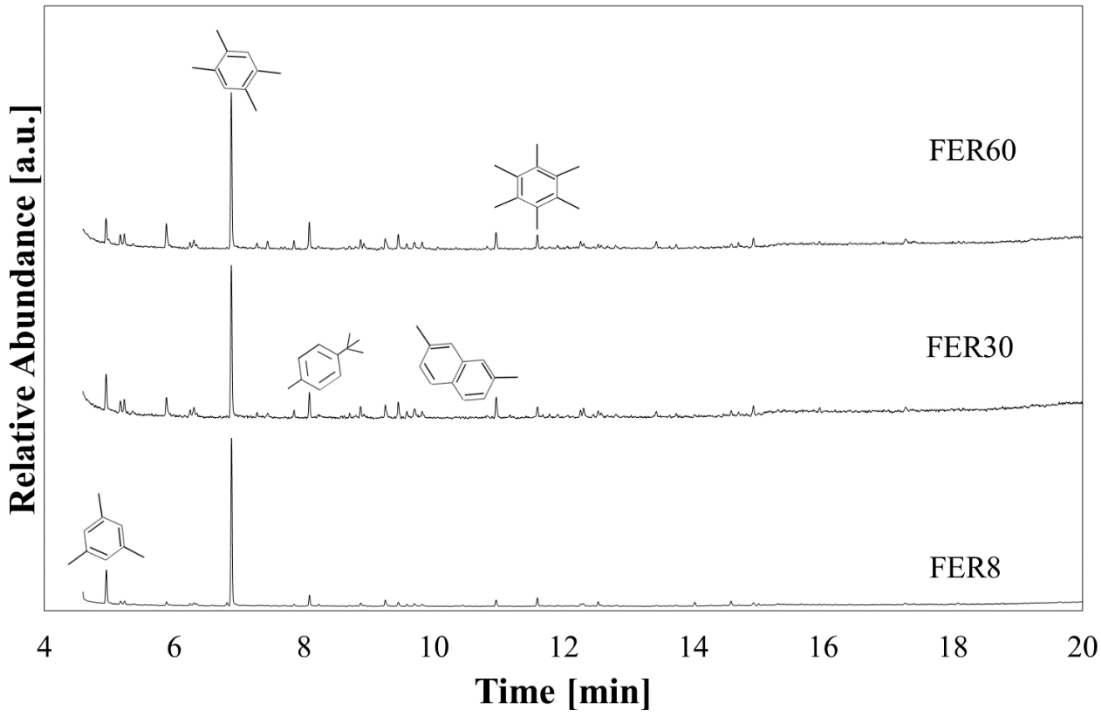

Figure 6.6 – GC–MS spectra of coke molecules extracted from soluble coke deposited on FER(8), FER(30) and FER(60) at 280 °C and WHSV = 4.5 h^{-1}.

6.2 The effect of SDA on catalytic behavior of FER-type catalyst

In this paragraph, catalytic performances of FER-type materials synthesized with different structure directing agent are compared during methanol dehydration reaction. This investigation permits to elucidate the effect of crystal size and acid sites distribution on deactivation and coke formation of ferrierite catalyst. In order to better discuss the obtained results, Table 6.2 reports the main physicochemical properties of investigated materials.

SAMPLE	Acid capacity[a]	Weak sites[b]	Strong sites[c]	Lewis[d]	B. E. T. [e]	M. V.[f]	Crystal size[g]
	[µmol/g]			[%]	[m^2/g]	[cm^3/g]	[µm]
Py-FER	787	347	440	34	339	0.136	5-8
En-FER	1052	316	736	41	306	0.127	1-2
DAO-FER	1418	567	851	40	287	0.115	≈1
THF-FER	929	288	641	15	280	0.125	10-15
Nano-FER	787	354	433	32	340	0.133	0.3-0.5

[a] Cumulative NH_3-uptake in the range 100-700 °C

[b] NH_3-uptake in the range 100-300 °C

[c] NH_3-uptake in the range 300-700 °C

[d] Lewis acid sites fraction measured by FT-IR analysis of adsorbed D_3-acetonitrile

[e] Specific area calculated by B.E.T. method

[f] Micropore volume by *t*-plot method

[g] SEM analysis

Table 6.2 – Physicochemical properties of investigated FER-type catalysts synthesised with different SDA (Py=pyrrolidine, En=ethylediammine, DAO=1,8-diamminooctane, THF=tetrahydrofuran, Nano-FER=synthesized with pyrrolidine and sodium lauryl sulphate)

Figure 6.7 shows the methanol conversion at different reaction temperatures over the synthesised catalysts. The reported data were calculated as an arithmetic media over three independent measurements during 30 min of Time-On-Stream resulting in conversion variation below 10%.

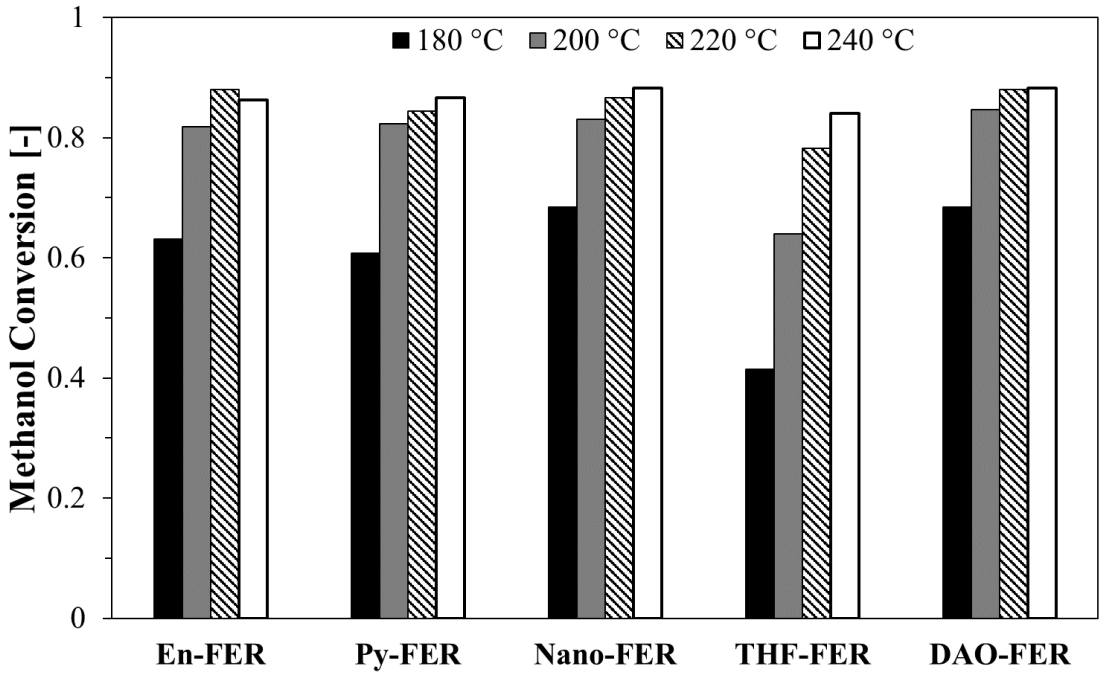

Figure 6.7 – Methanol conversion on FER samples synthesised with different SDA and nano-sized sample, WHSV=4.5h^{-1}

Results show that investigated materials exhibit different catalytic activity. At the lowest temperature, Nano-FER and DAO-FER exhibit the highest activity in terms of methanol conversion followed by En-FER and Py-FER whilst the sample synthesised with tetrahydrofuran, THF-FER, exhibits the lowest value of methanol conversion on the investigated reaction conditions. The lower activity of THF-FER can be attributable to the large crystal size of this sample (10-15 µm) that causes a higher mass transfer limitation. The effect of crystal size is also evident by comparing Py-FER and Nano-FER that exhibit similar acidity (acid sites concentration and distribution) but different activity. At the reaction temperature of 180 °C, methanol conversion on Py-FER is 0.60 while on Nano-FER is 0.68. DME selectivity data reported in Figure 6.8 suggest that over both THF-FER and DAO-FER sample only DME is formed at 180 °C while a slightly lower selectivity is observed over the other samples. For all the samples, DME selectivity progressively decreases as the reaction temperature increases and methane, ethylene, propylene and butenes were observed in the reactor out-stream via GC analysis.

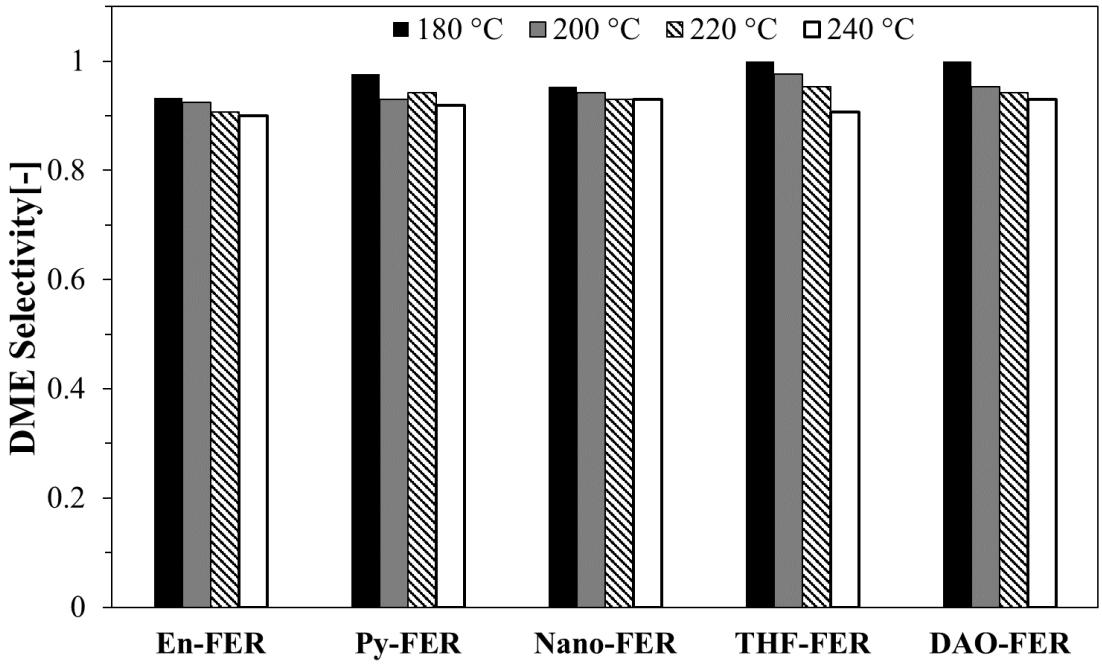

Figure 6.8 – DME selectivity on FER samples synthesised with different SDA and nano-sized sample, WHSV=4.5h^{-1}

At the reaction temperature of 240 °C the methanol conversion was monitored for about 1000 minutes and experimental data are reported in Figure 6.9.

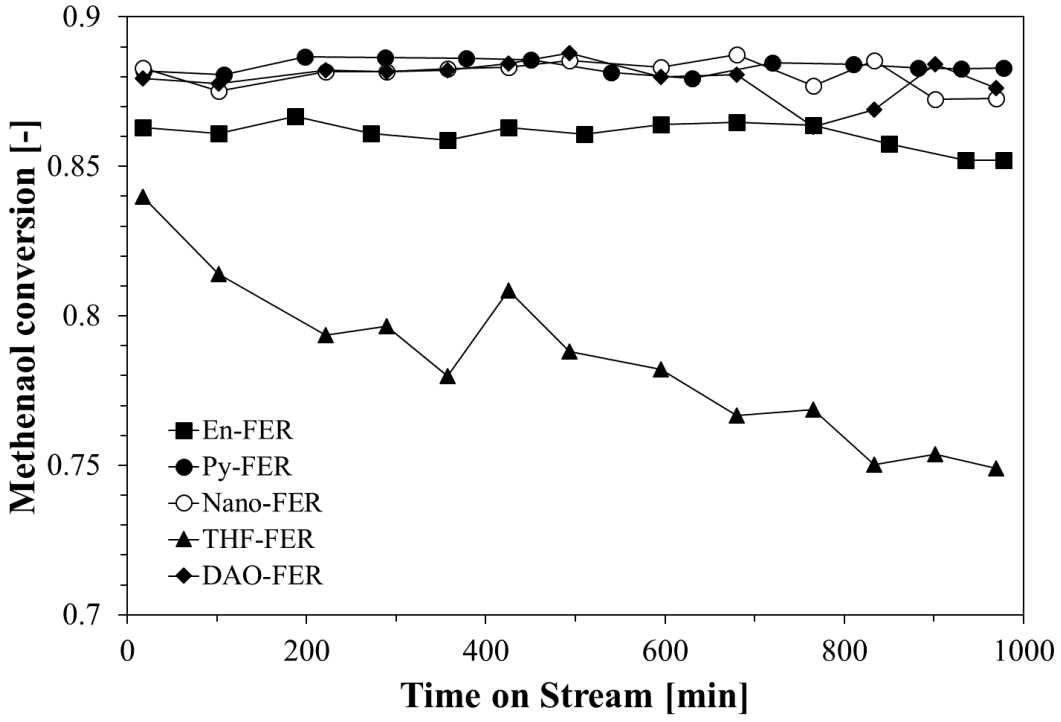

Figure 6.9 – Methanol conversion versus Time on Stream observed at 240 °C and WHSV= 4.5 h^{-1}.

Results show that FER-type catalysts synthesised with amines as OSDA, namely En-FER, Py-FER and DAO-FER, offer a high stability in the considered time range. On the contrary, THF-FER shows a progressively deactivation since methanol conversion is ca. 10% lower at the end of TOS test. The higher deactivation rate observed for THF-FER sample is associated to the higher amount of deposited coke as reported in Figure 6.10.

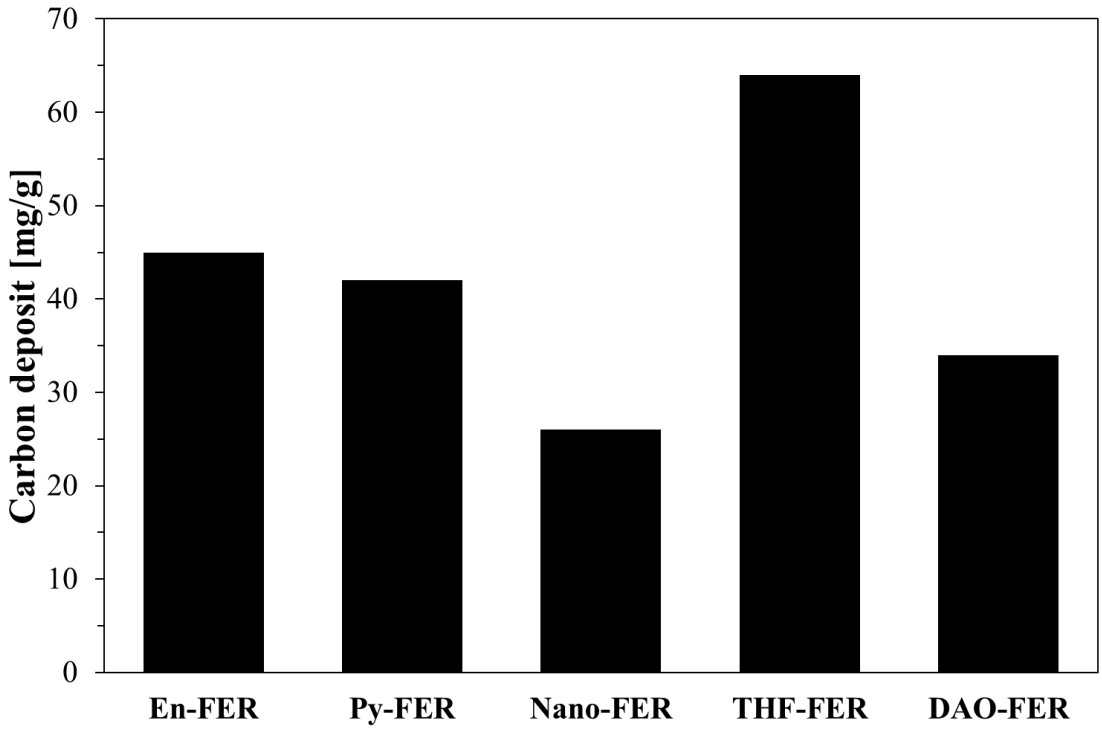

Figure 6.10 - Carbon deposit over investigated sample after 1000 min of TOS at 240 °C and WHSV= 4.5 h^{-1}

The higher carbon deposit level and the associated more rapid deactivation can be promoted by both presences of Brønsted acid sites or large crystal size [205, 271]. THF-FER have both higher Brønsted sites concentration and larger crystal size that can cooperate to have a faster carbon deposition and deactivation. On the contrary, since Nano-FER and Py-FER have similar acidic properties, the lower carbon deposit level offered by Nano-FER can be associated reasonably to its nano-sized crystals that retard coke formation [271]. Despite its higher acid sites concentration, DAO-FER sample shows a carbon deposit lower that the others micro-sized samples confirming that crystal morphology play an important role in catalysis.

CHAPTER 7

CO_2 hydrogenation to DME: the superiority of FER over the other zeolites

Introduction

In this Chapter, catalytic results of DME synthesis reaction from CO_2-H_2 mixture are presented and discussed. As described in Chapter 4, hybrid catalysts were prepared by by co-precipitation of the metals precursors (Cu, Zn and Zr) over MOR, FER8 and MFI samples. As discussed in Chapter 4, morphology of zeolite crystallites significantly affects the surface distribution of metal-oxides and the nature of active sites created during the co-precipitation step. Catalytic results show that the better performances observed for CZZ-FER catalyst may be related to a better efficiency in mass transferring ensured by the interaction of neighboring sites of different nature on ferrierite after metal-oxide co-precipitation.

7.1 Catalytic behavior of hybrid system: activity and selectivity

In Table 7.1 the catalytic behaviour of the single grain hybrid samples tested as a function of reaction temperature is shown.

SAMPLE	T_R [°C]	X_{CO2} [%]	S_{DME} [%]	S_{MeOH} [%]	S_{CO} [%]	Y_{DME} [%]
CZZ-MOR	200	5.2	78.0	0.7	21.3	4.1
	220	11.2	60.8	4.7	34.5	6.8
	240	17.1	51.0	9.5	39.5	8.8
	260	23.2	50.8	11.2	38.1	11.8
CZZ-FER	200	5.6	79.6	0.2	20.2	4.5
	220	11.7	63.4	3.1	33.5	7.4
	240	20.0	52.4	8.6	39.0	10.5
	260	26.0	55.7	12.8	31.5	14.5
CZZ-MFI	200	4.2	71.0	6.7	22.3	3.0
	220	10.3	51.9	12.1	36.0	5.4
	240	16.9	42.7	11.7	45.6	7.2
	260	21.3	40.5	12.9	46.6	8.6

Table 7.1 – Catalytic testing in direct CO_2-to-DME hydrogenation reaction (P_R, 5 MPa; GHSV, 8800 $NL/kg_{cat}/h$; CO_2:H_2:N_2, 3:9:1)

On the whole, the activity-selectivity pattern looks quite similar. In particular, the conversion of CO_2 tends to increase with the temperature, while the selectivity to DME decreases but not with a linear trend. In fact, at a temperature exceeding 240 °C for all the single grain hybrid samples the selectivity to DME tends to stabilize at a value close to 50-55 %. CZZ-FER appears the most active system, reaching a CO_2 conversion of 26% at 260 °C and maintaining a selectivity to DME close to 56%. It is also important to note that, contrarily to what expected, by increasing the reaction temperature from 240 to 260 °C the selectivity to CO tends to decrease and this phenomenon is much evident on CZZ-FER sample. This result can be explained by considering that, as the reaction proceeds, also the contribution of the methanol synthesis reaction from CO ($CO + 2H_2 \leftrightarrow CH_3OH$) starts to become important. Although only FER better exploits the increasing concentration of methanol in favour of the DME formation. With the aim to better elucidate the different role played by the zeolite on the catalytic behavior, the specific activity was compared with respect to the number of surface sites considered as most active in the CO_2-to-DME hydrogenation reaction.

The results, shown in Fig. 7.1, reveal that the rates of CO_2 conversion and DME formation are both linearly dependent on strong basic and acid sites (R^2>0.98).

Considering a superior availability of strong basic sites, associated to a larger population of strong acid sites in comparison with CZZ-MOR and CZZ-MFI catalysts, these data suggest that FER plays a decisive role in CZZ-FER system to create a higher number of oxygen vacancies (strong Lewis basic sites for CO_2 activation) and also a larger availability of Brønsted acid sites for the MeOH-to-DME dehydration reaction. Therefore, since the three systems can be considered absolutely equivalently in terms of copper surface area (27-31 m^2/g) and particle size (8-9 nm), it is clear that surface strong basic sites, generated from a suitable metal-oxide distribution on zeolite, can have a key role in CO_2 activations. So the rate of CO_2 conversion cannot be exclusively dependent upon H_2 activation on metallic site (Cu^0).

This demonstrates that CO_2 activation is a key factor to take into account in the global reaction context to achieve high DME productivity.

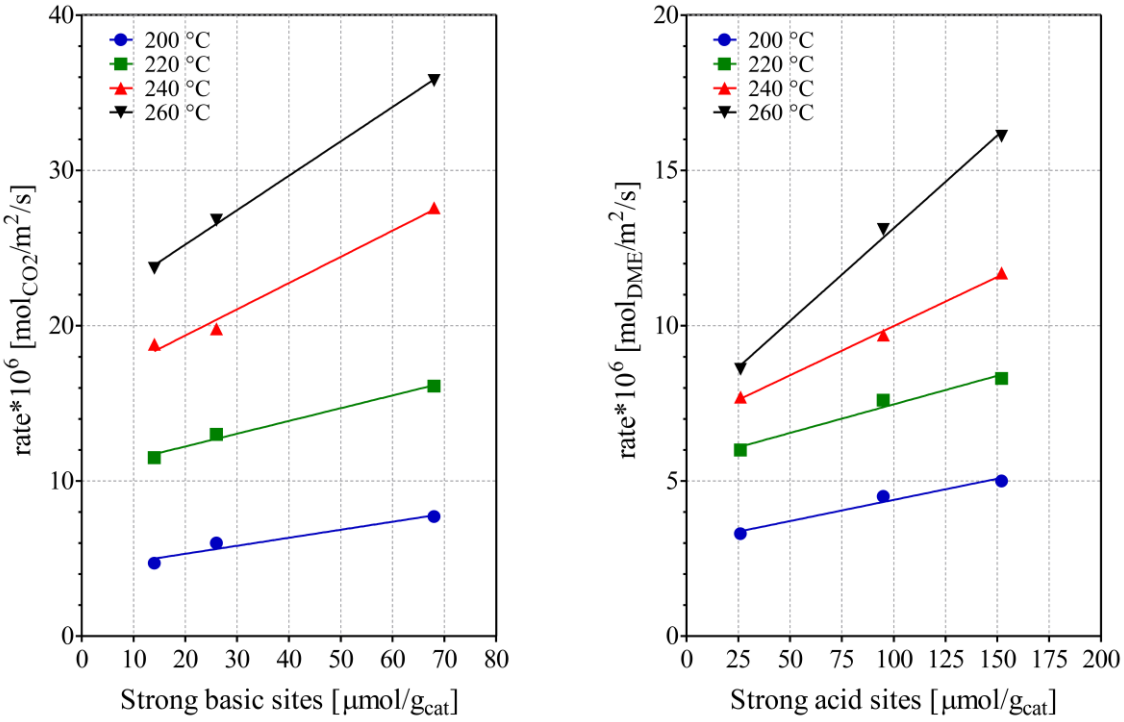

Figure 7.1 – Specific surface rate of CO_2 conversion (left) and DME formation (right): (P_R, 5 MPa; GHSV, 8800 NL/kg_{cat}/h; CO_2:H_2:N_2, 3:9:1)

Indeed, the peculiar structure of ferrierite allows (upon metal-oxide co-precipitation) the formation of oxygen vacancies, acting as active sites available for CO_2 adsorption and stepwise hydrogenation with the dissociative adsorbed atomic hydrogen on metallic copper. MeOH, so formed, is then dehydrated to DME thanks to a larger accessibility of acid sites favoured by a proper porous structure of FER (see APD value in Table 4.18). So, the larger population of weak basic sites on CZZ-MFI (109 μmolCO_2/g_{cat}) could be responsible for the superior selectivity towards CO formation, due to a prevailing number of metal-oxygen pairs generally more active in the reverse water gas shift reaction [259]. Therefore, all these findings clearly demonstrate that the superior catalytic behavior of the hybrid CZZ-FER catalyst is mainly linked to the particulate properties of the ferrierite crystallites with a more uniform and close distribution of the active sites of different nature as showed in Fig. 4.18 (Chapter 4).

Considering that few papers dealing with the direct CO_2-to-DME catalytic hydrogenation on hybrid systems has been published, a comparison in terms of DME_{STY} (STY= Space Time Yield) has been possible and data has collected as shown in Fig. 7.2.

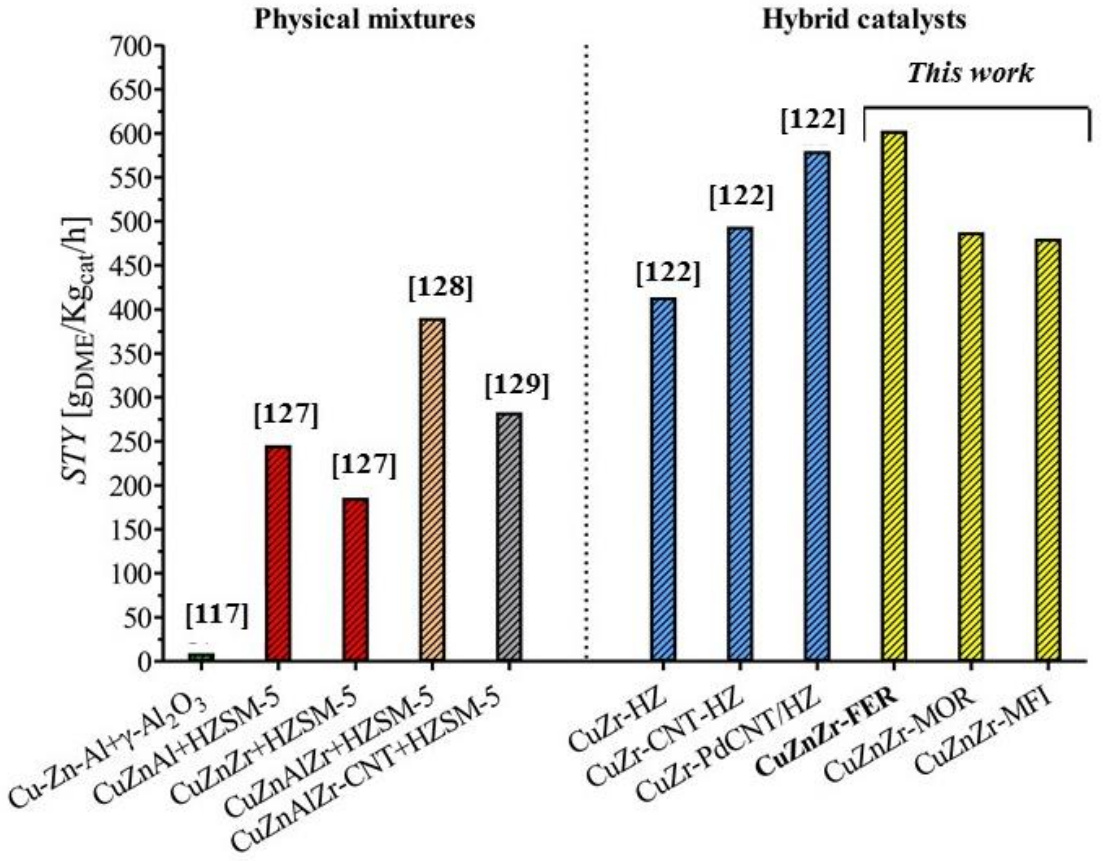

Figure 7.2 – DME productivity over multifunctional systems: physical mixtures vs. hybrid catalysts (P_R, 5 MPa; GHSV, 8800 NL/kg_{cat}/h; T_R=260 °C, CO_2:H_2:N_2, 3:9:1). The numbers into brackets refer to the literasture references.

As it is possible to observeby using a physical mixtures a minor space-time yield DME_{STY} than hybrid catalysts is obtained. In particular, among the physical mixtures investigated, HZSM-5 represents a more effective solid acid catalyst than γ-Al_2O_3; moreover, within the system mixed with HZSM-5, the quaternary CuZnAlZr catalyst works better than ternary CuZnZr or CuZnAl catalysts, reaching a STY close to 400 g_{DME}/Kg_{cat}/h. Regarding the hybrid catalysts, the interaction of metal-oxide and acid sites at level of single grain significantly enhances the global process performance. So, Zhang *et al.* [122] report that, by promoting a slurry mixing of Cu-ZrO2/HZSM-5 with multi-walled carbon nanotubes (CNT) followed by decoration with Pd, it is possible to progressively increase the DME productivity at very high values, thanks to an excellent capability of adsorbing H_2 and CO_2, facilitating the increase of the specific reaction rate of CO_2 hydrogenation. However, in this work, as before reported, by using ferrierite as an acidic carrier

alternative to classical MFI or MOR zeolites, even adopting a very simple and reproducible preparation method (i.e., gel-oxalate co-precipitation), it was possible to develop a novel and very effective single grain hybrid system leading to a final STY as high as 600 $g_{DME}/Kgc_{at}/h$, which represent one of the best data up to now reported. The outstanding result obtained over a hybrid catalyst in respect of a mechanical mixture indirectly demonstrates that, by promoting the mass transfer of methanol from the metal-oxide site to the acid site of the zeolite, the equilibrium of CO_2 hydrogenation reaction is shifted too and higher conversion can be obtained. Really, here is reported a clear example that CO_2 conversion can be promoted by subtracting MeOH at equilibrium reaching so a cumulative DME/MeOH selectivity close to 70 %

7.2 Catalyst deactivation

At last, a stability test on the CZZ-FER sample was performed for a time-on-stream (TOS) of approximately 150 h. As displayed in Figure 7.3, a sensible decrease of activity was recorded during the first 75 hours of experiment, with CO_2 conversion values decreasing from 26 to 18%.

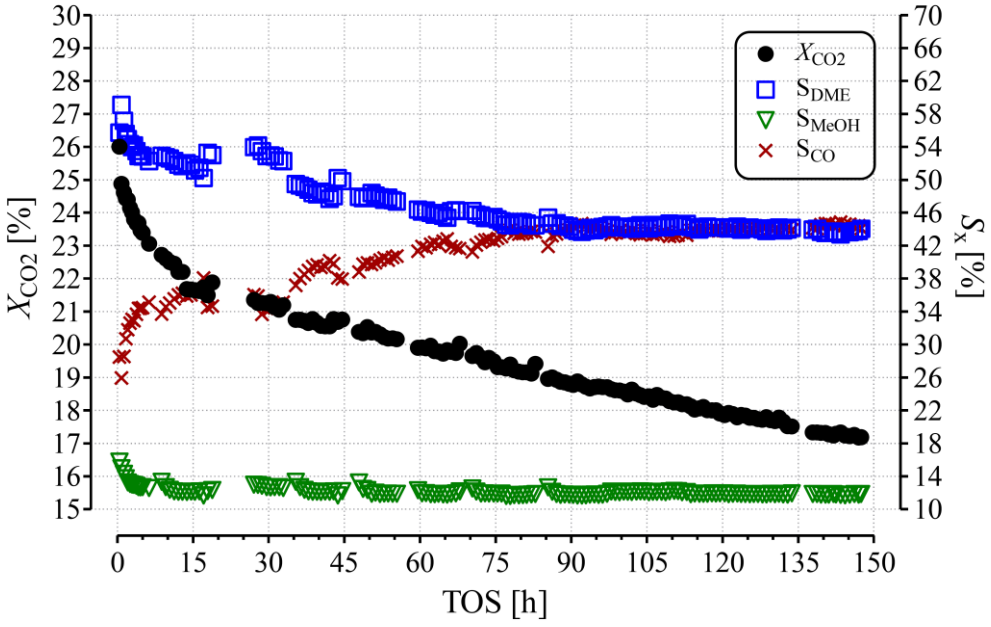

Figure 7.3 – Test of stability over the CZZ-FER sample (P_R, 5 MPa; GHSV, 8800 $NL/kg_{cat}/h$; T_R=260 °C, CO_2:H_2:N_2, 3:9:1)

During this phase, the selectivity to DME also showed a clear decrease (from 60 to 44 %) mirrored by an increase of CO (26 to 44 %), while the MeOH selectivity remained almost

unchanged at a value of ca. 12-13% for all the experiment duration. In the last hours of experiment, a progressive decrease of activity was observed yet, although at a minor extent, resulting in a final value of CO_2 conversion of 17 % after 150 h of TOS. During this period, no change in the selectivity values was recorded. TEM investigation performed at high magnification on the "used" catalyst (see Figure 7.4) evidenced the complete absence either of coke formation or metal sintering, since the copper particles size remain close to 10 nm as observed for the fresh sample (see Table 4.19, Chapter 4).

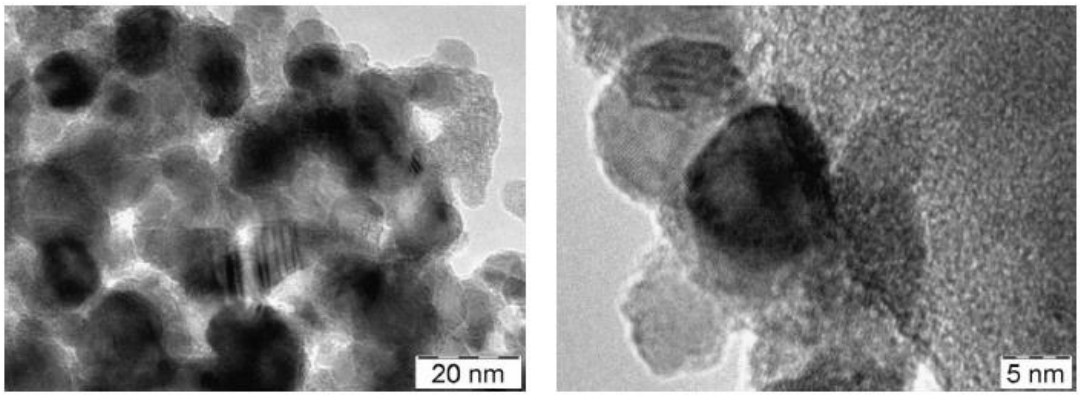

Figure 7.4 – TEM images at different magnification on the "used" CZZ-FER sample after the stability test

By considering that also the distribution of oxides on FER only slightly change after a so long reaction time, the progressive loss of activity may be correlated with the "negative" role exerted by water formed during reaction. Probably, water occupies the oxygen vacancies responsible for CO_2 activation reducing the catalyst activity. However, at moment this is only a hypothesis and new investigations are necessary to verify if, by enhancing the hydrophobic character of catalytic system, more stable catalyst can be designed.

Conclusions

Aim of this work was to perform investigation on methanol dehydration reaction step to produce dimethyl ether by applying zeolites as acid catalysts. In this part, a summary of the previous chapters is reported and commentated.

In **Chapter 1**, the motivations to produce dimethyl ether (DME) were discussed. As largely reported in open literature, DME can be considered as a reliable alternative fuel for Diesel engine as such as a reactant to produce olefins. The main industrial for DME production were reported and advantages and disadvantages were discussed. In indirect route, methanol is synthesised from syngas over copper based redox catalyst and dehydrated to DME over an acid catalyst. γ-Al_2O_3 exhibits high selectivity towards DME but a relative high reaction temperature (300 °C) is requested to obtain high methanol conversion. In direct route, DME is synthesised directly from syngas by using a bi-functional redox/acid. Recently, synthesis of DME by CO_2 hydrogenation is receiving a growing attention from academic research because the possibility to reduce the impact of CO_2 on environmental pollution and valorising it to produce an high value product as methanol/DME (*Methanol economy theory*). In direct route, γ-Al_2O_3 exhibits a low DME yield because its activity is repressed by strong adsorption of water produced during the involved reaction (water gas shift reverse, methanol dehydration). Zeolites, because their well-known higher hydrophobicity than γ-Al_2O_3, represent a reliable catalyst for both direct and indirect route but a careful process optimization is necessary to obtain reliable DME productivities. Although zeolites offer high versatility in terms of both acidity and structure (shape selectivity), they can be easily deactivated by coke deposition due the presence of strong acid sites that promote oligomerization reactions. In this concern, experimental assessment is of paramount importance in order to optimize physicochemical properties of catalyst obtaining high reactant conversion, high product selectivity, low coke deposition and high stability over time.

In **Chapter 2**, the main catalytic properties of zeolites were discussed. Alumino-silicate molecular sieves (zeolites), can be considered as reliable catalyst for acid catalysed reactions, thanks to their high versatility in terms of both acidity (quantity, typology, distribution and strength of acid sites) and channel system that governs the well-known shape-selectivity. Zeolites, mainly ZSM-5, are industrially applied to convert methanol

into gasoline or high value products as olefins. The same products can be formed during DME production causing selectivity drop and catalyst deactivation by coke deposition. A careful evaluation of acidity, channel system and crystal morphology (e.g. size) can permit to optimize the catalytic system to produce DME with high selectivity, high methanol conversion at relative low temperature (below 300 °C) and high resistance to deactivation in both direct and indirect route.

In **Chapter 3**, the investigated materials and the methods adopted to characterize them are presented and discussed. In this work, zeolites with different channels size (small, medium and large) and orientation (1-, 2- and 3-dimensional) were synthesised and their catalytic behaviour was studied during methanol dehydration reaction step. The investigated structure were MOR (mordenite), TON (ZSM-22), EUO (EU-1), MTW (ZSM-12), FER (ZSM-35), MFI (ZSM-5), BEA (Beta) and CHA (SAPO-34). Moreover, FER structures with different acidity and different structure directing agent (ethyneldiammine, pyrrolidine, 1,8-diamminoctane and tetrahydrofurane) were also synthesised. Synthesis procedure assessment permitted to synthesise FER crystals with nanometric size (300-500 nm). All of investigated catalysts were characterized by XRD, SEM, TEM, TG/DTA, chemical analysis by atomic absorption, textural analyses (B.E.T surface area, micropore volume) by nitrogen adsorption isotherm, and acidity analyses by NH_3-TPD (acid sites concentration, distribution and strength) and FT-IR (Brønsted and Lewis acid sites). Methanol dehydration reaction was performed in an atmospheric quartz reactor in the temperature range 160-280 °C by using the above mentioned zeolitic catalysts while CO_2 hydrogenation was carried out under 5.0 MPa pressure and reaction temperature range 200-280 °C by using hybrid catalyst obtained by co-precipitation of redox species (CuZnZr) over zeolite crystals. The deposited coke was analysed by thermogravimetric analysis in order to estimate the deposited quantity and a GC-MS based procedure to evaluate coke composition.

In **Chapter 4**, the main physicochemical properties of investigated materials are discussed. All on synthesised catalysts exhibit high crystallinity and purity with textural and chemical properties according to the open literature. Particular discussion was dedicated to acidic properties. NH_3-TPD showed that acid sites concentration is related to Si/Al ratio on the bulk of catalyst and ammonia desorption profiles consist on two main peak. The peak observed at lower temperature (below 300 °C) is related to both weak acid sites and physically adsorbed ammonia while the peak observed at higher

temperatures (above 300 °C) can be attributed to catalytic active acid sites. For these reasons, the latter was used to evaluated the effect of acidity on catalytic activity (Turnover frequency analysis). For FER samples synthesised with different Si/Al ratio, an estimation of strength of acid sites in terms of ammonia desorption heat was possible, and results suggested that the strength of acid sites was similar independently of the aluminium content. Interesting results were revealed by FT-IR analysis in terms of Brønsted and Lewis acid sites distribution. In particular, aluminium content affects strongly acid sites distribution in FER sample. FER with Si/Al in the range 22-45 exhibits mainly Brønsted acidity (more than 90%) while on FER with lower Si/Al, acidic properties depend on structure directing agent used during the synthesis despite the similar aluminium content. In particular, samples synthesised with ethylendiammine and tetrahydrofurane, exhibits a high Lewis acid sites concentration (ca. 40%), followed by the sample synthesised with pyrrolidine (ca. 34%). On the contrary, by using tetrahydrofurane as organic molecule, a low Lewis acid sites concentration (ca. 15%) was obtained suggesting that synthesis condition affects strongly acid sites distribution.

In **Chapter 5**, a preliminary screening of investigated structure was reported in order to evaluate the channel system configuration leading a high DME selectivity and high resistance deactivation during vapour-phase methanol dehydration reaction. At the reaction temperature of 200 °C all of investigated catalysts offer a selectivity towards DME close to the unity. FER with Si/Al≈8 and MOR catalysts, exhibits a DME productivity close to the theoretical equilibrium value higher than γ-Al_2O_3 that exhibits a very low activity. At the reaction temperature of 200 °C, FER offers a space-time DME productivity of ca. 10 $kg_{DME}/kg_{cat}/h$ whilst a value of ca. 3 $kg_{DME}/kg_{cat}/h$ was observed for γ-Al_2O_3, suggesting that FER represents a reliable catalyst for methanol-to-DME process with reaction temperature lower than the actual one with γ-Al_2O_3 as catalyst (200 °C vs. 300 °C). The effect of zeolite structure on catalyst deactivation and coke formation was also investigated and discussed. 1-dimensional channel systems with large openings (e.g. MOR and MTW) cause a rapid deactivation with a high carbon deposit level. 1-dimensional channel systems with medium openings exhibit a higher resistance to deactivation (TON) but the presence of large side-pockets as in EU-1 sample causes an important deposition of coke causing deactivation. 3-dimensional channel systems can deactivate the catalyst as a function of channel configuration. Despite the narrow channels

openings, CHA framework (SAPO-34) is rapidly deactivated with a high carbon deposit level due the presence of large channel intersection with wide cages. Although BEA structure have large channels, it is only partially deactivated because the side products can easily diffuse along the crystals without causing pore filling. Medium pore MFI structure exhibit a high stability over time. The 2-dimensional small pore channel system of FER zeolite ranks as the best structure in terms of resistance to deactivation and coke formation.

In **Chapter 6**, catalytic performances of FER-type materials with different Si/Al and different Brønsted/Lewis distribution, are discussed. Catalytic tests suggest the presence of Lewis acid sites promote methanol conversion and nano-sized crystals permit to strongly reduce carbon deposit level. On the other hand, large crystals (10-15 μm) deactivated due a high coke deposition level.

Finally, in **Chapter 7**, FER, MOR and MFI zeolites were also tested in CO_2-to-DME catalytic system and results suggest the FER is reliable catalyst for DME production via direct route with a space-time DME productivity of 600 $g_{DME}/kg_{cat}/h$ that is one of the best results up to now published. In particular, hybrid catalyst obtained by co-precipitation of redox species on zeolites exhibit a higher DME productivity than physical mixture. Stability tests show that FER-based hybrid catalyst deactivates over time. CO_2 conversion loss may be associated to copper particle deactivation due strong water adsorption.

The catalytic behaviour of FER zeolite in DME production via both indirect and direct route is quite interesting. More specifically, FER with high Lewis acid sites and high acid sites concentration exhibit a high catalytic activity in terms of methanol conversion and a relatively high DME selectivity with an excellent stability and resistance to deactivation by coke deposition. No experimental tests were performed in order to investigate the effect of water on catalytic activity. Competitive adsorption of water is an important challenge for DME production as discussed in Chapter 1. Experimental tests could be carry out by feeding mixture of methanol/water and investigate the effect of water on catalytic activity, kinetic parameter and carbon deposit. In this sense, the role of acid sites types (Brønsted and Lewis) would be investigated in order to minimize the eventual effect

of water on catalytic activity. Location of acid sites (inside the channels, on the external crystal surface, etc) should be also investigated because its importance in both direct and indirect DME synthesis. In particular, crystal surface properties would be analysed with the aim to study their effect of metal oxides distribution during the synthesis of hybrid catalysts.

Regeneration of exhausted catalyst should be also deeply investigated. Stability of acid sites can be studied by FT-IR and catalytic tests of catalysts after coke burning and catalytic activity as a function of regeneration cycles could give more information for industrial applications. Furthermore, other solutions can be 'scanned' for a further reduction of carbon deposit. Crystals with smaller size or with hierarchical structure can be investigated for a further catalyst optimization. Furthermore, more methods would be investigated for hybrid catalyst preparation in order to improve metal oxides surface homogeneity with the aim to increase CO_2 conversion rate and DME productivity. Because DME is an important intermediate to produce olefins, direct synthesis of olefins from CO_2 can be considered as an important challenge for future industry in according to the novel policies suggested by the recent Conference on Climate Change in Paris (COP21, December 2015). In this sense, catalysts exhibiting high selectivity towards olefins (e.g. SAPO-34, ZSM-5, ZSM-22) could be investigated in CO_2-to-DME by studying the effect of catalyst structure, feed composition, contact time, reaction temperature and pressure on olefins selectivity and productivity. A preliminary study in DME/Methanol-to-olefins process can be useful to elucidate the role of DME on olefins production even if this topic is well documented as discussed in Chapter 1. Finally, both DME and olefins production starting from bio-syngas (e.g. produced from biomass gasification) may be an important and enticing future challenge.

References

[1] BP Energies Outlook, 2016 Ed.

[2] D. A. Wood, C. Nwaoha, B. F. Towler, J. Nat. Gas Sci. Eng. 9 (2012) 196 – 208.

[3] K. Aasberg-Petersen, J. H. Hansen, T. S. Christensen, I. Dybkjaer, P. Seier Christensen, C. Stub Nielsen, S. E. L. Winter Madsen, J. R. Rostrup-Nielsen, Appl. Catal., A 221 (2001) 379 – 387.

[4] P. Lv, Z. Yuan, C. Wu, L. Ma, Y. Chen, N Tsubaki, Energy Convers. Manage. 48 (2007) 1132 – 1139.

[5] A. Molino, M. Migliori, F. Nanna, P. Tarquini, G. Braccio, Fuel 112 (2013) 249 – 253.

[6] A. Molino, M. Migliori, F. Nanna, Fuel 115 (2014) 41 – 45.

[7] T. A. Semelsberg, R. L. Borup, H. L. Greene, J. Power Sources 156 (2006) 497 – 511.

[8] C. Arcoumanis, C. Bae, R. Crookes, E. Kinoshita, Fuel 87 (2008) 1014 – 1030.

[9] T. Ogawa, N. Inoue, T. Shikada, Y. Ohno, J. Natural Gas Chem. 12 (2003) 219 – 227.

[10] C. Cheng, H. Zhang, W. Ying, D. Fang, Korean J. Chem. Eng. 28 (2011) 1511 – 1517.

[11] T. H. Fleisch, A. Basu, R. A. Sills, J. Natural Gas Sci. Eng. 9 (2012) 94 – 107.

[12] US Patent 5, 632, 786, May 27, 1997, A. Basu et al. (Eds.).

[13] S. Parathoner, G. Centi, Chem. Sus. Chem. 7 (2014) 1274 – 1282.

[14] M. De Falco, M. Capocelli, G.Centi, Chem. Eng. J. 294 (2016) 400 – 409.

[15] M. Marchionna, R. Patrini, D. Sanfilippo, G. Migliavacca, Fuel Process. Technol. 89 (2008) 1255 – 1261.

[16] T. A. Semelsberger, R. L. Borup, H. L. Greene, J. Power Sourc. 156 (2006) 497 – 511.

[17] C. Arcoumanis, C. Bae, R. Crooks, E. Kinoshita, Fuel 87 (2008) 1014 – 1030.

[18] S. H. Park, C. S. Lee, Prog. Energ. Combust. 39 (2013) 147 – 168.

[19] S. Sidhu, J. Graham, R. Striebich, Chemosphere 42 (2001) 681 – 690.

[20] M. Y. Kim, S. H. Yoon, B. W. Ryu, C. S. Lee, Fuel 87 (2008) 2779 – 2786.

[21] R. Egnell, SAE tech paper 2001. SAE 2001-01-0651 (2001).

[22] H. Teng, JC McCandless, JB Schneyer. SAE tech paper 2001. SAE 2001-01-0154 (2001).

[23] K. K. Gupta, A. Rehman, R. M. Sarviya, Renew. Sust. Energ. Rev. 14 (2010) 2946 – 2955.

[24] M. C. Lee, S. B. Seo, J. H. Chung, Y. J. Joo, D. H. Ahn, Fuel 87 (2008) 2162 – 2167.

[25] M. C. Lee, S. B. Seo, J. H. Chung, Y. J. Joo, D. H. Ahn, Fuel 88 (2009) 657 – 662.

[26] M. C. Lee, Y. Yoon, Fuel 102 (2012) 823 – 830.

[27] A. Haryanto, S. Fernando, N. Murali, S. Adhikari, Energ. Fuel. 19 (2005) 2098 – 2106.

[28] A. F. Ghenciu, Curr. Opin. Solid. St. M. 6 (2002) 389 – 399.

[29] D. R. Palo, R. A. Dagle, J. D. Holladay

[30] K. Takeishi, H. Suzuki, Appl. Catal. A: Gen. 260 (2004) 111 – 117.

[31] J. Vicente, A. G. Gayubo, J. Ereña, A. T. Aguayo, M. Olazar, J. Bilbao, Appl. Catal. B: Env. 130-131 (2013) 73 – 83.

[32] A. Gazsi, I. Ugrai, F. Solymosy, Appl. Catal. A: Gen. 391 (2011) 360 – 366.

[33] T. A. Semelsberger, K. C. Ott, R. L. Borup, H. L. Greene, Appl. Catal. B: Env. 65 (2006) 291 – 300.

[34] H. Xue, X. Huang, E. Ditzel, E. Zhan, M. Ma, W. Shen, Ind. Eng. Chem. Res. 52 (2013) 11510 – 11515.

[35] A. Sardesai, S. Lee, T. Tartamella, Energ. Source 24 (2002) 301 – 317.

[36] H. Liu, E. Iglesia, J. Catal. 208 (2002) 1 – 5.

[37] H. Liu, P. Cheung, E. Iglesia, J. Catal. 217 (2003) 222 – 232.

[38] https://www.eia.gov/

[39] U. Olsbye, S. Svelle, M. Bjørgen, P. Beato, T.V. Janssens, F. Joensen, S. Bordiga, K.P. Lillerud, Angew. Chem. Int. Ed. 51 (2012) 5810-5831.

[40] S. Yurchak, Stud. Surf. Sci. Catal. 36 (1988) 251 – 272.

[41] P. Tian, Y. Wei, M. Ye, Z. Liu, ACS Catal. 5 (2005) 1922 – 1938.

[42] K. Y. Lee, H. K. Lee, S. K. Ihm, Top. Catal. 53 (2010) 247 – 253.

[43] J. Li, Y. Wei, G. Liu, Y. Qi, P. Tian, B. Li, Y. He, Z. Liu, Catal. Today 171 (2011) 221-228.

[44] N. Tajima, T. Tsuneda, F. Toyama, K. Hirao, J. Am. Chem. Soc. 120 (1998) 8222 – 8229.

[45] S. Teketel, U. Olsbye, K. P. Lillerud, P. Beato, S. Svelle, Appl. Catal. A: Gen. 494 (2015) 68 – 76.

[46] J. Li, Z. Wei, Y. Chen, B. Jing, Y. He, M. Dong, H. Jiao, X. Li, Z. Qin, J. Wang, W. Fan, J. Catal. 317 (2014) 277 – 283.

[47] L. Qi, Y. Wei, L. Xu, Z. Liu, ACS Catal. 5 (2015) 3973 – 3982.

[48] M. Seiler, W. Wang, A. Buchholz, M. Hunger, Catal. Lett. 88 (2003) 187 – 191.

[49] J. Li, Z. Wei, Y. Chen, B. Jing, Y. He, M. Dong, H. Jiao, X. Li, Z. Qin, J. Wang, W. Fan, J. Catal. 317 (2014) 277 – 283.

[50] W. Song, D. M. Marcus, H. Fu, J. O. Ehresmann, J. F. Haw, J. Am. Chem. Soc. 124 (2002) 3844 – 3845.

[51] M. Bjørgen, F. Joensen, K. P. Lillerud, U. Olsbye, S. Svelle, Catal. Today 142 (2009) 90 – 97.

[52] S. Svelle, F. Joensen, J. Nerlov, U. Olsbye, K. P. Lillerud, S. Kolboe, M. Bjørgen, J. Am. Chem. Soc. 105 (2008) 12553 – 12558.

[53] F. Wei, Z. M. Cui, X. Meng, C. Cao, F. Xiao, E. Song, ACS Catal. 4 (2014) 529 – 534.

[54] R. Y. Brogaard, R. Henry, Y. Schuurman, A. J. Medford, P. G. Moses, P. Beato, S. Svelle, J. K. Norskov, U. Olsbye, J. Catal., 314 (2014) 159 – 169.

[55] S. Park, Y. Watanable, Y. Nishita, T. Fukuoka, S. Inagaki, Y. Kubota, J. Catal. 319 (2014) 265 – 273.

[56] Z. Liu, X. Dong, Y. Zhu, A. H. Emwas, D. Zhang, Q. Tian, Y. Han, ACS Catal. 5 (2015) 5837 – 5845.

[57] J. M. Campelo, F. Lafont, J. M. Marinas, M. Ojeda, Appl. Catal. A: Gen. 192 (2000) 85 – 96.

[58] L. Palumbo, F. Bonino, P. Beato, M. Bjørgen, A. Zecchina, S. Bordiga, J. Phys. Chem. C 112 (2008) 9710 – 9716.

[59] Y. T. Chua, P.C. Stair, J. Catal. 213 (2003) 39 – 46.

[60] U. V. Mentzel, K. Hojholt, M. S. Holm, R. Fehrmann, P. Beato, Appl. Catal.s A: Gen. 417 – 418 (2012) 290 – 297.

[61] N. Nushyama, M. Kawaguchi, Y. Hirota, D. Van Vu, Y. Egashira, K. Ueyama, Appl. Catal. A: Gen. 362 (2009) 193 – 199.

[62] M. Higo, K. Dowaki, Appl. Energ. 87 (2010) 58 – 67.

[63] L. R. Clausen, B. Elmergaard, N. Houbak, Energy 35 (2010) 4831 – 4842.

[64] J. R. Rostrup-Nielsen, Cat. Today 18 (1993) 305 – 324.

[65] A. Molino, M. Migliori, D. Macrì, V. Valerio, A. Villone, F. Nanna, P. Iovane, T. Marino, Renew. Energ. 91 (2016) 451 – 455.

[66] G. Maschio, A. Lucchesi, G. Stoppato, Bioresource Technol. 48 (1994) 119 – 126.

[67] P. Lv, Z. Yuan, C. Wu, L. Ma, Y. Chen, N. Tsubaki, Energ. Convers. Manage. 48 (2007) 1132 – 1139.

[68] Z. Azizi, M. Rezaeimanesh, T. Tohidian, M. R. Rahimpour, Chem. Eng. Process. 82 (2014) 150 – 172.

[69] Y. Tavan, S. H. Hosseini, M. Ghavipour, M. R. K. Nikou, A. Shariati, Chem. Eng. Process. (2013), http://dx.doi.org/10.1016/j.cep.2013.06.006.

[70] A. Khaleel, Fuel 90 (2011) 2422 – 2427.

[71] D. Liu, C. Yao, J. Zhang, D. Fan, D. Chen, Fuel 90 (2011) 1738 – 1742.

[72] M. Mollavalli, F. Yaripour, Sh. Mohammadi-Jam, H. Atashi, Fuel Process. Technol. 90 (2009) 1093 – 1098.

[73] J. Xia, D. Mao, B. Zhang, Q. Chen, Y. Zhang, Y. Tang, Catal. Comm. 7 (2006) 362 – 366.

[74] F. Yaripour, Z. Shariatinia, S. Sahebdelfar, A. Irandoukht, Fuel 139 (2015) 40 – 50.

[75] M. Xu, J. H. Lunsford, D. W. Goodman, A. Bhattacharyya, Appl. Catal. A 149 (1997) 289 – 301.

[76] F. Yaripour, F. Baghaei, I. Schmidt, J. Perregaard, Catal. Commun. 6 (2005) 147 – 152.

[77] K. W. Jun, H. S. Lee, H. S. Roh, S. E. Park, Bull. Korean Chem. Soc. 24 (2003) 106 – 108.

[78] J. Tao, K. Jun, K. Lee, Appl. Organomet. Chem. 15 (2001) 105 – 108.

[79] V. Vishwanathan, K. Jun, J. Kim, H. Roh, Appl. Catal. A 276 (2005) 251 – 255.

[80] S. D. Kim, S. C. Baek, Y. Lee, K. Jun, M. J. Kim, I. S. Yoo, Appl. Catal. A 309 (2006) 139 – 143.

[81] S. Hassanpour, F. Yaripour, M. Taghizadeh, Fuel Process. Technol. 91 (2010) 1212 – 1221.

[82] N. Khandan, M. Kazemeini, M. Aghaziarati, Iran. J. Chem. Eng. 6 (2009) 3 – 1.

[83] S. Hassanpour, M. Taghizadeh, F. Yaripour, Ind. Eng. Chem. Res. 49 (2010) 4063 – 4069.

[84] M. Migliori, A. Aloise, G. Giordano, Catal. Today 227 (2014) 138 – 143.

[85] G. Bonura, C. Cannilla, L. Frusteri, A. Mezzapica, F. Frusteri, Catal. Today (2016) DOI: 10.1016/j.cattod.2016.05.057

[86] N. Khandan, M. Kazemeini, M. Aghaziarati, Appl. Catal. A 349 (2008) 6 – 12.

[87] Q. Tang, H. Xu, Y. Zheng, J. Wang, H. Li, J. Zhang, Appl. Catal. A 413 – 414 (2012) 36 – 42.

[88] M. Rutkowska, D. Macina, Z. Piwowarska, M. Gajewska, U. Diaz, L. Chmielarz, Catal. Sci. Technol., (2016), DOI: 10.1039/C6CY00040A.

[89] J. Bandiera, C. Naccache, Appl. Catal. 69 (1991) 139 – 148.

[90] L. Kubelková, J. Nováková, K. Nedomová, J. Catal. 124 (1990) 441 – 450.

[91] A. K. Kiss, D. J. P. C. Suszwalak, Comput. Chem. Eng. 38 (2012) 74 – 81.

[92] T. Ogawa, N. Inoue, T. Shikada, Y. Ohno, J. Nat. Gas. Chem. 12 (2003) 219 – 227.

[93] K. C. Waugh, Catal. Today 15 (1992) 51 – 75.

[94] T. Fujitani, J. Nakamura, Catal. Lett. 56 (1998) 119 – 124.

[95] H. Y. Chen, S. P. Lau, L. Chen, J. Lin, C. H. A. Huan, K. L. Tan, J. S. Pan, Appl. Surf. Sci. 152 (1999) 193 – 199.

[96] M. Kurtz, H. Wilmer, T. Genger, O. Hinrichsen, M. Muhler, Catal. Lett. 86 (2003) 77 – 80.

[97] J. T. Sun, I. S. Metcalfe, M. Sahibzada, Ind. Eng. Chem. Res. 38 (1998) 3868 – 3872.

[98] M. V. Twing, M. S. Spencer, Appl. Catal. A: Gen. 212 (2001) 161 – 174.

[99] F. S. Ramos, A. M. Duarte de Farias, L. E. P. Borges, J. L. Monteiro, M. A. Fraga, E. F. Sousa-Aguiar, L. G. Appel, Catal. Today 101 (2005) 39 – 44.

[100] P. S. S. Prasad, J. W. Bae, S. Kang, Y. Lee, K. Jun, Fuel Process. Technol. 89 (2008) 1281 – 1286

[101] G. R. Moradi, S. Nosrati, F. Yaripor, Catal. Comm. 8 (2007) 598 – 606.

[102] J. Li, X. Zhang, T. Inui, Appl. Catal. A: Gen. 147 (1996) 23 – 33.

[103] J. W. Bae, S. Kang, Y. Lee, K. Jun, J. Ind. Eng. Chem. 15 (2009) 566 – 572.

[104] S. Baek S. Kang, J. W. Bae, Y. Lee, D. Lee, K. Lee, Energ. Fuel 25 (2011) 2438 – 2443.

[105] X. Zhang, L. Zhong, Q. Guo, H. Fan, H. Zheng, K. Xie, Fuel 89 (2010) 1348 – 1352.

[106] A. García-Trenco, A. Vidal-Moya, A. Martínez, Catal. Today 179 (2012) 43 – 51.

[107] M. Cai, A. Palcic, V. Subramanian, S. Moldovan, O. Ersen, V. Valtchev, V. V. Ordomsky, A. Y. Khodakov, J. Catal. 338 (2016) 227 – 238.

[108] V. V. Ordomsky, M. Cai, V. Sushkevich, S. Moldovan, O. Ersen, C. Lancelot, V. Valtchev, A. Y. Khodako, Appl. Catal. A: Gen. 486 (2014) 266 – 275.

[109] L. Wang, D. Fang, X. Huang, S. Zhang, Y. Qi, Z. Liu, J. Nat. Gas. Chem. 15 (2006) 38 – 44.

[110] F. Hayer, H. Bakhtiary-Davijany, R. Myrstad, A. Holmen, P. Pfeifer, H. J. Venvik, Chem. Eng. J. 167 (2011) 610 – 615.

[111] J. Ereña, R. Garoña, J. M. Arandes, A. T. Aguayo, J. Bilbao, Int. J. Chem. React. Eng. 3 (2005).

[112] Y. Han, H. Zhang, W. Ying, D. Fang, Chin. J. Chem. Eng. 17 (2009) 108 – 112.

[113] D. Mao, W. Yang, J. Xia, B. Zhang, Q. Song, Q. Chen, J. Catal. 230 (2005) 140 – 149.

[114] G. A. Olah, Angew. Chem. Int. Ed. 52 (2013) 104 – 107.

[115] G. Centi, S. Perathoner, Chem. Sus. Chem. 22 (2010) 195 – 208.

[116] G. Bonura, M. Cordaro, C. Cannilla, A. Mazzepica, L. Spadaro, F. Arena, F. Frusteri, Catal. Today 228 (2014) 51 – 57.

[117] X. An, Y. Z. Zuo, Q. Zhang, D. Z. Wang, J. F. Wang, Ind. Eng. Chem. Res. 47 (2008) 6547 – 6554.

[118] S. Wang, D. Mao, X. Guo, X. Wu, G. Lu, Catal. Commun. 10 (2009) 1367 – 1370.

[119] J. Ereña, R. Garoña, J.M. Arandes, A.T. Aguayo, J. Bilbao, Catal. Today 107-108 (2005) 467 – 473.

[120] J.H. Kim, M.J. Park, S.J. Kim, O.S. Joo, K.D. Jung, Appl. Catal. A 264 (2004) 37 – 41.

[121] R. Nie, H. Lei, S. Pan, L. Wang, J. Fei, Z. Hou, Fuel 96 (2012) 419-425.

[122] M.-H. Zhang, Z.-M. Liu, G.-D. Lin, H.-B. Zhang, Appl. Catal. A: Gen. 451 (2013) 28 – 35.

[123] R. Khoshbin, M. Haghighi, Chem. Eng. Res. Des. 91 (2013) 1111 – 1122.

[124] D. Mao, W. Yang, J. Xia, B. Zhang, G. Lu, J. Mol. Catal. A 250 (2006) 138 – 144.

[125] A. García-Trenco, A. Martínez, Appl. Catal. A: Gen. 411– 412 (2012) 170 – 179.

[126] J. Abu-Dahrieh, D. Rooney, A. Goguet, Y. Saih, Chem. Eng. J. 203 (2012) 201 – 211.

[127] S.P. Naik, H. Du, H. Wan, V. Bui, J.D. Miller, W.W. Zmierczak, Ind. Eng. Chem.Res. 47 (2008) 9791 – 9794.

[128] G. Bonura, M. Cordaro, L. Spadaro, C. Cannilla, F. Arena, F. Frusteri, Appl. Catal. B: Environ. 140 – 141 (2013) 16 – 24.

[129] Q. Zhang, Y.-Z. Zuo, M.-H. Han, J.-F.Wang, Y. Jin, F. Wei, Cata. Today 150 (2010) 55 – 60.

[130] F. Frusteri, M. Cordaro, C. Cannilla, G. Bonura, Appl. Catal. B: Environ. 162 (2015) 57 – 65.

[131] D. Wang, Y. Han, Y. Tan, N. Tsubaki, Fuel Process. Technol. 90 (2009) 446 – 451.

[132] N. Diban, A.M. Urtiaga, I. Ortiz, J. Ereña, J. Bilbao, A.T. Aguayo, Chem. Eng. J. 234 (2013) 140 – 148.

[133] I. Iliuta, F. Larachi, P. Fongarland, Ind. Eng. Chem. Res. 49 (2010) 6870-6877.

[134] J.F. Haw, W. Song, D.M. Marcus, J.B. Nicholas, Acc. Chem. Res. 36 (2003) 317 – 326.

[135] I. Stich, J.D. Gale, K. Terakura, M.C. Payne, J. Am. Chem. Soc. 121 (1999) 3292 – 3302.

[136] S. Ivanova, C. Lebrun, E. Vanhaecke, C. Pham-Huu, B. Louis, J. Catal. 265 (2009) 1 – 7.

[137] R. Montesano, A. Narvaez, D. Chadwick, Appl. Catal. A: Gen. 482 (2014) 69–77.

[138] Y. Zhao, J. Chen, J. Zhang, J. Nat. Gas. Chem. 16 (2007) 389 – 392.

[139] Y. Park, S.Baek, S. Ihm, Fuel Chem. Div. Prep. 47 (2002) 293 – 294.

[140] Y. Zhang, D. Li, Y. Zhang, Y. Cao, S. Zhang, K. Wang, F. Ding, J. Wu, Catal. Comm. 55 (2014) 49 – 52.

[141] W. Gao, H. Wang, Y. Wang, W. Guo, M. Jia, J. Rare Earths 31 (2013) 470 – 476.

[142] G. X. Qi, J. H. Fei, X. M. Zheng, Z. Y. Hou, Catal. Lett. 72 (2001) 121 – 124.

[143] K. Sun, W. Lu, M. Wang, X. Xu, Catal. Comm. 5 (2004) 367 – 370.

[144] F. Zha, H. Tian, J. Yan, Y. Chang, Appl. Surf. Sci. 285 (2013) 945 – 951.

[145] S. P. Naik, T. Ryu, V. Bui, J. D. Miller, N. B. Drinnan, W. Zmierczak, Chem. Eng. J. 167 (2011) 362 – 368.

[146] F. Zha, J. Ding, Y. Chang, J. Ding, J. Wang, J. Ma, Ind. Eng. Chem. Res. 51 (2012) 345 – 352.

[147] R. Liu, Z. Qin, H. Ji, T. Su, Ind. Eng. Chem. Res. 52 (2013) 16648 - 16655

[148] R. Aiello, J. B.Nagy, G. Giordano, A. Katovic, F. Testa, C. R. Chimie 8 (2005) 321 – 329.

[149] J. B.Nagy, P. Bodart, I. Hannus, I. Kiricsi, Synthesis, characterization and use of zeolitic microporous material, DecaGEN ed., 1998, ISBN 9630497506.

[150] B. M. Lok, T. R. Cannan, C. A. Messina, Zeolites 3 (1983) 282 – 291.

[151] C. Colella, Miner. Deposita 31 (1996) 554 – 562.

[152] M. Pansini, C. Colella, M. De Gennaro, Desalination 83 (1991) 145 – 157.

[153] A. G. Pelmenschikov, E. A. Paukshtis, M. O. Edisherashvili, G. M. Zhidomirov, J. Phys. Chem. 96 (1992) 7051 – 7055.

[154] E. M. Flanigen, Pure Appl. Chem. 52 (1980) 2191 – 2211.

[155] M. Boveri, C. Márquez-Álvarez, M. A. Laborde, E. Sastre, Catal. Today 114 (2006) 217 – 225

[156] L. Tosheva, V. Valtchev, Chem. Mater. 17 (2005) 2494 – 2513.

[157] S. Mintova, V. Valtchev, Microp. Mesop. Mater. 55 (2002) 171 – 179.

[158] K. E. Hamilton, E. N. Coker, A. Sacco, A. G. Dixon, R. W. Thompson, Zeolites 13 (1993) 645 – 653.

[159] F. Testa, L. Pasqua, F. Crea, R. Aiello, K. Lázár, P. Fejes P. Lentz, J. B.Nagy, Microp. Mesop. Mater. 57 (2003) 57 – 72.

[160] Z. Gabelica, N. Blom, E. G. Derouane, Appl. Catal. 5 (1983) 227 – 248.

[161] B. M. Lok, T. R. Cannan, C. A. Messina, Zeolites 3 (1983) 282 – 291.

[162] Y. Cheng, L. Wang, J. Li, Y. Yang, X. Sun, Mater. Lett. 59 (2005) 3427 – 3430.

[163] A. B. Pinar, C. Márquez-Álvarez, M. Grande-Casas, J. Pérez-Pariente, J. Catal. 263 (2009) 258 – 265.

[164] V. Valtchev, L. Tosheva, Chem. Rev. 113 (2013) 6734 – 6760.

[165] A. Madani, A. Aznar, J. Sanz, J. M. Serratosa, J. Phys. Chem. 94 (1990) 760 – 765.

[166] Ullmann's Encyclopedia of Industrial Chemistry, 6th edition, Vol. 39, ISBN 3-527-30385-5.

[167] A. Vimont, F. Thibault-Starzyk, M. Daturi, Chem. Soc. Rev. 39 (2010) 4928 – 4950.

[168] T. C. Tsai, S. B. Liu, I. Wang, Appl. Catal. A: Gen. 181 (1999) 355 – 398.

[169] J. Xiao, J. Wei, Chem. Eng. Sci. 47 (1992) 1123 – 1141.

[170] W. W. Kaeding, C. Chu, L. B. Young, B. Weinstein, S. A. Butter, J. Catal. 67 (1981) 159 – 174.

[171] F. Di Renzo, Catal. Today 41 (1998) 37 – 40.

[172] D. Chen, K. Moljord, T. Fuglerud, A. Holmen, Microp. Mesop. Mater. 29 (1999) 191 – 203.

[173] S. Mintova, J. P. Gilson, V.Valthcev, Nanoscale 5 (2013) 6693 – 6703.

[174] H. Awala, J. P. Gilson, R. Retoux, P. Boullay, J. M. Goupil, V. Valtchev, S. Mintova, Natur. Mater. 14 (2015) 447 – 451.

[175] T. Wakihara, R. Ichikawa, J. Tatami, A. Endo, K. Yoshida, Y. Sasaki, K. Komeya, T. Meguro, Cryst. Growth Des. 11 (2011) 955 – 958.

[176] M. Hartmann, Angew. Chem. Int. Ed. 43 (2004) 5880 – 5882.

[177] J. Pérez-Ramírez, C. H. Christensen, K. Egablad, C. H. Christensen, J. C. Groen, Chem. Soc. Rev. 37 (2008) 2530 – 2542.

[178] N. Nashiyama, M. Kawaguchi, Y. Hirota, D. V. Vu, Y. Egashira, K. Ueyama, Appl. Catal. A: Gen. 362 (2009) 193 – 199.

[179] D. Chen, K. Moljord, A. Holmen, Microp. Mesop. Mater. 164 (2012) 239 – 250.

[180] J. Kim, M. Choi, R. Ryoo, J. Catal. 269 (2010) 219 – 228.

[181] F. L. Bleken, K. Barbera, F. Bonino, U. Olsbye, K. P. Lillerud, S. Bordiga, P. Beato, T. V. W. Janssens, S. Svelle, J. Catal. 307 (2013) 62 – 73.

[182] R. Ch. Deka, R. K. Roy, K. Hirao, Chem. Phys. Lett. 332 (2000) 576 – 582.

[183] M. Elanany, M. Koyama, M. Kubo, E. Broclawik, A. Miyamoto, Appl. Surf. Sci. 246 (2005) 96 – 101.

[184] T. Armaroli, L. J. Simon, M. Digne, T. Montanari, M. Bevilacqua, V. Valtchev, J. Patarin, G. Busca. Appl. Catal. A: Gen. 306 (2006) 78 – 84.

[185] B. Bonelli, L. Forni, A. Aloise, J. B.Nagy, G. Fornasari, E. Garrone, A. Gedeon, G. Giordano, F. Trifirò, Microp. Mes. Mater. 101 (2007) 153 – 160.

[186] T. W. Cynthia, Ch. D. Chang, Cl. D. Chang, J. Phys. Chem. 89 (1985) 1569 – 1571.

[187] D. Barthomeuf, Mater. Chem. Phys. 17 (1987) 49 – 71.

[188] S. Li, A. Zheng, Y. Su, H. Zhang, L. Chen, J. Yang, C. Ye, F. Deng, J. Am. Chem. Soc. 129 (2007) 11161 – 11171.

[189] R. Carvajal, P. Chu, J. H. Lunsford, J. Catal. 125 (1990) 123 – 131.

[190] G. L. Woolery, G. H. Kuehl, H. C. Timken, A. W. Chester, J. C. Vartuli, Zeolites 19 (1997) 288 – 296.

[191] J. W. Ward, J. Catal. 9 (1967) 225 – 236.

[192] J. C. Jansen, E. J. Creyghton, S. L. Njo, H. van Koningsveld, H. van Bekkum, Catal. Today 38 (1997) 205 – 212.

[193] B. Witchterlová, N. Žilkova, E. Uvarova, J. Čejka, P. Sarv, C. Paganini, J. A. Lercher, Appl. Catal. A: Gen. 182 (1999) 297 – 308.

[194] M. Sawa, M. Niwa, Y. Murakami, Zeolites 10 (1990) 307 – 309.

[195] B. Wichterlová, Z. Tvarůžková, Z. Sobalík, P. Sarv, Microp. Mesop. Mater. 24 (1998) 223 – 233.

[196] W. Zhang, P. G. Smirniotis, M. Gangoda, R. N. Bose, J. Phys. Chem. B 104 (2000) 4122 – 4129.

[197] F. Jin, Y. Li, Catal. Today 145 (2009) 101 – 107.

[198] S. Bordiga, E. E. Platero, C. O. Areá, C. Lamberti, A. Zecchina, J. Catal. 137 (1992) 179 – 185.

[199] I. Kiricsi, C. Flego, G. Pazzuconi, W. O. Jr. Parker, R. Millini, C. Perego, G. Bellussi, J. Phys. Chem. 98 (1994) 4627 – 4634.

[200] D. Freude, M. Hunger, H. Pfeifer, Chem. Phys. Lett. 128 (1986) 62 – 66.

[201] A. Corma, C. Corell, V. Fornés, W. Kilodziejski, J. Pérez-Pariente, Zeolites 15 (1995) 576 – 582.

[202] G. Engelhardt, M. Hunger, H. Koller, J. Weitkamp, Stud. Surf. Sci. Catal. 84 (1994) 421 – 428.

[203] D. Barthomeuf, Catal. Rev: Sci. Eng. 38 (1996) 521 – 612.

[204] P. E. Hathaway, M. E. Davis, J. Catal. 116 (1989) 263 – 278.

[205] P. Forzatti, L. Lietti, Catal. Today 52 (1999) 165 – 181.

[206] M. Guisnet, P. Magnoux, Appl. Catal. A: Gen. 212 (2001) 83 – 96.

[207] M. Guisnet, P. Magnoux, F. R. Ribeiro, J. Mol. Catal. A: Chem. 305 (2009) 69 – 83.

[208] D. Chen, H. P. Rebo, K. Moljord, A. Holmen, Ind. Eng. Chem. Res. 46 (2007) 4116 – 4123.

[209] W. G. Song, H. Fu, J. F. Haw, J. Am. Chem. Soc. 123 (2001) 4749 – 4754.

[210] M. A. Djieugoue, A. M. Prakash, L. Kevan, J. Phys. Chem. B 104 (2000) 6452 – 6461.

[211] M. Bjørgen, S. Svelle, F. Joensen, J. Nerlov, S. Kolboe, F.Bonino, L. Palumbo, S. Bordiga, U. Olsbye, J. Catal. 248 (2007) 195 – 207.

[212] H. Schulz, Catal. Today, 154 (2010) 183 – 194.

[213] F. Bleken, M. Bjørgen, L. Palumbo, S. Bordiga, S. Svelle, K. P. Lillerud, U. Olsbye, Top. Catal. 52 (2009) 52, 218 – 228.

[214] M. Bjørgen, S. Alkyalcin, U. Olsbye, S. Benard, S. Kolboe, S. Svelle, J. Catal. 275 (2010) 170 – 180.

[215] X. Chen, T. Todorova, A. Vimont, V. Ruaux, Z. Qin, J. –P- Gilson, V. Valtchev, Microp. Mesop. Mater. 200 (2014) 334 – 342.

[216] G. Guo, Y. Sun, Y. Long, Chem. Commun. 19 (2000) 1893 – 1894.

[217] R. B. Khomane, B. D. Kulkami, R. K. Ahedi, J. Coll. Inter. Sc. 236 (2001) 208 – 213.

[218] Y. Kamimura, C. Kowenje, K. Yamanaka, K. Itabashi, A. Endo, T. Okubo, Microp. Mesop. Mater. 181 (2013) 154 – 159.

[219] G. Liu, P. Tian, J. Li, D. Zhang, F. Zhou, Z. Liu, Microp. Mesop. Mater. 111 (2008) 143 – 149.

[220] G. Giordano. J. B.Nagy, E. G. Derouane, J. Mol. Catal. A: Chem.305 (2009) 34 – 39.

[221] C. G. Pope, J. Chem. Educ. 74 (1997) 129 – 131.

[222] G. Leofanti, M. Padovan, G. Tozzola, B. Venturelli, Catal. Today 41 (1998) 207 – 219.

[223] N. Katada, H. Igi, J. Kim, M. Niwa, J. Phys. Chem. B 101 (1997) 5969 – 5977.

[224] M. Niwa, M. Iwamoto, K. I. Segawa, Bull. Chem. Soc. Jap. 59 (1986) 3735 – 3739.

[225] M. Niwa, N. Katada, Chem. Record 13 (2013) 432 – 455.

[226] R. J. Cvetanović & Y. Amenomiya, Catal. Rev. Sci. Eng. 6 (1972) 21 – 48.

[227] M. Migliori, A. Aloise, E. Catizzone, G. Giordano, Ind. Chem. Eng. Res. 53 (2014) 14885 – 14891.

[228] S. Jong., A. Pradhan, J. Wu, T. Tsai, S. Liu, J. Catal. 174 (1998) 210-218.

[229] E. W. Valyocsik, US Patent 4 902 406

[230] M. Ali, B. Brisdon, W.J. Thomas, Appl. Catal. A: Gen. 252 (2003) 149-162.

[231] F. Frusteri, G. Bonura, C. Cannilla, G. Drago Ferrante, A. Aloise, E. Catizzone, M. Migliori, G. Giordano, Appl. Catal. B. 176 (2015) 522 – 531.

[232] D. Vuono, L. Pasqua, F. Testa, R. Aiello, A. Fonseca, T.I. Korányi, J. B.Nagy, Micropor. Mesopor. Mat. 97 (2006) 78 – 87.

[233] N.R. Forbes, L.V.C. Rees, Zeolites 15 (1995) 444-451.

[234] N.R. Forbes, L.V.C. Rees, Zeolites 15 (1995) 452-459.

[235] L.D. Rollmann, J.L. Schlenker, S.L. Lawton, C.L. Kennedy, G.J. Kennedy, D.J. Doren, J. Phys. Chem. B 103 (1999) 7175-7183.

[236] B. Qian, G. Guo, X. Wang, Y. Zeng, Y. Sun, Y. Long, Phys. Chem. Chem. Phys. 3 (2001) 4164-4169.

[237] B. Lu, T. Tsuda, Y. Oumi, K. Itabashi, T. Sano, Microp. Mesop. Mater. 76 (2004) 1-7.

[238] G.J. Kim, W.S. Ahn, Zeolites 11 (1991) 745 – 750.

[239] http://www.iza-online.org/synthesis/Recipes/ZSM-12.html

[240] N. Katada, K. Suzuki, T. Noda, T. Sastre, M. Niwa, J. Phys. Chem. C 113 (2009) 19208–19217.

[241] F. Lónyi, J. Valyon, Microporous Mater. 47 (2001) 293–301.

[242] A. Auroux, Top. Catal. 4 (1997) 71–89.

[243] L. Forni, F.P. Vatti, E. Ortoleva, Microporous Mater. 3 (1995) 367–375.

[244] R.W. Weber, J.C.Q. Fletcher, K.P. Moller, C.T. O'Connor, Microporous Mater. 7 (1996) 15–25.

[245] G. Bagnasco, J. Catal. 159 (1996) 249–252.

[246] N. Katada, M. Niwa, Catal. Surv. Asia 8 (2004) 161 – 170.

[247] D.J. Parrillo, C. Lee, R.J. Gorte, Appl. Catal. A 110 (1994) 67–74.

[248] C.V. Hidalgo, H. Itoh, T. Hattori, M. Niwa, Y. Murakami, J. Catal. 85 (1984) 362-369.

[249] C. Costa, I.P. Dzikh, J.M. Lopes, F. Lemos, F.R. Ribeiro, J. Mol. Catal. A: Chem. 154 (2000) 193-201.

[250] Y.P. Khitev, Y.G. Kolyagin, I.I. Ivanova, O.A. Ponomareva, F. Thibault-Starzyk, J.-P. Gilson, C. Fernadez, F. Fajula, Microp. Mesop. Mater. 146 (2011) 201-207.

[251] J. Datka, M. Kawalek, K. Góra-Marek, Appl. Catal. A: Gen. 243 (2003) 293-299.

[252] P. Cañozares, A. Carrero, P. Sánchez, Appl. Catal. A: Gen. 190 (2000) 93-105

[253] D.P.B. Peixoto, S.M. Cabral de Menezes, M.I. Pais da Silva, Mater. Lett. 57 (2003) 3933-3942.

[254] R. Rachwalik, Z. Olejniczak, J. Jiao, J. Huang, M. Hunger, B. Sulikowski, J. Catal. 252 (2007) 161-170.

[255] A. Bonilla, D. Baudouin, J. Pérez-Remírez, J. Catal. 265 (2009) 170-180.

[256] C.P. Grey, A.J. Vega, J. Am. Chem. Soc. 117 (1995) 8232-8242.

[257] D. Verboekend, K.C. Groen, J. Pérez-Remírez, Adv. Funct. Mater. 20 (2010) 1441-1450.

[258] F. Deng, Y. Yue, C. Ye, Solid State Nucl. Magn. Reson. 10 (1998) 151-160.

[259] P. Gao, F. Li, N. Zhao, F. Xiao, W. Wei, L. Zhong, Y. Sun, Appl. Catal. A: Gen. 468 (2013) 442-452.

[260] M. Boudart, Chem. Rev. 95 (1995) 661-666.

[261] C. Wang, B. Li, Y. Wang, Z. Xe, J. Energy Chem. 22 (2013) 914-918.

[262] P. Dejaifve, A. Auroux, P.C. Gravelle, J.C. Védrine, Z. Gabelica, E.G. Derouane, J. Catal. 70 (1981) 123-136.

[263] A. T. Aguayo, A.E. Sánchez del Campo, A. G. Gayubo, A. Tarrío, J. Bilabo, J. Chem. Technol. Biotechnol 74 (1999) 315-321.

[264] Q. Wang, Z.-M. Cui, C.-Y. Cao, W.-G. Song, J. Phys. Chem. C 115 (2011) 24987-24992.

[265] S. Teketel, W. Skistad, S. Benard, U. Olsbye, K.P. Lillerud, P. Beato, S. Svelle, ACS Catal. 2 (2012) 26-37.

[266] M. Guisnet, P. Magnoux, Appl. Catal A: Gen. 54 (1989) 1-27.

[267] Y. Gao, B. Zheng, G. Wu, F. Ma, C. Liu, RSC Adv. 6 (2016) 83581-83588.

[268] J. Chen, J. Li, Y. Wei, C. Yuan, B. Li, S. Xu, Y. Zhou, J. Wang, M. Zhang, Z. Liu, Catal. Commun. 46 (2014) 36-40.

[269] J. Jae, G.A. Tompsett, A.J. Foster, K.D. Hammond, S.M. Auerbach, R.F. Lobo, G.W. Huber, J. Catal. 279 (2011) 257–268.

[270] J.W. Park, S.J. Kim, M. Seo, S.Y. Kim, Y. Sugi, G. Seo, Appl. Catal. A: Gen. 349 (2008) 76 – 85.

[271] G. Yang, Y. Wei, S. Xu, J. Chen, J. Li, Z. Liu, J. Yu, R. Xu, J. Phys. Chem. C 117 (2013) 8214-8222.

APPENDIX A

XRD pattern of the investigated catalysts

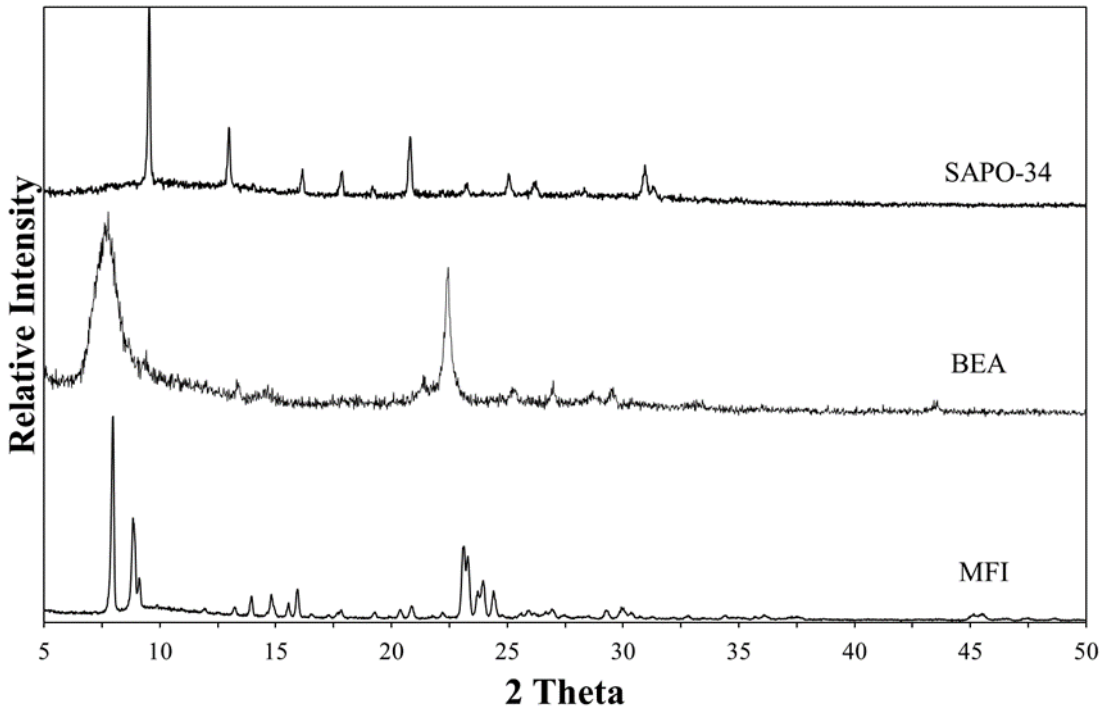

Figure A1 – XRD pattern of 3-dimensional molecular sieves

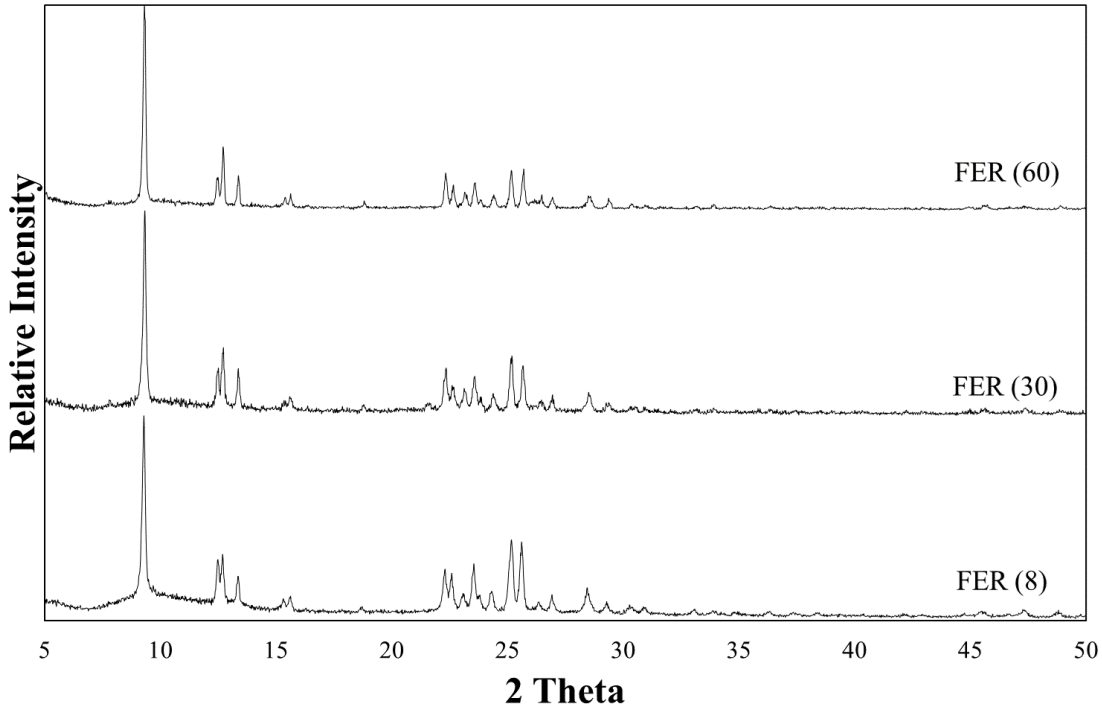

Figure A2 – XRD pattern of FER samples synthesised with different Si/Al ration (the relative Si/Al value is indicated in branckets)

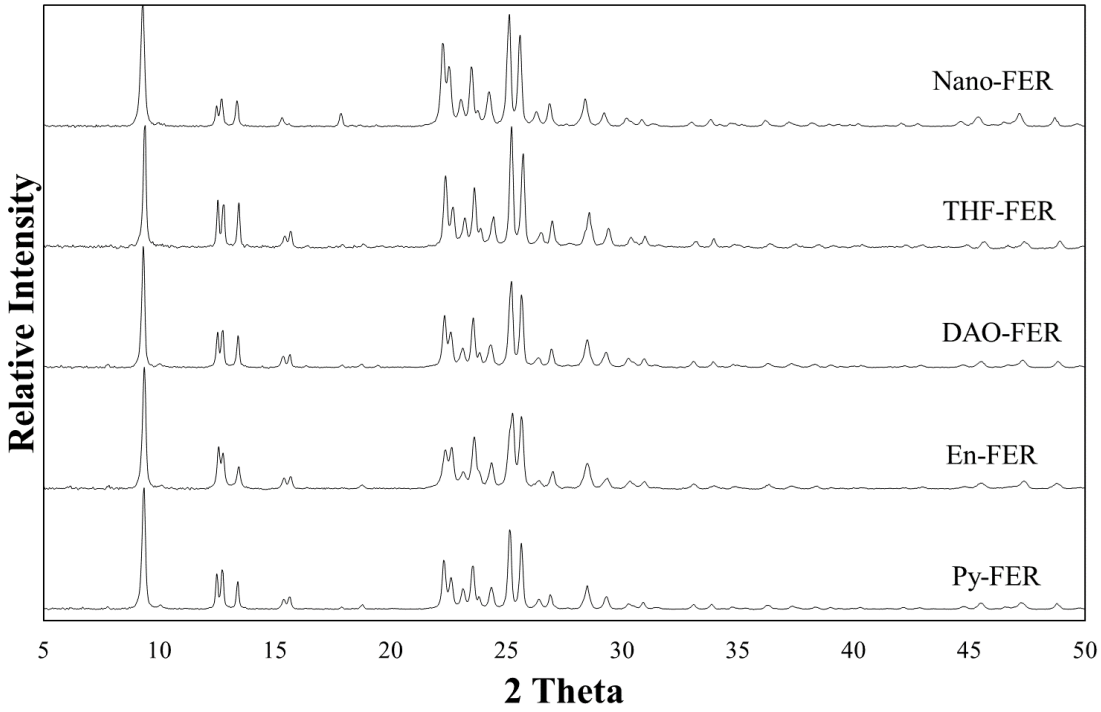

Figure A3 – XRD pattern of FER samples synthesised with different SDA (Py=pyrrolidne, En=ethylendiammine, DAO=1,8-diamminooctane, THF=tetrahydrofurane) and nanosized ferrierite crystals (nano-FER)

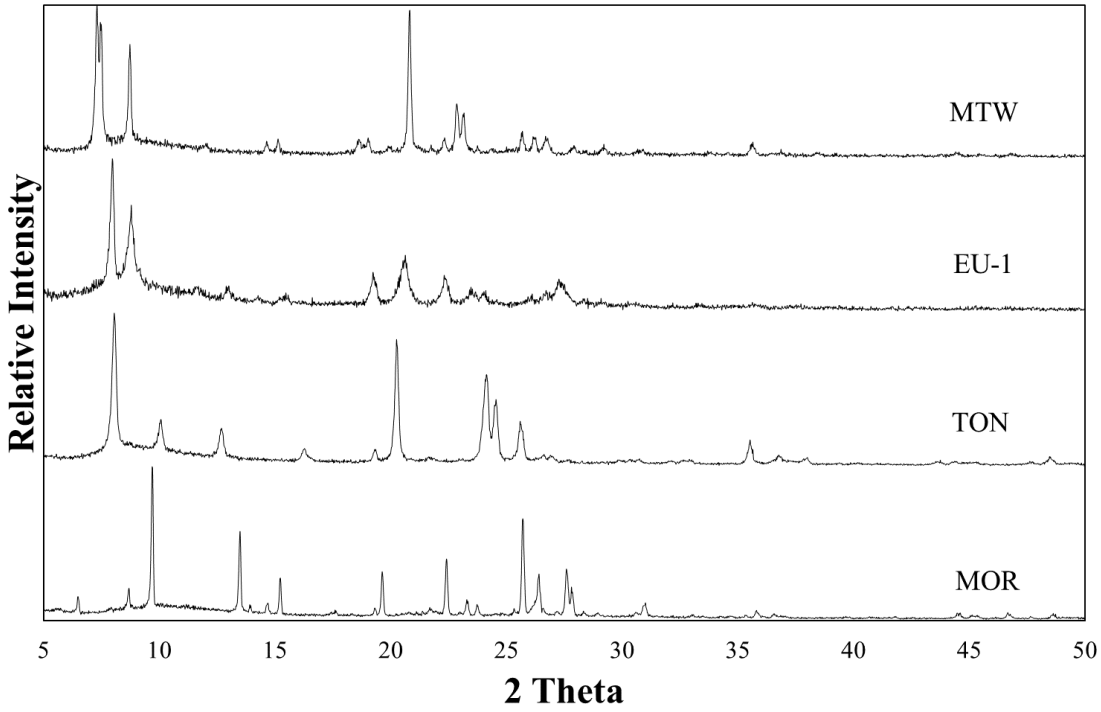

Figure A4 – XRD pattern of the investigated 1-dimensional zeolite catalysts

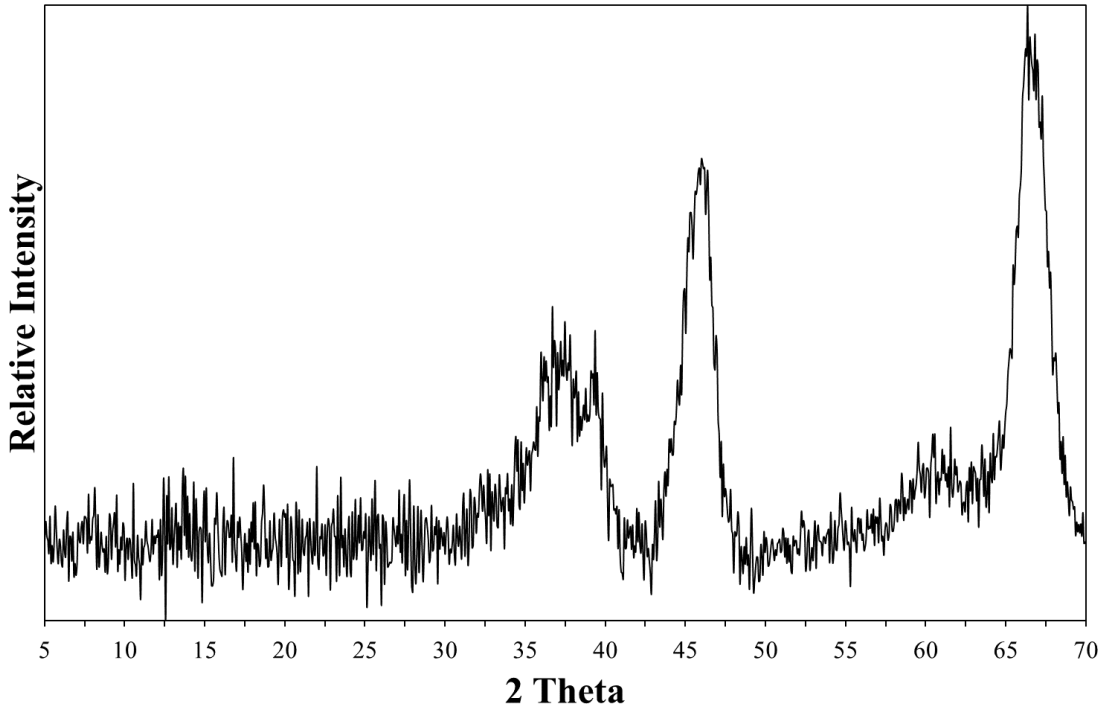

Figure A5 – XRD pattern of the investigated commercial γ-Al_2O_3

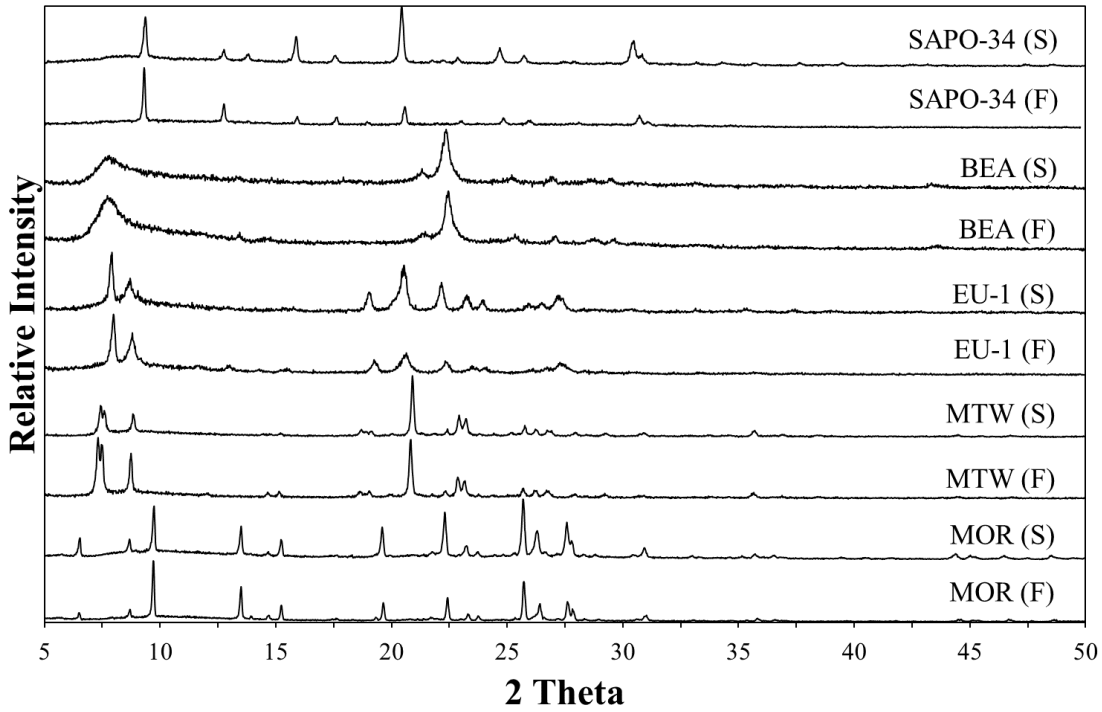

Figure A6 – XRD pattern of the fresh (F) and spent (S) catalysts.

APPENDIX B

Adsorption isotherms of N_2 at 77 K of the investigated catalysts

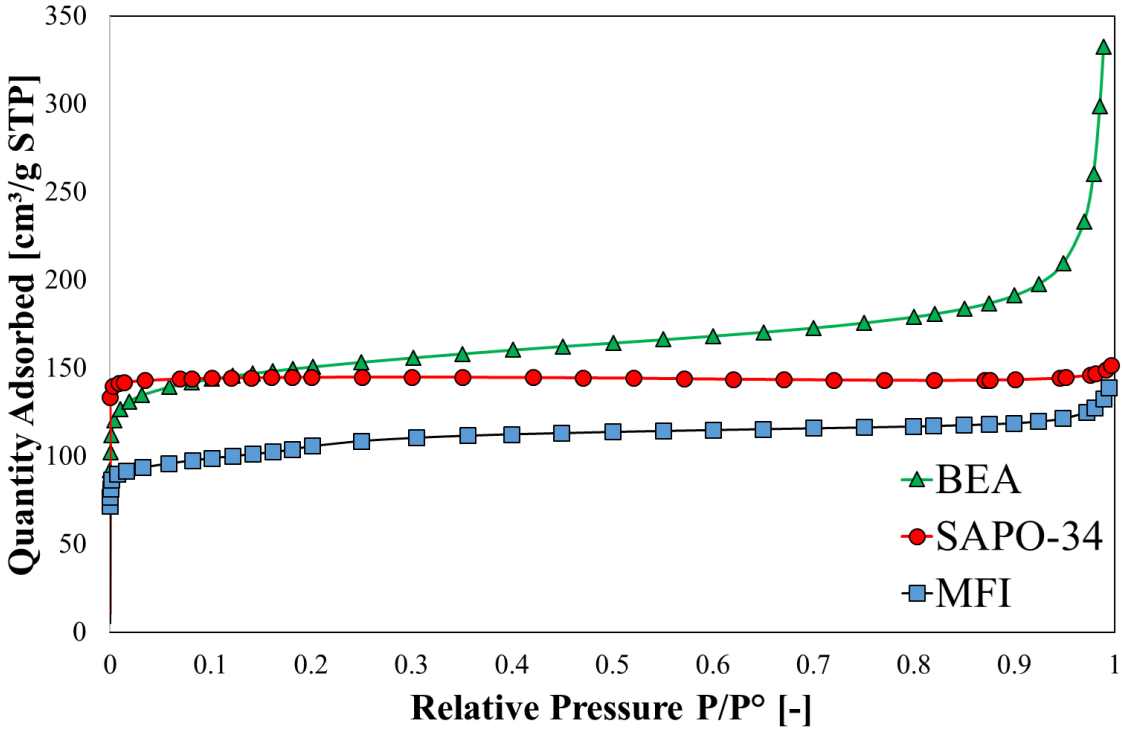

Figure B1 – N_2 adsorption isotherms at 77 K of investigated 3-dimensional molecular sieves catalysts

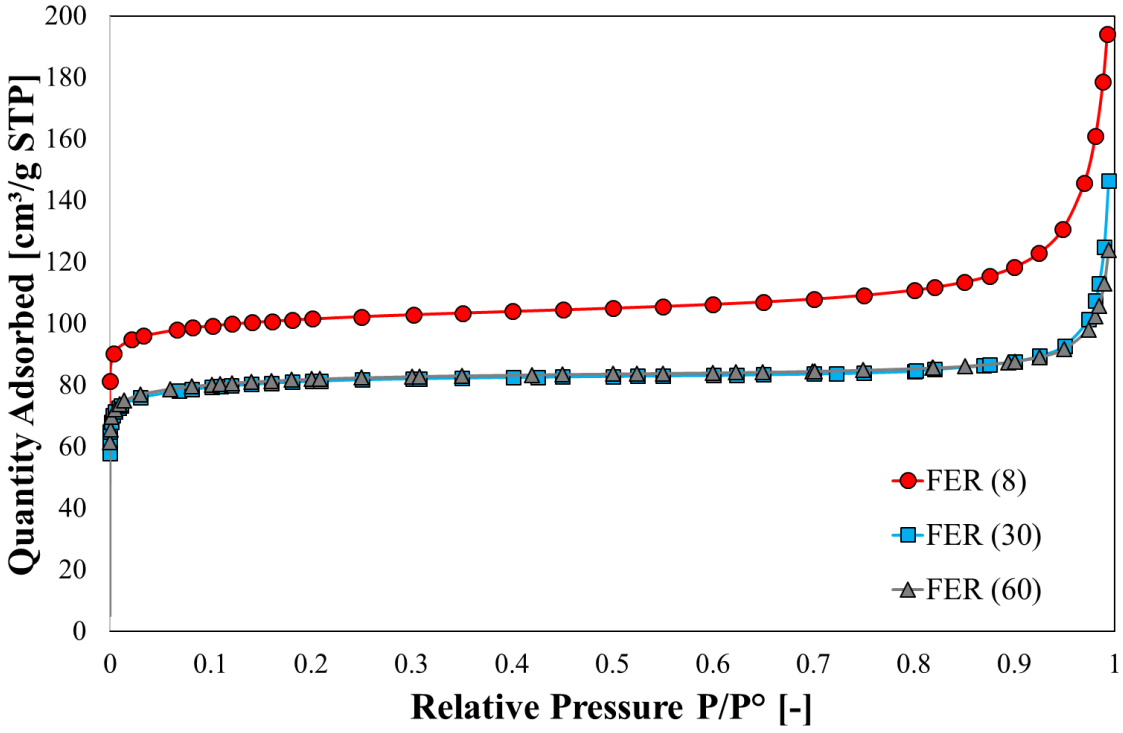

Figure B2 – N_2 adsorption isotherms at 77 K of FER samples synthesised with different Si/Al ration (the relative Si/Al value is indicated in brackets)

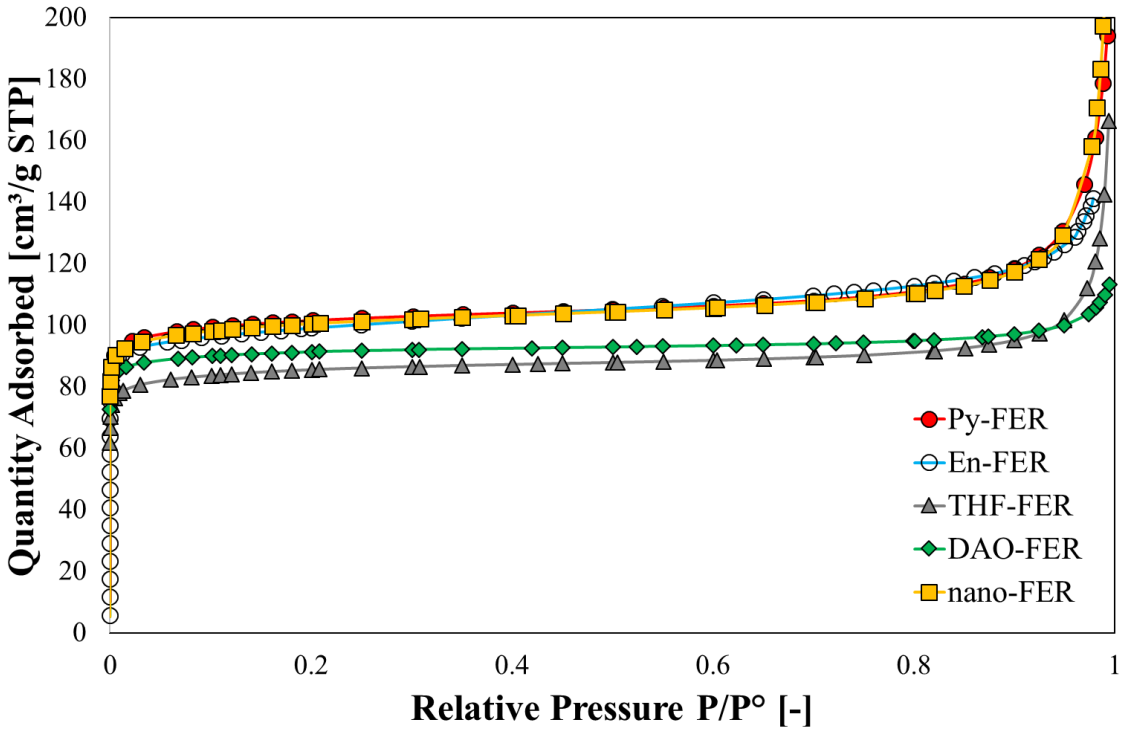

Figure B3 – N2 adsorption isotherms at 77 K of FER samples synthesised with different SDA (Py=pyrrolidne, En=ethylendiammine, DAO=1,8-diamminooctane, THF=tetrahydrofurane) and nanosized ferrierite crystals (nano-FER)

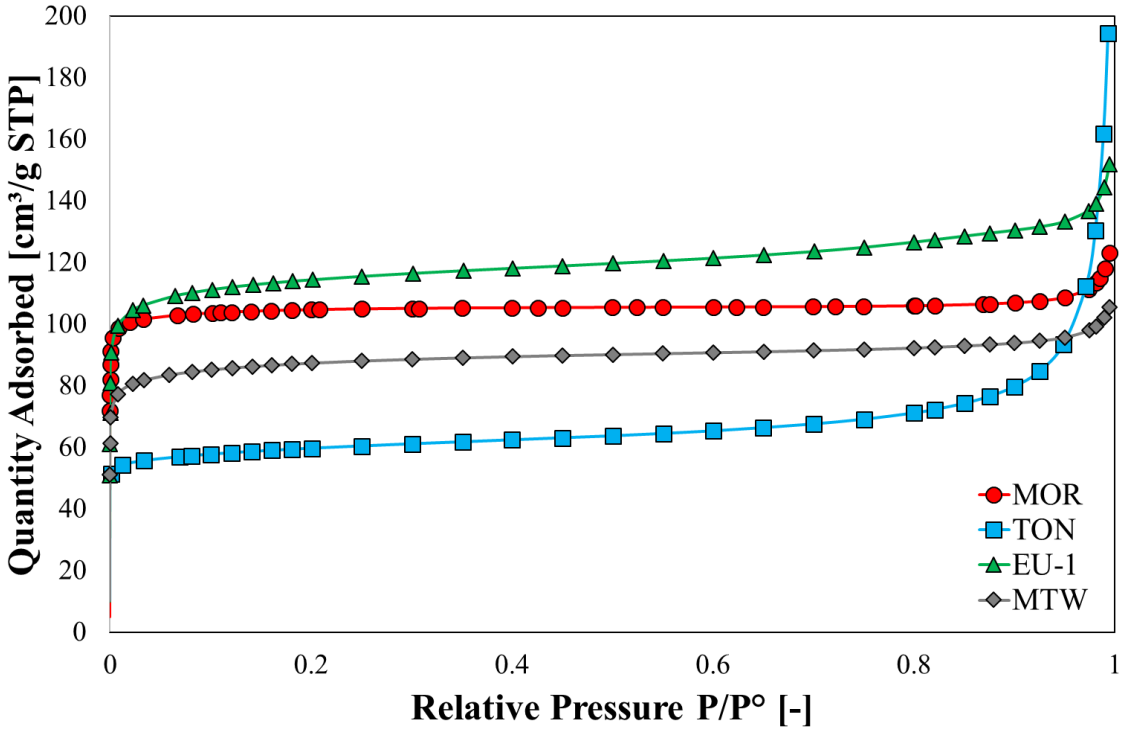

Figure B4 – N_2 adsorption isotherms at 77 K of the investigated 1-dimensional molecular sieves catalysts

List of Table

List of Figures

List of Publications

Paper I: *Kinetic analysis for methanol to dimethyl ether reaction over H-MFI catalyst*, M. Migliori, A. Aloise, E. Catizzone G. Giordano, **Industrial and Engineering Chemistry Research**, 53 (2014) 14885-14891.

Paper II: *Dimethyl ether synthesis via methanol dehydration: effect of zeolite structure,* E. Catizzone, A. Aloise, M. Migliori, G. Giordano, **Applied Catalysis A: General**, 502 (2015) 215-220.

Paper III: *Stepwise tuning of metal-oxide and acid sites of CuZnZr-MFI hybrid catalysts for the direct DME synthesis by CO_2 hydrogenation*. F. Frusteri, G. Bonura, C. Cannilla, G. Drago Ferrante, A. Aloise, E. Catizzone, M. Migliori, G. Giordano, **Applied Catalysis B: Environmental**, 176-177 (2015) 522-531.

Paper IV: *Catalytic features of CuZnZr-zeolite hybrid systems for the direct CO_2-to-DME hydrogenation reaction,* G. Bonura, F. Frusteri, C. Cannilla, G. Drago Ferrante, A. Aloise, E. Catizzone, M. Migliori, G. Giordano, **Catalysis Today**, 277 (2016) 48-54.

Paper V: *Modelling of adsorption of textile dyes over multi-walled carbon nanotubes: equilibrium and kinetic,* D. Vuono, E. Catizzone, A. Aloise, G. Giordano, R. G. Agostino, A. Policicchio, **Chinese Journal of Chemical Engineering**, 25 (2017) 523-532

Paper VI: *The effect of FER zeolite acid sites in methanol-to-dimethyl ether catalytic dehydration,* E.Catizzone, A. Aloise, M. Migliori, G. Giordano, **Journal of Energy Chemistry**, 2017, DOI: 10.1016/j.jechem.2016.12.005

Paper VII: *From 1-D to 3-D zeolite structure: performance assessment in catalysis of vapour-phase methanol dehydration to DME,* E. Catizzone, A. Aloise, M. Migliori, G. Giordano, **Microporous and Mesoporous Materials**, 243 (2017) 102-111.

Paper VIII: *Direct CO_2-to-DME hydrogenation reaction: evidences of superior behaviour of FER-based hybrid systems to obtain high DME yield,* G. Bonura, F. Frusteri, M. Migliori, C.Cannilla, L. Frusteri, E.Catizzone, A. Aloise, G. Giordano, **Journal of CO_2 Utilization**, 18 (2017) 353-361.

Paper IX: *Catalytic behaviour in propane aromatization using Ga-MFI catalyst,* A. Aloise, E. Catizzone, M. Migliori, J. B.Nagy, G. Giordano, **Chinese Journal of Chemical Engineering** (2017), in press.

List of Publications in preparation (May 2017)

Paper I: *DME synthesis by methanol dehydration reaction over different zeolites: features on carbon formation evolution affecting catalyst stability,* M. Migliori, E. Catizzone, A. Aloise, G. Bonura, L. Frusteri, C. Cannilla, F. Frusteri, G. Giordano, *to be submitted* (2017).

Paper II: *Propane aromatization over H-Ga-MFI zeolites: experimental investigation and kinetic modellingt,* Massimo Migliori, Alfredo Aloise, Enrico Catizzone, Alessio Caravella, Girolamo Giordano, *in preparation* (2017).

Paper III *Tailoring of physicochemical and catalytic properties of FER-type crystals by using different structure directing agents,* E. Catizzone, M. Migliori, A. Aloise, G. Giordano, V. Valtchev, *in preparation* (2017).

Conference contributions

I *Synthesis and catalytic performances evaluation of FER-based catalysts*, M. Migliori, E. Catizzone, A. Aloise, G. Braccio, G. Giordano, VI International Workshop on Oxide-based Materials joined with Annual Meeting of Italian Zeolite Association, September 21-24, 2016, Napoli, Italy, Poster communication.

II *Study of adsorption behaviour of multi-walled carbon nanotubes towards dyes applied in textile applications*, D. Vuono, E. Catizzone, A. Aloise, A. Policicchio, R.G. Agostino, M. Migliori, G. Giordano, VI International Workshop on Oxide-based Materials joined with Annual Meeting of Italian Zeolite Association, September 21-24, 2016, Napoli, Italy, Poster communication.

III *Effect of acidity on the FER catalytic activity in DME synthesis via methanol dehydration*, M. Migliori, E. Catizzone, A. Aloise, V. Valtchev, G. Giordano, International Congress on Catalysis 16th, July 3-8 , 2016, Beijing, China, Poster communication.

IV *Effect of organic template on crystal size and morphology of FER zeolite.* E. Catizzone, M. Migliori, A. Aloise, V. Valtchev, G. Giordano, International Zeolite Conference 18th, June 19-24 , 2016, Rio de Janeiro, Brazil, Oral communication

V *Synthesis of dimethyl ether: the role of acid sites of FER catalysts type.* M. Migliori, E. Catizzone, A. Aloise, V. Valtchev, G. Giordano, International Zeolite Conference 18th, June 19-24 , 2016, Rio de Janeiro, Brazil, Poster communication

VI *High efficient novel catalyst based on mixed oxides supported on bidimensional zeolite for one step DME production by CO_2 hydrogenation.* F. Frusteri, C. Cannilla, A. Mezzapica, M. Migliori, A. Aloise, E. Catizzone, G. Giordano, G. Bonura, International Zeolite Conference 18th, June 19-24 , 2016, Rio de Janeiro, Brazil, Poster communication.

VII *Stepwise tuning of multi-sites CuZnZr-HZSM5 Catalysts for direct DME synthesis from CO2-H2 mixtures*, F. Frusteri, G. Bonura, C. Cannilla, G. Drago Ferrante, A. Aloise, E. Catizzone, M. Migliori, G. Giordano,

EuropaCat-XII, August 30 – September 4, 2015, Kazan, Russia, Oral Communication

VIII *Synthesis of DME via methanol dehydration over zeolite catalysts: catalytic performances of FER, MOR and SAPO-34.* E. Catizzone, A. Aloise, M. Migliori, G. Giordano, International Symposium on Advanced Micro and Mesoporous Materials 6th, September 6 -9 , 2015, Burgas, Bulgaria, **Oral communication.**

IX *Effect of Ga-Al content and process parameter assessment in propane aromatization using Ga-MFI catalyst.* A. Aloise, I. Santoro, E. Catizzone, M. Migliori, J. B.Nagy, G. Giordano, International Symposium on Advanced Micro and Mesoporous Materials 6th, September 6 -9 , 2015, Burgas, Bulgaria, Poster communication.

X *Effect of zeolitic system on methanol to DME reaction.* M. Migliori, E. Catizzone, A. Aloise, G. Giordano, ZMPC 2015, June 28 – July 2, 2015, Sapporo, Japan, Oral communication.

XI *Catalytic behaviour in propane aromatization using Ga-MDFI catalyst,*A. Aloise, E. Catizzone, M. Migliori, J. B.Nagy, G. Giordano, CIS6 Conference joint with GIC2015 Congress and AIZ2015 Congress, June 14-17, 2015- Amantea (CS), Italy, Poster communication.

XII *Synthesis of DME via methanol dehydration over zeolite catalysts: comparison of catalytic performances of FER, MOR, BEA and SAPO-34*, E. Catizzone, A. Aloise, M. Migliori, G. Giordano, CIS6 Conference joint with GIC2015 Congress and AIZ2015 Congress, June 14-17, 2015- Amantea (CS), Italy, **Oral communication as winner of "G. Gottardi Award 2015"**.

XIII *Catalytic performance of different zeolite structures in Methanol to DME dehydration*, M. Migliori, E. Catizzone, A. Aloise, G. Giordano, 2nd Euro-Asia Zeolite Conference, January 25-28, 2015 – Nice, France, Oral Communication.

XIV *The influence of the zeolitic framework on the synthesis of dimethyl ether*, Invited lecture, M. Migliori, E. Catizzone, A. Aloise, G. Giordano, 3rd Workshop on zeolites, May 19-20, 2014- Caen, France.

XV *Kinetic analysis for methanol to DME dehydration over H-MFI zeolites*, M. Migliori, A. Aloise, E. Catizzone G. Giordano, TOCAT7 KYOTO2014, June 1-6 2014, Kyoto, Japan, Poster Communication.

XVI *Catalytic performance of different zeolites structure in methanol to DME dehydration*. M. Migliori, A. Aloise, E. Catizzone G. Giordano, Post-TOCAT7 KYOTO2014, Waseda University, June 7-8 2014, Tokyo, Japan, Poster Communication.

XVII *Effect of zeolite structure in methanol-to-dimethyl ether reaction*, M. Migliori, E. Catizzone, A. Aloise, G. Giordano, AIZ DAY 2014, September 6 2014, Unical, Rende (CS), Italy, **Oral Communication**.

XVIII *Effect of gallium substitution on MFI in propane aromatisation reaction,* A. Aloise, E. Catizzone, M. Migliori G. Giordano, AIZ DAY 2014, September 6 2014, Unical, Rende (CS), Italy, Oral Communication.

XIX *Dimethyl ether synthesis over H-ZSM-5:effect of hydrophobicity*, M. Migliori, E. Catizzone, A. Aloise, G. Giordano, AIZ DAY 2014, September 6 2014, Unical, Rende (CS), Italy, Oral Communication.

XX *Dimethyl ether synthesis via methanol dehydration: effect of zeolite structure*. E. Catizzone, A. Aloise, M. Migliori, G. Giordano, XXV Congresso della Società Chimica Italiana, September 7-12 2014, Unical, Rende (CS), Italy, Oral Communication

XI *Effect of zeolite acidity in hybrid Cu-ZnO-ZrO2/H-ZSM-5 system for one step synthesis of DME by CO2 hydrogenation*. G. Bonura, C. Cannilla, F. Frusteri, M. Migliori, A. Aloise, E. Catizzone, G. Giordano, 6th FEZA Conference, September 8-11 2014, Leipzig, , Germany, Oral Communication.

Scientific Awards

Winner of XII "Glauco Gottardi Award" conferred by AIZ Italian Zeolite Association

during CIS6 Conference joint with GIC2015 Congress and AIZ2015 Congress, June 14-17, 2015- Amantea (CS), Italy